AD-A189 258 COMPOSITES STRENGTHENING(U) MARYLAND UNIV COLLEGE PARK 1/2
METALLURGICAL MATERIALS LAB R J ARSENAULT NOV 87
MML-1987-1 N00014-85-K-0007

UNCLASSIFIED F/G 11/4 NL

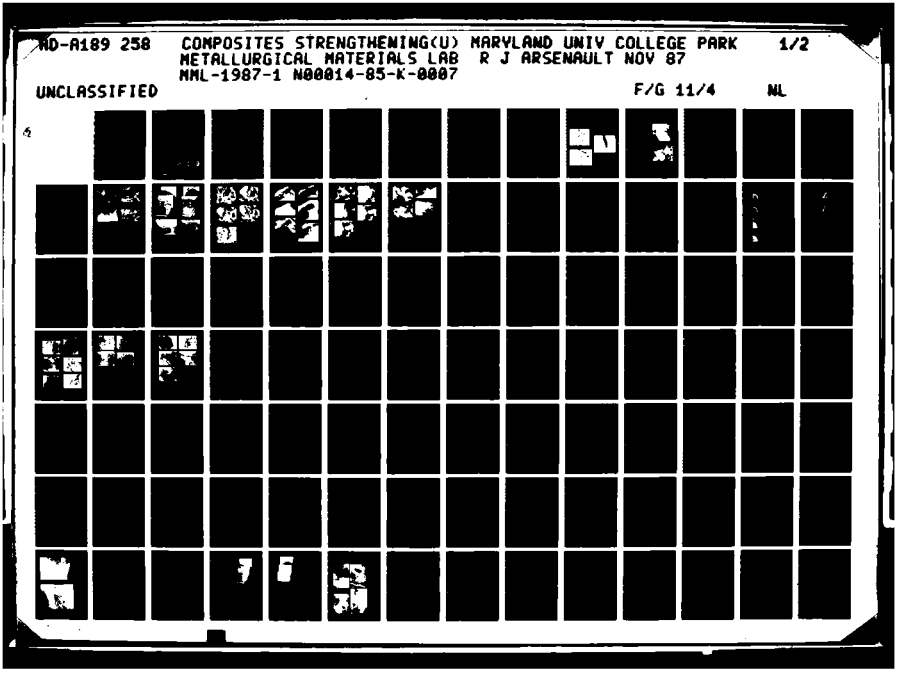

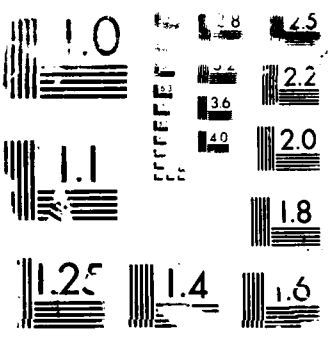
1.0
1.1
1.25
1.4
1.6
1.8
2.0
2.2
2.5
3.6
4.0

COMPOSITE STRENGTHENING

FINAL REPORT

OF

N00014-85-K-0007

FROM

OFFICE OF NAVAL RESEARCH

BY

R.J. ARSENAULT

METALLURGICAL MATERIALS LABORATORY

UNIVERSITY OF MARYLAND

COLLEGE PARK, MD 20742-2111

NOVEMBER 1987

REPORT DOCUMENTATION PAGE

1a REPORT SECURITY CLASSIFICATION: None	1b RESTRICTIVE MARKINGS
2a SECURITY CLASSIFICATION AUTHORITY: None	3. DISTRIBUTION/AVAILABILITY OF REPORT
2b DECLASSIFICATION/DOWNGRADING SCHEDULE: None	
4 PERFORMING ORGANIZATION REPORT NUMBER(S): MML-1987-1	5. MONITORING ORGANIZATION REPORT NUMBER(S)
6a NAME OF PERFORMING ORGANIZATION: University of Maryland; 6b. OFFICE SYMBOL (If applicable)	7a. NAME OF MONITORING ORGANIZATION
6c ADDRESS (City, State and ZIP Code): Chemical Engineering Bldg., University of Maryland, College Park, Md 20742-2111	7b. ADDRESS (City, State and ZIP Code)
8a. NAME OF FUNDING/SPONSORING ORGANIZATION: Office of Naval Research; 8b. OFFICE SYMBOL (If applicable): N00014	9. PROCUREMENT INSTRUMENT IDENTIFICATION NUMBER
8c. ADDRESS (City, State and ZIP Code): Program Mgr., Non-Metallic Materials Div., Office of Naval Research, Code 1131N, Arlington, Va 22217-5000	10. SOURCE OF FUNDING NOS.
11 TITLE (Include Security Classification): Composite Strengthening	
12 PERSONAL AUTHOR(S): Richard J. Arsenault	
13a TYPE OF REPORT: Final; 13b. TIME COVERED: FROM 1985 TO 1987	14. DATE OF REPORT (Yr., Mo., Day): 1987 Nov.
16 SUPPLEMENTARY NOTATION	15. PAGE COUNT: 169

PROGRAM ELEMENT NO.	PROJECT NO.	TASK NO.	WORK UNIT NO.

17 COSATI CODES			18. SUBJECT TERMS (Continue on reverse if necessary and identify by block number)
FIELD	GROUP	SUB. GR.	

19 ABSTRACT (Continue on reverse if necessary and identify by block number)

In all cases of discontinuous SiC/Al metal matrix it was previously shown that classical composite strengthening mechanisms could not be used to explain the data. A high dislocation density model was proposed to account for the strengthening, but other factors such as residual stress and texture could contribute. These were investigated and it was shown that texture had no effect and residual stress reduced the tensile yield stress. The fracture process is matrix controlled up to SiC particle sizes of 20 μm and above where fracture of SiC begins to dominate. The matrix is influenced by residual hydrostatic tension and high density of dislocations generated at SiC/Al interfaces. Crack initiation fracture toughness does not depend on SiC particle size. Crack growth fracture toughness increases as the size of the SiC particles increases.

20 DISTRIBUTION/AVAILABILITY OF ABSTRACT	21. ABSTRACT SECURITY CLASSIFICATION
UNCLASSIFIED/UNLIMITED ☒ SAME AS RPT. ☐ DTIC USERS ☐	None

22a NAME OF RESPONSIBLE INDIVIDUAL	22b TELEPHONE NUMBER (Include Area Code)	22c OFFICE SYMBOL
Richard J. Arsenault	301-454-4075	

DD FORM 1473, 83 APR EDITION OF 1 JAN 73 IS OBSOLETE.

TABLE OF CONTENTS

Summary

In all cases of discontinuous SiC/Al metal matrix it was previously shown that classical composite strengthening mechanisms could not be used to explain the data. A high dislocation density model was proposed to account for the strengthening, but other factors such as residual stress and texture could contribute. These were investigated and it was shown that texture had no effect and residual stress reduced the tensile yield stress. The fracture process is matrix controlled up to SiC particle sizes of 20 μm and above where fracture of SiC begins to dominate. The matrix is influenced by residual hydrostatic tension and high density of dislocations generated at SiC/Al interfaces. Crack initiation fracture toughness does not depend on SiC particle size. Crack growth fracture toughness increases as the size of the SiC particles increases.

Following is a list of the publications and copies of the publications which resulted from the research supported by contract number N00014-85-K-0007.

LIST OF PUBLICATIONS
RESEARCH SUPPORTED BY N00014-85-K-0007

1. ANOMALOUS DIFFUSION AT INTERFACES IN METAL COMPOSITES
   R.J. Arsenault and C.S. Pande, The Interface Migration and Control of Microstructure, ed. C.S. Pande, et al., AIME 1986.

2. AN IN SITU HVEM STUDY OF DISLOCATION GENERATION AT Al/SiC INTERFACES IN METAL MATRIX COMPOSITES
   M. Vogelsang, R.J. Arsenault and R.M. Fisher, Met. Trans. 17A (1986) 379.

3. DEFORMATION IN SiC/Al COMPOSITES DUE TO THERMAL STRESSES
   Y. Flom and R.J. Arsenault, Mat. Sci. Eng. 75 (1985) 151.

4. INTERFACIAL BOND STRENGTH IN AN ALUMINUM ALLOY 6061-SiC COMPOSITE
   Y. Flom and R.J. Arsenault, Mat. Sci Eng. 77 (1986) 191.

5. THE EFFECTS OF DIFFERENCES IN THERMAL COEFFICIENTS OF EXPANSION IN SiC WHISKER 6061 ALUMINUM COMPOSITES
   R.J. Arsenault and M. Taya, Proc. 5th Internatl. Conf. Composite Materials, ed., W.C. Harrigan, Jr., et al. (1985) 21.

6. THERMAL RESIDUAL STRESS IN METAL MATRIX COMPOSITE
   R.J. Arsenault and M. Taya, Acta Met. 35 (1987) 651.

7. UNUSUAL ASPECTS OF THE BAUSCHINGER EFFECT IN METALS AND METAL MATRIX COMPOSITES
   Materials Forum, 1 (1987) 10.

8. DISLOCATION GENERATION DUE TO DIFFERENCES IN COEFFICIENTS OF THERMAL EXPANSION
   R.J. Arsenault and N. Shi, Mat. Sci. Eng. 81 (1986) 175.

9. DEFORMATION OF SiC/Al COMPOSITES
   Y. Flom and R.J. Arsenault, J. of Metals 38 (1986) 31.

10. A COMPARISON BETWEEN A SHEAR LAG TYPE MODEL AND AN ESHELBY TYPE MODEL IN PREDICTING THE MECHANICAL PROPERTIES OF A SHORT FIBER COMPOSITE
    M. Taya and R.J. Arsenault, Scripta Met. 21 (1987) 349.

11. STRENGTH DIFFERENTIAL AND BAUSCHINGER EFFECTS IN SiC/Al COMPOSITES
    R.J. Arsenault and S.B. Wu, Mat. Sci. Eng. 96 (1987) 77.

12. THE STRENGTHENING OF SiC/Al COMPOSITES DUE TO DIFFERENCES IN THE MATRIX AND SiC MORPHOLOGY
Composites '86: Recent Advances in Japan and the United States, Proc. Japan-U.S. CCM-III, ed. K. Kawata, et al., Tokyo (1986) 521.

13. DEFORMATION OF SiC/Al COMPOSITES
Mechanical Behavior of Materials, ed. M.G. Yan, S.H. Zhang and Z.M. Zhang (1987) 1253.

14. FRACTURE OF SiC/Al COMPOSITES
Y. Flom and R.J. Arsenault, ICCM VI and ECCM 2, ed F.L. Mathews, et al. (1987) 2.189.

15. STRENGTHENING MECHANISMS IN DISCONTINUOUS SiC/Al COMPOSITES
Composite Structures, ed. I.H. Marshall (1987) 70.

16. ROLE OF INTERFACES IN SiC/Al COMPOSITES
R.J. Arsenault and Y. Flom, Structure and Deformation of Boundaries, ed. K.N. Subramanian and M.A. Iman, AIME (1986) 261.

ANOMALOUS DIFFUSION AT INTERFACES IN METAL-MATRIX COMPOSITES

R. J. Arsenault
University of Maryland
College Park, MD 20740, USA

C. S. Pande
Naval Research Laboratory
Washington, DC 20375-5000, USA

ABSTRACT

A basic premise of most theories of composite strengthening is that a bond of some type exists between the matrix and the reinforcement. Such bonding, in two composites, Al-SiC, and Cu-W was investigated by high resolution electron microscopy and scanning Auger microprobe analysis. The chemistry and microstructure of the interfaces were investigated in detail. Surprisingly high penetration of the matrix into the reinforcement was detected by the Auger analysis. Independent x-ray analysis in thin films of the composites in STEM confirmed the Auger results in Al-SiC. Observed penetration depths were several order of magnitudes higher than that predicted by a bulk diffusion mechanism.

IN ORDER TO HAVE OBSERVABLE PENETRATION of one element (A) into a solid block of a second element (B) at least two requirements have to be satisfied: first, there has to be some solubility of A in B, and second, the rate, i.e., the diffusivity, has to be rapid enough so that the investigation can be completed in a reasonable amount of time. Because of the considerable interest in composites consisting of SiC in Al alloys matrices (1,2), the nature of the interface between SiC and Al is important.

There have been several investigations of the diffusion of Al into SiC (3,4), where Al is used as an agent in the sintering of SiC. Al has also been used in the joining of SiC pieces (5). Chang et al (3) and Tajima et al (4) obtained the activation energy of diffusion and D_0. However, these investigations were conducted at high temperatures (~2000 K). A solubility limit of 1 wt% Al in SiC at 2073 K was determined by an ion implantation investigation (6). There have been several investigations of the reaction of Al and SiC to determine the conditions under which Al_4C_3 will form (7-9). All of these investigations were conducted at temperatures above the melting point of Al, and in most cases reactions were reported. Iseki et al conducted a systematic investigation of the reaction molten Al with two different types of sintered SiC (5). In one case, they observed a reaction with the formation of particles of Al_4C_3 of about 0.1 to 1 μm in diameter. In the other case (which had excess Si in the SiC) Al_4C_3 did not form, but they did find, by means of transmission electron microscopy (TEM), that cracks had formed in the SiC due to the difference in thermal coeficient of expansion.

The purpose of this investigation was to determine whether a reaction between Al and SiC had occurred during the fabrication of commercial SiC/Al composites produced by ARCO-Silag and DWA. We also wanted to determine if any Si or C had diffused into the Al matrices or if the highly unlikely case of Al diffusion into SiC had occurred.

RESULTS

A scanning Auger microprobe analysis* was undertaken of fractured SiC/Al samples from composites purchased from ARCO-Silag. These samples were produced by hot pressing Al powder and SiC whiskers, followed by hot extrusion. Although the exact maximum temperature to which the composite was exposed is not known, it was less than 933 K. These samples were fractured in the scanning Auger microprobe and examined shortly thereafter. There were no differences in signal as a function of position; in other words, a 100% Al signal was obtained from the matrix as well as from all possible areas on the SiC whiskers, as

Research support in part by the Office of Naval Research under Contract No. N00014-85-K-0007

*The Auger microprobe analysis was performed at the Center for Research in Surface Science and Submicron Analysis, Montana State University.

shown in Figure 1. A possible explanation of the essentially 100% Al content on the whisker is that the Al could just be mechanically adhering. This is analogous to having a coating of butter on a knife when it is pulled out of a tub of butter. Therefore, a series of etching experiments were conducted in the microprobe, but it was only after considerable sputtering (which is basically an Ar ion milling operation) that a Si and C signal could be obtained. The sputtered etching was interrupted at intervals and surfaces of the whiskers were examined, there were no indications of SiO_2, Al_2O_3, Al_4C_3. The fracture surface had to be sputter etched to a considerable depth before Si or C was detectable. Figure 2 is a scanning electron micrograph (SEM) taken in the microprobe after sufficient sputter etching had taken place so that SiC could be detected. This result led us to the belief that the Al had diffused into the SiC.

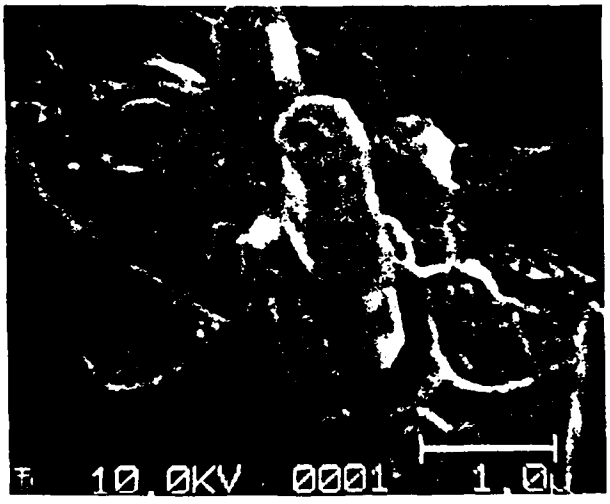

Fig. 1 - A SEM micrograph taken in the Auger microprobe of the fracture surface of a whisker SiC-Al composite.

Fig. 2 - A SEM micrograph taken in the Auger microprobe of the surface of SiC-Al composite after sputter etching (Ar ion milling).

In order to determine whether this is a real effect and not a sputtering artifact, several samples, which were metallographically polished, were examined in the Auger microprobe. The data from a platelet of SiC sample from DWA, are shown in Figure 3. The samples were produced by hot pressing Al alloy powder with platelet SiC, and again, the exact temperature at which the hot pressing occurred is not known. In the SEM the scanning Auger probe traces are superimposed: one for Al and the other for Si. This shows that Al has penetrated or diffused into the SiC, but there is no Si or C in the matrix. When the sample was sputter etched and the process repeated, the result was basically the same. In order to determine the effect of sputtering (i.e., could the sample surface become cross-contaminated by the sputtering operation), the sample was removed, etched slightly with Keller's etch, and then put back into the microprobe. The process was then repeated and again the same results were obtained. Figure 4 is the detailed Auger probe analysis of the Si and Al traces; the C trace superimposes right on the Si trace. The interface is then defined as having finite width which is the maximum probe size that is associated with the scanning microprobe apparatus.

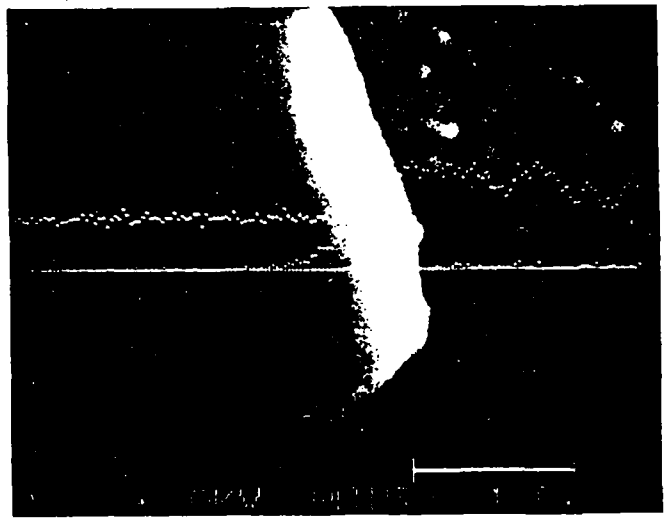

Fig. 3 - A SEM micrograph taken in the Auger microprobe, on which the Al and Si Auger probe traces have been superimposed.

A scanning transmission electron microscope (STEM) analysis was conducted on SiC/Al samples in order to further validate these results, and Figure 5 is a result of an energy dispersive X-ray analysis from the STEM using a thin foil of the composite. It is obvious that again there is evidence of Al diffusion into the SiC. In this particular case the probe size is much smaller (~5.0 nm) than that in the scanning Auger analysis. The thickness of the specimen was 100-150 nm (accelerating voltage, of the electrons 200 kV); thus, the spatial resolution of the technique was about 30 nm, several times times smaller than the range of penetration observed.

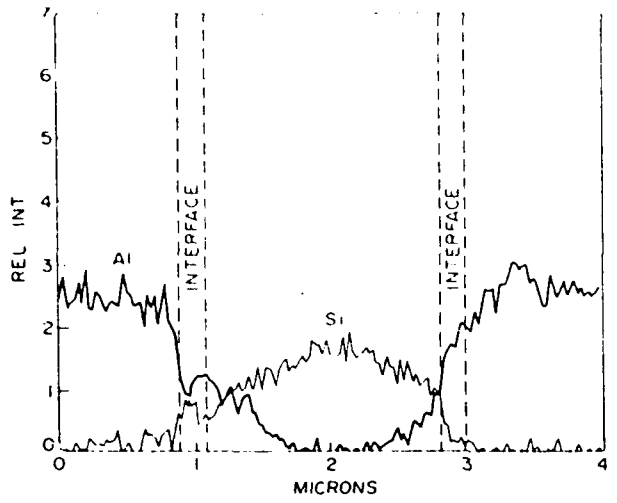

Fig. 4 - An Auger microprobe analysis of SiC-Al. The relative intensities of Si and Al are plotted across the matrix, a particle of SiC and again the matrix.

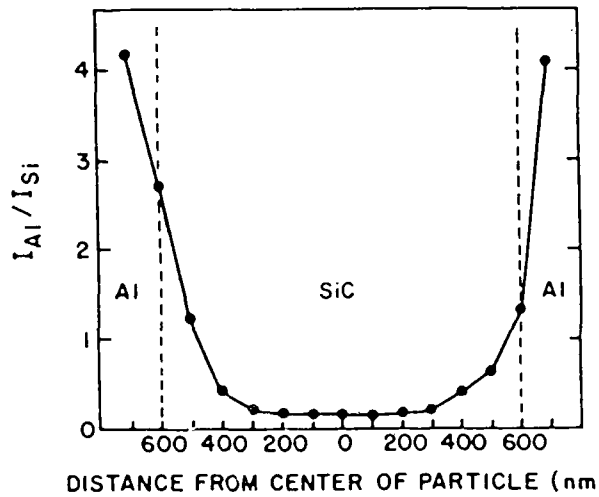

Fig. 5 - A STEM EDAX analysis of Al concentration as a function of location (I_{Al}/I_{Si} plotted in arbitrary units).

DISCUSSION

In the Introduction, it was mentioned that a solubility limit of 1 wt% Al in SiC had been measured at 2073 K. However, the maximum temperature to which these samples were exposed was less than 933 K. Warren and Anderson have theoretically produced two constant temperature terniary diagrams at 773 K and 1073 K for SiC-Al-C. In both of these diagrams there is zero solubility of Al in SiC. However, from the second law of thermodynamics the presence of Al in SiC can be explained, for is a reduction in the free energy due to entropy of mixing, but if the solubility limit is 1 wt% at 2073 K it is very difficult to understand how the solubility could be greater at less than 933 K. If an approximation is made for the relative intensities of SiC and Al, it appears that there is a significant concentration of Al in the SiC. The nature of the Al in SiC, i.e., whether it is interstitially, substitutionally, or nonuniformally distributed, is not known. It may be possible that very small microcracks occur along the microtwin boundaries in the SiC. Figures 6 and 7 are TEM of a SiC whisker and a SiC platelet, respectively. The stirations in the SiC have been identified as microtwins (10). It should be kept in mind that Iseki and co-workers (5) has reported the existence of microcracks in SiC due to difference in coefficient of thermal expansion between Al and SiC.

Fig. 6 - A TEM micrograph of SiC whisker produced by ARCO-Silag.

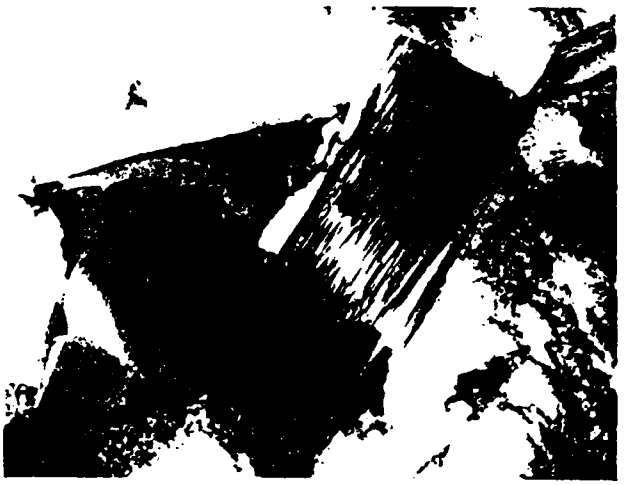

Fig. 7 - A TEM micrograph of a SiC platelet which was produced by DWA.

As stated above, the observations of Al penetration into SiC to the extent observed are unexpected. There have been at least two investigations of Al diffusion into SiC (3,4), and from those investigations it is possible to calculate the mean diffusion distance X at 773 K,

$$X = \sqrt{Dt} \quad (1)$$

where $D = D_0 e^{-Q/RT}$, t is the time of diffusion, Q for Al-SiC system is 471 kJ/mol, and D_0 equals 1.8 cm^2/sec. The value of X is less than 0.1 nm per year. (The values of D_0 and Q given in literature vary substantially from each other. However, all of these values give a value of X orders of magnitude lower than the observed penetration.) Obviously, this does not agree with the present data.

CONCLUSIONS

From a consideration of the experimental results, the following conclusions can be made:

1. It is highly unlikely that the presence of Al in SiC can be explained by a conventional diffusion analysis.
2. It is possible that the penetration observed is due to the presence of Al along microcracks which may occur at the microtwin interfaces. The microtwin interfaces themselves should not act as short circuit diffusion packs.
3. It is possible that the observed penetrations of Al into SiC are experimental artifacts.

ACKNOWLEDGMENTS

The authors wish to acknowledge M. Lammers of the University of Maryland for assistance with the experiments. Liaison with Dr. S. Fishman of the Office of Naval Research in Arlington, VA has been very helpful to this project.

REFERENCES

1. Arsenault, R.J., Met. Sci. and Eng. 64, 171 (1984).
2. Arsenault, R.J. and Fischer, R.M., Scripta Met 17, 67 (1983).
3. Chang, H.C., LeMay, C.Z., and Wallace, L.F., "Silicon Carbide," p. 496, Pergamon Press, Oxford (1960).
4. Tajima, Y., Kijima, K. and Kinery, W.D., J. Chem. Phys. 77, 2592 (1982).
5. Iseki, T., Kameda, T., and Maruyama, T., J. Mater. Sci. 19, 1692 (1984).
6. Tajima, Y. and Kinery, W.D., Com. of the Am. Cer. Soc., C-27 (1982).
7. Clinton, D.J., Lay, L.A., and Morrell, R., NPL Rept. Chem. 113, 4 (1980).
8. Kohara, S. and Muto, N., J. Jpn. Inst. Met. 45, 411 (1981).
9. Naidich, N.B. and Nevodnik, G.M., Bull. Acad. Sci.-USSR-Inorganic Materials 5, 2066 (1969).
10. Feng, J., unpublished research of the Metal. Mat. Lab., University of Maryland (1980).

An *In Situ* HVEM Study of Dislocation Generation at Al/SiC Interfaces in Metal Matrix Composites

MARY VOGELSANG, R. J. ARSENAULT, and R. M. FISHER

Annealed aluminum/silicon carbide (Al/SiC) composites exhibit a relatively high density of dislocations, which are frequently decorated with fine precipitates, in the Al matrix. This high dislocation density is the major reason for the unexpected strength of these composite materials. The large difference (10:1) between the coefficients of thermal expansion (CTE) of Al and SiC results in sufficient stress to generate dislocations at the Al/SiC interface during cooling. In this *in situ* investigation, we observed this dislocation generation process during cooling from annealing temperatures using a High Voltage Electron Microscope (HVEM) equipped with a double tilt heating stage. Two types of bulk annealed composites were examined: one with SiC of discontinuous whisker morphology and one of platelet morphology. In addition, control samples with zero volume percent were examined. Both types of composites showed the generation of dislocations at the Al/SiC interface resulting in densities of at least 10^{13} m^{-2}. One sample viewed end-on to the whiskers showed only a rearrangement of dislocations, whereas, the same material when sectioned so that the lengths of whiskers were in the plane of the foil, showed the generation of dislocations at the ends of the whiskers on cooling. The control samples did not show the generation of dislocations on cooling except at a few large precipitate particles. The results support the hypothesis that the high dislocation density observed in annealed composite materials is a result of differential thermal contraction of Al and SiC. The SiC particles act as dislocation sources during cooling from annealing temperatures resulting in high dislocation densities which strengthen the material.

I. INTRODUCTION

THE incorporation of 20 vol pct discontinuous SiC whiskers into a 6061 Al matrix increases the yield strength of annealed powder compacted 6061 Al alloy by more than a factor of two. This increase in strength cannot be explained directly by continuum mechanics theories. Continuum mechanics formulations developed by Piggott[1] and applied to the case of discontinuous Al/SiC composites by Arsenault[2] predict an ultimate strength of only 186 MPa for 20 vol pct SiC composite, whereas the measured value of ultimate strength for this material is 448 MPa. Arsenault and Fisher[3] proposed that the increased strength could be accounted for by a high dislocation density in the Al matrix which is observed in bulk composite material annealed for as long as 12 hours at 810 K.

The dislocation generation mechanism proposed by Arsenault and Fisher to account for this high dislocation density is based on the large difference (10:1) in coefficients of thermal expansion (CTE) of Al and SiC.[4] When the composite is cooled from elevated temperatures of annealing or processing, misfit strains occur due to differential thermal contraction at the Al/SiC interface which are sufficient to generate dislocations.

Chawla and Metzger, in an elegant investigation of Cu/W composites using etch-pitting techniques, observed a high dislocation density at the Cu/W interface which decreased with increasing distance from the interface.[5] They observed that if the volume fraction of W was 15 pct, the minimum dislocation density in the matrix was 7×10^{11} m^{-2} increasing to 4×10^{12} m^{-2} at the interface of W and Cu, and concluded that the dislocations were caused by the differences (4:1) in CTE of Cu and W. Recalling that the CTE difference between Al and Si is 10:1, *i.e.*, more than twice as great as the Cu/W system, one would expect thermal stresses in Al/SiC to be sufficient to generate dislocations in this composite.

Other causes may also contribute to the high dislocation density observed in annealed Al/SiC material. Dislocations are introduced into this material during the plastic deformation processes of manufacturing, such as extrusion. During annealing, the dislocations introduced during processing may not be annihilated; they could be trapped by the SiC, resulting in a high dislocation density after annealing.

It is important to determine the origins of the high dislocation density in the composite since the strength of the composite depends on the high density. If the differential thermal contraction is the cause of the dislocations, as Arsenault and Fisher[3] suggest, then dislocations should be observed being generated in a composite thin foil sample on cooling from annealing temperatures in an *in situ*, HVEM experiment.

In situ dynamic HVEM experiments have certain advantages over other experimental techniques. The major advantage is that direct observation of a dynamic process altering a microstructure is possible while the deforming force, in this case a thermal stress, is operating. Operating at higher voltages allows penetration of thicker samples so that surface effects are minimized and bulk behavior is more closely approximated. Also, a high voltage microscope can better accommodate special stages required for *in situ* work because of the large pole piece region.

Numerous *in situ* HVEM heating stage investigations of Al have been performed. Hale *et al.*[6] and Caillard and Martin[7] investigated dislocation motion during creep at

MARY VOGELSANG and R. J. ARSENAULT, Director, are with the Metallurgical Materials Laboratory, University of Maryland, College Park, MD 20742. R. M. FISHER is with Center for Advanced Materials, Lawrence Berkeley Laboratory, University of California, Berkeley, CA 94720.

Manuscript submitted April 8, 1985.

elevated temperatures using HVEM. Kivilahti *et al.*[8] observed an Al-2 pct Mg alloy *in situ* during recovery processes at elevated temperatures recording dislocation interactions on videotape. Shimotomori and Hasiguti[9] observed *in situ* prismatic punching of dislocation loops at second phase precipitates in an Al-1.3 pct Li alloy. Electron irradiation of Al at elevated temperatures has been extensively studied using HVEM.[10,11]

There have been several non-dynamic, non-*in situ* TEM investigations of dislocations about particles in a metal matrix. Weatherly[12] observed multiple slip mode dislocation tangles around silica in Cu, and concluded they were caused by differential thermal contraction of the two materials on quenching. Ashby *et al.*[13] observed dislocations about pressurized silica-Cu, noting a critical size dependence for dislocation generation. Williams and Garmong[14] reported a high incidence of dislocations at the Ni/W interface in this directionally solidified eutectic composite.

Calculations of the dislocation density in Al/SiC due to thermal stresses predict high dislocation densities. The misfit strain which develops at the circumference of a 1 μm diameter SiC particle due to differential thermal contraction during cooling is approximately 1 pct. The plastic strain at one-half the interparticle spacing, obtained from Lee *et al.*,[15] ranges from 1 to 2 pct. The dislocation density can be simply calculated from the following equation:

$$\varepsilon_p = \rho L b . \qquad [1]$$

where ε_p is the plastic strain (1 pct), ρ is the dislocation density (m^{-2}) generated, L is the average distance moved by the generated dislocations, which was taken to be 1/2 the inter-whisker spacing, *i.e.*, 2 μm, and b is the Burgers vector of Al. The ρ obtained is 1.8×10^{13} m^{-2}.

Consideration of another type of dislocation described by Ashby[16] predicts additional dislocations in the matrix. These dislocations are called "geometrically necessary" dislocations by Ashby, and occur in order to allow compatible deformation of a system with geometrical constraints such as hard particles which do not deform as the surrounding ductile matrix. These geometrically necessary dislocations are required if the deformation takes place without the formation of voids about the hard particles. Slip dislocations are a function of the material properties of the system, and are not dependent on the microstructural constraints. According to Ashby, the density of geometrically necessary dislocations, ρ^G, is given by:

$$\rho^G = \frac{4\gamma}{\lambda^G b} \qquad [2]$$

where λ^G is the "geometrical slip distance" analogous to the slip distance in pure crystals. For platelet particles, λ^G is equal to the length of the plate and γ is the shear strain. For a 1 pct shear strain and $\lambda^G = 4$ μm, ρ^G equals approximately 3×10^{13} m^{-2}. Taking these dislocations into account results in a further addition to the predicted dislocation density in the Al matrix.

The purpose of this investigation was to determine if dislocation generation occurs at the Al/SiC interface on cooling a composite from annealing temperatures, and to determine if the observed densities of dislocations generated during cooling are in agreement with densities predicted by theoretical calculations.

II. MATERIAL

Three types of material were examined. The first was a SiC whisker composite purchased from ARCO-Silag. It is a powder metallurgy product: 6061 Al alloy powder is compressed with SiC whiskers to form a billet; then the billet is extruded to align the whiskers and form a 12.5 mm diameter rod. Three different volume fractions of SiC were considered: 0 pct, 5 pct, and 20 pct. The zero vol pct material served as a control.

The second type of composite was purchased from DWA, and contains SiC of platelet morphology. The platelets are 5 to 7 μm long and have an aspect ratio of two to three. This composite is also a powder metallurgy product supplied in the form of a plate, and the third type of material was wrought 1100 grade Al in the form of a 12.5 mm diameter rod, and it was in the as-received condition. This material also served as a control.

III. SAMPLE PREPARATION AND EXAMINATION PROCEDURE

An ion milling technique was required for the production of TEM samples due to the SiC in the Al matrix.

These two types of composite and the 0 vol pct control were machined into rods (12 mm in diameter, 4 cm long), annealed for 12 hours at a solutionizing temperature of 810 K, and furnace cooled. After annealing, slices of 0.76 mm thickness were cut by electric discharge machining (EDM) at 80 to 100 V. Deformation damage from EDM is estimated to extend 0.20 mm beneath the surface.[17,18] The slices were fixed to a brass block with double-sided tape and surrounded by brass shims, then mechanically thinned on a rotating water flooded wheel covered with 400 then 600 grit paper to remove the EDM damage and reduce the thickness to approximately 0.127 mm. Final thinning was carried out using argon ion plasma bombardment, operating at 6 kV, and ion current of 50 micro amperes and a sample inclination of 15 deg to the ion beam. For these operating parameters the projected range, or average distance the argon ion travels into the foil, is only 20 nm.[19,20] Dupuoy[21] conducted an *in situ* ion thinning experiment on Fe and Al-Ag specimens using a 3 MV microscope. Dislocation arrangements and microstructures in Al-Ag and Fe were not altered by ion thinning even though some point defects are introduced into the near surface region of the sample by ion bombardment. Therefore, it can be concluded that ion-milling does not introduce or remove dislocations in the TEM foils.

The 1100 grade Al control samples were prepared from the as-received wrought rod in the same manner as the composite samples, except electro-polishing was employed instead of ion-thinning.

The thinned samples were then observed in the HVEM operating at 800 kV with a beam current of 2.3 μA. A double tilt, side-entry, furnace type heating stage was used to heat the specimen. While being observed in the microscope, the samples were heated to 800 K and held for 15 minutes, then cooled to ambient temperature. Subgrains exhibiting dislocations in contrast were chosen for observation. During heating and cooling, thermal drift of the stage and thermal expansion and contraction of the sample caused the chosen subgrain to move. In order to maintain the

same subgrain in the field of view at the same crystallographic orientation, it was necessary to slightly translate and tilt the specimen almost continuously. Since changing to SAD conditions during cycling to monitor orientation would have resulted in loss of the chosen area from the field of view, the orientation was maintained constant by monitoring the contrast of microstructures such as a subgrain boundary or SiC/Al interface in the bright-field mode. One thermal cycle required about one hour, and most of the samples were observed throughout several thermal cycles. The thickest regions of the sample penetrated by the beam were chosen for observation, and at operating voltage of 800 KV the beam will penetrate 0.8 μm thick Al.[22] The dislocation density, ρ, was determined by a line intercept method adapted from Hale.[23] A grid of lines is placed over the TEM micrograph, then the intersections of dislocation lines with the grid lines are counted. The dislocation density, ρ, is given by

$$\rho = \frac{2N}{LT}$$

where N is the number of dislocation intersections with the grid lines, L is the length of the grid lines divided by the magnification, t is the thickness of the sample (0.8 μm), and the length of the lines on the grids was 0.58 m. Each reported dislocation density is an average value obtained from 3 to 10 micrographs.

IV. RESULTS

The discussion of the experimental results will be divided into three parts: 0 vol pct, 5 vol pct, and 20 vol pct of SiC. In all cases, typical results will be described. A total of 800 micrographs were taken.

A. *Controls, 0 Vol Pct SiC, 6061 Al, and 1100 Al*

The 0 vol pct 6061 Al control sample had a large subgrain size (approximately 5 μm) and a low dislocation density (8×10^{12} m^{-2}) (Figure 1(a)). A few of the larger second phase precipitate particles (Mg_2Si) were surrounded by dislocation tangles bowing out from the precipitate interface (Figure 1(b)). On heating, the dislocations began to move in the sample, migrating away from the particles. Other dislocations were also generated in other areas of the subgrain and moved through the matrix, occasionally being pinned by precipitate particles. Eventually, at elevated temperatures (670 K), all of the dislocations disappeared. Slip traces left behind when the dislocations moved also disappeared at temperatures close to 700 K, possibly due to surface diffusion. The sample was held at 800 K for about 15 minutes.

The image tended to be out of focus at high temperatures due to thermal drift of the stage (Figures 1(b) and 1(c)). On cooling, dislocations reappeared at the large particle interface at about 500 K, sometimes moving faster than could be seen. The dislocations formed tangles in the vicinity of the precipitate; however, most of the matrix did not accumulate any dislocations (Figure 1(d)). There were a few dislocations generated at subgrain or grain boundaries.

The 1100 Al sample had a dislocation density initially of 4×10^{12} m^{-2}, and a large subgrain size, 5 μm (Figures 2(a) and 2(b)). Thicker regions containing few precipitates were chosen for observation. On heating, most of the dislocations had disappeared upon reaching 673 K. At this temperature, the heating stage mechanism failed; therefore, the sample never reached 800 K, but heating was sufficient to remove the dislocations from the area under observation. The dislocations in this area did not return on cooling, except a few which were connected to precipitate particles (Figures 3(a) and 3(b)).

B. *5 Vol Pct—Transverse and Longitudinal Whisker SiC*

The 5 vol pct whisker sample, sectioned transverse to the whiskers so that the hexagonal whiskers are viewed end-on in the microscope, had a small subgrain size, 2.0 μm, and a high dislocation density, 4×10^{13} m^{-2}, in the subgrains (Figure 4(a)). In this case, on heating the dislocations did not disappear but straightened from an initially bowed configuration and became more regularly spaced: a polygonized configuration. These dislocations did not disappear at high temperatures (Figures 4(b) and 4(c)). On cooling, the dislocations again bowed away from the Al/SiC interface but the density of dislocations did not increase; if anything, the number slightly decreased (Figures 4(d) and 4(e)). Several of the subgrains appeared to change shape during the thermal cycle; however, their boundaries did not move past the surrounding SiC whiskers.

The longitudinal 5 vol pct sample, sectioned parallel to the SiC whisker axis so that the whiskers could be viewed lengthwise, did show the characteristic disappearance of dislocations at high temperatures, and then the return of dislocations on cooling, especially at the ends of the whiskers (Figures 5(a) through (f)). The parallel lines in the whiskers have been previously identified as microtwins.[24]

C. *20 Vol Pct Whisker and Platelet*

The microstructure of the 20 vol pct whisker sample before heating is characterized by a small subgrain size of the order of 2 to 3 μm and also by a dislocation density of about 10^{13} m^{-2} (Figure 6(a)). The sample was heated while focusing on a single subgrain surrounded by several SiC whiskers. The dislocations began to move and rearrange, some moving very quickly, and eventually disappearing. Upon reaching 470 K most of the dislocations had disappeared. The sample was heated further to 800 K (Figure 6(b)), held for a few minutes, and then cooled. On cooling, dislocations reappeared and emanated from the whisker interface forming a tangle of dislocations in the small subgrain. Although some dislocations began appearing on cooling at about 473 K, a great number of them formed at temperatures less than 373 K. The dislocation density after cooling was comparable to the dislocation density before the thermal cycle (Figures 6(c), 6(d), and 6(e)). When black spots began obscuring the picture, another area free of the black spots was moved into the field of view.

The 20 vol pct platelet sample (Figure 7(a)) exhibited behavior similar to the whisker sample, in that most of the dislocations disappeared upon reaching 650 K (Figure 7(b)), and then on cooling, dislocations reappeared (Figures 7(c) and 7(d)). However, certain aspects of the microstructural alterations on cooling were peculiar to the platelet sample. In the first cycle, the dislocations disappeared and then reappeared on cooling. An unusual subgrain was observed

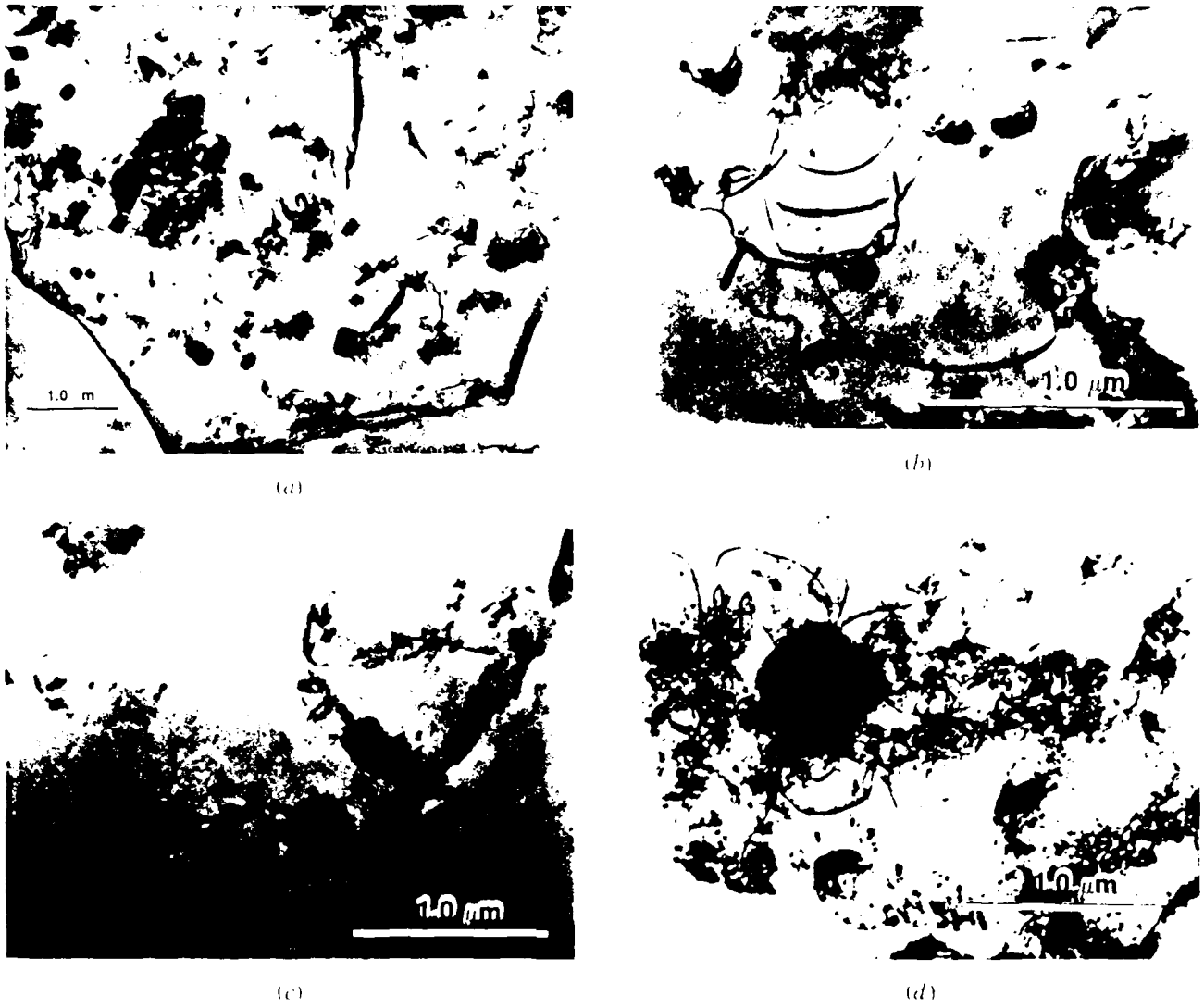

(*a*) (*b*) (*c*) (*d*)

Fig. 1—(*a*) Micrograph of a control sample illustrating the low dislocation density and the large grain size of annealed powder compacted 6061 Al with no SiC. The few dislocations present in this control sample are associated with the second phase precipitates of the 6061-Al alloy. Compare the dislocation densities and subgrain sizes with those of composites shown in Figs. 4(a), 6(a), and 7(a). (*b*) A large second phase precipitate (top center) surrounded by dislocations at the beginning of the thermal cycle (340 K). (*c*) As temperature increased to annealing temperatures in the microscope (780 K), the dislocations gradually disappeared until only a few remained (same area as Fig. 1(b)). (*d*) During *in situ* cooling of the control sample, dislocations reformed in the area of the precipitates, shown here. However, most of the matrix remained free of dislocations (same area as Figs. 1(a) and 1(b)).

which was filled with slip traces. This area was chosen as the area of focus in the next cycle. The parallel lines disappeared on heating; then on subsequent cooling, packets of slip traces appeared emanating from the SiC platelet. The slip traces formed in three directions at angles of about 82 deg and 45 deg to each other and were associated with dislocations which had appeared. The dislocations causing the slip traces moved too rapidly to be seen. After the third thermal cycle, many subgrains were filled with slip traces originating at the SiC platelet interface.

D. *Dislocation Densities*

The dislocation densities of all samples before and after *in situ* annealing are shown in Table I. The densities are higher in the composite samples than in the control samples both before and after *in situ* thermal cycling, *i.e.*, annealing. However, the dislocation densities reported are lower limit densities. There was difficulty in taking selected area diffraction patterns of a given subgrain and then tilting to a specific reflection, *i.e.*, {420} and assuring that the same orientation was maintained throughout. Therefore, the reported densities could be ½ to ⅓ of the actual density.[25]

The distribution of the dislocations within the samples was not uniform; there was a higher density, as to be expected, near the SiC. Also greater dislocation generation was observed at larger SiC platelets and whiskers than at the smaller ones, and more dislocations were generated at the ends of the SiC whiskers where plastic strain during cooling is greatest, than at the middle of the whisker length. The dislocation generation in the platelet sample was much greater than the dislocation generation in the

(*a*)

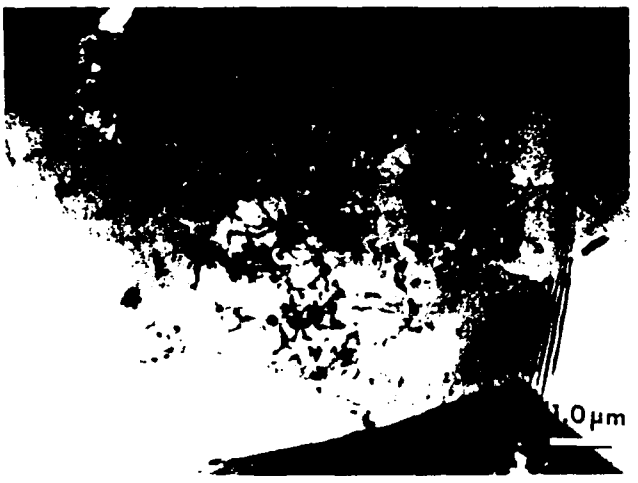

(*b*)

Fig. 2—(*a*) Wrought 1100 Al control sample, as-received condition. Before *in situ* thermal cycling, this control sample with no SiC had a high dislocation density. Like the 6061 Al control, this sample has a large grain size, and the dislocations present are often associated with precipitates. The white structure is a corrosion tunnel from electropolishing. (*b*) Low magnification view of 1100 control sample including area of Fig. 2(a).

(*a*)

(*b*)

Fig. 3—(*a*) The same areas in Fig. 2(a) after *in situ* thermal cycling. In the absence of SiC, few dislocations reappear in a thermally cycled sample; the few dislocations present are associated with second phase precipitate particles.(*b*) Low magnification view of area in Fig. 3(a) after thermal cycling.

(a)

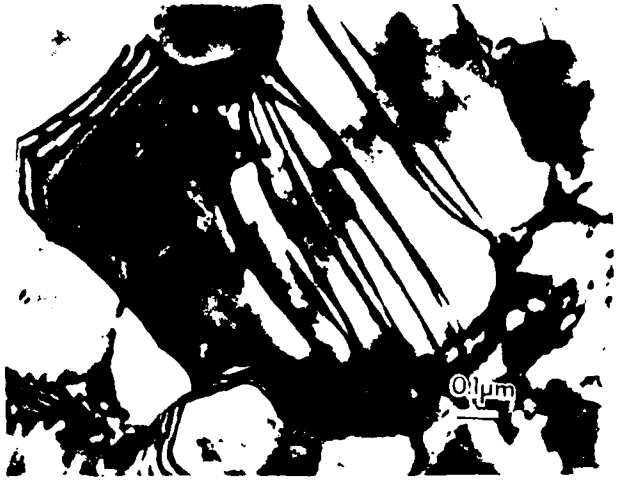

(b)

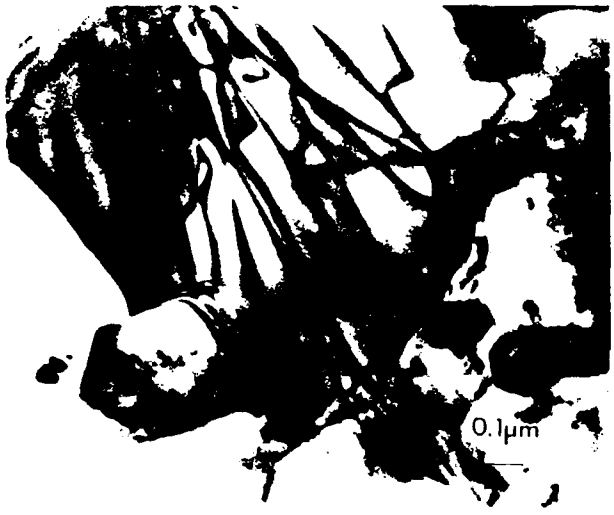

(c)

(d)

(e)

Fig. 4 — (a) A foil cut transverse to the whisker axis (5 vol pct SiC). At the beginning of the thermal cycle, 370 K, the dislocations tended to bow away from the two hexagonal SiC whiskers. (b) The dislocations straighten on further heating to 570 K (same area as Fig. 4(a)). (c) Further rearrangement of the dislocations occurred on heating to the annealing temperature of 800 K in the microscope. The dislocations straightened and moved to more equally spaced positions (same area as Figs. 4(a) and 4(b)). (d) During cooling to 570 K the dislocations again began to bow away from the SiC whiskers (same area as Figs. 4(a-c)). (e) On cooling to 360 K, the curvature of the dislocations became pronounced, indicating the operation of a thermal stress; however, the generation of new dislocations did not occur (same area as Figs. 4(a-d)).

whisker samples, for SiC platelets are about 5 times larger than SiC whiskers.

As a consequence, of all the dislocation generation, there is a possibility of void formation at the SiC-Al interface. Voids were not observed in any of the samples.

V. DISCUSSION

The presence of SiC particles of either whisker or platelet morphology in an Al metal matrix composite resulted in the generation of dislocations at the Al-SiC interface when the

(a)

(b)

(c)

(d)

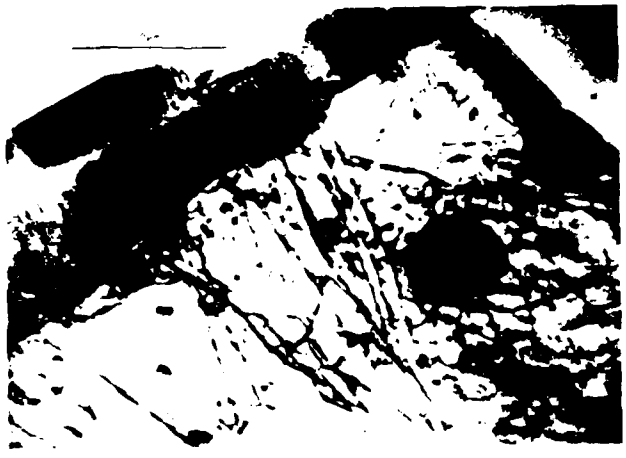

(e)

(f)

FIG. 5—(a) This sample was prepared from the same 5 vol pct whisker content as shown in Figs. 3(a) to (c), only sectioned parallel to the SiC whisker axis. Dislocations are associated with the SiC and second phase precipitates at the beginning of the thermal cycle at 340 K. Also visible are parallel slip traces from the previous thermal cycle. (b) The same region at annealing temperature, 580 K, after most dislocations have disappeared. (c) The same area after one dislocation has reappeared on cooling to 580 K. (d) On further cooling the sample to 480 K, more dislocations have formed, some leaving slip traces as they moved away from the Al-SiC interface. (e) On cooling to 430 K, dislocation activity greatly increased as evidenced by the higher density of dislocations and slip traces. (f) Another location in the sample at 340 K which also shows dislocation generation clearly associated with the SiC. This area was not irradiated by the electron beam during the [illegible]

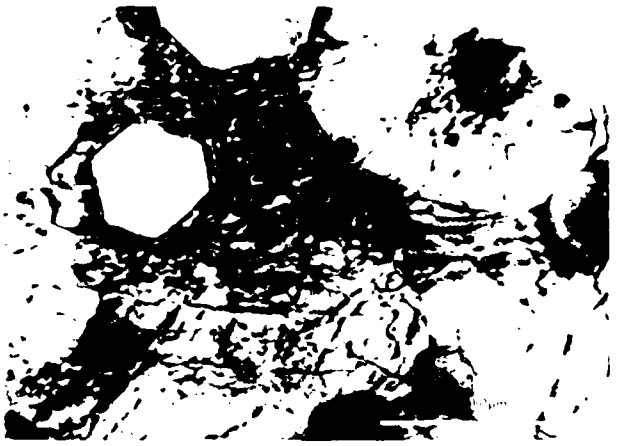

(*a*)

(*b*)

(*c*)

(*d*)

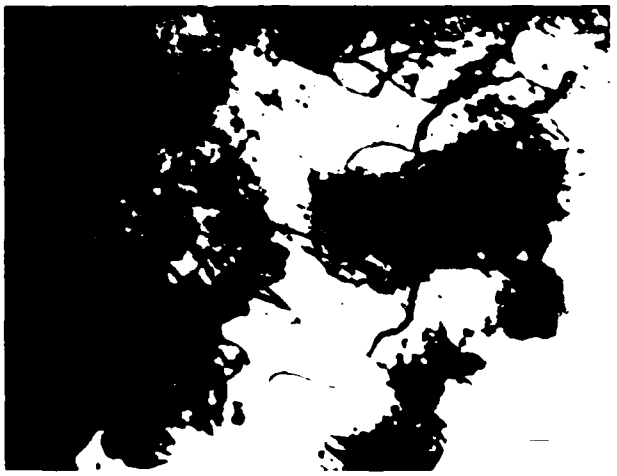

(*e*)

Fig. 6—(*a*) The initial high dislocation density and small subgrain size of the 20 vol pct whisker composites is shown here. (*b*) The dislocations disappeared from the sample during *in situ* heating to 800 K. Thermal drift of the stage prevented sharp focusing of the image. (*c*) On cooling to 375 K, dislocations had reappeared in the sample, emanating from the Al/SiC interface and moving into the matrix until a dislocation tangle formed. (*d*) The clear area at 375 K (Fig. 6(c)) as temperature decreased to 340 K. Black spots also began to form on the sample at this temperature. (*e*) At lower center, the appearance of a hook-shaped dislocation is observed. The black spots have become more prominent, 330 K.

composite was cooled from the annealing temperature. In general, the high density of dislocations originally present in the composite samples disappeared at 500 to 650 K, then reappeared on cooling at densities close to the high densities originally observed in the annealed specimens. In contrast, dislocations were not generated to the same extent in either of the control samples during cooling.

The small subgrain size and high dislocation densities previously observed by Arsenault and Fisher[7] can be associated with the presence of the SiC in the composite, specifically the CTE differential. The difference in CTE resulted in stresses large enough to cause plastic deformation, *i.e.*, the generation of dislocations. These dislocations can be defined as slip dislocations. Dislocation generation is also required to accommodate the heterogeneous plastic flow in the vicinity of the deforming matrix since voids are not observed. We can conclude, therefore, that both of

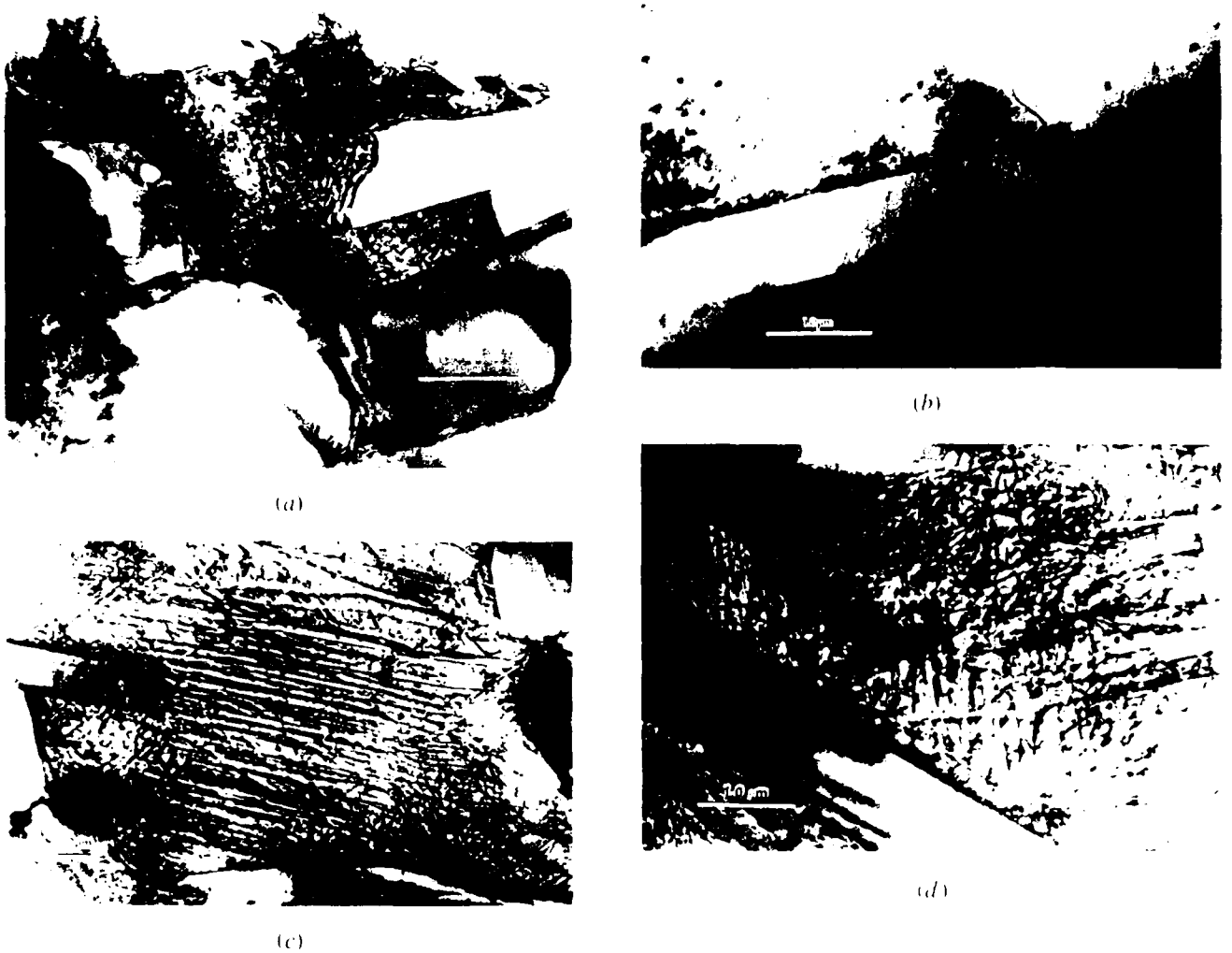

(a) (b) (c) (d)

Fig. 7—(a) The diffraction contrast of the high dislocation density in the central subgrain darkens the subgrain in this 20 vol pct SiC platelet composite. The subgrain is surrounded by at least three irregularly shaped SiC platelets which are approximately the same size as the subgrain. (b) During heating to 650 K, most of the dislocations disappeared from the sample. The pebble-like second phase precipitates can be clearly distinguished here. The same area is shown in (d) filled with slip traces. (c) On cooling to 340 K, dislocations reappeared, resulting in the formation of dense slip traces showing the paths of the dislocations as they moved across or out of the sample. (d) This is the same area as shown in (b) after cooling to 340 K. The area was free of almost all dislocations at high temperature. The subgrain is now filled with slip traces and dislocations. The slip traces are clearly associated with the SiC platelets indicating that the origin of the dislocations seen in the sample at low temperature is the Al-SiC interface.

Table I. Dislocation Density before and after Thermal Cycling of Samples; Dislocation Density (m^{-2})

Sample	Before Thermal Cycle	After Thermal Cycle
(1) 20 vol pct whisker	$2.0 \times 10^{\dagger}$	1.0×10
(2) 20 vol pct platelet	$2.0 \times 10^{\dagger}$	4.0×10
(3) 5 vol pct whisker	$4.0 \times 10^{\dagger}$	$2.0 \times 10^{\dagger}$
(4) 0 vol pct whisker	8.0×10	6.4×10
(5) 1100 Al sample*	$4.0 \times 10^{\dagger}$	5.3×10

†Bulk annealed 12 hours at 800 K
*As received 1100 grade wrought Al alloy

these mechanisms are operating, which results in a high dislocation density due to the SiC in the matrix. In the vicinity of precipitates, transformation strains can also produce dislocations.

The exception to the generally observed disappearance of dislocations on heating was the 5 vol pct transverse sample for which no satisfactory explanation has been found. A stable polygonized substructure appeared to prevent the disappearance of the dislocations at high temperatures. Backstresses from these dislocations on cooling could have prevented further generation of dislocations in the small subgrains on cooling.

The intensity of dislocation generation at the SiC-Al interface is related to size and shape of SiC particle. The intensity

of generation is lowest for small, nearly spherical particle. As the particle size increases, *i.e.*, from 1 μm to 5 μm, the intensity of generation increases significantly. Also the intensity is much greater at the corner of a particle than along the sides as is evidenced in the longitudinal whisker and platelet composite samples. The relationship between the size of the particle and the plastic zone has been qualitatively described by Lee *et al.*,[15] and they predicted that as the particle size increases the plastic zone size increases. Also, Lo[16] has shown that the plastic strain about the corner of a particle is greater than along the side (which should be intuitively obvious).

Experimental conditions which may influence the results must be recognized and considered in an HVEM experiment, because the sample is exposed to high energy electrons, and thin foil samples are used to approximate bulk behavior. Surface effects are among the most important effects to be considered, since it is easy for dislocations generated at the Al/SiC interface to move out of the sample through the surfaces of a TEM foil. Thick sections of the foil were examined in the HVEM in order to reduce surface effects; nevertheless, dislocation relaxation out the surface occurred, and resulted in a reduction of the observed dislocation density. This effect is most apparent in the 20 vol pct platelet sample where the slip traces, indicating that dislocations have moved out of the sample, nearly cover the entire surface of the sample. In bulk specimens, dislocations would accumulate in the subgrains until the ensuing backstresses due to the pile-up exceeded the local yield stress surrounding the particle. Also, the geometry of a thin foil specimen allows elastic relaxation of stresses on cooling by buckling, also giving an artificially low value of the dislocation density.

The effects of irradiation of the samples by the high energy electrons of the beam must also be considered. Electron irradiation of the sample can result in the formation of vacancy clusters and small dislocation loops which appear as black spots and then grow to form dislocation tangles.[11] The observation of black spots on some of the samples (Figures 1(d) and 6(d)) indicated that electron irradiation damage most probably occurred.

The control samples were invaluable in determining that the dislocations generated on cooling were not artifacts due to the effects of electron irradiation. In the 6061 0 vol pct SiC control sample a few dislocations were generated at a few large precipitates.

The 1100 control samples were also exposed to the high energy electron beam and substantial formation of dislocations did not occur (Figures 3(a) and 3(b)). Also the intensity of dislocation generation can be correlated with the size, volume fraction, and shape of the SiC or second phase precipitate particles present, indicating that the particles and not the electrons of the beam were the cause of the dislocations being generated. A more likely explanation of the appearance of the black spots is beam contamination. The decontaminator was not always operating, and beam contamination usually condenses on samples at temperatures less than 473 K which coincides with our observations.[27,28] Some of the black spots could also be due to second phase precipitation in the samples on cooling, since the spots were sometimes preferentially associated with interfaces and grain boundaries (Figures 1(d) and 7(d)).

Beam heating is another factor to be considered. For our operating conditions, beam heating of the sample is approximately 10 to 15 K, and this could have had an effect on dislocation generation in the sample due to the thermal gradient which is induced.[27,29] But examination of the same composite samples without thermal cycling did not result in dislocation generation at the Al/SiC interface, and these samples were exposed to the same beam conditions.

Due to the difficulty associated with tilting a very fine subgrained material to the various diffracting conditions required to image all of the dislocations in the subgrain, the reported densities could be ⅓ to ½ below the actual number. Although more rigorous tilting would give more precise values, a good idea of the relative densities in the samples can be obtained by imaging dislocations in many subgrains for each material and assuming that the value will be systematically low for all the samples.

The net result of considering all of the experimental factors which may influence the experimentally determined dislocation densities after a thermal cycle, is: (1) the dislocation generation observed during cooling can be readily attributed to differential thermal contraction of the Al and SiC, (2) the observed densities are lower than the densities which would be observed if bulk samples could be examined and if diffracting conditions were controlled to image all dislocations.

It should also be pointed out that slip line generation about a SiC cylinder in an Al disk due to thermal cycling has been demonstrated by Flom and Arsenault.[30]

VI. CONCLUSIONS

From a consideration of the experimental results, the following conclusions can be drawn:

1. The high dislocation density (10^{14} m^{-2}) previously observed in bulk annealed composites is due to differential thermal contraction of Al and SiC on cooling from the elevated temperatures of annealing.
2. The density of dislocations observed in this experiment as a result of thermal cycling is lower than the actual density generated during thermal cycling because dislocations are lost through the surfaces of the thin foil samples during cooling.
3. The densities of dislocations observed (10^{13} m^{-2}) would be equal to the high densities previously observed in bulk annealed composites if it were not for dislocation loss through the surfaces, and the observed densities would be closer to densities predicted by calculations 4×10^{13} m^{-2}, if it were not for dislocation loss through the surfaces.
4. Thermal cycling causes the disappearance of dislocations at high temperatures and the generation of dislocations at Al/SiC interfaces and precipitates on cooling. Subgrain growth is hindered by the presence of SiC particles. Transformation strains also cause dislocation generation at precipitates, and polygonized configurations prevent the disappearance of dislocations at high temperatures.
5. Precipitation occurs on the thermally-generated dislocations during cooling.

ACKOWLEDGMENTS

The authors wish to acknowledge A. Szirmae and J. W. Conroy of the U.S. Steel Research Laboratory, and C. R. Feng and Y. Flom of the University of Maryland for assistance with the experiments. Effective liaison with Drs. Bruce McDonald and Steve Fishman of the Office of Naval Research in Arlington, VA has been very helpful to the project.

REFERENCES

1. M. R. Piggott: *Loading Bearing Fibre Composites*, Pergamon Press, Oxford, 1980.
2. R. J. Arsenault: *Mat. Sci. and Eng.*, 1984, vol. 64, p. 171.
3. R. J. Arsenault and R. M. Fisher: *Scr. Metall.*, 1983, vol. 17, p. 67.
4. A. Taylor and R. M. Jones: *Silicon Carbide*, J. R. O'Connor and J. Smiltens, eds., Pergamon Press, Oxford, 1960, pp. 147-54.
5. K. K. Chawla and M. Metzger: *J. of Mat. Sci.*, 1972, vol. 7, p. 34.
6. K. F. Hale, M. Henderson-Brown, and Y. Ishida: *Proc. 5th European Congress on Electron Microscopy*, 1972, p. 350.
7. D. Caillard and S. L. Martin: *Acta Metall.*, 1983, vol. 31, p. 813.
8. J. K. Kivilahti, V. K. Lindroos, and B. Lehtinen: *Proc. 3rd Int. Conf. on HVEM*, P. R. Swann, C. J. Humphreys, and M. J. Goringe, eds., Academic Press, London, 1974, p. 19.
9. M. Shimotomori and R. R. Hasiguti: *J. Japan Inst. Met.*, 1979, vol. 43, p. 4.
10. A. Wolfenden: *Radiat. Eff.*, 1972, vol. 14, p. 225.
11. J. O. Stiegler and K. Farrell: *Proc. 3rd Int. Conf. on HVEM*, P. R. Swann, C. J. Humphreys, and M. J. Goringe, eds., Academic Press, London, 1974, p. 341.
12. G. C. Weatherly: *Met. Sci. J.*, 1968, vol. 2, p. 237.
13. M. F. Ashby, S. H. Gelles, and L. E. Tanner: *Phil. Mag.*, 1969, vol. 19, p. 757.
14. J. C. Williams and G. Garmong: *Metall. Trans. A*, 1975, vol. 6A, p. 1699.
15. J. K. Lee, Y. Y. Earmme, H. I. Aaronson, and K. C. Russell: *Metall. Trans. A*, 1980, vol. 11A, p. 1837.
16. M. F. Ashby: *Phil. Mag.*, 1970, vol. 21, p. 399.
17. A. Szirmae and R. M. Fisher: "Techniques of Electron Microscopy, Diffraction, and Microprobe Analysis", Special Technical Publ. #372, ASTM, 1965.
18. L. E. Samuels: *Metallographic Polishing Methods*, Sir Issac Pitman & Sons, Ltd., Melbourne, 1971, p. 79.
19. D. G. Howitt: *Analytical Electron Microscopy*, Roy H. Geis, ed., San Francisco Press, San Francisco, CA, 1981, p. 252.
20. P. D. Townsend, J. C. Kelly, N. E. W. Hartley: *Ion Implantation, Sputtering, and Their Applications*, Academic Press, London, 1976, p. 311.
21. G. Dupuoy: "Megavolt Electron Microscopy", *Proc. 3rd Int. Conf. on HVEM*, P. R. Swann, C. J. Humphreys, and M. J. Goringe, eds., Academic Press, London, 1974, p. 447.
22. H. Fujita, T. Tabata, N. Sumida, and K. Yoshida: *Proc. 3rd Int. Conf. on HVEM*, P. R. Swann, C. J. Humphreys, and M. J. Goringe, eds., Academic Press, London, 1974, p. 427.
23. K. F. Hale and M. Henderson-Brown: *Micron*, 1973, vol. 4, p. 69.
24. J. Feng: Master's Thesis, Univ. of Maryland, College Park, MD, 1981.
25. P. B. Hirsch, R. B. Nicholson, A. Howie, D. W. Pashley, and M. J. Whelan: *Electron Microscopy of Thin Crystals*, Butterworth & Co., London, 1965, p. 423.
26. J. Lee: private communications, Michigan Technological University, Houghton, MI, 1984.
27. E. P. Butler and K. F. Hale: "Dynamic Experiments in the Electron Microscope", in *Practical Methods in Electron Microscopy*, Audrey M. Glauert, ed., Elsevier/North Holland Biomedical Press, Amsterdam, 1981, vol. 9.
28. G. M. Scamans and E. P. Butler: *Metall. Trans. A*, 1975, vol. 6A, p. 2055.
29. S. B. Fisher: *Radiat. Eff.*, 1970, vol. 5, p. 239.
30. Y. Flom and R. J. Arsenault: *Mater. Sci. and Eng.*, 1985, vol. 75, p. 151.

Materials Science and Engineering, 75 (1985) 151-167

Deformation in Al-SiC Composites Due to Thermal Stresses

Y. FLOM and R. J. ARSENAULT

Metallurgical Materials Laboratory, University of Maryland, College Park, MD 20742 (U.S.A.)

(Received January 2, 1985; in revised form March 13, 1985)

ABSTRACT

Plastic strains and the extent of the plastic zone due to differential thermal expansion were experimentally determined in an Al-SiC composite. The combined plastic shear strains γ_{cpss} at the Al-SiC interface for furnace-cooled, air-cooled and quenched samples were found to be 1.32%, 1.23% and 0.99% respectively. Profiles of γ_{cpss} were plotted versus distance from the interface and compared with the theoretical distribution of effective strain $\bar{\epsilon}$. The theoretical extent of the plastic zone measured from the interface was found to be 1.3 multiplied by the particle radius. This value was slightly less than the observed value. The plastic deformation on the heating half of the thermocycle was found to be at least equal to the deformation on the cooling half. A theoretical treatment of the local plastic deformation in a short composite cylinder was suggested, from which the effective plastic strain $\bar{\epsilon}$ and the extent of the plastic zone were determined.

1. INTRODUCTION

When a composite material is subjected to a temperature change, local plastic deformation can occur. The plastic deformation is due to a stress created by the difference between the coefficients of thermal expansion of the component phases, and this stress is at the matrix-reinforcement interfaces. The magnitude of the stress is equal to $\Delta\alpha\,\Delta T$ where $\Delta\alpha$ is the difference between the coefficients of thermal expansion of the phases under consideration and ΔT is the temperature change. The relatively large (10 to 1) difference between the coefficient of thermal expansion of SiC and that of aluminum should result in the creation of a substantial misfit strain at the Al-SiC interface during cooling from the fabricating or annealing temperature. The mechanical properties of the composite should be affected by the magnitude and extent of the plastic deformation that takes place in the soft matrix around a hard particle as a result of the misfit relaxation in the interface region. Recent investigations [1-4] have indeed shown the important role of the interfacial regions in the composite strengthening. Thus, knowledge of the magnitude of plastic strains and the size of the plastic zone as well as other characteristics of the interfacial region (the bond strength, the microstructure etc.) should contribute to the understanding of the mechanism of composite strengthening.

The experimental determinations of plastic strains and plastic zone radii about a particle in the matrix due to the difference between the coefficients of thermal expansion of the phases, to our knowledge, have not been reported in the literature.

Several theoretical investigations have been undertaken to predict the magnitude of the plastic strain in the plastic zone around a particle. The relaxation of the misfit caused by the introduction of an oversized spherical particle into a spherical hole in the matrix has been analytically described by Lee *et al.* [5]. Using the misfitting sphere model, they calculated strains in the plastic zone that surrounds a hard sphere and also the plastic zone radius. Hoffman [6] calculated the overall total strains in the tungsten-fiber-reinforced 80Ni-20Cr matrix, using a thick-wall long-cylinder approach and assuming that a hydrostatic stress state exists within each constituent.

Garmong [7], assuming uniformity of the stresses and strains in the matrix, calculated deformation parameters for a hypothetical eutectic composite and reported values of matrix plastic strains that were of the order of 0.4%.

0025-5416/85/$3.30

Dvorak *et al.* [8] developed a new axisymmetric plasticity theory of fiberous composites involving large thermal changes. The long-composite-cylinder model was adopted as a composite unit cell, and the microstress distribution as well as the yielding surfaces were obtained for Al-W composites.

Mehan [9] calculated the residual strains in an Al-α-Al_2O_3 composite due to cooling from the fabricating temperature. He considered an idealized composite consisting of a long sapphire cylinder surrounded by an aluminum matrix. This is equivalent to the long-composite-cylinder model used by Dvorak *et al.* This model implies that the thermal strain along the cylinder axis is a constant, *i.e.* that

$$\epsilon_z = \frac{dl}{l} = \text{constant}$$

where l is the length of the cylinder. This simplifies the procedure of obtaining the radial ϵ_r and the tangential ϵ_θ strains which was done using incompressibility and boundary conditions. The effective strain $\bar{\epsilon}$ at the Al-α-Al_2O_3 interface was found to be 1.6%.

However, the above-mentioned composite models do not give an accurate description of the plastic strain state in the short-composite-cylinder model. A short-cylinder model nearly duplicates the situation in the whisker and platelet Al-SiC composites at present produced.

The purpose of this work was to determine experimentally the magnitude of the local plastic strain produced in the aluminum matrix around a short SiC cylinder during a thermocycle and also to estimate the extent of the plastic zone around the cylinder. Also an effort was made to develop a theoretical model of the plastic zone around the short cylinder.

2. EXPERIMENTAL PROCEDURE

The small particle interspacing (several micrometers) in a commercially available Al-SiC composite makes it impossible to measure the local plastic strain at the Al-SiC interface directly. Thus a composite model consisting of an SiC cylinder embedded in an aluminum matrix was fabricated so that direct strain measurements could be attempted.

Aluminum of 99.99% purity (to eliminate the influence of the alloying elements) and commercial carborundum were used to produce the composite model. Selected properties of these materials are given in Table 1.

Platelets of SiC were separated from carborundum conglomerates that are used in the production of abrasives. These platelets were spark planed on an electric discharge machine to plates approximately 1 mm thick. These flat plates were cut into rectangular rods approximately 1 mm × 1 mm. After this, each rod was spark machined to cylinders of about 1 mm diameter.

Pure aluminum rods, 12.5 mm in diameter in the as-received condition, were cut into studs 37 mm long. Two aluminum studs and one SiC rod were assembled together and put in a specially built compaction die, where they were hot pressed to produce one compact. Compaction was done on the Instron testing machine. During the entire compaction cycle (Table 2), a vacuum of about 10^{-3} Torr was maintained using a mechanical vacuum pump.

TABLE 1

Selected properties of the aluminum and SiC used in this paper

Material	*Yield strength* (MPa)	*Elastic modulus* (MPa)	*Bulk modulus* (MPa)	*Poisson's ratio*	*Thermal expansion coefficient* ($m\ m^{-1}\ K^{-1}$) *in the temperature range 293–773 K*	*Melting point* (K)	*Reference*
Al	11.73	62×10^3	57.5×10^3	0.31	28×10^{-6}	933	[10, 11]
SiC	34.5 + (tension) 1380 + (compression)	483×10^3	96.6×10^3	0.19	3×10^{-6}	3373	[12, 13]

TABLE 2

Flow chart of the compaction of an Al-SiC composite cylinder

Heating	
Heating time	≈ 1 h
Temperature	≈ 843 K
Compression	
Cross-head speed	0.1 cm min^{-1}
Total travel	10 mm
Holding at constant load	
Time	2 h
Pressure	2.28 MPa
Incremental cooling under pressure	
Time	12 h
Pressure	2.28 MPa

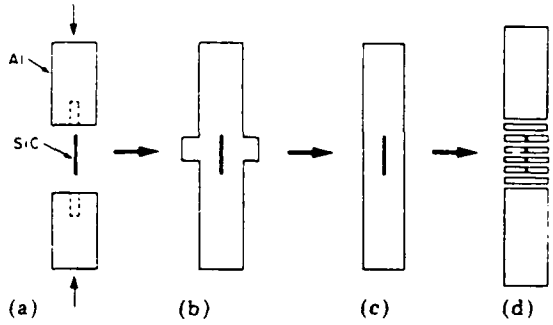

Fig. 1. A schematic diagram of the fabrication sequence of the Al-SiC composite model.

The central portion of the compacted sample was sliced in the transverse direction into disks 1 mm thick using the electric discharge machine, set at a low power, and each disk contained an SiC cylinder very close to the perfect center (Fig. 1). All Al-SiC disks were metallographically and then electrolytically polished to remove the thin cold-worked surface layer of aluminum.

The method adopted for the evaluation of plastic deformation was based on the direct observation of slip bands on the polished surface of the sample around the SiC particles. The amount of slip is a characteristic of the amount of plastic deformation (when deformation occurs by slip) in a crystalline solid. The plastic strain can be evaluated if the number of slip bands and the displacement on each band are known The concept of combined plastic shear strain γ_{cpss} has been introduced where γ_{cpss} is equivalent to the product of slip band density N and the amount of slip S, *i.e.*

$$\gamma_{cpss} = KNS \tag{1}$$

where K is a coefficient which takes into consideration different crystallographic situations. A detailed treatment of γ_{cpss} is given in Appendix A. Thus, the method reduces the data collection to the measurements of slip band densities and their heights in the area of interest.

The electropolished Al-SiC disks were separated into three groups: A, B and C. Each group was heated to about 823 K and then cooled as follows: group A, furnace cooled; group B, air cooled; group C, quenched in alcohol.

Since the surface of each disk had a high quality polish, slip bands could be observed around the SiC in an optical microscope. Slip band density and height measurements were obtained using a Zeiss interference microscope. Areas containing slip bands were photographed in white light and in green monochromatic light. Pictures taken in white light gave the actual image of the slip bands. Pictures of the same areas taken in monochromatic light gave interference fringe patterns (Figs. 2-4). Thus, the correlation between slip bands and interference fringes was established.

When a furrow is present in the plane surface of the object, the straight interference bands are deflected by the furrow and the furrow depth t can be determined from the deflection:

$$t = \frac{d}{b}\frac{\lambda}{2} \tag{2}$$

where d is the deflection of the interference band, b is the band interval, taken as the distance from the middle of one band to the middle of the next band and $\lambda/2 = 0.27$ μm for the thallium light. Band deflection can be estimated to be one-tenth of the band interval. Thus the height measurements can be as accurate as $\pm 0.1 \times 0.27 = \pm 0.027$ μm.

The slip band density was determined by using the "mesh" method which consisted of the following. Pictures of slip band images and interference patterns were enlarged to 10 cm × 12.5 cm on high contrast photographic paper. After that, a transparent plastic

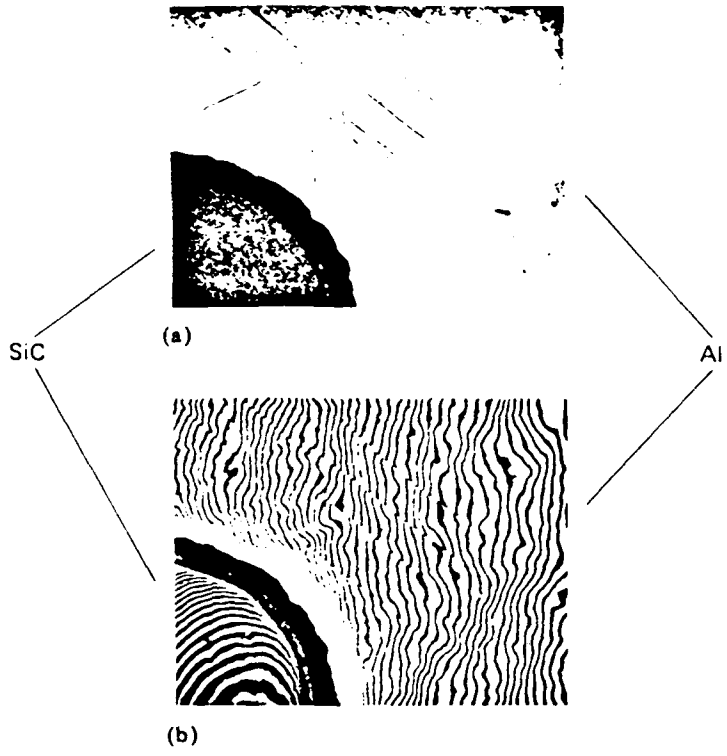

Fig. 2. (a) Slip bands and (b) interference fringe patterns of different areas around the SiC. (Magnification, 32×.)

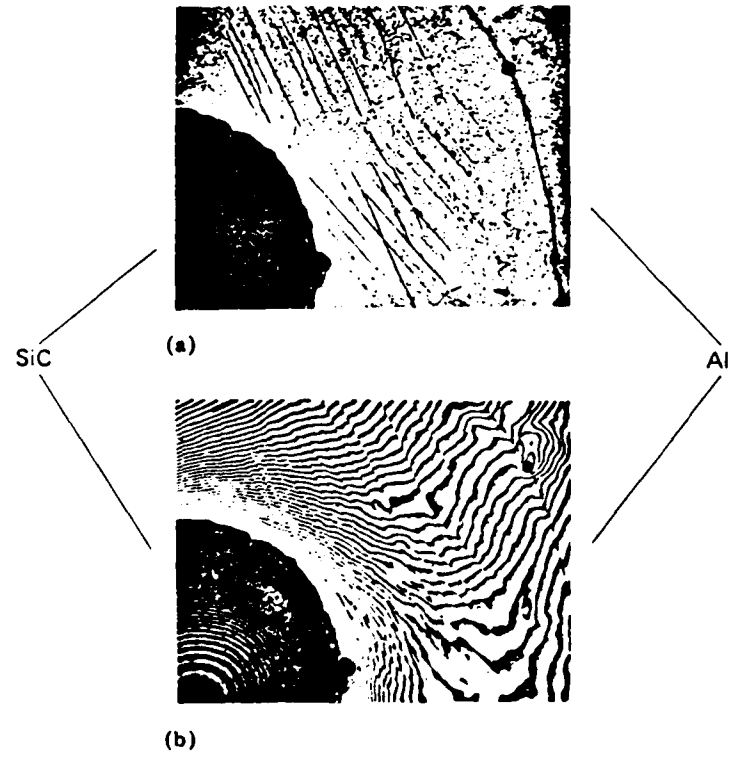

Fig. 3. (a) Slip bands and (b) interference fringe patterns of different areas around the SiC. (Magnification, 32×.)

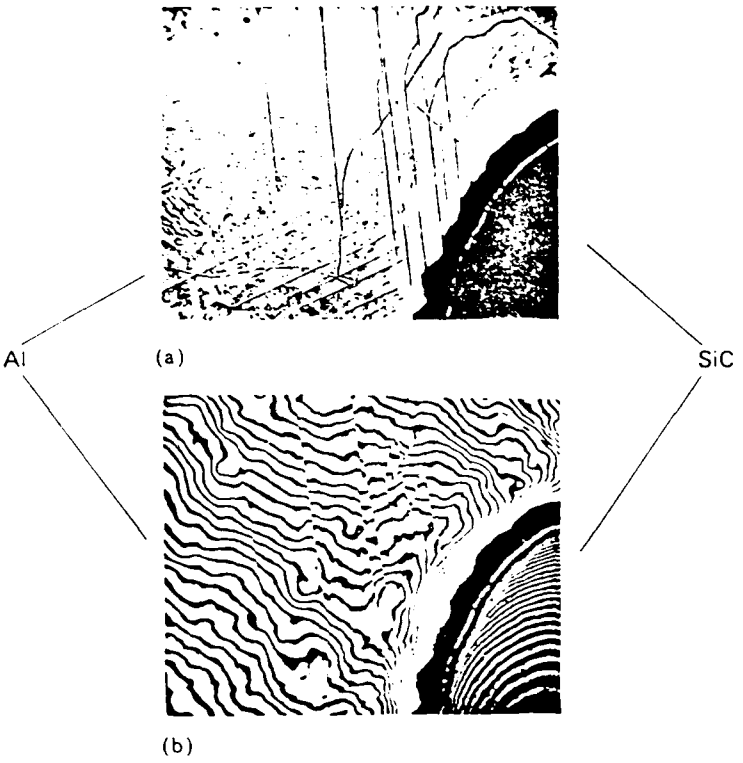

Fig. 4. (a) Slip bands and (b) interference fringe patterns of different areas around the SiC. (Magnification, 32×.)

film with a square mesh of a specific size (1.0 cm × 1.0 cm square for pictures with a magnification of 80× and 2.5 cm × 2.5 cm square for pictures with a magnification of 200×) was overlaid on the photograph and the total length of the slip bands within each square along the radial direction was measured. If M is the magnification of the picture, L (m) the total length of slip bands in one square and A (mm^2) the area of the square, then the slip band density N is

$$N = M\frac{L}{A} \times 10^{-3}\,\mu m^{-1} \qquad (3)$$

The accuracy of slip band density measurements is much higher than that of height measurements. Therefore, the main source of error in combined plastic shear strain γ_{cpss} evaluation is the height of the slip band (provided that, of course, the assumptions and results of discussion given in Appendix A are reasonably correct).

2.1. *Hot-stage experiment*

Two Al-SiC disks were reduced in diameter to 7 mm and thermocycled in the hot stage of a Leitz optical microscope. A reduction in size was necessary in order to fit the holder into the hot stage. The entire thermocycle was recorded on videotape using an RCA industrial television camera. The time was recorded by means of a digital generator interfaced to the recording unit, and the temperature was recorded on the sound track of the tape at 20 K intervals. The total length of the thermocycle was approximately 8 min. The maximum temperatures were around 873 K. The heating and cooling rates were around 100 K min^{-1}.

3. EXPERIMENTAL RESULTS

3.1. *Combined plastic shear strain*

The experimentally determined values of combined plastic shear strain γ_{cpss} are presented in Tables 3–5. These combined plastic shear strains γ_{cpss} are plotted *versus* distance in the form of a histogram in Fig. 5. In the same figure we have a plot of effective strain $\bar{\epsilon}$ which was determined theoretically (see Appendix B). The histogram represents the

TABLE 3

Combined plastic shear strain γ_{cpss} for group A samples (furnace cooled)

Sample	*Path*[a]	*Combined plastic shear strain*[b] γ_{cpss} (%) *for the following distances from the Al-SiC interface*[c]				
		6.25×10^{-2} mm	18.75×10^{-2} mm	31.25×10^{-2} mm	43.75×10^{-2} mm	56.25×10^{-2} mm
1	1	0.86	0.35	0.18	0.09	0.026
1	2	0.61	0.40	0.22	0.06	0.07
1	3	0.41	0.140	0.24	0.08	
1	4	0.26	0.21	0.19	0.16	
1	5	0.42	0.32	0.32	0.13	0.03
1	6	0.51	0.41	0.30	0.08	
2	1	0.30	0.21	0.06		
2	2	0.45	0.28			
3	1	0.43	0.24	0.22	0.22	0.22
3	2	0.26	0.27	0.22	0.11	
3	3	0.39	0.22	0.26	0.16	
3	4	0.46	0.18	0.23		
3	5	0.45	0.26			
4	1	0.43	0.24	0.04		
Average		0.44	0.24	0.21	0.16	0.05

[a] The path is the route in the radial direction from the Al-SiC interface into the matrix, which was selected for slip band density and height measurements. Selection was based on the amount of slip that occurred, and those routes were selected in which the amount of slip bands appeared to be the greatest.
[b] The given strain is actually the result of the product NS. It does not include the coefficient K which was found to be equal to 3 (see Appendix A). Values of γ_{cpss} that incorporate K are given in Table 6.
[c] The distance given here is the distance from the Al-SiC interface to the centers of the first, second etc. squares. Therefore, values of γ_{cpss} represent the strain over the entire square.

TABLE 4

Combined plastic shear strain γ_{cpss} in group B samples (air cooled)

Sample	*Path*[a]	*Combined plastic shear strain*[b] γ_{cpss} (%) *for the following distances from the Al-SiC interface*[c]					
		6.25×10^{-2} mm	18.75×10^{-2} mm	31.25×10^{-2} mm	43.75×10^{-2} mm	56.25×10^{-2} mm	68.75×10^{-2} mm
1	1	0.34	0.32	0.35	0.13		
1	2	0.25	0.25	0.17	0.19	0.13	0.11
1	3	0.56	0.31	0.19	0.11		
1	4	0.47	0.55				
1	5	0.25	0.07	0.014	0.08		
2	1	0.23	0.17				
4	1	0.65	0.41				
4	2	0.47	0.22				
4	3	0.54	0.29	0.1			
4	4	0.31	0.21	0.25			
4	5	0.48	0.25				
Average		0.41	0.27	0.18	0.12	0.13	0.11

[a] The path is the route in the radial direction from the Al-SiC interface into the matrix, which was selected for slip band density and height measurements. Selection was based on the amount of slip that occurred, and those routes were selected in which the amount of slip bands appeared to be the greatest.
[b] The given strain is actually the result of the product NS. It does not include the coefficient K which was found to be equal to 3 (see Appendix A). Values of γ_{cpss} that incorporate K are given in Table 6.
[c] The distance given here is the distance from the Al-SiC interface to the centers of the first, second etc. squares. Therefore, values of γ_{cpss} represent the strain over the entire square.

TABLE 5

Combined plastic shear strain γ_{cpss} in group C samples (quenched)

Sample	*Path*[a]	*Combined plastic shear strain*[b] γ_{cpss} (%) *for the following distances from the Al-SiC interface*[c]		
		6.25×10^{-2} mm	18.75×10^{-2} mm	31.25×10^{-2} mm
1	1	0.40	0.16	
1	2	0.19	0.27	
1	3	0.09		
2	1	0.37	0.29	0.16
2	2	0.31	0.11	0.05
2	3	0.22	0.24	0.12
2	4	0.55	0.23	0.14
3	1	0.31	0.18	
3	2	0.44	0.24	0.23
4	1	0.25	0.21	0.08
4	2	0.25	0.10	0.04
4	3	0.18	0.13	0.05
Average		0.33	0.20	0.1

[a] The path is the route in the radial direction from the Al-SiC interface into the matrix, which was selected for slip band density and height measurements. Selection was based on the amount of slip that occurred, and those routes were selected in which the amount of slip bands appeared to be the greatest.
[b] The given strain is actually the result of the product NS. It does not include the coefficient K which was found to be equal to 3 (see Appendix A). Values of γ_{cpss} that incorporate K are given in Table 6.
[c] The distance given here is the distance from the Al-SiC interface to the centers of the first, second etc. squares. Therefore, values of γ_{cpss} represent the strain over the entire square.

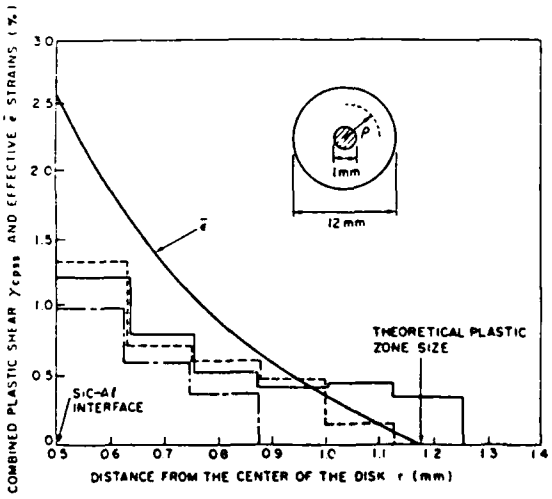

Fig. 5. Theoretical $\bar{\varepsilon}$ *vs.* r and experimental γ_{cpss} *vs.* r profiles around the SiC in Al-SiC composite disks thermocycled between 298 and 823 K (ρ is the plastic zone radius): - - -, group A; ——, group B; ——— —, group C.

actual discrete character of the measurements of γ_{cpss}. Each horizontal portion of the histogram corresponds to the average value of γ_{cpss} obtained from the increment of the area of the specimen.

The largest combined plastic shear strain γ_{cpss} of 1.3% was observed at the Al-SiC interface in group A samples; group C showed the smallest amount of strain, 0.99% (Table 6). In addition, the extent of the plastic zone (*i.e.* the largest distance from the interface at which slip bands can still be measured) was smaller in samples from group C than in samples from groups A and B. This result corresponds to the effect of strain rate (which is proportional to the cooling rate) on the relative amount of plastic and elastic strains during deformation. Generally, higher heating and cooling rates will cause the elastic stresses to be larger, and lower heating and cooling rates will allow greater plastic relaxation [7].

The height of the slip bands was measured to ± 0.1 of a band interval. This gives an error of $\pm 0.1 \times 0.27\ \mu m = \pm 0.027\ \mu m$ in the height values. As was mentioned before, the slip band density measurements introduce much less error. Therefore, the error range for

TABLE 6

Values of γ_{cpss} incorporating K for group A, B and C samples

Group	Combined plastic shear strain γ_{cpss} (%) for the following distances from the Al-SiC interface					
	6.25×10^{-2} mm	18.75×10^{-2} mm	31.25×10^{-2} mm	43.75×10^{-2} mm	56.25×10^{-2} mm	68.75×10^{-2} mm
A	1.32	0.72	0.63	0.48	0.15	
B	1.23	0.81	0.54	0.36	0.39	0.33
C	0.99	0.60	0.3			

γ_{cpss} determination can be evaluated as $\pm (0.027/0.135) \times 100 \approx 20\%$ where 0.135 μm is taken as the average slip band height. This is obviously a large error range.

3.2. *Hot-stage observations*

3.2.1. *Heating*

Slip bands began to appear even before the temperature reached 373 K and were forming as widely spaced deep lines. As the temperature increased, the density of the slip bands increased also, reaching an apparent maximum at around 573 K. At around 533 K a new group of broken lines began to form with no relation to the previously formed slip bands. The development of these lines became more intensive at higher temperatures. When the temperature approached about the 653 K mark, the separation between the matrix and the SiC became fairly visible. At approximately 693 K, slip bands began to fade and disappeared almost totally by the time the temperature reached 853–873 K. At the maximum temperatures, the surface did not appear as flat as it did at the beginning.

3.2.2. *Cooling*

On cooling, previously formed slip band patterns began to show up again but they did not reach the size and extent of the former slip band patterns. The development of the slip bands in new areas was not observed.

The broken line which encircled the entire SiC particle began to develop radial spokes that connected this line to the interface. When the sample cooled to room temperature, the surface of the sample remained rippled.

Subsequent thermocycles did not show any changes in slip band morphology. A broken line around the SiC cylinder became much more clearly defined with repeated thermocycles. The matrix appeared to be separated from the particle all the time.

4. DISCUSSION

Composite models discussed in the literature for the theoretical determination of stresses and strains in the matrix (spherical particle in a matrix, long composite cylinder etc.) cannot be applied to a short composite disk. Therefore, an attempt was made to evaluate the radius of the plastic zone and the plastic strains around the SiC particle using the approach described in Appendix B.

The resultant profile of the effective plastic strain $\bar{\epsilon}$ around the SiC particle and the extent of the plastic zone are shown in Fig. 5. As can be seen, $\rho \approx 1.15$ mm, and $\bar{\epsilon} = 2.5\%$ at the interface. The theoretical plastic strain is higher than the observed plastic strain, and the theoretical plastic zone radius is smaller than the observed plastic zone radius. The theoretical plastic zone size is estimated on the assumption that deformation is homogeneous, *i.e.* uniform around the SiC particle. In the real case we have "bursts" of plastic flow in accordance with a particular crystallographic situation. Thus, the extent of the burst of plastic deformation can be larger than that of homogeneous deformation since the same amount of metal flow must be accommodated. The explanation of the difference between observed and calculated strains can be given as follows. On heating, because of the differential expansion between the aluminum and the SiC, the aluminum matrix tends to pull away from the SiC. If the bonding between the aluminum and the SiC is sufficient to resist the pulling action, the matrix undergoes deformation proportional to ΔT of the cycle. If, however, the bonding is weak, the matrix breaks away from the SiC at a certain temperature T_B, and subsequent temperature increase has no effect on matrix deformation since it is now free to expand.

Hot-stage observations showed that slip band formation started at a temperature of less than 373 K. Accurate evaluation of the temperature at which slip became visible was not possible because the thermocouple in the hot stage was not sensitive enough in the temperature range between 298 and 373 K. It was noticed that more slip bands were formed on the heating half of the thermocycle than on the cooling half. The slip band arrangement on the cooling half repeated the arrangement developed during the heating half. When the temperature approached about 773 K, slip bands began to disappear. This can be explained from the surface tension point of view.

Another possible explanation of the stoppage of slip band development is that the aluminum matrix breaks away from the SiC and continues to expand freely without any restraint from the SiC. It is also possible that very fine slip bands still continued to form (high temperature creep, for example), but we did not see this because of the limitation in resolution of our optical system. It should be mentioned, however, that the disappearance of the slip bands corresponds to a similar observation made by Lammers *et al.* [14] in their *in situ* transmission electron microscopy investigation of Al-SiC composites. They observed "slip lines" in thermally cycled transmission electron microscopy foils, and these slip lines disappeared at high temperatures.

The fact that slip band patterns formed on cooling repeat themselves shows that the same slip systems are engaged in the "reversed" deformation, proving at least partially that there is a certain reversibility of the plastic deformation that occurs when the load is reversed.

The broken lines that form around SiC appeared to be the boundaries of recrystallized grains. If this is indeed the case, recrystallization took place at the interface and occurred very rapidly (2-3 min).

5. CONCLUSION

From the experimental data and the theoretical model the following conclusions were obtained.

(1) A new experimental technique for measuring local plastic strains was developed and utilized in the Al-SiC system.

(2) The theoretical treatment of the short composite cylinder gave the distribution and extent of the plastic strains, which are in fair agreement with the experimental results. There is a disagreement, however, between the experimental and theoretical values of plastic strains immediately at the Al-SiC interface.

(3) An Al-SiC bond is a very important factor influencing the plastic deformation around SiC particles.

REFERENCES

1 R. J. Arsenault and R. M. Fisher, *Scr. Metall.*, *17* (1983) 67.
2 R. J. Arsenault and R. M. Fisher, in J. Carlsson and M. Ohlson (eds.), *Proc. 4th Int. Conf. on the Mechanical Behavior of Materials, Stockholm*, 1983, Vol. 1, Pergamon, Oxford, 1983, p. 451.
3 R. J. Arsenault, *Mater. Sci. Eng.*, *64* (1984) 171.
4 R. J. Arsenault and C. S. Pande, *Scr. Metall.*, *18* (1984) 1131.
5 J. K. Lee, Y. Y. Earmme, H. I. Aaronson and K. C. Russell, *Metall. Trans. A*, *11* (1980) 1837.
6 C. A. Hoffman, *J. Eng. Mater. Technol.*, *95* (1973) 55.
7 G. Garmong, *Metall. Trans.*, *5* (1974) 2183.
8 G. J. Dvorak, M. S. M. Rao and J. Q. Tarn, *J. Compos. Mater.*, *7* (1973) 194.
9 R. L. Mehan, *Metal Matrix Composites, ASTM Spec. Tech. Publ. 438*, 1968, p. 29.
10 G. E. Dieter, *Mechanical Metallurgy*, McGraw-Hill, New York, 2nd edn., 1976, p. 51.
11 *Metals Handbook*, Vol. 1, American Society for Metals, Metals Park, OH, 1961.
12 A. Taylor and R. M. Jones, in J. R. O'Connor and J. Smiltens (eds.), *Silicon Carbide*, Pergamon, Oxford, 1960, p. 147.
13 *Handbook of Material Science*, Vol. II, CRC Press, West Palm Beach, FL, 1975.
14 M. E. Lammers, R. J. Arsenault and R. M. Fisher, to be published.

APPENDIX A

A.1. Combined plastic shear strain γ_{cpss}

The relation between the slip band density N, the amount S of slip or displacement on the band and the plastic strain γ has been discussed in a number of publications [A1-A3]. In their classical works, Yamaguchi *et al.* [A1] and Brown [A2] found direct proportionality between the strain and amount of slip during plastic deformation. Cottrell

[A3] summarized their results and arrived at the expression $\gamma = NS$ for the case when there is only one slip system in operation.

For a multiple-slip-system case, however, this expression must be modified to take into account the different crystallographic orientations of the slip systems.

The attempt to carry out this modification is offered in the present work and consists of the following: the highlights of the one-slip-system case; a description of the rigorous approach for multislip cases; a simplified approximation with the introduction of the combined plastic shear strain γ_{cpss} concept.

Let us assume first that slip occurs in one slip system only. Let us consider an imaginary block (Fig. A1) that is cut out of material in such a way that slip planes are perpendicular to the facets of the block. This block is oriented in such a way that its height is measured along the z axis.

Let us suppose that a shear stress τ_{yz} is applied to the block which causes the block to slip as shown in Fig. A1.

By definition, the shear strain in this case is expressed as

$$\gamma_{yz} = \frac{\Delta S_y}{Z}$$

where ΔS_y is the total displacement in the y direction and Z is the height of the block.

The total displacement ΔS_y is equal to the sum of the displacements on each slip plane, *i.e.*

$$\Delta S_y = \sum_{i=1}^{n} S_i$$

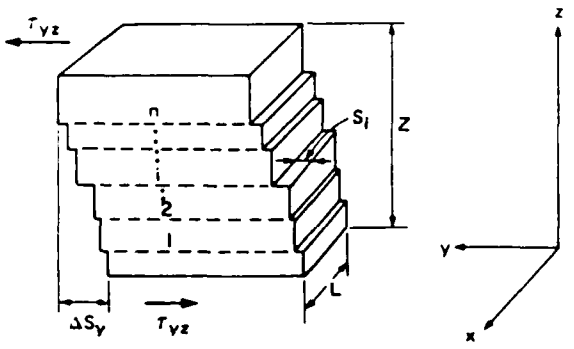

Fig. A1. Hypothetical block with one slip system. S_i is the displacement on the slip plane; ΔS_y is the total displacement along the y axis.

where S_i is the slip or the displacement in the ith band*. (Here S_i is analogous to the furrow depth t in eqn. (2).) If n is the total number of slip bands involved in the slip and $\bar{S}_y$ is the average value of slip per one band, then

$$\Delta S_y = \sum_{i=1}^{n} S_i \approx n\bar{S}_y$$

As can be seen from Fig. A1, n is the number of intersects that the z axis makes with the slip bands and is equal to the total number of slip bands along the z direction. If the number N of slip bands per unit length along z is known (*i.e.* the slip band density), then

$$n = Nz$$

where N (cm^{-1}) is the slip band density along the z direction. Now the total strain γ_{yz} can be expressed [A3] as

$$\gamma_{yz} = \frac{\Delta S_y}{z} = \frac{n\bar{S}_y}{z} = \frac{Nz\bar{S}_y}{z} = N\bar{S}_y \qquad \text{(A1)}$$

N can be evaluated as the total slip band length divided by the total area. To do this we can take eqn. (A1) and multiply the numerator and the denominator by the width L of the block:

$$\gamma_{yz} = \frac{\Delta S_y}{z} = \frac{n\bar{S}_y}{z} = \frac{n\bar{S}_y}{z}\frac{L}{L} = \frac{(nL)\bar{S}_y}{zL} = N_A\bar{S}_y$$

*Generally, the slip direction does not have to be perpendicular to the y plane as shown in Fig. A1. However, despite this and other rather crude assumptions that are made later, the purpose is to show the complexity of the rigorous treatment.

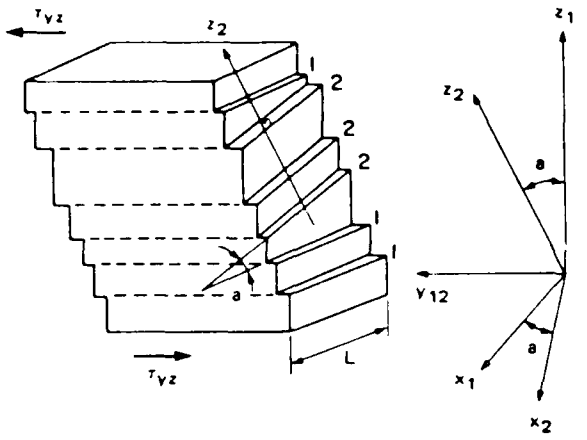

Fig. A2. Hypothetical block with two operational slip systems 1 and 2.

Here, nL is the total length of the slip bands on the side of the block, zL is the total area of this side and N_A (cm^{-1}) = nL/zL is the slip band density. Thus,

$$\gamma_{yz} = N\bar{S}_y$$

In the case when more than one slip system is involved in plastic deformation, slip bands are not parallel but instead each slip system has its own orientation* (Fig. A2). In this situation the equation for shear strain has to be modified to take into account the different orientations of the slip bands. The rigorous way to do this would be as follows.

(1) Determine the plastic strain $\gamma_{y_1z_1}$ using the same approach described previously for slip system 1.

(2) Rotate the coordinate system x_1, y_1, z_1 to align it with system x_2, y_2, z_2 where z_2 is the direction perpendicular to slip bands in slip system 2. In the coordinate system x_2, y_2, z_2, determine $\gamma_{y_2z_2}$ using the relation

$$\gamma_{y_2z_2} = a_{y_2i}a_{z_2j}\gamma_{ij} \qquad \text{(A2)}$$

where $a_{y_2i}a_{z_2j}$ is the rotation matrix and γ_{ij} is the strain tensor in the x_1, y_1, z_1 coordinate system and is given by

$$\gamma_{ij} = \begin{bmatrix} 0 & 0 & 0 \\ 0 & 0 & \gamma_{y_1z_1} \\ 0 & \gamma_{z_1y_1} & 0 \end{bmatrix}$$

*Here, the hypothetical assumption is made that slip planes from the second slip system are also perpendicular to the facets of the block.

(3) Combine the terms determined in step (3) with the terms from step (1) having the same indices. Now we have obtained the total strain tensor ϵ_{ij} in the x_1, y_1, z_1 coordinate system due to all slip systems:

$$\epsilon_{ij} = \begin{bmatrix} 0 & 0 & 0 \\ 0 & 0 & \gamma_{yz} \\ 0 & \gamma_{zy} & 0 \end{bmatrix}$$

(4) Determine the principal components of the strain tensor ϵ_{ij} solving the following equation:

$$\begin{bmatrix} -\lambda & 0 & 0 \\ 0 & -\lambda & \gamma_{yz} \\ 0 & \gamma_{zy} & -\lambda \end{bmatrix} = 0 \qquad \text{(A3)}$$

for λ. The three roots λ_1, λ_2 and λ_3 are the three principal strains ϵ_1, ϵ_2 and ϵ_3 respectively.

(5) Determine the effective strain

$$\bar{\epsilon} = \frac{2^{1/2}}{3}\{(\epsilon_1 - \epsilon_2)^2 + (\epsilon_2 - \epsilon_3)^2 + (\epsilon_3 - \epsilon_1)^2\}^{1/2}$$

As a result of all these steps we finally get one data point on the plot $\bar{\epsilon} = f(r)$. This procedure is simple in principle but complicated to implement, since the crystallographic orientation has to be determined for each grain. As an alternative way of estimating the amount of plastic deformation that occurred around the SiC particle, the following approximation is offered.

First, the concept of *combined plastic shear strain* γ_{cpss} is introduced. We shall define γ_{cpss} as

$$\gamma_{cpss} = KN\bar{S}$$

where $\bar{S}$ is the average step height. In general, the slip plane is not perpendicular to the surface and therefore the coefficient K is incorporated. K is a coefficient which will be evaluated later. N is the slip band density, which is obtained from the total slip band length of all slip systems divided by the area where the total slip band length is the length of all the slip bands enclosed in a selected area (*e.g.* a square mesh of some net). The selection of the size of the area is based on considerations of the scale. It is realized that the combined plastic shear strain γ_{cpss} has no direct correlation with the effective strain $\bar{\epsilon}$, the octahedral shear strain γ_{oct} or any other

specific strain. However, the relative simplicity in the determination of γ_{cpss} and the fact that γ_{cpss} takes into account direct proportionality between the amount of plastic deformation and the slip band density makes it very attractive for use as a criterion for plastic deformation in our case and in other similar cases in general.

A.2. Determination of the coefficient K

The coefficient K takes into account the different crystallographic orientations of slip systems. Let us consider the case when we have three slip systems operating, *i.e.* we see three slip band groups. The individual slip systems contribute the strain $N_1\bar{S}_1$, $N_2\bar{S}_2$ and $N_3\bar{S}_3$ to the total γ_{cpss}, *i.e.*

$$\gamma_{cpss} = N_1\bar{S}_1 + N_2\bar{S}_2 + N_3\bar{S}_3$$

where N_1, N_2 and N_3 are the slip band densities and $\bar{S}_1$, $\bar{S}_2$ and $\bar{S}_3$ are the average displacements on the band within each slip system, given by

$$\bar{S}_1 = \frac{\bar{S}_{M1}}{\sin\theta_1}$$

$$\bar{S}_2 = \frac{\bar{S}_{M2}}{\sin\theta_2}$$

and

$$\bar{S}_3 = \frac{\bar{S}_{M3}}{\sin\theta_3}$$

where $\bar{S}_{M1}$, $\bar{S}_{M2}$ and $\bar{S}_{M3}$ are the average heights of the slip bands in the three slip systems, measured perpendicularly to the surface, and θ_1, θ_2 and θ_3 are the angles between the slip planes and the surface plane. Thus,

$$\gamma_{cpss} = N_1\bar{S}_{M1}\frac{1}{\sin\theta_1} + N_2\bar{S}_{M2}\frac{1}{\sin\theta_2} + N_3\bar{S}_{M3}\frac{1}{\sin\theta_3}$$

Now we shall assume that the amounts of strain $N_1\bar{S}_{M1}$, $N_2\bar{S}_{M2}$ and $N_3\bar{S}_{M3}$ are approximately equal because of the symmetry of the specimen and provided that no voids or cracks are created. Furthermore,

$$\gamma_{cpss} = N\bar{S}_M\left(\frac{1}{\sin\theta_1} + \frac{1}{\sin\theta_2} + \frac{1}{\sin\theta_3}\right)$$

or

$$\gamma_{cpss} = KN\bar{S}_M$$

where

$$K = \frac{1}{\sin\theta_1} + \frac{1}{\sin\theta_2} + \frac{1}{\sin\theta_3}$$

Let us evaluate the range within which K can change by considering a unit triangle (Fig. A3). Let the directions shown on the triangle correspond to the poles of the surface of the sample. Then the values of K would be as shown in Table A1. The average value of K is about 4.5 when three slip systems are operating. Thus, the average correction factor per one slip system is 4.5/3 = 1.5. In general, slip band densities were measured along directions going through areas where two slip systems, *i.e.* two sets of slip bands, were present. Thus for, two slip systems, $K = 2 \times 1.5 = 3$.

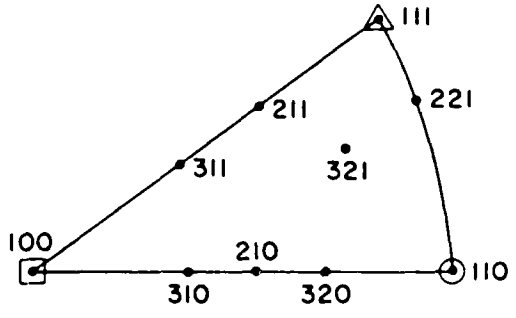

Fig. A3. Some orientations of the sample for which values of K were determined.

TABLE A1

Values of K corresponding to the orientations shown in Fig. A3

Surface plane pole	(111)	(110)	(100)	(210)	(211)	(221)	(310)	(311)	(320)	(321)
K for (111) slip plane	3.2	3.7	3.7	3.66	5.1	5.9	3.6	4.2	3.1	4.9

References for Appendix A

A1 K. Yamaguchi, *Sci. Paper Inst. Phys. Chem. Res. Tokyo, 8* (1928) 289; *11* (1929) 151.

A2 A. F. Brown, *J Inst. Met., 80* (1951) 115.

A3 A. H. Cottrell, *Dislocations and Plastic Flow in Crystals*, Clarendon, Oxford, 1965, p. 157.

APPENDIX B

Among the several composite models described in the literature, there is one that appears to be close to our case; this is known as the long-composite-cylinder model. It consists of long continuous fiber surrounded by the metal matrix. This model implies that plastic strain in the direction of the fiber (the z direction) resulted from unequal expansion or contraction of fiber and that the matrix is a constant, *i.e.* $\epsilon_z = dl/l$ = constant where l is the length of the fiber.

Therefore, the total plastic strain state becomes a plane strain case which enables two other plastic strains ϵ_r and ϵ_θ to be found without difficulty. Although short composite cylinders have the same symmetry as long composite cylinders, the strain in the z direction is not a constant but is in general a function of two variables: (1) the distance from the interface and (2) the position along the z axis. Since $\epsilon_z \neq$ constant, the long-cylinder approach cannot be used in our case.

We shall discuss the case shown in Fig. B1. Let us consider an Al-SiC disk that cools from a temperature T. As a result of cooling, a certain amount of aluminum will be pushed back because of the differential shrinkage of SiC and aluminum. If we did not have SiC in the center of the aluminum disk, the aluminum ring would shrink without any restraint and the size of the bore would be reduced by

$$U_a = \Delta a = a\,\Delta\alpha\,\Delta T$$

where a is the radius of the SiC, $\Delta\alpha$ ($\approx 25 \times 10^{-6}$ K^{-1}) is the difference between the coefficient of thermal expansion of aluminum and that of SiC, ΔT (≈ 500 K) is the temperature interval and U_a is the displacement at the interface. The reduction in the radius of the bore does not occur when SiC is present in the center of the aluminum disk. The amount of aluminum that is not allowed to go towards the center of the bore would cause plastic flow of the adjacent matrix in all directions away from the SiC. Thus, some of the matrix will spill out (as shown in Fig. B1). As we go further away from the interface, the plastic flow is restricted by the matrix that surrounds the central portion. Two regions can be considered: the plastic region that we assume is adjacent to the SiC and the elastic region that encloses the plastic region. Let us make the following assumptions.

(1) In the plastic zone the matrix is a perfectly plastic material, *i.e.* no work hardening occurs.

(2) At the starting temperature T of 773 K, SiC and aluminum are just in contact with one another.

(3) The profile of the aluminum which has spilt out is a straight line.

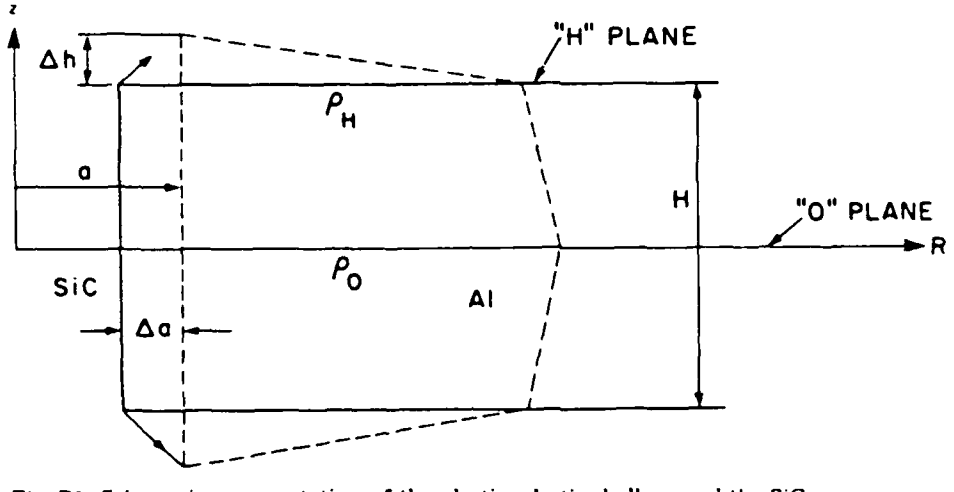

Fig. B1. Schematic representation of the plastic–elastic shell around the SiC.

(4) The plastic-elastic front is also a straight line.

Now let us consider the radius ρ of the plastic zone. It is a function of the vertical position of the transverse plane in which ρ is considered. According to our assumption,

$$\rho = \rho_0 - qz$$

(the equation of the straight line) where ρ_0 is the plastic zone radius in the "0" plane, which is the plane of symmetry between the upper and lower halves of the composite disk. To determine q we let $z = \frac{1}{2}H$, *i.e.* the top of the "H" plane is considered. When $z = \frac{1}{2}H$, $\rho = \rho_H$. Therefore

$$\rho_H = \rho_0 - q\tfrac{1}{2}H$$

From this

$$q = 2(\rho_0 - \rho_H)\frac{1}{H}$$

and now

$$\rho = \rho_0 - 2(\rho_0 - \rho_H)\frac{z}{H} \qquad \text{(B1)}$$

Let us consider now the portion of the matrix that spills out. From the triangle shown in Fig. B2 we can write

$$U_z = \Delta h \frac{\rho_H - r}{\rho_H - a} \qquad \text{(B2)}$$

where U_z is the vertical displacement. Generally speaking, the vertical displacement U_z is a function of z and r, *i.e.*

$$U_z = \phi\{f(z), g(r)\}$$

Equation (B2) gives only an expression for U_z when the "H" plane is considered. The problem thus is to find a general expression for U_z. To do this, let us replace ρ_H in eqn.

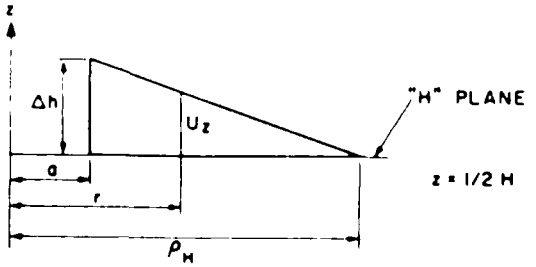

Fig. B2. "Spill-out" portion of the aluminum matrix.

(B2) with a general expression for ρ (eqn. (B1)) when $z = \frac{1}{2}H$

$$U_z = \Delta h \frac{\rho_0 - 2(\rho_0 - \rho_H)^{\frac{1}{2}} - r}{\rho_0 - 2(\rho_0 - \rho_H)^{\frac{1}{2}} - a}$$

$$\Delta h = \tfrac{1}{2}H\,\Delta\alpha\,\Delta T$$

and

$$U_z = \tfrac{1}{2}H\,\Delta\alpha\,\Delta T \frac{\rho_0 - 2(\rho_0 - \rho_H)^{\frac{1}{2}} - r}{\rho_0 - 2(\rho_0 - \rho_H)^{\frac{1}{2}} - a} \qquad \text{(B3)}$$

If we simplify eqn. (B3) it reduces to eqn. (B2), but let us leave eqn. (B3) in its form and examine it in more detail. First let us substitude $H = 1$ mm in eqn. (B3), since this is a convenient way of simplifying this expression and $H = 1$ mm happens to be the actual height of our composite disks. Now we can rewrite eqn. (B3) as

$$U_z = \tfrac{1}{2}\,\Delta\alpha\,\Delta T \frac{\rho_0 - 2(\rho_0 - \rho_H)^{\frac{1}{2}} - r}{\rho_0 - 2(\rho_0 - \rho_H)^{\frac{1}{2}} - a} \qquad \text{(B4)}$$

for $z = \frac{1}{2}H$ or if we normalize $z' = z/H = \frac{1}{2}$. Let us check the values of U_z at different z values. First, let $z = \frac{1}{2}$ ("H" plane), and so

$$U_z = \tfrac{1}{2}\,\Delta\alpha\,\Delta T \frac{\rho_0 - 2(\rho_0 - \rho_H)^{\frac{1}{2}} - r}{\rho_0 - 2(\rho_0 - \rho_H)^{\frac{1}{2}} - a}$$

Then, when $r = a$,

$$U_z = \tfrac{1}{2}\,\Delta\alpha\,\Delta T = \Delta h$$

and, when $r = \rho_H$,

$$U_z = 0$$

Let $z = 0$ ("0" plane), and so $U_z = 0$, since the "0" plane is the plane of vertical symmetry. At this point we can see a certain logic in eqn. (B4), which enables us to suggest the general expression for U_z in the following form:

$$U_z = z'\,\Delta\alpha\,\Delta T \frac{\rho_0 - 2(\rho_0 - \rho_H)z' - r}{\rho_0 - 2(\rho_0 - \rho_H)z' - a} \qquad \text{(B5)}$$

(since $H = 1$). It is realized that eqn. (B5) lacks rigorous proof. However, since it incorporates our boundary conditions and since we do not have any additional information, it is reasonable to adopt eqn. (B5) and to see what results we can obtain and then to judge the validity of this expression. Let us consider the cylindrical coordinate system in which the z axis coincides with the z axis of our sample. By definition

$$\epsilon_r = \frac{dU_r}{dr}$$

$$\epsilon_\theta = \frac{U_r}{r}$$

$$\epsilon_z = \frac{dU_z}{dz}$$

$$\epsilon_z = \frac{dU_z}{dz}$$

$$= \Delta\alpha\,\Delta T\,\frac{\rho_0 - 2(\rho_0 - \rho_H)z - r}{\rho_0 - 2(\rho_0 - \rho_H)z - a} + \qquad \text{(B5)*}$$

$$+ z\,\Delta\alpha\,\Delta T\,\frac{2(\rho_0 - \rho_H)(a - r)}{[\rho_0 - 2(\rho_0 - \rho_H)z - a]}$$

Incompressibility requires that

$$\epsilon_r + \epsilon_\theta + \epsilon_z = 0$$

or

$$\frac{dU_r}{dr} + \frac{U_r}{r} + \epsilon_z = 0 \qquad \text{(B6)}$$

Let us consider the "0" plane, where $z = 0$; then

$$\epsilon_z = \Delta\alpha\,\Delta T\,\frac{\rho_0 - r}{\rho_0 - a} \qquad \text{(B7)}$$

Equation (B6) then becomes

$$\frac{dU_r}{dr} + \frac{U_r}{r} + \Delta\alpha\,\Delta T\,\frac{\rho_0 - r}{\rho_0 - a} = 0 \qquad \text{(B8)}$$

$$\frac{dU_r}{dr} + \frac{U_r}{r} + M - Nr = 0 \qquad \text{(B9)}$$

where

$$M = \Delta\alpha\,\Delta T\,\frac{\rho_0}{\rho_0 - a}$$

and

$$N = \Delta\alpha\,\Delta T\,\frac{1}{\rho_0 - a}$$

The solution of eqn. (B9) is

$$U_r = -\frac{M}{2}r + \frac{C}{r} + \frac{N}{3}r^2 \qquad \text{(B10)}$$

*From here on we omit the superscript prime in z' and use z instead to prevent confusion, but it should be borne in mind that the value z is normalized with respect to H.

To find the constant C we use the boundary condition $U_{r=a} = U_a = a\,\Delta\alpha\,\Delta T$:

$$U_a = a\,\Delta\alpha\,\Delta T = -\frac{M}{2}a + \frac{C}{a} + \frac{N}{3}a^2$$

$$C = aU_a + \frac{M}{2}a^2 - \frac{N}{3}a^3$$

Now eqn. (B10) becomes

$$U_r = -\frac{M}{2}r + \frac{U_a a}{r} + \frac{Ma^2}{2r} - \frac{Na^3}{3r} + \frac{N}{3}r^2 \qquad \text{(B11)}$$

Now we can find the strains ϵ_r, ϵ_θ and ϵ_z for the "0" plane:

$$\epsilon_r = \frac{dU_r}{dr} = -\frac{M}{2} - \frac{U_a a}{r^2} - \frac{Ma^2}{2r^2} + \frac{Na^2}{3r^2} + \frac{2}{3}Nr$$

$$\epsilon_\theta = \frac{U_r}{r} = -\frac{M}{2} + \frac{U_a a}{r^2} + \frac{Ma^2}{2r^2} - \frac{Na^3}{3r^2} + \frac{N}{3}r$$

$$\epsilon_z = M - Nr \qquad \text{(B12)}$$

Let us consider the tip of the plastic-elastic interface, *i.e.* $r = \rho_0$. Then ($\epsilon_z = 0$ from eqn. (B7))

$$\epsilon_r = -\epsilon_\theta$$

$$= -\frac{U_{\rho_0}}{\rho_0} \qquad \text{(B13)}$$

where U_{ρ_0} is the displacement of the tip of the plastic-elastic front:

$$U_{r=\rho_0} = U_{\rho_0}$$

Each point of the plastic-elastic front is in the state of incipient yielding, *i.e.*

$$\bar{\epsilon} = \epsilon_0$$

where $\bar{\epsilon}$ is the effective strain at the interface and ϵ_0 is the yielding strain taken from the yielding condition of the tensile sample in uniaxial loading:

$$\sigma_y = E\epsilon_0$$

Therefore

$$\epsilon_0 = \frac{\sigma_y}{E}$$

$$= \frac{11.73}{62 \times 10^3}$$

$$\approx 2 \times 10^{-4}$$

where $\sigma_y = 11.73$ MPa and $E = 62 \times 10^3$ MPa for pure aluminum. Thus we have a system of equations:

$$\epsilon_{r(r=\rho_0)} = -\frac{U_{\rho_0}}{\rho_0}$$

$$\epsilon_{\theta(r=\rho_0)} = \frac{U_{\rho_0}}{\rho_0} \qquad \text{(B14)}$$

$$\epsilon_{z(r=\rho_0)} = 0$$

Applying the von Mises yielding condition,

$$\bar{\epsilon} = \frac{2^{1/2}}{3}\{(\epsilon_1 - \epsilon_2)^2 + (\epsilon_1 - \epsilon_3)^2 + (\epsilon_2 - \epsilon_3)^2\}^{1/2}$$

where ϵ_1, ϵ_2 and ϵ_3 are the principal strains. Generally speaking, the strains ϵ_r, ϵ_θ and ϵ_z do not coincide with the principal strains ϵ_1, ϵ_2 and ϵ_3, because of the existence of the shear component in the total strain tensor, which is given by

$$\gamma_{zr} = \frac{dU_z}{dr} + \frac{dU_r}{dz}$$

The components $\gamma_{\theta r}$ and $\gamma_{z\theta}$ are equal to zero because of the symmetry around SiC.

$$\frac{dU_z}{dr} = -\frac{\Delta\alpha\,\Delta T\,z}{\rho_0 - 2(\rho_0 - \rho_H)z - a}$$

for the "0" plane; when $z = 0$, $dU_z/dr = 0$. To evaluate dU_r/dz, let us consider the region of the matrix adjacent to the "0" plane as shown in Fig. B3. Point A is displaced to point A′, and point B to point B′. (B is a mirror image of A.) The displacements $U_{AA'}$ and $U_{BB'}$ are equal because of the symmetry and from the assumption that no voids are created. The displacement U_r varies as we go along the z axis and presents a continuous function of z. Since the function is continuous and symmetrical about the "0" plane, it goes through its local *maximum* or *minimum* point when it crosses the "0" plane and therefore $dU_z/dz = 0$ when $z = 0$. Thus we found that, within the "0" plane, *all* the shear components of the strain tensor are equal to zero, which means that $\epsilon_r = \epsilon_1$, $\epsilon_\theta = \epsilon_2$ and $\epsilon_z = \epsilon_3$ for the "0" plane. Thus, if we go back to the von Mises condition of yield, the effective strain $\bar{\epsilon}$ can now be expressed as

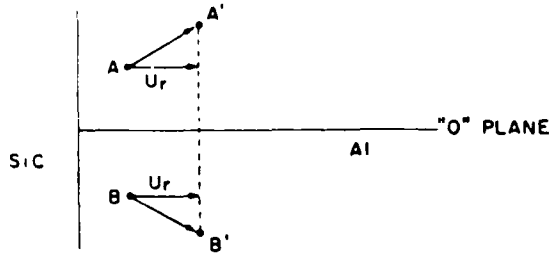

Fig. B3. Displacements AA′ and BB′ of the matrix symmetrical about the "0" plane.

$$\bar{\epsilon} = \frac{2^{1/2}}{3}\{(\epsilon_r - \epsilon_\theta)^2 + (\epsilon_\theta - \epsilon_z)^2 + (\epsilon_r - \epsilon_z)^2\}^{1/2}$$

and, from eqn. (B14),

$$\bar{\epsilon} = \frac{2^{1/2}}{3}\left\{\left(\frac{U_{\rho_0}}{\rho_0}\right)^2 + \left(\frac{2U_{\rho_0}}{\rho_0}\right)^2 + \left(\frac{U_{\rho_0}}{\rho_0}\right)^2\right\}^{1/2}$$

$$= 1.155\,\frac{U_{\rho_0}}{\rho_0}$$

However,

$$\bar{\epsilon} = \epsilon_0$$

$$= 2 \times 10^{-4}$$

$$= 1.155\,\frac{U_{\rho_0}}{\rho_0}$$

Therefore

$$\frac{U_{\rho_0}}{\rho_0} = 1.7 \times 10^{-4} \qquad \text{(B15)}$$

From eqn. (B11) we get

$$U_{\rho_0} = -\frac{M}{2}\rho_0 + \frac{U_a a}{\rho_0} + \frac{Ma^2}{2\rho_0} - \frac{Na^3}{3\rho_0} + \frac{N}{3}\rho_0^2$$

and, substituting for M and N, we obtain

$$U_{\rho_0} = \frac{\Delta\alpha\,\Delta T}{\rho_0}\left\{\frac{\rho_0^2 + a\rho_0 + a^2}{3} - \frac{(a+\rho_0)\rho_0}{2} + a^2\right\} \qquad \text{(B16)}$$

Equations (B15) and (B16) can be solved as a system of two equations with two unknowns, U_{ρ_0} and ρ_0. Solving them, we obtain $\rho_0 = 1.15$ mm. In order to find ρ_H we can follow the same procedure. However, for the "H" plane case the strains ϵ_r, ϵ_θ and ϵ_z are not equal to ϵ_1, ϵ_2 and ϵ_3. Therefore the procedure has to be modified. The new procedure would be to find an expression for

$$\gamma_{zr} = \frac{dU_z}{dr} + \frac{dU_r}{dz}$$

for $z = \frac{1}{2}$ and then to solve the equation

$$\begin{bmatrix} \epsilon_r - \lambda & 0 & \gamma_{rz} \\ 0 & \epsilon_\theta - \lambda & 0 \\ \gamma_{zr} & 0 & \epsilon_z - \lambda \end{bmatrix} = 0$$

This is a cubic equation. Three roots give the values for the principal strains:

$$\lambda_1 = \epsilon_1$$

$$\lambda_2 = \epsilon_2$$

and

$$\lambda_3 = \epsilon_3$$

This is simple in principle but very complex to implement for the following reason. The individual components of this tensor are of the type expressed by eqns. (B11) and (B15). If the coefficients of the cubic equation were numerical, then we could solve it using the trial-and-error method. In our case, all the coefficients have a general expression. The general solution of the cubic equation has the form

$$\lambda_1 = \left[-\frac{q}{2} + \left\{\left(\frac{q}{2}\right)^2 + \left(\frac{p}{3}\right)^3\right\}^{1/2}\right]^{1/3} + \left[-\frac{q}{2} - \left\{\left(\frac{q}{2}\right)^2 + \left(\frac{p}{3}\right)^3\right\}^{1/2}\right]^{1/3}$$

Each q and p would be a combination of the expressions for ϵ_r, ϵ_θ, ϵ_z and γ_{zr}. Because of the difficulty of determining ρ_H in a rigorous way we can use an approximate solution by treating strains ϵ_r, ϵ_θ and ϵ_z as the principal strains ϵ_1, ϵ_2 and ϵ_3. This implies that we ignore the influence of the shear strain γ_{zr}. It is realized that the resulting value for ρ_H will not be a true value but it will at least give an idea of the extent of the plastic zone on the surface of the sample. Additionally, if the magnitude of γ_{zr} is small, the deviation of ϵ_r, ϵ_θ and ϵ_z from ϵ_1, ϵ_2 and ϵ_3 will also be small.

Now, considering $z = \frac{1}{2}$ and using the yielding condition at the plastic-elastic front, we can follow steps similar to those that we used for the "0" plane. As a result $\rho_H = 1.11$ mm. It is useful to find a general expression for $\bar{\epsilon}$ in the "0" plane. After substitution of the numerical values for a and ρ, eqn. (B12) becomes, for $z = 0$,

$$\epsilon_z = \frac{1.15 - r}{0.65} \Delta\alpha\, \Delta T$$

$$\epsilon_\theta = \frac{0.513r^3 + 0.407 - 0.885r^2}{r^2} \Delta\alpha\, \Delta T$$

$$\epsilon_z = \frac{0.667r^3 - 0.575r^2 - 0.265}{0.65r^2} \Delta\alpha\, \Delta T$$

$$\bar{\epsilon} = 9.077 \times 10^{-3} \times \times \left(4.668r^2 - 10.35r + 5.952 - \frac{0.531}{r} - \frac{0.42}{r^4}\right)^{1/2}$$

This effective strain is plotted as a function of r in Fig. 5. When $\bar{\epsilon} = \epsilon_0 = 2 \times 10^{-4}$ is substituted in the expression above, the theoretical plastic zone radius can be obtained from $r = \rho = 1.15$ mm. The radius of the fiber is 0.5 mm. Thus $\rho = 1.15/0.5 = 2.3 \times$ fiber radius. This radius includes the fiber size. Thus the extent of the plastic zone measured from the interface is $(2.3 - 1) \times$ fiber radius $= 1.3 \times$ fiber radius.

Materials Science and Engineering, 77 (1986) 191-197

Interfacial Bond Strength in an Aluminum Alloy 6061 – SiC Composite

Y. FLOM and R. J. ARSENAULT

Metallurgical Materials Laboratory, University of Maryland, College Park, MD 20742 (U.S.A.)

(Received April 1, 1985; in revised form July 25, 1985)

ABSTRACT

An investigation was undertaken to evaluate the strength of the interfacial bond between SiC and the aluminum alloy 6061 matrix. Approximate bounding analysis provided the conditions for separation of the inclusion from the ductile matrix under the local negative pressure (the triaxial tensile stress). The experimental data were analyzed to determine the local interfacial stresses at the particle-matrix interfaces. The lower bound value of the bond strength was determined to be equal to at least 1690 MPa. Debonding of SiC particulates from the matrix was found to be a rare event.

1. INTRODUCTION

The quality of the interfacial bond between aluminum and SiC is important in composite strengthening, independent of the strengthening mechanism that is assumed to be operative. One of the key elements in the continuum mechanics treatment of the composite strengthening is that the interface transfers the load from the matrix into the reinforcement [1-3]. The rule of mixtures that emerges from continuum mechanics relates a given property of the composite to the properties of its constituent materials. The credibility of this approach depends on, among other factors, the bond integrity and the efficiency of the load transfer from the matrix to the reinforcement.

Recently it has been shown [4-6] that in Al-SiC systems the interfaces are a major source of the dislocation generation (on cooling from fabricating temperature because of the difference in the coefficient of thermal expansion). The resultant dislocation densities at the Al-SiC interfaces can be very high (10^9-10^{10} cm^{-2}), which significantly contributes to the overall composite strength. Interestingly, when an Al-SiC system is subject to heating, the Al-SiC interface also generates dislocations (provided that the Al-SiC bond is quite strong) [7]. If the bond is weak, the aluminum just pulls away from the particle and is free to expand without any restrictions on the part of the SiC and, in the subsequent cooling, no dislocations are generated. Therefore a good bond is required to produce the high dislocation density.

Several investigators have reported that the Al-SiC bond is generally good [8, 9], but a systematic evaluation of the bond strength has not been, to our knowledge, reported in the literature. Direct measurements of the interfacial shear strength in metal matrix systems have been made using flat plate and fiber pull-out tests [10]. The fiber pull-out test, which is of more interest for this investigation, was used to determine the interfacial shear strength in Cu-W and Cu-Mo systems [11]. Several attempts were made to carry out a direct measurement of the interfacial bond shear strength in Al-SiC using the pull-out test because of its apparent simplicity. However, all these attempts resulted in the brittle failure of SiC (single-crystal, very-large-grain and sintered SiC were used) at very moderate loads.

In addition, an effort was made to perform a punch test using aluminum disks with pieces of the SiC embedded in the center. This effort also resulted in premature failure of the SiC.

Another way to evaluate the interfacial bond strength is based on the general understanding of the mechanism of the ductile fracture [12-15] and was applied for the determination of the interfacial bond strength in spheroidized type 1045 steel,

0025-5416/86/$3.50

Cu-0.6%Cr alloy and maraging steel containing Fe_3C, Cu-Cr and TiC particles [16, 17]. Provided that the ductile fracture starts by void nucleation at the inclusions and second-phase particles, the theoretical bounding analysis [15] allows the evaluation of the interfacial strength in the systems with the small volume fraction of the second phase.

The purpose of this investigation was to determine experimentally the bond strength between SiC and aluminum in a commercial composite material using the analysis of separation of the inclusion from the matrix under the negative pressure.

2. EXPERIMENTAL PROCEDURE

A 1 vol.% SiC particulate in an aluminum alloy 6061 matrix composite purchased from DWA was used for this investigation. The low volume percentage of the particulate was necessary in order (1) to provide favorable conditions for ductile fracture and thus to activate the mechanism of a void nucleation and growth type of failure and (2) to satisfy criteria of non-interacting particles [17]. At higher volume concentrations the Al-SiC composites exhibited very little ductility. The theoretical analysis of the inclusion separation from the matrix that was used in this investigation was based on the assumption that there is no interaction between the particles, which is a reasonable statement for a small-volume concentration.

The composite material was machined to standard tensile test specimens. In order to introduce a local triaxial stress state, a circumferential groove was electricodischarge machined in the center of the specimen (Fig. 1). Subsequently, the specimens were solution annealed at 823 K for 12 h and iced water quenched in order to keep the Mg_2Si phase in the solution and thus to limit the presence of particles other than SiC. After quenching, the samples were placed in the freezer of a commercial refrigerator where they were stored at 265 K, and within a few minutes the samples were warmed up to the testing temperature of 295 K. The specimens were tested in tension to fracture using the Instron testing machine at a cross-head speed of 0.05 cm min^{-1}. The fractured halves were electric discharge

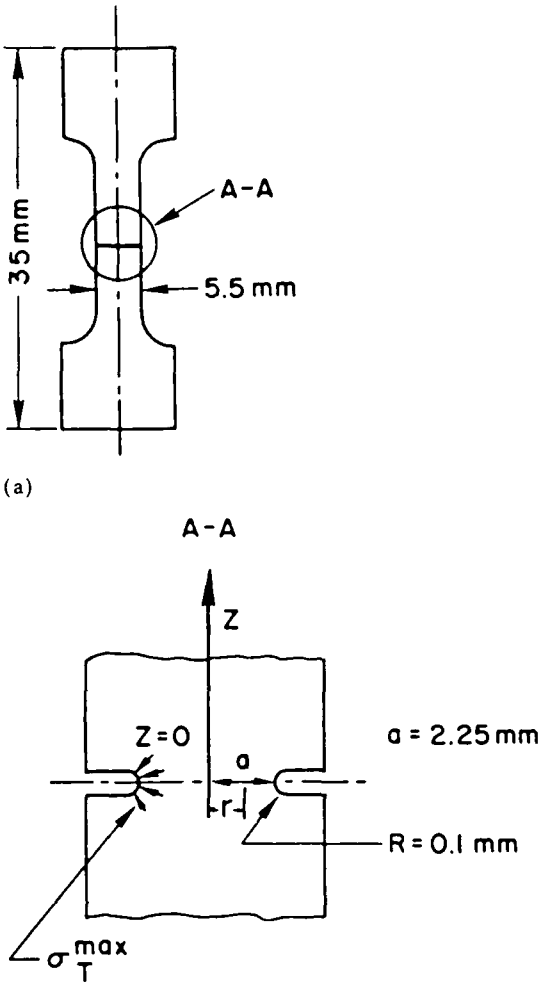

Fig. 1. A schematic view of (a) the specimen and (b) an enlarged portion of the groove showing the groove geometry and the location of the maximum triaxial stresses.

machined, cut longitudinally (parallel to the tensile axis) and mechanically polished. Final polishing was done using a colloidal silica suspension as abrasive (Buehler's Mastermet) on the special moderate-length nap cloth (Buehler's Mastertex). Since this suspension has a slightly alkali reaction, the final polishing was accomplished both mechanically and chemically. Therefore the surface was ready for inspection without the necessity of etching to delineate the SiC particulates. Polished sections were examined for void and particle separation using scanning electron microscopy.

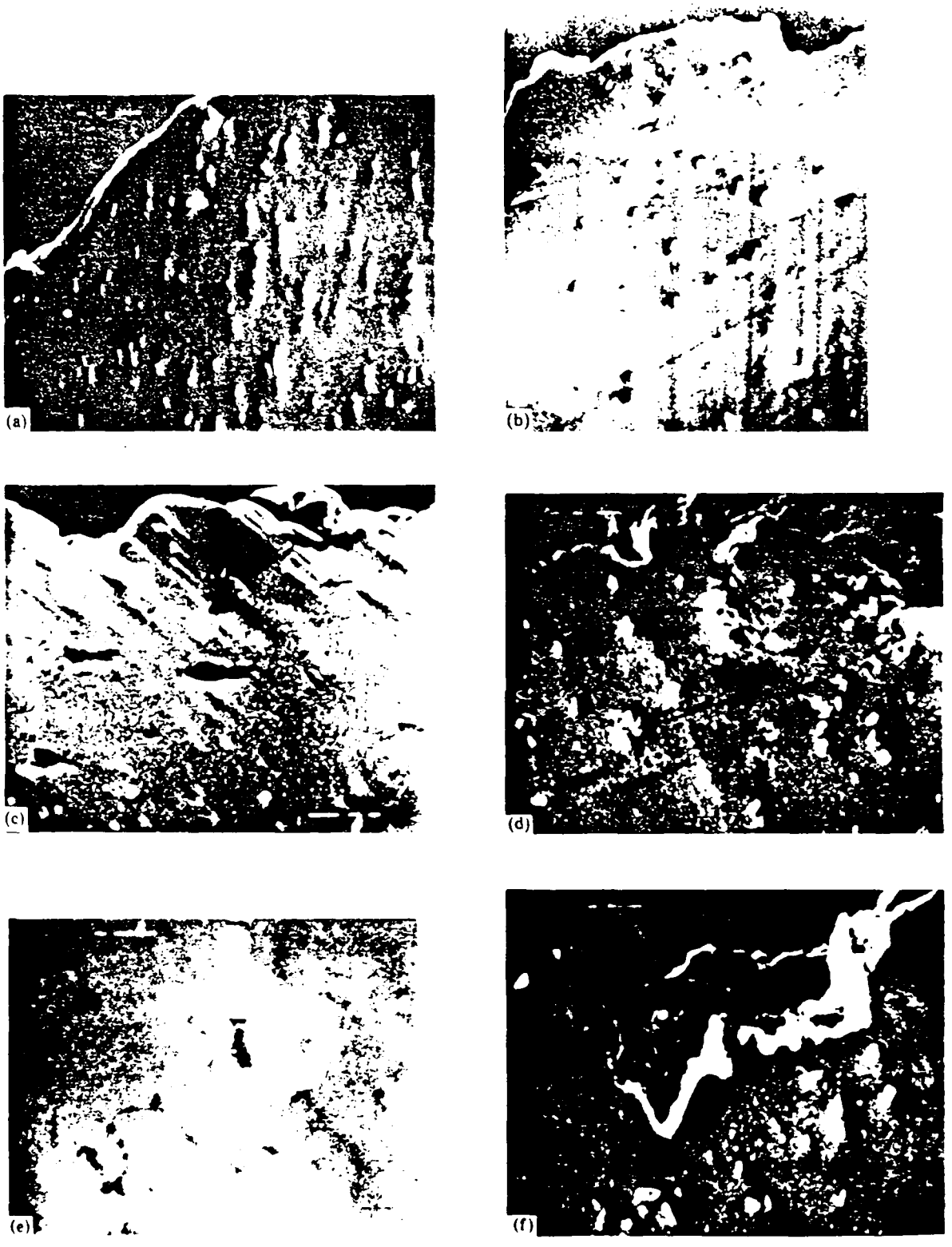

Fig. 2 *(continued)*.

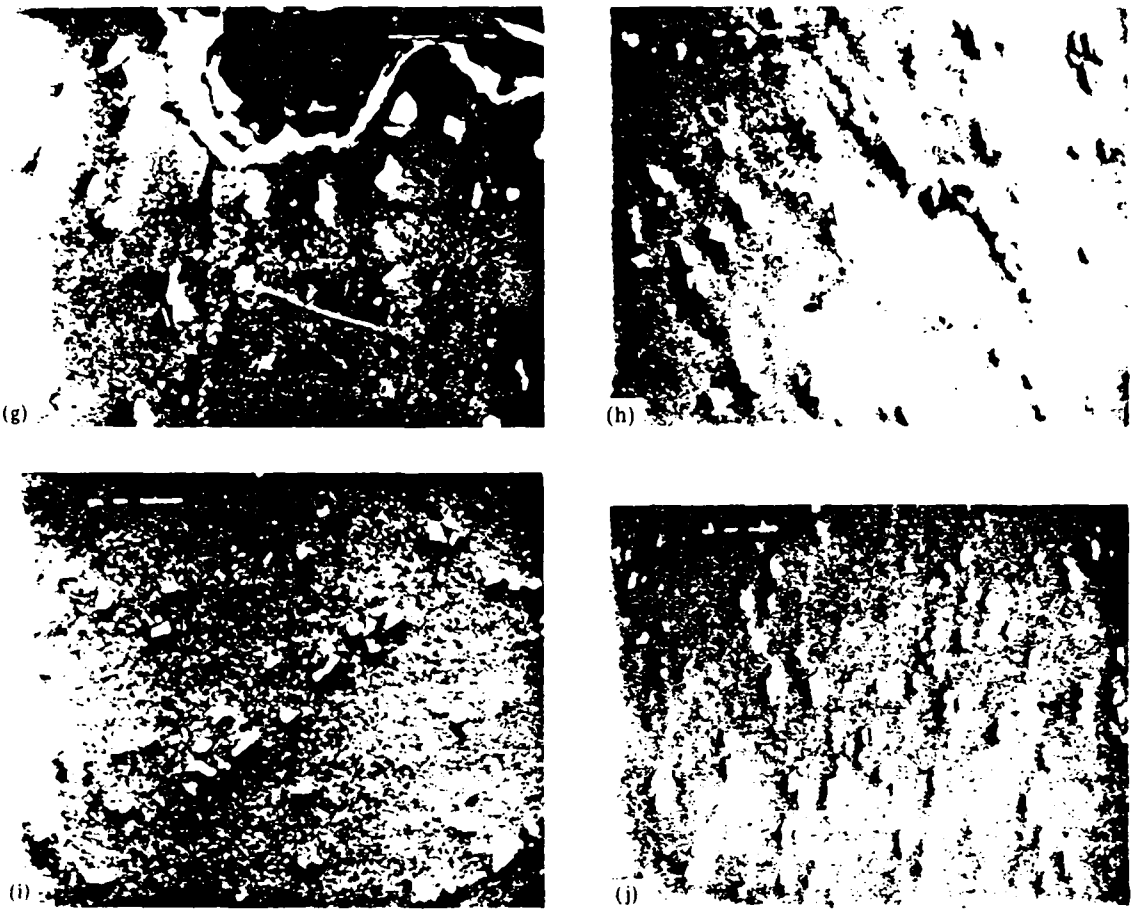

Fig. 2. Electron micrographs of the different areas of the longitudinal cross sections of the fractured Al–1vol.%SiC specimens: (a), (b) taken in the vicinity of the bottom of the groove (no apparent debonding is present at the position of maximum triaxial stress); (c)–(g) taken below the fracture surface away from the groove; (h)–(j) taken far away from the fracture and representing the bulk of the specimen. (Magnifications: (a) 428×; (b) 540×; (c) 500×; (d) 490×; (e) 930×; (f) 623×; (g) 720×; (h) 475×; (i) 598×; (j) 428×.)

3. EXPERIMENTAL RESULTS AND DISCUSSION

The experimental technique adopted in this work was based on the determination of local stresses during plastic deformation under a triaxial stress state [16]. The bonding analysis [16] showed that the interfacial stress σ_{rr} can be expressed as

$$\sigma_{rr} = \sigma_T + Y(\bar{\varepsilon}^p) \qquad (1)$$

where σ_T is the local negative pressure (the triaxial tensile stress) and $Y(\bar{\varepsilon}^p)$ is true flow stress in tension corresponding to the local average plastic strain, had the second-phase particle been absent. This analysis was based on the assumption that (1) particles have an equiaxed shape and (2) the volume fraction of the second phase is small. Also, it can be mentioned that SiC is rigid and undeformed. This physical property agrees very well with the assumption of rigidity of the inclusions [16].

The distribution of the triaxial tensile stress along the radial line in the plane of the groove was obtained from the theory of stress concentrations on circumferentially grooved elastic bars originally considered by Neuber and then expressed [16] as

$$\frac{\sigma_T}{\sigma_0} = \frac{c}{\{1-(r/a)^2\}^{1/2}} \qquad (z=0) \qquad (2)$$

where σ_T/σ_0 represents the triaxiality, σ_T is the negative pressure, σ_0 is the flow stress or average ligament stress, z is equal to the

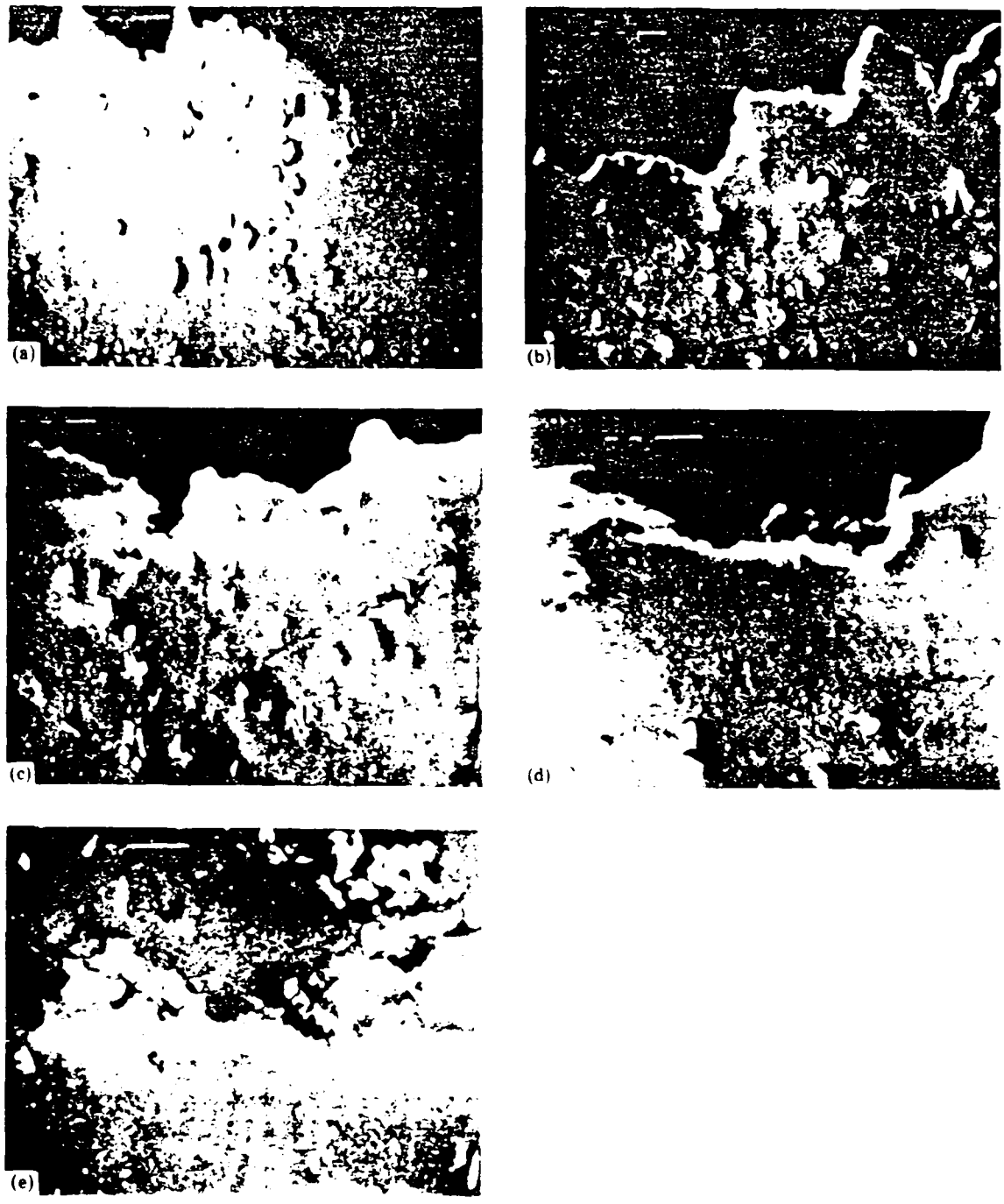

Fig. 3. Electron micrographs of the areas below the fracture surface (a) at the bottom of the groove and (b)-(e) away from it where debonding was observed. (Magnifications: (a) 576×; (b) 450×; (c) 495×; (d) 720×; (e) 768×.)

vertical distance along the z axis, *i.e.* the tensile axis center-line of sample, and r is the distance from the z axis. Since the triaxiality σ_T/σ_0 reaches its maximum value at the bottom of the groove, r should be equal to a where $2a$ is the diameter of the ligament (see Fig. 1). The parameters c and $\bar{a}$ are defined as follows:

$$c = \frac{1 + a/R + (1 + a/R)^{1/2}}{2\{2 + a/R + (1 + a/R)^{1/2}\}} \quad (3)$$

$$\bar{a} = \frac{a(1 + a/R)}{a/R} \quad (4)$$

where a is the radius of the ligament and R is the radius of the groove (see Fig. 1(b)). The longitudinal sections of the tested specimen are shown in Fig. 2. In general, the number of voids associated with the debonding of SiC particulates was much smaller than the total number of voids related to the fracture. Several examples of the areas where debonded SiC particulates can be observed are shown in Fig. 3. The debonding shown in Fig. 3 is a rather rare event and is not typical of Al-SiC fractured samples [18].

According to the Neuber analysis, the largest negative pressure occurs at the outer surface of the groove (see Fig. 1). Since, in general, no separation between the SiC particulates and the aluminum matrix was observed, it is reasonable to assume that, for the Al-SiC bond,

$$\sigma_n \geqslant \sigma_T^{max} + Y(\bar{\epsilon}^p)$$

The value of $Y(\bar{\epsilon}^p)$ was obtained from the stress-strain curve as

$$Y(\bar{\epsilon}^p) = \frac{P_f}{A_f} = \sigma_0 \quad (5)$$

where P_f will equal the load at failure which will be 750 kgf and A_f will equal the area across the grooved region. The values of c and $\bar{a}$ can be obtained from eqns. (3) and (4) respectively. At the bottom of the circumferential grove ($z = 0$), these values are $c = 0.48$ and $\bar{a} = 2.3$ mm.

Substituting eqns. (5) and (2) into eqn. (1), we obtain

$$\sigma_n = \sigma_0 \frac{c}{\{1 - (r/\bar{a})^2\}^{1/2}} + \sigma_0$$

$$\approx 1690 \text{ MPa}$$

Thus the lower bound value for the Al-SiC bond strength is 1690 MPa; the Neuber analysis is applicable to a linear solid, *i.e.* to a material with linear strain hardening. From the stress-strain curves obtained, it was felt that the behavior of the tested specimen could be approximated to a linear body.

4. CONCLUSIONS

Provided that the above-mentioned assumptions are reasonable (and there is no reason to question the assumptions if a lower limit of the bond strength is determined), it can be concluded that the bond strength between aluminum alloy 6061 and SiC is at least 1690 MPa. (This is 40 times higher than the yield stress of the annealed aluminum alloy 6061.) It is thought that debonding can be attributed to the defects during fabrication of the composite material. The ductile fracture of Al-SiC composite with a low volume percentage of SiC occurs by void nucleation at SiC particulates and also at the matrix imperfections (pre-existing voids, inclusions, $MgSi_2$ etc.). A separate investigation, however, is required to determine explicitly the origin of the ductile fracture in Al-SiC systems. It is realized that the assumption of equiaxiality of the SiC is rather poor. This results in further underestimation of the bond strength since, under the same macrostress state, irregularly shaped particles would have higher stress concentrations and, thus, separation from the matrix would be expected to occur at an earlier stage than for a spherical particle. If the irregular shape of the particle could be taken into account, the lower limit would increase.

ACKNOWLEDGMENT

This research was supported through Grant N00014-85K-0007 from the Office of Naval Research.

REFERENCES

1 A. Kelly, *Strong Solids*, Clarendon, Oxford, 2nd edn., 1972.
2 M. R. Piggott, *Load-bearing Fibre Composites*, Pergamon, Oxford, 1980.
3 B. D. Agarwal and L. J. Broutman, *Analysis and Performance of Fiber Composites*, Wiley, New York, 1980.
4 R. J. Arsenault and R. M. Fisher, *Scr. Metall.*, *17* (1983) 67.

5 R. J. Arsenault and R. M. Fisher, in J. Carlsson and N. G. Ohlson (eds.), *Proc. 4th Int. Conf. on the Mechanical Behaviour of Materials, Stockholm, 1983*, Vol. 1, Pergamon, Oxford, 1983, p. 451.
6 R. J. Arsenault, *Mater. Sci. Eng.*, *64* (1984) 171.
7 Y. Flom and R. J. Arsenault, *Mater. Sci. Eng.*, to be published.
8 A. P. Divecha, S. G. Fishman and S. D. Karmarkar, *J. Met.*, *33* (1981) 12.
9 D. L. McDanels, *NASA Tech. Memo. 83610*, 1984 (National Aeronautics and Space Administration).
10 L. J. Broutman and R. H. Krock, Interfaces in metal matrix composites, *Compos. Mater.*, *1* (1974) 57.
11 A. Kelly and W. R. Tyson, *J. Mech. Phys. Solids*, *13* (1965) 328.
12 L. M. Brown and J. D. Embury, *Proc. 3rd Int. Conf. on the Strength of Metals and Alloys, Cambridge, Cambridgeshire, August 20-25, 1973*, Iron and Steel Institute, Institute of Metals, London, 1974, p. 164.
13 G. LeRoy, J. D. Embury, G. Edward and M. F. Ashby, *Acta Metall.*, *29* (1981) 1509.
14 J. D. Embury, Ductile fracture, in R. C. Gifkins (ed.), *Proc. 6th Int. Conf. on the Strength of Metals and Alloys, Melbourne, August 16-20, 1982*, Vol. 3, Pergamon, Oxford, 1982.
15 A. S. Argon, J. Im and R. Safoglu, *Metall. Trans. A*, *6* (1975) 825.
16 A. S. Argon, J. Im and A. Needleman, *Metall Trans. A*, *6* (1975) 815.
17 A. S. Argon and J. Im, *Metall. Trans. A*, *6* (1975) 839.
18 Metallurgical Materials Laboratory, University of Maryland, unpublished results, 1982-1985.

THE EFFECTS OF DIFFERENCES IN THERMAL COEFFICIENTS OF EXPANSION IN SiC WHISKER 6061 ALUMINUM COMPOSITE*

Richard J. Arsenault

Metallurgical Materials Laboratory
University of Maryland
College Park, MD 20742 USA

Minoru Taya
Department of Mechanical and Aerospace Engineering
University of Delaware
Newark, DE 19716 USA

Summary

When a metal matrix composite is cooled down to room temperature from the fabrication or annealing temperature, residual stresses are induced in the composite due to the mismatch of the thermal expansion coefficients between the matrix and whisker.

An investigation was undertaken of the extent of the thermal residual stresses by an X-ray diffraction technique as well as of the difference of the yield stresses $\Delta\sigma_y$ between tension and compression resulting from the thermal residual stresses. A theoretical model based on the Eshelby's method was then constructed for the prediction of the thermal residual stresses and $\Delta\sigma_y$. The agreement obtained was very good between the experimental results and the theoretical predictions.

* This research was supported in part under a contract from the Office of Naval Research, Contract No. N00014-85K-0007.

Introduction

Metal matrix composites (MMCs), including eutectic composites, are becoming important in their application to structural components which are to be used at intermediate and high temperatures. When MMCs are fabricated at high temperature or annealed at a certain high temperature and cooled down to room temperature, undesirable results, such as low tensile yield stress and strength of the MMC upon mechanical testing at room temperature, are produced. These results are mainly due to residual stresses that are caused by the mismatch of the thermal expansion coefficients between the matrix and fiber. This subject has been studied by a number of researchers (for examples see references 1-13). The residual stresses so induced have been observed in tungsten fiber/copper composites[7] and in SiC whisker/6061 Al composites[8,9]. Most of the models purposed to estimate the residual stress were based on one-dimensional analysis[1-3], continuous fiber system[4,5], or spherical particle system[10].

The model based on Eshelby's equivalent inclusion method[7] has been used to solve the problem of thermal residual stress[12-14]. The advantages of the Eshelby's model are that it can solve a three-dimensional composite system such as short whisker composite and also can take into account the effect of the volume fraction of whisker (V_w) easily.

Eshelby's method has been used also for predicting the yield stress and work-hardening rate of metal matrix composites[15-19]. The effect of the thermally induced residual stress on the yield stresses has been discussed by Wakashima et al.[18] who predicted that the yield stress in compression (σ_y^c) exceeds that in tension (σ_y^t) for continuous B fiber/Al composites which were cooled down, although no comparison with the experimental data was made.

In this paper we focus on the residual stresses induced in a short whisker MMC due to the temperature drop and its effect on the yield stresses. The target short whisker MMC is SiC whisker/6061 Al composite.

Experimental Procedure

Materials

The target short fiber MMC was SiC whisker/6061 Al composite and was purchased from ARCO/SILAG. The composite was in the form of an extruded rod 15.5 mm in diameter. Three different volume fractions of whisker (V_w) were used: V_w = 0, 0.05 and 0.2. The composite was supplied as-fabricated (no heat treatment made), was machined into samples (Fig. 1a and 1b), annealed for 12 hours at 810 K, and then furnace cooled.

Testing Methods

Tension and Compression Tests. The testing was performed in an Instrom testing machine using a liquid metal container as the lower gripping device. This method of gripping was employed to ensure very good alignment of the sample. This test procedure is described in greater detail elsewhere[20]. Samples of two different gauge lengths were used to determine if there was a gauge length effect (there was none). The effective gauge length of the

samples was determined by glueing strain gauges on the center portion of the sample and comparing the results obtained from a clip on an extensometer which mounted into the "V" grooves. If the extensometer is mounted directly to the uniform gauge section, there is a high probability that the sample will fracture where the "knife" edge of the extensometer makes contact with the sample. Several tests in the low stress range were conducted using both the extensometer and the strain gauge; from these tests the effective gauge length was determined. Subsequent tests were conducted using only the extensomenter. The samples, which were tested in the range from 8×10^{-5} sec^{-1} to 2×10^{-3} sec^{-1}, showed no effect on strain rate.

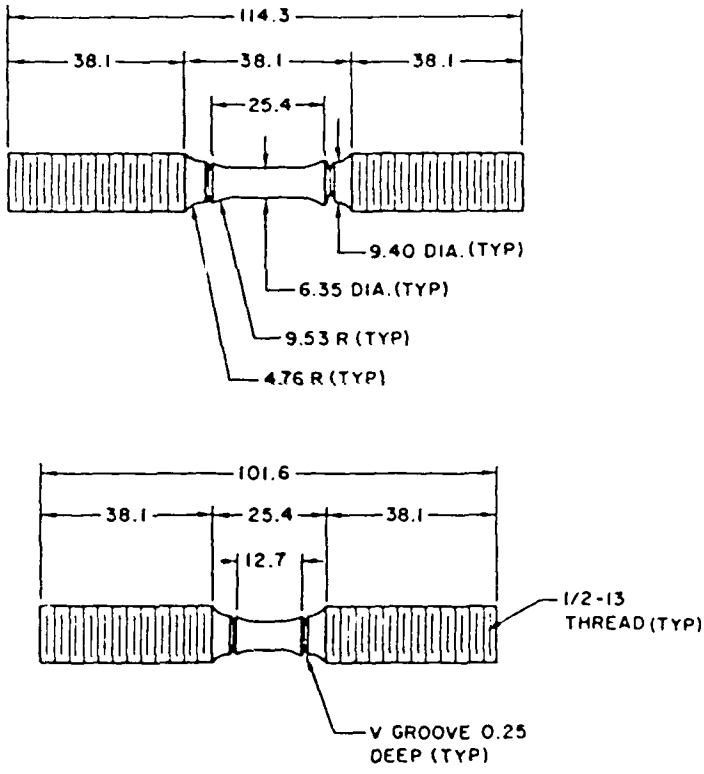

Figure 1 - A schematic diagram of the sample configuration which was used in the tension and compression testing. The dimensions are in millimeters.

Residual Stress Measurement by X-ray Diffraction. The X-ray diffraction technique was used to measure residual stress. Two components of the residual stress were focused on: the stress along the extrusion direction (longitudinal direction), which coincides with the whisker axis of a majority of whiskers (σ_L), and the one in the transverse direction (σ_T). The data were obtained and reduced by standard techniques as outlined by Cohen et al.[21].

Experimental Results

The stress-strain curves of V_w = 0, 0.05 and 0.2 composites are plotted in Fig. 2a, 2b, and 2c, respectively. The solid and dashed curves denote the tensile and compressive test results, respectively. The yield stress was measured as 0.2% off set strain and is indicated in the figures by arrows.

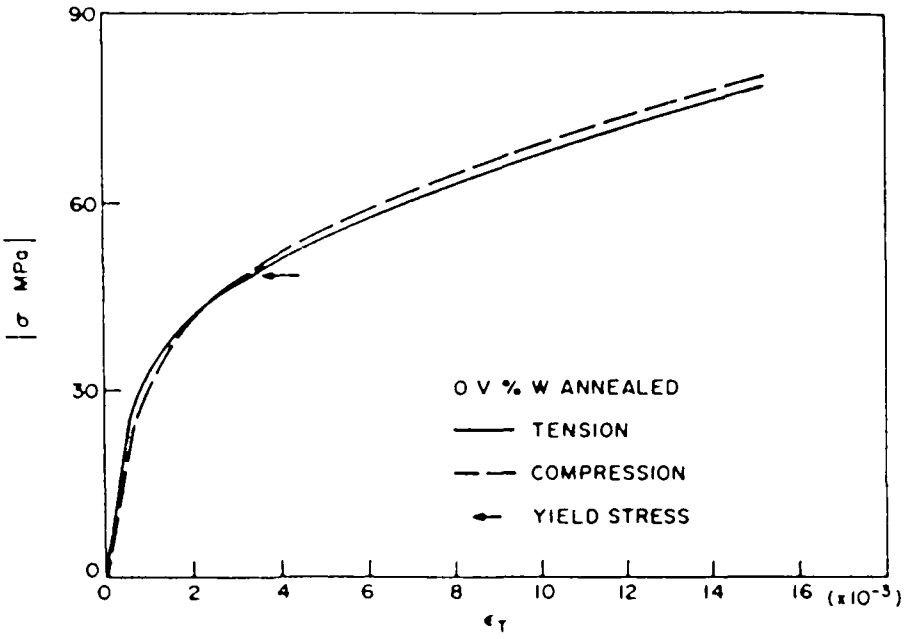

Figure 2a - The absolute stress vs. strain curves for tension and compression test of 0 volume % whisker material in the annealed condition.

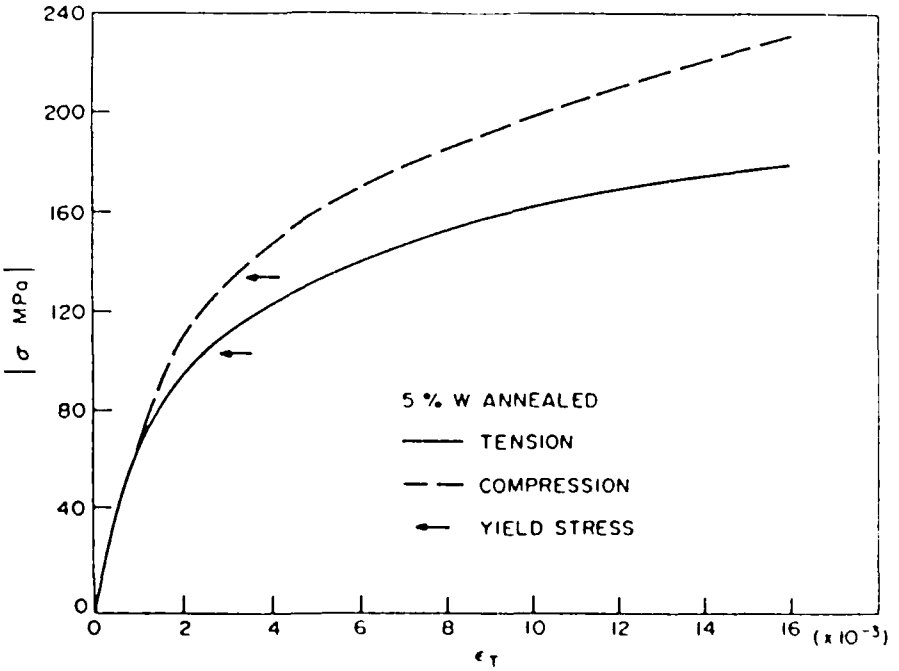

Figure 2b - The absolute value of stress vs. strain for 5 volume % whisker composite in the annealed condition.

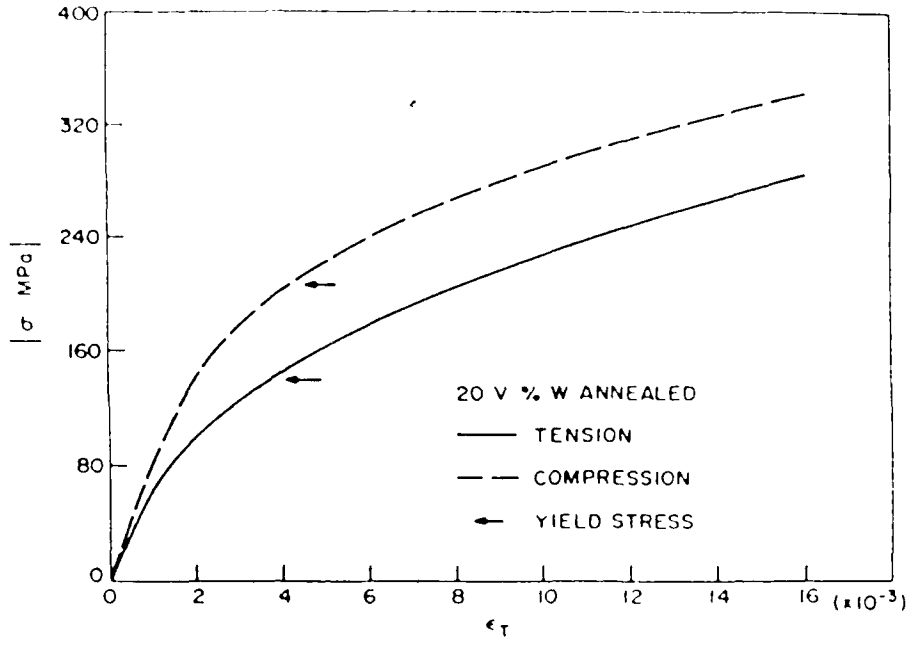

Figure 2c - The absolute value of the stress as a function of strain for 20 volume % whisker material in the annealed condition.

The residual stresses were measured by X-ray diffraction on three different values of V_w (0, 0.05, and 0.2) and are tabulated in Table 1 where the range of scattered data is also shown. It is noted that the values of σ_L and σ_T represent the volume average quantity in the matrix (6061 Al). It should also be noted that a compressive residual stress was found for all cases.

Table I

Residual Stresses X-Ray Determination

Sample Designation V_w %	Trans. σ_T MPa	Long. σ_L MPa
0	-37 to -44	-18 to -22
5	-17 to -41.4	-29 to -41.4
20	-49 to -57.3	-24 to -44.2

- compressive residual stress

Theoretical Procedure

The theoretical model used here is based on Eshelby's equivalent inclusion model. Mori and his co-workers[15-17] extended Eshelby's method to predict the yield stress (σ_y) and work-hardening rate of aligned short whisker composites. Wakashima et al.[18] extended the above approach to predict σ_y by considering the mismatch of the thermal expansion coefficients of the matrix and fiber. Following the above models, Takao and Taya[14]

have recently computed the stress field in and around a short fiber in a short fiber composite where the fiber is anisotropic both in stiffness and thermal expansion.

In this paper we focus on the average thermal residual stress induced in the matrix by the cool-down process and also the yield stresses in tension (σ_y^t) and compression (σ_y^c) when the composite is tested at the room temperature. The former case is essentially based on the model by Takao and Taya[14], and as the latter case, we extend the model by Wakashima et al.[18] to account for the bi-linear stress-strain curve of the matrix.

Formulation

Consider an infinite body (D) which contains ellipsoidal whiskers (Ω) aligned along the x_3-axis (Fig. 3). This composite body D is subjected to the applied stress field σ_{ij}^o. The stiffness tensors of the matrix (D-Ω) and whisker (Ω) are denoted by C_{ijke} and C_{ijke}^w, respectively. Following Eshelby, the transformation strain[11] or eigenstrain[22] is given in the fiber domain Ω as α_{ij}^*, where α_{ij}^* is the strain due to the mismatch of the thermal expansion coefficients and the uniform plastic strain e_{ij}^p is prescribed in the matrix[15]. As far as the stress field is concerned, the model of Fig. 4 is equivalent to that of Fig. 3. Thus, the present problem is reduced to "inhomogeneous inclusions problem" (Fig. 4)[22]. The model of Fig. 4 will be used not only to predict the yield stresses and work-hardening rate, but also to compute the thermal residual stress. For in the latter case, we will set $\sigma_{ij}^o = e_{ij}^p = 0$.

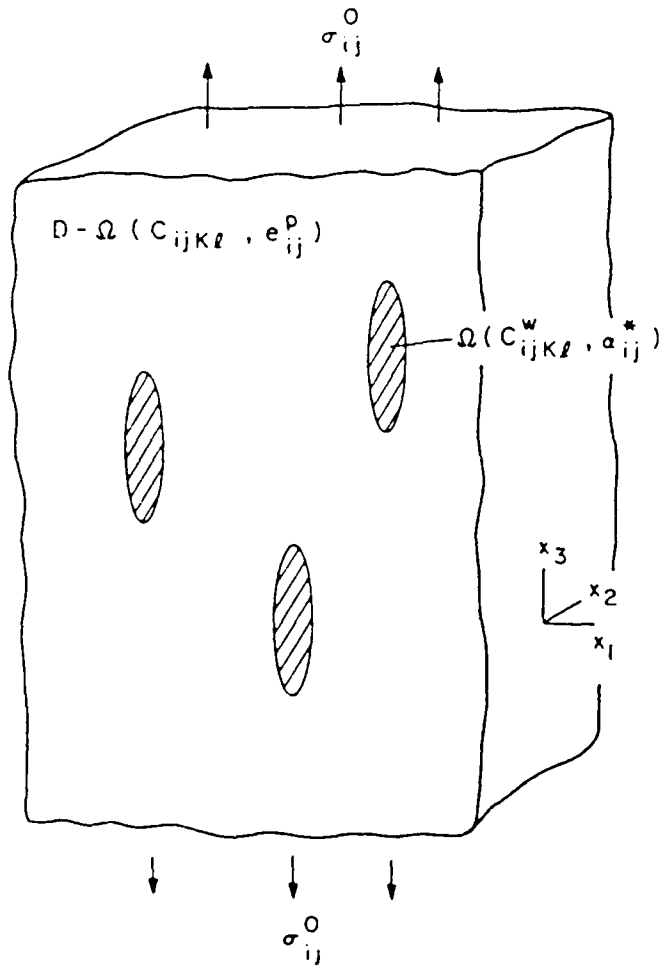

Figure 3 - Theoretical model; actual case

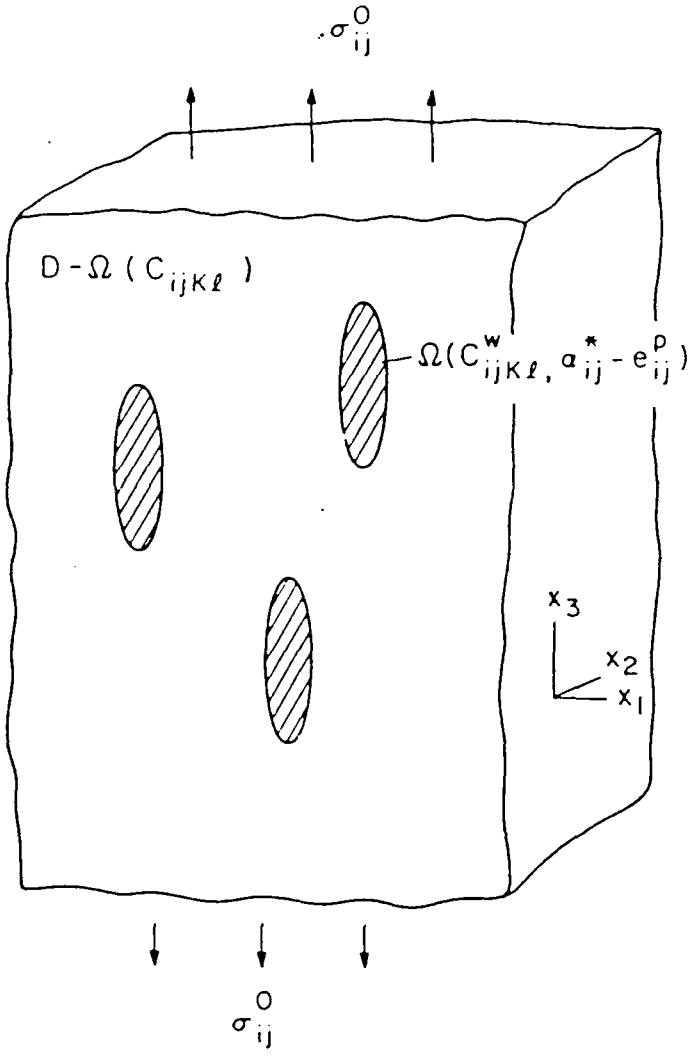

Figure 4 - The equivalent inclusion model converted from Figure 3.

Following the Eshelby's equivalent inclusion method modified for a finite volume fraction of whiskers[22,23], the total stress field in the fibers $\sigma^o_{ij} + \sigma_{ij}$ is given by

$$\sigma^o_{ij} + \sigma_{ij} = C^w_{ijkℓ}\{e^o_{kℓ} + \tilde{e}_{kℓ} + e_{kℓ} - (\alpha^*_{kℓ} - e^p_{kℓ})\}$$

$$= C_{ijkℓ}\{e^o_{kℓ} + \tilde{e}_{kℓ} + e_{kℓ} - (\alpha^*_{kℓ} - e^p_{kℓ}) - e^*_{kℓ}\} \qquad (1)$$

where

$$\sigma^o_{ij} = C_{ijkℓ}e^o_{kℓ} \qquad \text{in D} \qquad (2)$$

$$\langle \sigma_{ij} \rangle_m = C_{ijk\ell} \tilde{e}_{k\ell} \qquad \text{in } D-\Omega \tag{3}$$

In Eq. (1), e^*_{ke} is the fictitious eigenstrain[22] which was introduced to connect the present problem to "inclusion problem" and $\tilde{e}_{ij}$ is the average strain disturbance in the matrix and related to the average stress disturbance in the martix $\langle \sigma_{ij} \rangle_m$ by Eq. (3). $\langle \sigma_{ij} \rangle_m$ is defined by

$$\langle \sigma_{ij} \rangle_m = \frac{1}{V_{D-\Omega}} \int_{D-\Omega} \sigma_{ij} dv \tag{4}$$

where $V_{D-\Omega}$ is the total volume of the matrix and σ_{ij}, and e_{ij} in Eqs. (1) and (4) is the stress and strain disturbance, respectively, by a single fiber Ω when it is embedded in an infinite matrix. Since the stress disturbance when it is integrated in the entire domain D vanishes,

$$\int_D \sigma_{ij} dv = 0 \tag{5}$$

The stress disturbance σ_{ij} is obtained from Eqs. (1) and (2)

$$\sigma_{ij} = C_{ijk\ell}(\tilde{e}_{k\ell} + e_{k\ell} - e^{**}_{k\ell}) \tag{6}$$

where

$$e^{**}_{k\ell} = \alpha^*_{k\ell} + e^*_{k\ell} - e^p_{k\ell} \tag{7}$$

From Eqs. (3), (5) and (6), we obtain

$$\tilde{e}_{ij} = - V_w(e_{ij} - e^{**}_{ij}) \tag{8}$$

According to Eshelby, e_{ij} is related to the total eigenstrain $e^{**}_{k\ell}$ as

$$e_{ij} = S_{ijk\ell} e^{**}_{k\ell} \tag{9}$$

where S_{ijke} is the Eshelby's tensor and a function of $C_{ijk\ell}$, $C^w_{ijk\ell}$ and the geometry of the ellipsoidal whisker[22]. The fiber is assumed as a prolate spheroid, hence the whisker aspect ratio ℓ/d is a single geometrical parameter. For simplicity, we assume that the matrix and fiber are isotropic both in stiffness and thermal expansion coefficient. Thus, $C_{ijk\ell}$, $C^w_{ijk\ell}$ and α^*_{ij} are given by

$$C_{ijk\ell} = \lambda \delta_{ij}\delta_{k\ell} + \mu(\delta_{ik}\delta_{j\ell} + \delta_{i\ell}\delta_{kj}) \tag{10}$$

$$C^w_{ijk\ell} = \lambda^w \delta_{ij}\delta_{k\ell} + \mu^w(\delta_{ik}\delta_{j\ell} + \delta_{i\ell}\delta_{kj}) \tag{11}$$

$$\alpha^*_{ij} = - (\alpha_w - \alpha)\, \delta_{ij} \Delta T \tag{12}$$

In the above equations, δ_{ij} is the Kronecker's delta, λ (λ^w) and μ (μ^w) are Lame's constants of the matrix (whisker), α (α_w) is the thermal expansion coefficient of the matrix (fiber) and ΔT is the change in temperature ($\Delta T > 0$ corresponds to the temperature drop).

The stress field in the fiber is obtained from Eqs. (6), (8), (9) and (10)

$$\sigma_{ij} = (1 - V_w)\{(S_{kkmn}e^{**}_{mn} - e^{**}_{kk})\lambda\delta_{ij} + 2\mu(S_{ijmn}e^{**}_{mn} - e^{**}_{ij})\} \quad (13)$$

After solving for e^{**}_{ij} in Eq. (1) by use of Eqs. (8) and (9), we can compute the stress disturbance σ_{ij} in the whisker from Eq. (13).

Yield Stresses σ^t_y, σ^c_y and Work-Hardening Rate

The method of computing the yield stresses σ^t_y and σ^c_y and the work-hardening rate of the composite is described briefly. The total potential energy of Fig. 3, U, is given by

$$U = \frac{1}{2}\int_D (\sigma^o_{ij} + \sigma_{ij})(u^o_{ij} + \tilde{u}_{ij} + u_{ij} - e^p_{ij} - \alpha^*_{ij})dV$$

$$- \int_{|D|} \sigma^o_{ij}n_j(u^o_i + \tilde{u}_i + u_i)dS \quad (14)$$

where u^o_i, $\tilde{u}_i$ and u_i are the displacement components corresponding to e^o_{ij}, $\tilde{e}_{ij}$ and e_{ij}, respectively; the index j preceded by a comma denotes a partial differentiation with respect to x_j; $|D|$ is the boundary of D: and n_j is the j-th component of an unit vector outer normal to $|D|$. Then, the change in u due to the change in the plastic strain δe^p_{ij} is given by

$$\delta U = -\int_D (\sigma^o_{ij} + \sigma_{ij})\delta e^p_{ij}dV \quad (15)$$

In the above deviation, the Gauss' divergence theory and the following equation were used

$$\int_D \sigma_{ij}(\delta\tilde{u}_{ij} + \delta u_{ij})dV = 0$$

Noting that the plastic strain exists only in the matrix (D-Ω), Eq. (15) is reduced to

$$\delta U = -\delta e^p_{ij}\{(1-V_w)\sigma^o_{ij} - V_w\sigma_{ij}\} \quad (16)$$

Under the uniaxial stress along the x_3-axis (σ_o), σ^o_{ij} and e^p_{ij} are given by

$$\sigma^o_{ij} = \begin{matrix}0\\0\\\sigma_o\\0\\0\\0\end{matrix} \qquad e^p_{ij} = \begin{matrix}-1/2e_p\\-1/2e_p\\e_p\\0\\0\\0\end{matrix} \quad (17)$$

where the six components of σ^o_{ij} and e^p_{ij} are expressed in the order of (ij) = 11, 22, 33, 23, 31, and 12, and e_p is the plastic strain along the x_3-axis. On the other hand, the energy dissipation due to the plastic work in the matrix, δQ, is given by

$$\delta Q = (1-V_w)\sigma_y\delta e_p \quad (18)$$

where σ_y is the flow stress of the matrix for the bilinear model

$$\sigma_y = \sigma_y^o + E_T(e - e_p) \tag{19}$$

where σ_y^o and E_T are the initial yield stress and tangent, modulus of the matrix, respectively, and e is the total strain. Since $\delta U + \delta O = 0$, we obtain

$$\sigma_o = \sigma_y + \frac{V_w}{(1-V_w)}(\sigma_{33} - \sigma_{11}) \tag{20}$$

In the above deviation, $\sigma_{11} - \sigma_{22}$, $e_{11}^p = e_{22}^p = -\frac{1}{2} e_p$ were used. Combining the solutions of σ_{ij} in Eq. (13) and Eq. (20), we can obtain the yield stress of the composite in tension ($\sigma_y^t = \sigma_o$) and that in compression ($\sigma_y^c = \sigma_o$) as

$$\begin{aligned} \sigma_y^t/\sigma_y^o &= C_0 + C_1\, \alpha_m \Delta T \\ \sigma_y^c/\sigma_y^o &= C_0 - C_1\, \alpha_m \Delta T \end{aligned} \tag{21}$$

Similarly, the work-hardening rate of the composite, $\bar{E}_T$ is obtained as

$$\bar{E}_T/E_T = C_2 + C_3 \left(\frac{E_T}{E}\right) \tag{22}$$

In the above equations, C_0, C_1, C_2, and C_3 are functions of the mechanical properties of the matrix and whisker and the fiber aspect ℓ/d, E is the Young's modulus of the matrix.

Thermal Residual Stress

When the composite is cooled down by ΔT, the thermal residual stress is induced in the composite. The theoretical model for this problem is the same as that shown in Fig. 4 except that $\sigma_{ij}^o = e_{ij}^p = 0$ in the present case. Hence, the formulation up to Eq. (13) is valid and will be used to compute the thermal residual stress. Once the stress within the whisker $\sigma_{ij}^{(in)}$ is computed, the stresses just outside the whisker $\sigma_{ij}^{(out)}$ can be obtained by the following relation[13]

$$\sigma_{pq}^{(out)} = \sigma_{pq}^{(in)} + C_{pqmn}\left\{- C_{k\ell ij} e_{ij}^{**} n_\ell n_n \frac{(\lambda+2\mu)\delta_{km} - (\lambda+\mu) n_k n_m}{\mu(\lambda+2\mu)} + e_{mn}^{**}\right\} \tag{23}$$

where $\sigma_{pq}^{(in)}$ is given by Eq. (13), e_{ij}^{**} is solved by Eq. (1), λ and μ are previously defined and n_i is the i-th component of the unit vector prependicular to the surface of the whisker. If one wants to compute the stresses just outside the equator of the ellipsoidal whisker where n = (1, 0, 0), we can obtain the stresses in polar coordinates, σ_r, σ_θ and σ_z there as

$$\sigma_r^{(out)} = \sigma_r^{(in)}$$
$$\sigma_\theta^{(out)} = \sigma_\theta^{(in)} + 2\mu\left\{\frac{1}{1-\nu} e_{11}^{**} + \frac{\nu}{1-\nu} e_{33}^{**}\right\} \tag{24}$$
$$\sigma_z^{(out)} = \sigma_z^{(in)} + 2\mu\left\{\frac{\nu}{1-\nu} e_{11}^{**} + \frac{1}{1-\nu} e_{33}^{**}\right\}$$

where ν is the Poisson's ratio of the matrix.

Next the average stress field in the matrix, $\langle\sigma_{ij}\rangle_m$, can be also obtained from Eqs. (3), (8) and (9) as

$$\langle\sigma_{ij}\rangle_m = - V_w C_{ijk\ell}(S_{k\ell mn} e_{mn}^{**} - e_{k\ell}^{**}) \tag{25}$$

The average stress in the matrix, $\langle\sigma_r\rangle_m$, $\langle\sigma_\theta\rangle_m$ and $\langle\sigma_z\rangle_m$, will be computed by setting ij = 11, 22, and 33 in Eq. (25). It should be noted here that $\langle\sigma_r\rangle_m = \langle\sigma_\theta\rangle_m$ due to the assumptions of an aligned short whisker composite which results in the transverse isotropy of the volume average quantity.

Theoretical Results

The thermo-mechanical data of the matrix and whisker for the theoretical calculations are obtained from the stress-strain curve of the matrix (Fig. 2a) and the material properties handbook.

Annealed 6061 Al matrix (bilinear model):

$$\begin{aligned} E &= 47.5 \text{ GPa} \\ E_T &= 2.3 \text{ GPa} \\ \sigma_y^o &= 47.5 \text{ MPa} \\ \nu &= 0.33 \\ \alpha &= 23.6 \times 10^{-6}/^oC \end{aligned} \tag{26}$$

SiC Whisker:

$$\begin{aligned} E_w &= 427 \text{ GPa} \\ \nu_w &= 0.17 \\ \alpha_w &= 4.3 \times 10^{-6}/^oC \\ \ell/d &= 1.8 \end{aligned} \tag{27}$$

where the average value of the fiber aspect ratio (ℓ/d) was used[24] and the bilinear stress strain curve of the matrix is indicated by a dash-dot line in Fig. 2a. The temperature drop ΔT is defined as

$$\Delta T = T_1 - T_0 \tag{28}$$

where T_1 is taken as the temperature below which dislocation generation is minimal during the cooling process[9] and T_0 is the room temperature. Thus, for the present composite system ΔT is set equal to 200 K.

The theoretically predicted σ_y^c and σ_y^t can be obtained from Eq. (21). The differences between σ_y^c and σ_y^t ($\sigma_y^c - \sigma_y^t$) for various V_w are shown as the solid line in Fig. 5. The differences between σ_y^c and σ_y^t increase with increasing V_w. The experimentally determined differences between σ_y^c and σ_y^t are represented by the open circles in Fig. 5. The experimental values of the yield stresses are taken as the stresses 0.2% off-set strain. It follows (Fig. 5) that good agreement is obtained between the experimental

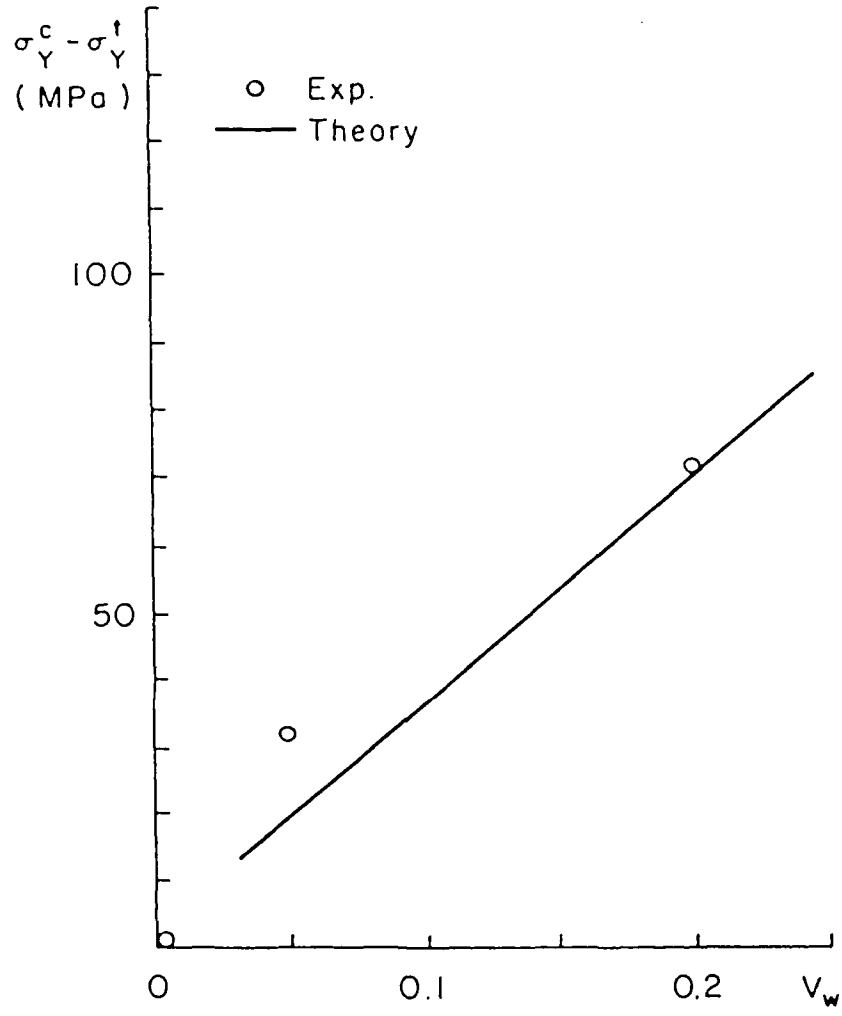

Figure 5 - The difference in yield stress between compression and tensin as a function of volume % silicon carbide whisker.

and theoretical results of the difference in the compressive tensile yield stresses. However, the experimental values of σ_y^c are greater than the theoretical values of σ_y^c, and similarly the experimental values of σ_y^t are greater than the theoretical values of σ_y^t.

From the data given by Eqs. (26) - (27) and the use of Eq. (25), we have computed the average stresses in the matrix and the stresses just outside the fiber and plotted schematically the σ_L and $\langle\sigma_L\rangle_m$ along the x (or x_2) and x_3 axes in Fig. 6.

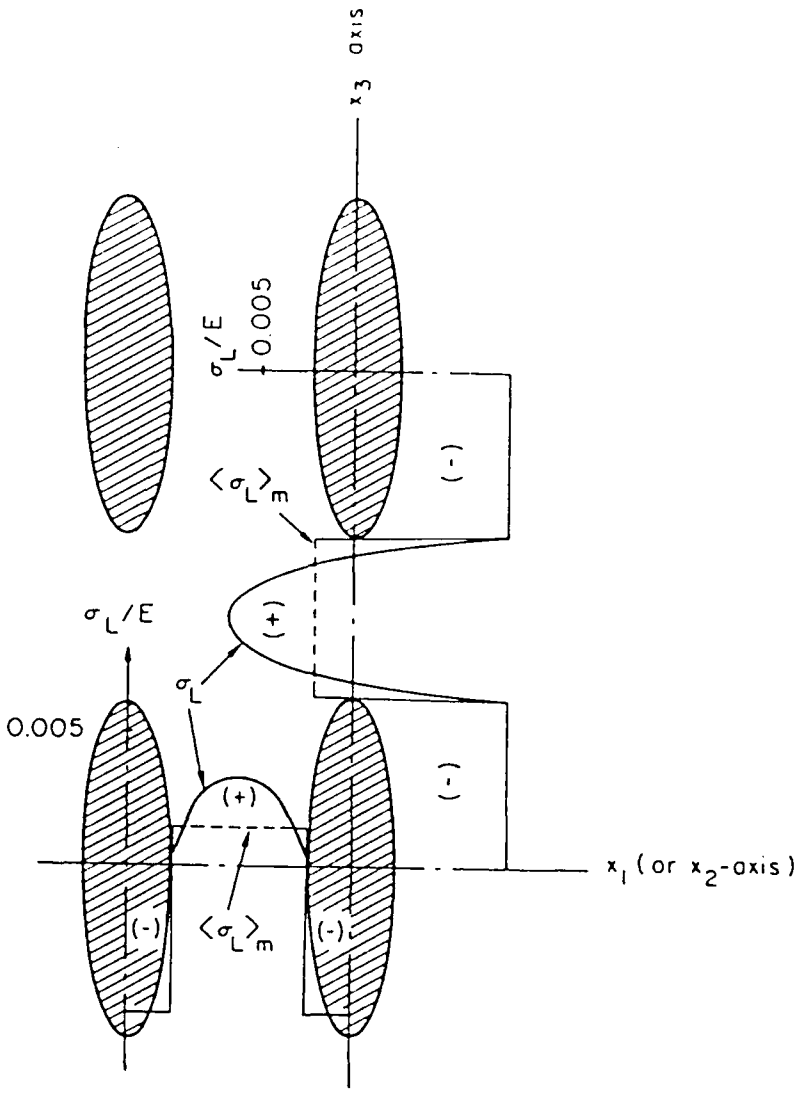

Figure 6 - Is a schematic of the stress distribution in the matrix and in the reinforcement due to the difference in thermal coefficient of expansion between the silicon-carbide and aluminum.

Next, the thermal residual stresses averaged in the matrix of the SiC whisker/6061 Al are predicted by Eq. (25) and the results on $\langle\sigma_T\rangle_m$ and $\langle\sigma_L\rangle_m$ are plotted in Fig. 7 as a function of the volume fraction of whisker (V_w), where the subscripts, T and L denote the component along the transverse direction (r and θ) and longitudinal direction (z). The average theoretical thermal-residual stress is predicted to be tensile in nature.

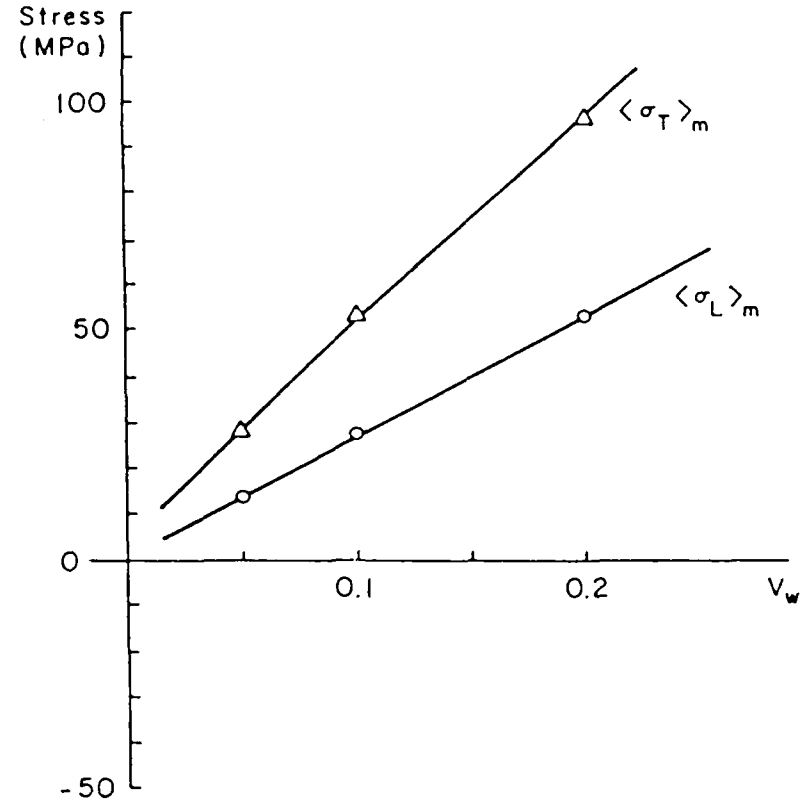

Figure 7 - Predicted residual stress in the matrix for the transverse and longitudinal directions.

Discussion and Conclusions

The theoretical predictions and experimental results are in very good agreement in most cases, and in some cases the differences are to be expected.

The theoretical model is based on an extension of previous work by Eshelby[11], Mura and Taya[13], and Tanaka and Mori[15], and it can predict the yield stress in tension and compression and the thermal residual stress. The predicted values of the yield stress in tension and compression are less than the experimentally determined values of the yield stress in tensional compression. This difference between the theoretical and experimental stresses is due to the fact that the $V_w = 0$ curves of stress vs. strain were used for the matrix in the composite cases. It has been demonstrated by Arsenault and Fisher[8] and Vogelsang, et al.[9] that there is a much higher dislocation density in the annealed composite matrix than in the $V_w = 0$ material. Therefore, the matrix is stronger then the annealed $V_w = 0$ matrix alloy. However, this increase in matrix strength due to a higher disloca-

tion density does not influence the difference in yield stress in the compression vs. tension. The theoretical prediction is that the yield stress in compression should be higher than the yield stress in tension, and this is exactly what is observed experimentally.

The theoretical prediction that the compressive yield stress is higher than the tensile yield stress suggests that a tensile residual stress exists in the matrix of composite. An average tensile residual stress is predicted in the matrix as shown in Figs. 6 and 7. However, the experimentally determined residual stress is compressive, i.e., opposite of the prediction. This difference can qualitatively be explained in terms of the magnitude of the tensile and compressive residual stresses in the matrix. If the compressive regions of the matrix were eliminated and only the tensile regions were examined, then there would be no change in the diffraction peak conditions, because the limit of detection is ~ 50 MPa. If a similar experiment were conducted, but in this case only the compressive regions were kept then there would be a change in peak position because the compressive residual stress is greater than the detection limit. Now, if both tensile and compressive regions are combined, the net result, a small compressive residual, will be experimentally detected, which is in agreement with the X-ray residual stress measurements.

It is possible to arrive at the following conclusions from the theoretical model and the experimental results.

1. The theoretical model predicts a higher compression yield stress than tensile yield stress, which is in agreement with the experimental results.
2. The absolute magnitude of the predicted yield stress (tensile and compressive) is less than the experimental yield stress due to an increase in matrix strengthening. The increased matrix strength is due to a higher dislocation density in the matrix; the higher dislocation density is a consequence of the difference in coefficient of thermal expansion between the Al alloy matrix and the SiC.
3. The magnitude of the average residual stress is small, but at the SiC-Al alloy interface there can be a large compressive stress.
4. The residual stress, in the region between SiC whiskers, is tensile and this is the likely region where plastic deformation would begin. For in this region the matrix contains a lower dislocation density than adjacent to the SiC whisker, i.e., in this region the matrix is weaker.

References

1. E. R. Thompson, D. A. Koss, and J. C. Chestnutt, Metall. Trans. 1 (1970), p. 2807.

2. D. A. Koss and S. M. Copley, Metall. Trans. 2 (1971), p. 1557.

3. J. K. Lees, Polymer Eng. Sci. 8 (1968), p. 195.

4. S. S. Hecker, C. H. Hamilton and L. J. Ebert, J. Mater. Sci. 5 (1970), p. 868.

5. J. Gayda and L. J. Ebert, Metall. Trans. 10A (1979), p. 349.

6. S. D. Tsai, D. Mahulikar, H. L. Marcus, I. C. Noyan and J. B. Cohen, Mater. Sci. & Eng. 47 (1981), p. 145.

7. K. K. Chawla and M. Metzger, J. Mater. Sci. 7 (1972), p. 34.

8. R. J. Arsenault and R. M. Fisher, Scripta Metall. 17 (1983), p. 67.

9. M. Vogelsang, R. J. Arsenault, and R. M. Fisher, submitted for publication.

10. J. K. Lee, Y. Y. Earmme, H. I. Aaronson and K. C. Russell, Metall. Trans. 11A (1980), p. 1837.

11. J. D. Eshelby, Proc. Roy. Soc. London A241 (1957), p. 376.

12. K. Wakashima, M. Otsuka and S. Umekawa, J. Comp. Mater. 8 (1976), p. 391.

13. T. Mura and M. Taya, Proc. of the 2nd U.S.-Japan Conf. on Comp. Mater. ASTM, under review.

14. Y. Takao and M. Taya, J. Appl. Mech., under review.

15. K. Tanaka and T. Mori, Acta Metall. 18 (1970), p. 931.

16. K. Tanaka, K. Wakashima and T. Mori, J. Mech. Phys. Solids 21 (1973), p. 207.

17. S. C. Lin, T. Mura, M. Shibata and T. Mori, Acta Metall. 21 (1973), p. 505.

18. K. Wakashima, S. Kurihara and S. Umekawa, Japan Soc. Comp. Mater. 2 (1976), p. 1.

19. A. Daimaru and M. Taya, Proc. of the 4th Intl. Conf. on Comp. Materials, Edited by Hayashi et al., Japan Soc. Comp. Materials, Tokyo (1982), p. 199.

20. R. Hsu and R. J. Arsenault, Mat. Sci. & Eng. 66 (1984), p. 35.

21. J. B. Cohen and L. Schwartz, Diffraction Methods in Materials Science, MacMillan.

22. T. Mura, Micromechanics of Defects in Solids, Martinus Nijhoff Publishers, 1982.

23. T. Mori and K. Tanaka, Acta Metall. 21 (1973), p. 571.

24. R. J. Arsenault, Mater. Sci. & Eng., 64 (1984), p. 171.

Acta metall. Vol. 35, No. 3, pp. 651–659, 1987
Printed in Great Britain

0001-6160/87 $3.00 + 0.00

THERMAL RESIDUAL STRESS IN METAL MATRIX COMPOSITE†

R. J. ARSENAULT[1] and M. TAYA[2]

[1]Engineering Materials Group, Metallurgical Materials Laboratory, University of Maryland, College Park, MD 20742 and
[2]Department of Mechanical Engineering, University of Washington, Seattle, WA 98195, U.S.A.

(*Received* 6 *January* 1986; *in revised form* 6 *June* 1986)

Abstract—When a metal matrix composite is cooled down to room temperature from the fabrication or annealing temperature, residual stresses are induced in the composite due to the mismatch of the thermal expansion coefficients between the matrix and fiber. An investigation was undertaken of the magnitude of the thermal residual stresses by determining the difference of the yield stresses ($\Delta\sigma_y$) between tension and compression resulting from the thermal residual stresses. A theoretical model based on the Eshelby's method was then constructed for the prediction of the thermal residual stresses and $\Delta\sigma_y$. The agreement obtained was very good between the experimental results and the theoretical predictions.

Résumé—Quand on refroidit un composite à matrice métallique depuis la température d'élaboration ou de recuit jusqu'à la température ambiante, on introduit dans ce composite des contraintes internes provoquées par les coefficients de dilatation thermique différents de la matrice et de la fibre. Nous avons entrepris la mesure de ces contraintes thermiques résiduelles en déterminant la différence des limites élastiques ($\Delta\sigma_y$) en tension et en compression qui résultent des contraintes thermiques résiduelles. Nous avons ensuite construit un modèle théorique, basé sur la méthode d'Eshelby, pour prédire les contraintes thermiques résiduelles $\Delta\sigma_y$. Nous avons obtenu un très bon accord entre les résultats expérimentaux et les prédictions théoriques.

Zusammenfassung—Wenn eine Metallmatrix von der Herstellungs- oder Auslagerungstemperatur auf Raumtamperatur abgekühlt wird, dann entstehen in dem Werkstoff Spannungen, die aus der Fehlpassung durch die unterschiedlichen thermischen Ausdehnungskoeffizienten zwischen Matrix und Faser herrühren. Die Höhe dieser thermisch bedingten Restspannungen wurde untersucht, indem der Unterschied in den Fließspannungen zwischen Druck- und Zugverformung bestimmt wurde. Ein Model wurde für die Voraussage der thermischen Restspannungen und der Fließspannungen aufgestellt, welches auf der Methode von Eshelby beruht. Die erhaltene Übereinstimmung zwischen Experiment und Theorie ist sehr gut.

1. INTRODUCTION

Metal matrix composites (MMCs), including eutectic composites, are becoming important in their application to structural components which are to be used at intermediate and high temperatures. When MMCs are fabricated at high temperature or annealed at a certain high temperature and cooled down to room temperature, the MMCs have undesirable properties, such as low tensile yield and ultimate strengths. These results are mainly due to residual stresses that are caused by the mismatch of the thermal expansion coefficients between the matrix and fiber. This subject has been studied by a number of researchers (for examples see Refs [1–14]). The residual stresses so induced have been observed in tungsten fiber/copper composites [7] and in SiC whisker/6061 Al composites [8, 9]. Most of the models purposed to estimate the residual stress were based on one-dimensional analysis [1–3], continuous fiber system [4, 5], or spherical particle system [10].

The model based on Eshelby's equivalent inclusion method [11], has been used to solve the problem of thermal residual stress [12–14]. The advantages of the Eshelby's model are that it can solve a three-dimensional composite system such as short whisker composite and also can take into account the effect of the volume fraction of fiber (V_f) easily.

Eshelby's method has been also used for predicting the yield stress and work-hardening rate of metal matrix composites [15–19]. The effect of the thermally induced residual stress on the yield stresses has been discussed by Wakashima *et al.* [18] who predicted that the yield stress in compression (σ_y^c) exceeds that in tension (σ_y^t) for continuous B fiber/Al composites which were cooled down, although no comparison with the experimental data was made.

In this paper we focus on the residual stresses induced in a short whisker MMC due to the temperature drop and its effect on the yield stresses. The

†This research was supported in part under a contract from the Office of Naval Research, Contract No. N00014-85K-0007.

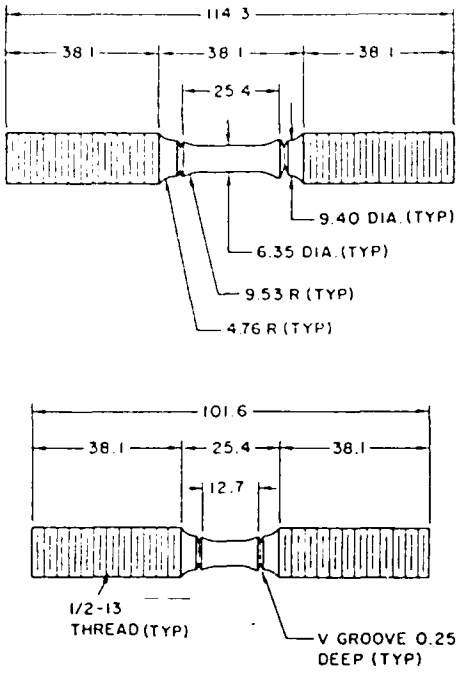

Fig. 1. A schematic diagram of the sample configuration which was used in the tension and compression testing. The dimensions are in millimeters.

target MMC is aligned fiber MMC with a special emphasis on SiC whisker/6061 Al composite.

2. EXPERIMENTAL

2.1. Materials

The target short fiber MMC was SiC whisker/6061 Al composite and was purchased from ARCO/SILAG. As a control MMC a SiC spherical 1100 Al composite was also purchased from ARCO/SILAG. The composite was in the form of an extruded rod 15.5 mm in diameter. Three different volume fractions of fiber (or whisker) V_f composites were used: $V_f = 0$, 0.05 and 0.2, and a composite with spherical SiC particles of 0.5 μm in diameter, having a volume fraction, V_s, equal to 0.2 was also used. All of the material was supplied as-fabricated (no heat treatment) condition, they then were machined into samples [Fig. 1(a) and (b)], annealed for 12 h at 810 K, and then furnace cooled.

2.2. Testing methods

The tension and compression tests were performed in an Instron testing machine using a liquid metal container as the lower gripping device. This method of gripping was employed to ensure very good alignment of the sample. This test procedure is described in greater detail elsewhere [20]. Samples of two different gauge lengths were used to determine if there was a gauge length effect (there was none). The effective gauge length of the samples was determined by glueing strain gauges on the center portion of the sample and comparing the results obtained from a clip on extensometer which was mounted into the "V" grooves. If the extensometer is mounted directly to the uniform gauge section, there is a high probability that the sample will fracture where the "knife" edge of the extensometer makes contact with the sample. Several tests in the low stress range were conducted using both the extensometer and the strain gauge; from these tests the effective gauge length was determined. Subsequent tests were conducted using only the extensometer. The samples, which were tested in the range from 8×10^{-5} s^{-1} to 2×10^{-3} s^{-1}, showed no strain rate effect.

The conventional X-ray technique [21] was used first, but it was determined that there were problems when this technique was applied to discontinuous composites. The residual stress was determined by measuring the change in lattice parameters. There is an implicit assumption made in using this procedure, i.e. the matrix remains cubic.

3. EXPERIMENTAL RESULTS

The stress–strain curves of the $V_f = 0$, 0.05 and 0.2 composites are plotted in Fig. 2(a), (b), and (c), respectively. The solid and dashed curves denote the tensile and compressive test results, respectively. The yield stress was measured as 0.2% off set strain and is indicated in the figures by arrows.

The shapes of the stress–strain curves of the $V_s = 0.2$ composites are very similar to those of whisker composites, except that the tension stress–strain curve is below that of the compression stress–strain curve. However, as in the case of $V_f = 0$, there was no difference in the stress–strain curves for tension and compression of $V_s = 0$.

The data obtained from the X-ray analysis is given in Table 1, and it was observed that there is a residual tensile stress in the matrix.

4. THEORETICAL PROCEDURE

The theoretical model used here is based on Eshelby's equivalent inclusion model. Mori and his co-workers [15–17] extended Eshelby's method to predict the yield stress (σ_y) and work-hardening rate of aligned short whisker composites. Wakashima *et al.* [18] extended the above approach to predict σ_y by considering the mismatch of the thermal expansion coefficients of the matrix and fiber. Following the above models, Takao and Taya [14] have recently computed the stress field in and around a short fiber in a short fiber composite where the fiber is anisotropic both in stiffness and thermal expansion.

In this paper we focus on the average thermal residual stress induced in the matrix by the cool-down process and also the yield stresses in tension (σ_y^t) and compression (σ_y^c) when the composite is tested at the room temperature. The former case is essentially based on the model by Takao and Taya [14], and as the latter case, we extend the model by Wakashima

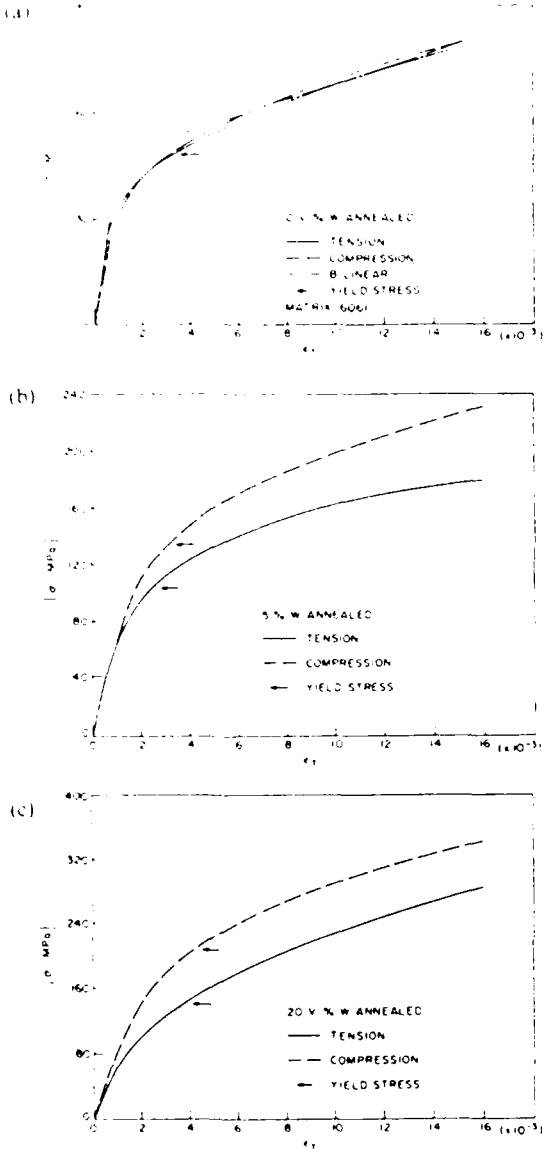

Fig. 2. (a) The absolute stress vs strain curves for tension and compression test of 0 vol. % whisker material in the annealed condition. (b) The absolute value of stress vs strain for 5 vol. % whisker composite in the annealed condition. (c) The absolute value of the stress as a function of strain for 20 vol. % whisker material in the annealed condition.

et al. [18] to account for the bi-linear stress–strain curve of the matrix.

4.1 Formulation

Consider an infinite body (D) which contains ellipsoidal whiskers (Ω) aligned along the x_3-axis (Fig. 3). This composite body D is subjected to the applied stress field, which is σ_{ij}^0 when the body is uniform in elastic constants. The stiffness tensors of the matrix ($D-\Omega$) and fiber (Ω) are denoted by C_{ijkl} and C_{ijkl}^f, respectively. Following Eshelby, the transformation strain [11] or eigenstrain [22] is given in the fiber domain Ω as α_{ij}^*, where α_{ij}^* is the strain due to the mismatch of the thermal expansion coefficients

Table 1. Thermal residual stress (tensile) X-ray measurements

Material	Longitudinal (MPa)	Transverse (MPa)
0 vol % whisker SiC 6061 matrix	0.0	0.0
5 vol % whisker SiC 6061 matrix	408	35
20 vol % whisker SiC 6061 matrix	231	58
Wrought 1100 Al	0.0	0.0

and the uniform plastic strain e_{ij}^p is prescribed in the matrix [15]. As far as the stress field is concerned, the model of Fig. 4 is equivalent to that of Fig. 3. Thus, the present problem is reduced to "inhomogeneous inclusions problem" (Fig. 4) [22]. The model of Fig. 4 will be used not only to predict the yield stresses and work-hardening rates, but also to compute the thermal residual stresses. For the latter case, we willl set $\sigma_{ij}^0 = e_{ij}^p = 0$.

Following the Eshelby's equivalent inclusion method modified for a finite volume faction of fibers [22, 23], the total stress field in the fibers $\sigma_{ij}^0 + \sigma_{ij}$ is given by

$$\begin{aligned}\sigma_{ij}^0 + \sigma_{ij} &= C_{ijkl}^f\{e_{kl}^0 + \tilde{e}_{kl} + e_{kl} \\ &\quad - (\alpha_{kl}^* - e_{kl}^p)\} \\ &= C_{ijkl}\{e_{kl}^0 + \tilde{e}_{kl} + e_{kl} \\ &\quad - (\alpha_{kl}^* - e_{kl}^p) - e_{kl}^*\} \qquad (1)\end{aligned}$$

where the repeated indices are to be summed over 1, 2 and 3.

$$\sigma_{ij}^0 = C_{ijkl}e_{kl}^0 \quad \text{in } D \qquad (2)$$

$$\langle\sigma_{ij}\rangle_m = C_{ijkl}\tilde{e}_{kl} \quad \text{in } D-\Omega. \qquad (3)$$

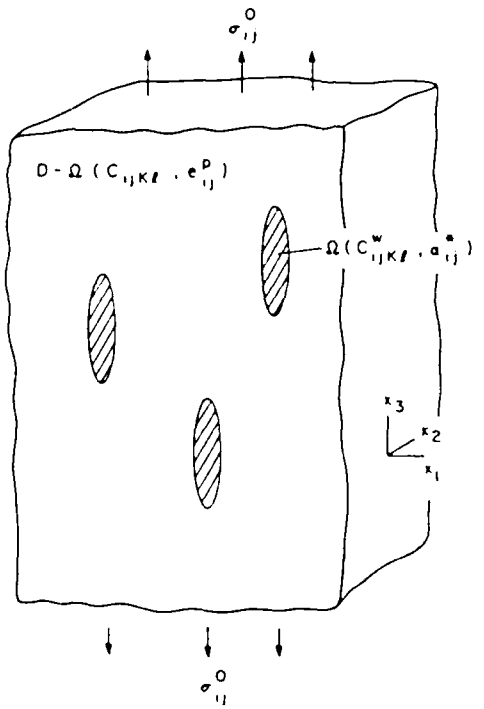

Fig. 3. Theoretical model, actual case

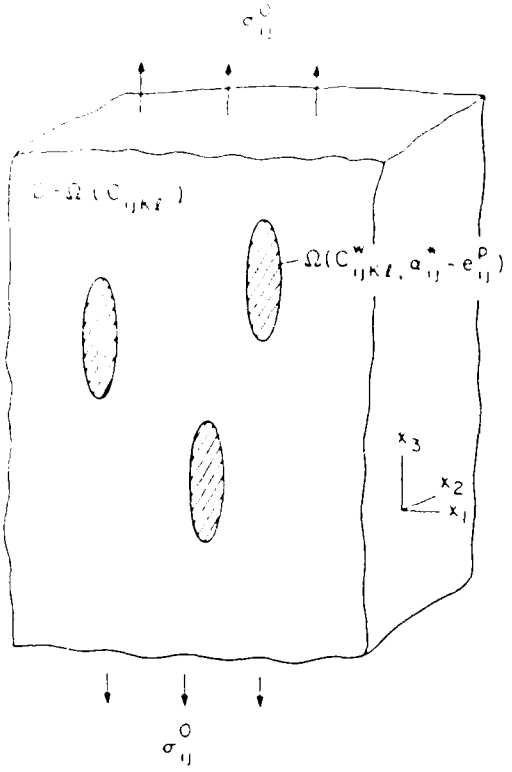

Fig. 4. The equivalent inclusion model converted from Fig. 3.

In equation (1), e^*_{kl} is the fictitious eigenstrain [23] which was introduced to connect the present problem to "inclusion problem" and $\tilde{e}_{ij}$ is the average strain disturbance in the matrix and related to the average stress disturbance in the matrix $\langle\sigma_{ij}\rangle_m$ by equation (3). $\langle\sigma_{ij}\rangle_m$ is defined by

$$\langle\sigma_{ij}\rangle_m = \frac{1}{V_{D-\Omega}}\int_{D-\Omega}\sigma_{ij}\,dv \tag{4}$$

where $V_{D-\Omega}$ is the total volume of the matrix and σ_{ij}, and e_{ij} in equation (1) and (4) is the stress and strain disturbance, respectively, by a single fiber Ω when it is embedded in an infinite matrix. Since the stress disturbance when it is integrated in the entire domain D vanishes

$$\int_D \sigma_{ij}\,dv = 0. \tag{5}$$

The stress disturbance σ_{ij} is obtained from equation (1) and (2)

$$\sigma_{ij} = C_{ijkl}(\tilde{e}_{kl} + e_{kl} - e^{**}_{kl}) \tag{6}$$

where

$$e^{**}_{kl} = \alpha^*_{kl} + e^*_{kl} - e^p_{kl}. \tag{7}$$

From equations (3), (5) and (6), we obtain

$$\tilde{e}_{ij} = -V_f(e_{ij} - e^{**}_{ij}). \tag{8}$$

According to Eshelby, e_{ij} is related to the total eigen-strain e^{**}_{kl} as

$$e_{ij} = S_{ijkl}e^{**}_{kl} \tag{9}$$

where S_{ijkl} is the Eshelby's tensor and a function of C_{ijkl} and the geometry of the ellipsoidal fiber. The fiber is assumed to be a prolate spheroid, hence the fiber aspect ratio l/d is a single geometrical parameter. For simplicity, we assume that the matrix and fiber are isotropic both in stiffness and thermal expansion coefficient. Thus, C_{ijkl}, C^f_{ijkl} and α^*_{ij} are given by

$$C_{ijkl} = \lambda\delta_{ij}\delta_{kl} + \mu(\delta_{ik}\delta_{jl} + \delta_{il}\delta_{kj}) \tag{10}$$

$$C^f_{ijkl} = \lambda^f\delta_{ij}\delta_{kl} + \mu^f(\delta_{ik}\delta_{jl} + \delta_{il}\delta_{kj}) \tag{11}$$

$$\alpha^*_{ij} = -(\alpha_f - \alpha)\delta_{ij}\Delta T. \tag{12}$$

In the above equations, δ_{ij} is the Kronecker's delta, λ (λ^f) and μ (μ^f) are Lame's constants of the matrix (fiber), α (α_f) is the thermal expansion coefficient of the matrix (fiber) and ΔT is the change in temperature ($\Delta T > 0$ corresponds to the temperature drop).

The stress field in the fiber is obtained from equations (6), (8), (9) and (10)

$$\sigma_{ij} = (1 - V_f)\{(S_{kkmn}e^{**}_{mn} - e^{**}_{kk})\lambda\delta_{ij} + 2\mu(S_{ijmn}e^{**}_{mn} - e^{**}_{ij})\}. \tag{13}$$

After solving for e^{**}_{ij} in equation (1) by use of equations (8) and (9), we can compute the stress disturbance σ_{ij} in the fiber from equation (13).

4.2. *Yield stresses σ^t_y, σ^c_y and work-hardening rate*

The method of computing the yield stresses σ^t_y and σ^c_y and the work-hardening rate of the composite is described briefly. The total potential energy of Fig. 3, U, is given by

$$U = \frac{1}{2}\int_D (\sigma^0_{ij} + \sigma_{ij})(u^0_{i,j} + \tilde{u}_{i,j} + u_{i,j} - e^p_{ij} - \alpha^*_{ij})\,dV - \int_{\P D\P}\sigma^0_{ij}n_j(u^0_i + \tilde{u}_i + u_i)\,dS \tag{14}$$

where u^0_i, $\tilde{u}_i$ and u_i are the displacement components corresponding to e^0_{ij}, $\tilde{e}_{ij}$ and e_{ij}, respectively; the index j preceded by a comma denotes a partial differentiation with respect to x_j; $\P D\P$ is the boundary of D; and n_j is the jth component of an unit vector outer normal to $\P D\P$. Then, the change in U due to the change in the plastic strain δe^p_{ij} is given by

$$\delta U = -\int_D (\sigma^0_{ij} + \sigma_{ij})\delta e^p_{ij}\,dV. \tag{15}$$

In the above derivation, the Gauss' divergence theorem and the following equation were used

$$\int_D \sigma_{ij}(\delta\tilde{u}_{i,j} + \delta u_{i,j})\,dV = 0.$$

Noting that the plastic strain exists only in the matrix $(D - \Omega)$, equation (15) is reduced to

$$\delta U = -\delta e^p_{ij}\{(1 - V_f)\sigma^0_{ij} - V_f\sigma_{ij}\}. \tag{16}$$

Under the uniaxial stress along the x_3-axis (σ_0), σ^0_{ij}

and e^0 are given by

$$\sigma^0 = \begin{Bmatrix} 0 \\ 0 \\ \sigma_0 \\ 0 \\ 0 \\ 0 \end{Bmatrix} \qquad e^0_{ij} = \begin{Bmatrix} -\frac{1}{2}e_p \\ -\frac{1}{2}e_p \\ e_p \\ 0 \\ 0 \\ 0 \end{Bmatrix} \tag{17}$$

where the six components of σ^0_{ij} and e^0_{ij} are expressed in the order of $(ij) = 11, 22, 33, 23, 31$, and 12, and e_p is the plastic strain along the x_3-axis. On the other hand, the energy dissipation due to the plastic work in the matrix, δQ, is given by

$$\delta Q = (1 - V_f)\sigma_y \delta e_p \tag{18}$$

where σ_y is the flow stress of the matrix for the bilinear model

$$\sigma_y = \sigma^0_y + E_T e_p \tag{19}$$

where σ^0_y and E_T are the initial yield stress and tangent, modulus of the matrix, respectively. Since $\delta U + \delta Q = 0$, we obtain

$$\sigma_0 = \sigma^0_y + \frac{V_f}{(1 - V_f)}(\sigma_{33} - \sigma_{11}). \tag{20}$$

In the above derivation, $\sigma_{11} = \sigma_{22}$, $e^0_{11} = e^0_{22} = -\frac{1}{2}e_p$ were used. Combining the solutions of σ_{ij} in equation (13) and equation (20), we can obtain the yield stress of the composite in tension ($\sigma^t_y = \sigma_0$) and that in compression ($\sigma^c_y = \sigma_0$) as

$$\begin{aligned} \sigma^t_y/\sigma^0_y &= C_0 + C_1\alpha\Delta T \\ \sigma^c_y/\sigma^0_y &= C_0 - C_1\alpha\Delta T. \end{aligned} \tag{21}$$

Similarly, the work-hardening rate of the composite, $\bar{E}_T$ is obtained as

$$\bar{E}_T/E_T = C_2 + C_3\left(\frac{E_T}{E}\right). \tag{22}$$

In the above equations, C_0, C_1, C_2, and C_3 are functions of the elastic stiffness of the matrix and fiber and the fiber aspect ratio l/d. E is the Young's modulus of the matrix.

4.3. Thermal residual stress

When the composite is cooled by ΔT, the thermal residual stress is induced in the composite. The theoretical model for this problem is the same as that shown in Fig. 4 except that $\sigma^0_{ij} = e^0_{ij} = 0$ in the present case. Hence, the formulation up to equation (13) is valid and will be used to compute the thermal residual stress. Once the stress within the fiber $\sigma^{(in)}_{ij}$ is computed, the stresses just outside the fiber $\sigma^{(out)}_{ij}$ can be obtained by the following relation [13]

$$\sigma^{(out)}_{pq} = \sigma^{(in)}_{pq} + C_{pqmn} \times \left\{ -C_{klmn}e^{**}_{ij}n_i n_n \frac{(\lambda + 2\mu)\delta_{km} - (\lambda + \mu)n_k n_m}{\mu(\lambda + 2\mu)} + e^{**}_{mn} \right\} \tag{23}$$

where $\sigma^{(in)}_{pq}$ is given by equation (13), e^{**} is solved by equation (11), λ and μ are previously defined and n_i is the ith component of the unit vector perpendicular to the surface of the fiber. If one wants to compute the stresses just outside the equator of the ellipsoidal fiber where $n = (1, 0, 0)$, we can obtain the stresses in polar coordinates, σ_r, σ_θ and σ_z there as

$$\begin{aligned} \sigma^{(out)}_r &= \sigma^{(in)}_r \\ \sigma^{(out)}_\theta &= \sigma^{(in)}_\theta + 2\mu\left\{\frac{1}{1 - \nu}e^{**}_{11} + \frac{\nu}{1 - \nu}e^{**}_{33}\right\} \\ \sigma^{(out)}_z &= \sigma^{(in)}_z + 2\mu\left\{\frac{\nu}{1 - \nu}e^{**}_{11} + \frac{1}{1 - \nu}e^{**}_{33}\right\} \end{aligned} \tag{24}$$

where ν is the Poisson's ratio of the matrix.

Next the average stress field in the matrix, $\langle\sigma_{ij}\rangle_m$, can be also obtained from equations (3), (8) and (9) as

$$\langle\sigma_{ij}\rangle_m = -V_f C_{ijkl}(S_{klmn}e^{**}_{mn} - e^{**}_{kl}). \tag{25}$$

The average stress in the matrix, $\langle\sigma_r\rangle_m$, $\langle\sigma_\theta\rangle_m$ and $\langle\sigma_z\rangle_m$, will be computed by setting $ij = 11$, 22, and 33 in equation (25). It should be noted here that $\langle\sigma_r\rangle_m = \langle\sigma_\theta\rangle_m$ due to the assumptions of an aligned short fiber composite which results in the transverse isotropy of the volume average quantity.

5. THEORETICAL RESULTS

We will apply the present theoretical model to two types of MMCs, short fiber MMC (SiC whisker/6061 Al) and continuous fiber MMC (Al_2O_3-γ/5056 Al).

5.1. Short fiber MMC

The thermo-mechanical data of the matrix and whisker for the theoretical calculations are obtained from the stress–strain curve of the matrix [Fig. 2(a)] and the material properties handbook.

Annealed 6061 Al matrix (bilinear model):

$$\begin{aligned} E &= 47.5\ \text{GPa} \\ E_T &= 2.3\ \text{GPa} \\ \sigma^0_y &= 47.5\ \text{MPa} \\ \nu &= 0.33 \\ \alpha &= 23.6 \times 10^{-6}/\text{K} \end{aligned} \tag{26}$$

SiC whisker:

$$\begin{aligned} E_f &= 427\ \text{GPa} \\ \nu_f &= 0.17 \\ \alpha_f &= 4.3 \times 10^{-6}/\text{K} \\ l/d &= 1.8 \end{aligned} \tag{27}$$

where the average value of the fiber aspect ratio (l/d) was used [24] and the bilinear stress strain curve of the matrix is indicated by a dash-dot line in Fig. 2(a). The temperature drop ΔT is defined as

$$\Delta T = T_1 - T_0 \tag{28}$$

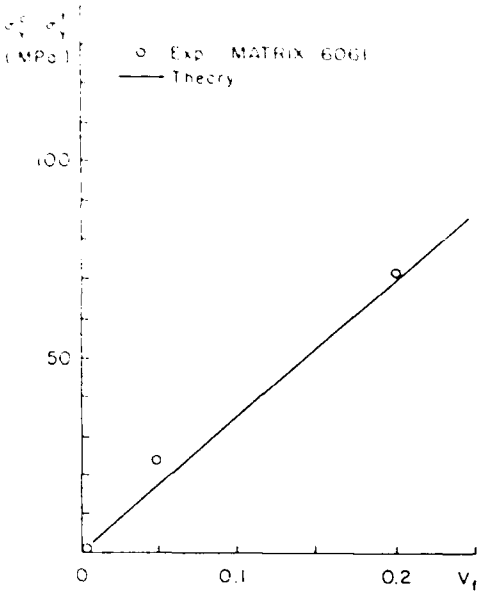

Fig. 5. The difference in yield stress between compression and tension as a function of vol. % silicon carbide whisker.

where T_1 is taken as the temperature below which dislocation generation is minimal during the cooling process [9] and T_0 is the room temperature. Thus, for the present composite system ΔT is set equal to 200 K.

The theoretically predicted σ_y^c and σ_y^t can be obtained from equation (21). The differences between σ_y^c and σ_y^t ($\sigma_y^c - \sigma_y^t$) for various V_f are shown as the solid line in Fig. 5. The differences between σ_y^c and σ_y^t increase with increasing V_f. The experimentally determined differences between σ_y^c and σ_y^t are represented by the open circles in Fig. 5. The experimental values of the yield stresses are taken as the stresses 0.2% off-set strain. It follows (Fig. 5) that good agreement is obtained between the experimental and theoretical results of the difference in the compressive tensile yield stresses. However, the experimental values of σ_y^c are greater than the theoretical values of σ_y^c, and similarly the experimental values of σ_y^t are greater than the theoretical values of σ_y^t.

From the data given by equation (26)–(27) and the use of equation (25), we have computed the stresses, its average value in the matrix and plotted schematically the σ_L (solid curve) and $\langle \sigma_L \rangle_m$ (dashed curve) along the x_2 and x_3 axes in Fig. 6.

Next, the thermal residual stresses, averaged in the matrix of the SiC whisker/6061 Al, are predicted by equation (25) and the results on $\langle \sigma_T \rangle_m$ and $\langle \sigma_L \rangle_m$ are plotted in Fig. 7 as a function of the volume fraction of fiber (V_f), where the subscripts, T and L denote the component along the transverse direction (r and θ) and longitudinal direction (z). The average theoretical thermal-residual stress is predicted to be tensile in nature, and that the average residual stress in the longitudinal direction is larger than the average residual stress in the transverse direction. The experimentally determined residual stresses (Table I) are tensile in nature and the longitudinal stress is larger than the transverse, but the experimentally determined stresses are larger than those theoretically predicted.

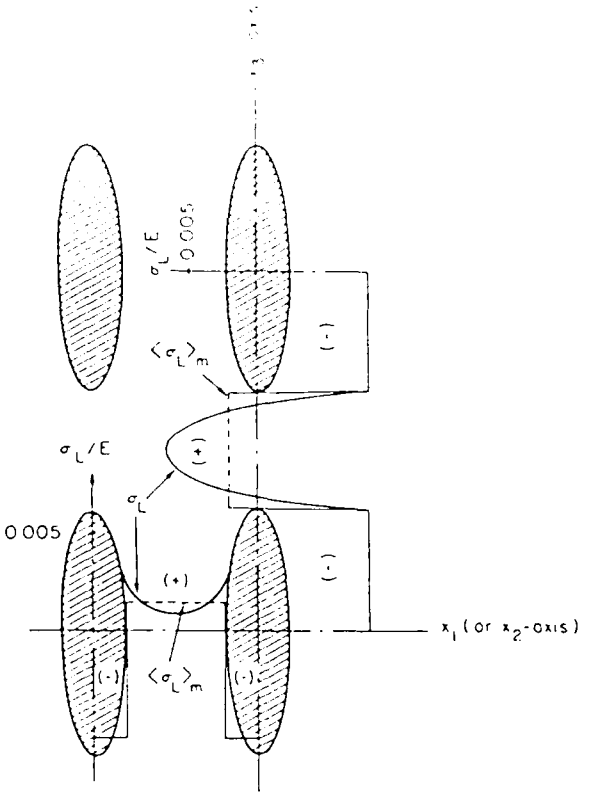

Fig. 6. A schematic of the stress distribution in the matrix and in the reinforcement due to the difference in thermal coefficient of expansion between the silicon–carbide and aluminum.

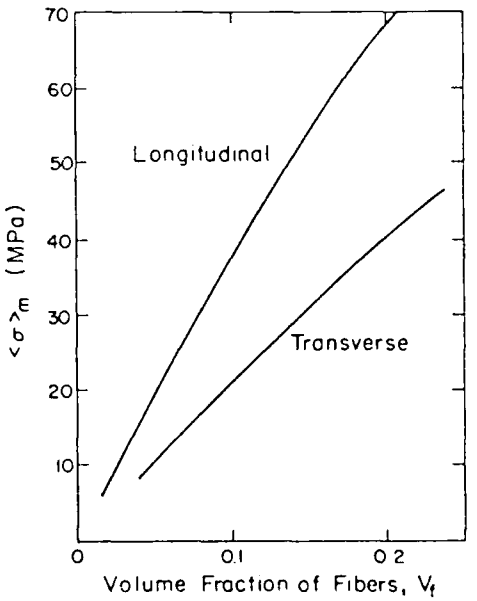

Fig. 7. Predicted residual stress in the matrix for the transverse and longitudinal directions.

For the case of spherical SiC composites the procedure for obtaining the difference in σ_y^c and σ_y^t is identical to the whisker case, with one exception, i.e. $l/d = 1$ in the spherical case. The theoretically predicted difference between σ_y^c and σ_y^t for $V_f = 0.2$ is zero, but experimentally it was observed that σ_y^t was slightly greater than σ_y^c by ~ 13 MPa.

5.2. Continuous fiber MMC

The present model is also applied to continuous fiber (Al_2O_3-γ) reinforced 5056 Al composite with $V_f = 0.5$ (Al_2O_3-γ/5056 Al in short abbreviation) to predict the yield stress in tension and compression, and also the work-hardening rate.

The material properties of the matrix metal and fiber are:

Annealed 5056 Al matrix (bilinear model):

$$E = 72.4\ \text{GPa}$$
$$E_T = 6.25\ \text{GPa}$$
$$\sigma_y^0 = 152\ \text{MPa} \qquad (29)$$
$$\nu = 0.33$$
$$\alpha = 23.6 \times 10^{-6}/\text{K}$$

Al_2O_3-γ Fiber [25]:

$$E_f = 210\ \text{GPa}$$
$$\nu_f = 0.2 \qquad (30)$$
$$\alpha_f = 8.8 \times 10^{-6}/\text{K}.$$

In this computation $\Delta T = 200$ K was used.

Figure 8 shows a comparison between the experimental results [25] (solid curve and solid circle) and the theoretical ones (dashed curve and open circle) where both solid and open circles denote the yield stresses. It follows from Fig. 8 that the yield stress and the work-hardening rate of the compressive stress–strain curve are well predicted by the present model, while for the tensile yield stress, the present model underestimates the experimental results.

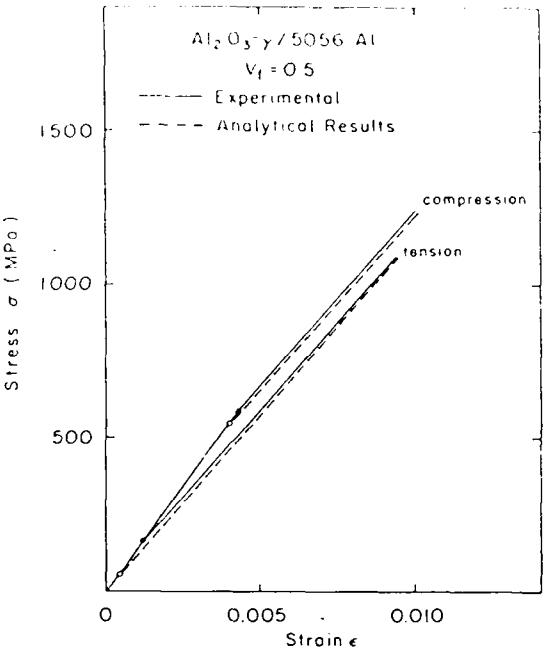

Fig. 8. Tension and compression stress–strain curves of continuous Al_2O_3-γ fiber/5056 Al composite with $V_f = 0.5$ [25]. The experimental and theoretical results are denoted by solid and dashed curves, respectively. The solid and open circles denote the yield stress of the experimental and theoretical results, respectively.

6. DISCUSSION

The theoretical predictions and experimental results are in very good agreement in most cases.

The theoretical model is based on an extension of previous work by Eshelby [11], Mura and Taya [13], Tanaka and Mori [15], and Wakashima *et al.* [18] and it can predict the yield stress in tension and compression and the thermal residual stress. The predicted values of the yield stress of the whisker composite in tension and compression are less than the experimentally determined values of the yield stress in tension and compression. This difference between the theoretical and experimental stresses is due to the fact that the $V_f = 0$ curves of stress vs strain were used for the matrix in the composite cases. It has been demonstrated by Arsenault and Fisher [8] and Vogelsang *et al.* [9] that there is a much higher dislocation density in the annealed composite matrix *than in the $V_f = 0$ material. Therefore*, the matrix is stronger than the annealed $V_f = 0$ matrix alloy. However, this increase in matrix strength due to a higher dislocation density does not influence the difference in yield stress in the compression vs tension. The theoretical prediction is that the yield stress of the whisker composite in compression should be higher than the yield stress in tension, and this is exactly what is observed experimentally, due to an average residual tension stress in the sample. This residual stress reduces the yield stress in tension and increases the yield stress in compression.

The theoretical prediction that the compressive yield stress is higher than the tensile yield stress suggests that a tensile residual stress exists in the matrix of composite. An average tensile residual stress is predicted in the matrix as shown in Figs 6 and 7.

Though the present model is based on the assumption that all fibers are aligned along a specified direction (the x_3-axis in Fig. 3), SiC whiskers in Sic whisker/6061 Al composites are misoriented. The misorientation of these whiskers is observed to be enhanced as V_f decreases. Thus the values of σ_y^t and σ_y^c predicted by the present model tends to overestimate the actual values. The fiber aspect ratio (l/d) of SiC whiskers has been observed to be variable [24], i.e. $0.5 \leqslant l/d \leqslant 25$ with most of l/d being around 1. In the present model we have used the average value of

l/d, 1.8 to predict the yield stress and work-hardening rate of the composite. Takao and Taya [26] have recently examined the effect of variable fiber aspect ratio on the stiffness and thermal expansion coefficients of a short fiber composite and concluded that the results predicted by using the average value of l/d are not much different from those of using actual variable aspect ratio unless the distribution of l/d is extraordinarily scattered. Thus, the use of the average value of l/d in the present model can be justified.

The present model is strongly dependent on ΔT $(=T_1 - T_0)$ as it appears in equations (12), (21) and (22). A choice of T_1 was made by noting the movement of dislocation generation being minimal [9] as discussed before. If temperature T_1 can be considered to correspond to the temperature T_r above which the relaxation of internal stress is highly promoted and below which the deformation of the matrix metal is basically controlled by elastic and time-independent plastic behavior, then the present model which is based on an elastic/time-independent plasticity becomes valid. If T_1 is not approximately equal to T_r, a more refined model to account for elastic/time-independent plastic/creep behavior of the matrix metal during a temperature excursion from T_1 to T_0 must be employed. Such a model for one-dimensional stress analysis has been proposed by Garmong [27].

In this present model, the relaxed mismatch strain is assumed to stay as surface dislocations. In reality, such surface dislocations are expected to relax by punching. Taya and Mori [28] have recently studied this punching phenomenon to conclude that the smaller the fiber aspect ratio is, the larger the punching distance. Therefore, the present model predicts the lower bound on σ_y^c. In fact, the predicted σ_y^c is smaller than the experimental value of σ_y^c.

Instead, if the mismatch strain is completely relaxed, then σ_y^t will increase, but "σ_y^c" will decrease, thus the difference will approach to zero, though the absolute value of the yield stress of the composite increases compared with the matrix yield stress (σ_y). In other words, the mismatch strain is partially relaxed by dislocation generation. The residual stresses under consideration are the remanant elastic stresses. It was assumed that below 495 K the residual stress was below the generation stress of dislocations (i.e. below the yield stress of the matrix). Therefore, the residual stress was only determined from 495 to 295 K, and not for the entire temperature range of cooling of the sample, e.g. from the annealing temperature of 810 K.

7. CONCLUSIONS

It is possible to arrive at the following conclusions from the theoretical model of the thermal residual stresses and the experimental results.

1. The theoretical model predicts a higher compression yield stress than tensile yield stress for the whisker composite, which is in agreement with the experimental results. The higher compressive yield stress is due to a tensile residual stress. This residual stress is due to the difference in coefficient of thermal expansion between fiber and matrix.

2. In the short fiber case, the theoretical model predicts that there should be an average residual stress which is in tension and experimental X-ray data confirms this prediction.

3. The absolute magnitude of the predicted yield stress (tensile and compressive) is less than the experimental yield stress due to the fact that in this model dislocation punching is not considered. In the actual cases there is dislocation punching which leads to matrix strengthening.

4. The residual stress, in the region between SiC whiskers, is tensile and this is the likely region where plastic deformation would begin. For in this region the matrix contains a lower dislocation density than adjacent to the SiC whisker, i.e. in this region the matrix is weaker.

5. The theoretical model predicts that the compressive yield stress should equal the tensile yield stress for composites containing spherical SiC. Experimentally it is observed that the tensile yield stress is slightly larger than the compressive yield stress.

6. The present model can predict the yield stress and work-hardening rate of continuous Al_2O_3-γ fiber/5056 Al composite reasonably well except for σ_y^t.

REFERENCES

1. E. R. Thompson, D. A. Koss and J. C. Chestnutt, *Metall. Trans.* **1**, 2807 (1970).
2. D. A. Koss and S. M. Copley, *Metall. Trans.* **2**, 1557 (1971).
3. J. K. Lees, *Polymer Engng Sci.* **8**, 195 (1968).
4. S. S. Hecker, C. H. Hamilton and L. J. Ebert, *J. Mater. Sci.* **5**, 868 (1970).
5. J. Gayda and L. J. Ebert, *Metall. Trans.* **10A**, 349 (1979).
6. S. D. Tsai, D. Mahulikar, H. L. Marcus, I. C. Noyan and J. B. Cohen, *Mater. Sci. Engng* **47**, 145 (1981).
7. K. K. Chawla and M. Metzger, *J. Mater. Sci.* **7**, 34 (1972).
8. R. J. Arsenault and R. M. Fisher, *Scripta metall.* **17**, 67 (1983).
9. M. Vogelsang, R. J. Arsenault and R. M. Fisher, *Metall. Trans.* **17A**, 379 (1986).
10. J. K. Lee, Y. Y. Earmme, H. I. Aaronson and K. C. Russell, *Metall. Trans.* **11A**, 1837 (1980).
11. J. D. Eshelby, *Proc. R. Soc.* **A241**, 376 (1957).
12. K. Wakashima, M. Otsuka and S. Umekawa, *J. comp. Mater.* **8**, 391 (1976).
13. T. Mura and M. Taya, in *Recent Advances in Composites in the United States and Japan* (edited by J. R. Vinson and M. Taya). ASTM STP864, 209 (1985).
14. Y. Takao and M. Taya, *J. appl. Mech.* **52**, 806 (1985).
15. K. Tanaka and T. Mori, *Acta metall.* **18**, 931 (1970).
16. K. Tanaka, K. Wakashima and T. Mori, *J. Mech. Phys. Solids* **21**, 207 (1973).
17. S. C. Lin, T. Mura, M. Shibata and T. Mori, *Acta metall.* **21**, 505 (1973).

18. K. Wakashima, S. Kurihara and S. Umekawa, *Japan Soc. Comp. Mater.* **2**, 1 (1976).
19. A. Daimaru and M. Taya, *Proc. 4th Int. Conf. on Comp. Materials* (Edited by Hayashi *et al.*), p. 199. Japan Soc. Comp. Materials, Tokyo (1982).
20. R. Hsu and R. J. Arsenault, *Mater. Sci. Engng* **66**, 35 (1984).
21. J. B. Cohen, *Diffraction Methods in Materials Science*. MacMaillan Series in Materials Science (1966).
22. T. Mura, *Micromechanics of Defects in Solids*. Martinus Nijhoff, The Hague (1982).
23. T. Mori and K. Tanaka, *Acta metall.* **21**, 571 (1973).
24. R. J. Arsenault, *Mater. Sci. Engng* **64**, 171 (1984).
25. Private communication with Y. Abe, Sumito Chemical Co., Japan.
26. Y. Takao and M. Taya, *J. Composite Mater.* In press.
27. G. Garmong, *Metall. Trans.* **15**, 2183 (1974).
28. M. Taya and T. Mori, *Acta metall.* **35**, 155–162.

Unusual Aspects of the Bauschinger Effect in Metals and Metal-Matrix Composites

R. J. Arsenault

SYNOPSIS. The Bauschinger effect (BE) has intrigued research investigators for a long time, and numerous theories have been proposed to account for the BE, but none of these theories takes into account the effect of removal of a thin surface layer at the end of the first half cycle, and the presence of an average unidirectional residual stress. A series of investigations was undertaken to determine the effect of these two conditions on the magnitude of BE and two models were developed: one to explain the surface removal effect, i.e., surface removal reduced the BE, and the second to explain the directionality of BE in the presence of a tensile residual stress. The BE is much larger in tension following initial testing in compression as compared to initially testing in tension followed by testing in compression.

1 INTRODUCTION

A logical conclusion that could be arrived at after considering the fact that the Bauschinger effect [1] was reported about a century ago is that there is nothing unusual remaining concerning the Bauschinger effect (BE). All is known about the BE, there should be nothing left to discover.

However, not only is there a lack of agreement as to what constitutes the BE, but also there has been no single parameter that satisfactorily quantifies the BE. Most investigators have chosen to define the BE in terms of a reduction in the initial flow stress or yield stress for reverse deformation [2, 3], while others preferred a more general definition, such as 'a certain dependence of the flow stress and rate of work hardening on the strain history' or they simply referred to the existence of different stress–strain curves by loading in the reverse direction [4, 5]. Orowan [6] considered only the transient softening of materials on stress reversal as the BE, whereas others [7, 8] included permanent softening as part of the effect.

In attempting quantification, the reverse loading curve is usually replotted with absolute shear stress and cumulative shear strain values starting from the intersection of the unloading curve and the shear-strain axis. One obvious approach is to consider the Bauschinger strain, which is the difference between the shear strain of the reverse loading curve and the shear strain of the loading curve at the final forward stress, before unloading on such a plot. Figures 1(a) and (b) are typical stress–strain curves for a Bauschinger test. There are two different Bauschinger stress factors defined. The Bauschinger strain will

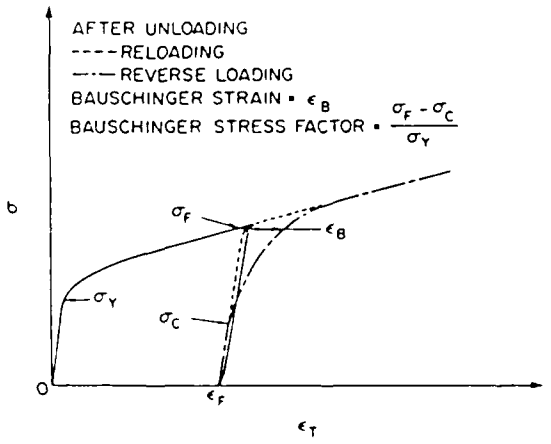

Fig. 1a. A plot of stress vs. strain showing the Bauschinger effect and the different parameters which are used in defining the Bauschinger effect.

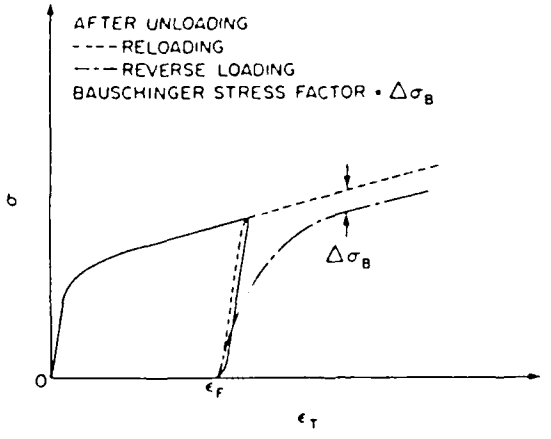

Fig. 1b. A stress vs. strain diagram for the case where permanent softening is observed.

Engineering Materials Group, University of Maryland, College Park, MD 20742. Manuscript received 2 June 1986.

increase almost linearly with prestrain, it can be expressed in a normalized form such as the Bauschinger strain factor, which is defined as the ratio of the Bauschinger strain to the prestrain. Another approach is to define the Bauschinger stress in terms of the difference between the final forward stress and the absolute value of the elastic limit under reverse loading. This Bauschinger stress will depend on the amount of work hardening before unloading. Thus a Bauschinger stress factor can be defined as the ratio of the Bauschinger stress to the stress increment during the prestrain. The second Bauschinger stress factor is the permanent softening.

The BE has been found in pure metals [9], ionic crystals [10] and single-phase [11, 12] or multiple-phase [13] alloys. The magnitudes of the BE in single-crystal and polycrystalline materials are comparable [5]. Single-crystal copper seems to have been studied most thoroughly [8, 14-21], and the experiments have involved primarily tension–compression [14, 15, 17-19], with only a few in simple shear [16-21], torsion [9] or bending [10]. The changes in dislocation configurations due to reverse loading have been studied using etch pit techniques [18, 19] or transmission electron microscopy [17, 20]. There also have been numerous investigations of the fundamental relationship of BE with temperature [9, 12], grain size [9, 12], prestrain [22-24], and the stress rate [25, 26]. The reduction in BE due to dynamic strain aging [27] or due to cyclic torsions [28] has also been studied. However, no attempts have been made to determine the surface effects on BE, which is quite surprising in view of the importance of the role of surface in fatigue failure.

By direct shearing of several fcc single crystals, Phillips [16] found new slip band formation on slip reversal (rather than de-slipping of the same slip bands) where there is non-primary slip. An explanation for this phenomenon was based on the assumption that it is easier to start new sources than to overcome barriers such as Cottrell-Lomer locks. Mori and Fujita [20] found that, during compression of Cu-Al, fine slip lines formed at the same positions as previous tensile slip-line clusters. When the reverse stress ratio reaches unity, almost all the compressive strains are produced by the new coarse slip bands in the virgin region, while the individual slip lines inside the tensile slip clusters are exhausted.

It is commonly believed that, under a reversed plastic strain, the dislocation loops already formed will shrink back on their sources, or the sources will produce loops of opposite sign and therefore annihilate the loops already present. Orowan [6] stated that 'the back stress of the pile-up would cause its generating Frank-Read source, as well as the sources in the intersecting planes, to produce dislocations of opposite sign, to dissolve the Cottrell-Lomer locks and to annihilate their separated mobile components'. Since total reversal can take place, Charsley and Desvaux [11] believed that the same sources act in compression on the same planes that were active in tension. Because only 20% of the dislocations generated in tension remain in the crystal, total reversal cannot take place without new sources acting in compression.

The number of models or theories that have been developed to explain the BE is almost equal to the number of investigators of the BE. However, all these models can be related to two dislocation mechanisms. The first mechanism is implied in Seeger's work-hardening theory [29]. The long-range internal stress, often called the back stress, which is created by the dislocation pile-up at barriers aids the dislocation movement and causes the drop in initial flow stress during reverse loading. The other mechanism is related to Orowan's idea of a directional resistance to dislocation motion due to prestraining [6]. The forward motion of dislocations becomes more difficult because there are an increasing number of stronger barriers ahead of the dislocations as the material work hardens. The barriers behind the dislocations are believed to be weaker and more sparsely spaced than those immediately in front. Thus the stress needed to push the dislocations backward is lower.

In the theories and the experimental results described above there is no mention of several factors

- The effect of removal of given amount from the surface of the sample after it has completed one half of a cycle.
- The direction of initial test, e.g. tension followed by compression or compression followed by tension.
- The effect of residual stress on the magnitude of the BE.

A consideration of these factors can lead to some unusual aspects of the BE.

An investigation both experimental and theoretical by Hsu and Arsenault [30] resulted in the prediction and observation that BE would be reduced if ~ 250 μm were reduced from the surface of the sample after the first half cycle.

A model by Arsenault and Taya [31] can be extended to consideration of the BE. This model predicts that there would be a difference in the magnitude of the BE depending upon the direction of initial loading. For example, if the sample was tested initially in tension followed by compression a smaller BE would result than if the sample was initially tested in compression followed by tension. In the other theories and models that have been put forward to predict the magnitude of the BE, the direction of initial loading is irrelevant. Experimentally it was shown that the direction of loading had a significant effect on the magnitude of the BE and the magnitude of the BE measured experimentally was in agreement with that predicted by the Arsenault and Taya theory.

In the following section the experimental and theoretical aspects of the effect of surface removal

will be discussed, and in the subsequent section the effect of residual stresses will be discussed. Finally the conclusion section will discuss the consequences of theories proposed and the agreement with experimental results.

2 SURFACE REMOVAL

2.1 Experimental procedure

Single crystal copper rods were grown by the Bridgeman technique and ground into samples as shown in Fig. 2. The samples were tested alternately in tension and compression. Because the alignment of the central axis of the specimen with the line of loading is very critical, a special apparatus was constructed to maintain good alignment in both tension and compression (Fig. 3). The surface layer was chemically removed from the sample *in situ*. Only the gauge length section was etched away with nitric acid jets while the two ends and holders were protected with varnish coatings. Further details of the experimental testing procedure have been given elsewhere [32]. An accurate stress–strain curve was obtained by the use of a specially mounted extensometer.

2.2 Experimental results

The experimental results are summarized in Table 1, in which both the Bauschinger stress factors and the Bauschinger strain factors are given. A batch number is assigned to all the specimens with the same orientation. The numerals in parentheses show the numbers of specimens with the same orientation. In the column labelled "No Etch" the average values of the Bauschinger stress factors for uninterrupted stress reversal testing of all specimens in the same batch are listed. In the column labelled "Etch" the average values for samples with surface removal are given. The percentage reduction in these factors as a ratio of the uninterrupted results is given in the following column. The last row gives the total average of all the values in each column.

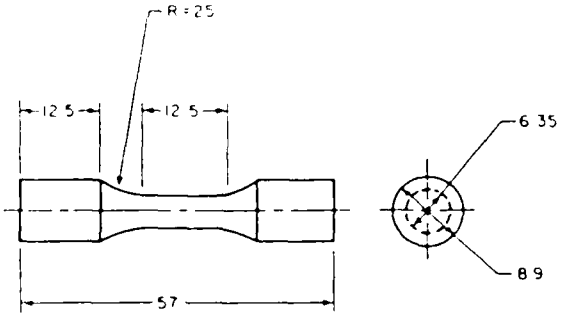

Fig. 2. The copper single crystal specimens. The dimensions of these specimens are given in millimetres.

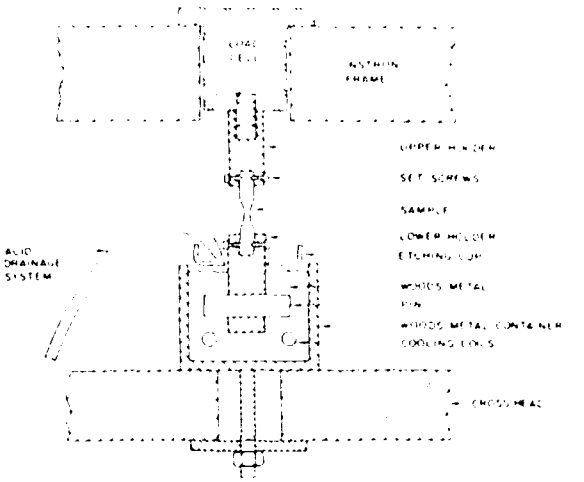

Fig. 3. The experimental arrangement for achieving good alignment and in situ surface removal.

Thus the experimental results indicate a rather large reduction in the BE by surface removal. For the Bauschinger stress factor the reduction ranges from 8.57% to 46.7%, with an average value of 26.8%. For the Bauschinger strain factor, the reduction varies from 21.4% to 85.2%, with an average value of 55.4%. The details of the analysis of experimental data can be found elsewhere [32].

Figure 4 is a plot of absolute shear stress versus total shear strain of two samples (samples 16-1 and

TABLE 1

Mean values of the Bauschinger factors for single-crystal copper (purity, 99.99%)

Batch (number of samples	Average Bauschinger stress factor		Reduction (%) in Bauschinger stress factor	Average Bauschinger strain factor		Reduction (%) in Bauschinger strain factor
	Etch	No Etch		Etch	No Etch	
10 (2)	0 8	1 5	46 7	0 025	0 135	85 2
13 (5)	0 794	1 16	31 6	0 0726	0 131	44 3
14 (3)	1 04	1 71	39 2	0 179	0 429	58 3
15 (2)	0 960	1 05	8 57	0 138	0 436	68 3
16 (2)	1 20	1 40	14 3	0 324	0 412	21 4
17 (4)	1 43	1 69	15 4	0 164	0 420	61 0
Total Average	1 04	1 42	26 8	0 146	0 327	55 4

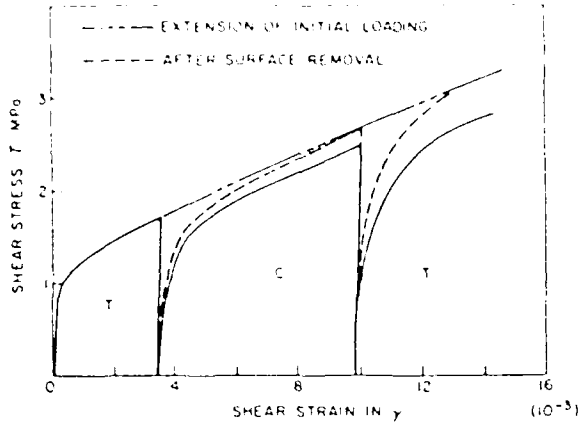

Fig. 4 The absolute shear stress vs. accumulated shear strain curve for samples 16-1 and 16-2; — - — - —, extension of initial loading; — — —, after surface removal; ———— no surface removal

16-2) which were chosen from the same single-crystal rod. Because the initial tensile portion of the stress-strain curve for sample 16-1 was nearly identical with that for sample 16-2, i.e., the yield stress and the work-hardening ratio of sample 16-1 were the same as those for sample 16-2, there was only one curve of stress versus strain for the initial loading in tension. Both samples were initially strained the same amount and then unloaded. Sample 16-2 was then loaded in compression, while for sample 16-1 the test was interrupted, the surface layer was removed and the test was continued in compression. Again both samples were strained an equal amount. The Bauschinger stress factor and strain factor for sample 16-1 (surface removal) were 1.20 and 0.334 respectively. The uninterrupted tension-compression test for sample 16-2 gave corresponding values of 1.40 and 0.412 respectively. Therefore, the reductions in the BE due to surface removal were only 14.3% and 21.4% respectively. However, when another tension loading was undertaken, the magnitude of the reduction in the BE was much larger. It is also interesting to note that the reverse loading curve for sample 16-1 (surface removal) approaches the extension of the initial loading curve beyond the unloading point. Thus the paramount BE is for all practical purposes completely eliminated by surface removal.

2.3 Model description

From a consideration of the results of the single-crystal copper experiments given in Section 2.2, it was found that the BE can be reduced by half if a surface layer of 250 μm is removed. A proposed dislocation model first has to be able to explain the following phenomena. (1) work hardening during loading; (2) the maintenance of plastic strain during unloading; (3) the continuation of the same stress-strain curve on reloading as an uninterrupted test.

Since the BE represents an easing of plastic deformation during reverse loading, a reduced BE means either increased resistance to a forward motion or reduced assistance for existing arrays of mobile dislocations to a backward motion. The latter is more likely to occur under a surface layer removal condition. A computer simulation model which was based on a previous computer simulation investigation [33] will be described to account for the changes in the BE due to surface removal.

This 'dislocation model' relies on two major assumptions: (i) that the dislocation motion is controlled by thermally activated jumping over short-range barriers; (ii) that the surface sources can be activated at a lower stress than the interior sources.

The surface source is basically a half-dislocation mill with one end anchored as depicted in Fig. 5. Under an applied shear stress τ_a, the pinned dislocation segment started to expand as a spiral until the leading edge swings to the free surface and a half-circle was gradually formed. A new dislocation segment with one end pinned would be left behind to continue its spiral motion and to keep grinding out more new dislocations under τ_a. The series of half-dislocation loops would continue to expand. Whenever a dislocation meets a short-range barrier, a very local perturbation in the loop shape may occur. As the dislocation keeps advancing, its segment will very soon sweep across the short-range barrier.

For simplicity the dislocation array shown in the side view of Fig. 5 will be considered first. The trailing dislocation segments are repelled by all the other generated dislocations. Once the applied stress becomes larger than the repulsive stress caused by the leading dislocations, new dislocations will continue to be generated. The leading dislocation is being pushed by all the trailing dislocations and thus can go

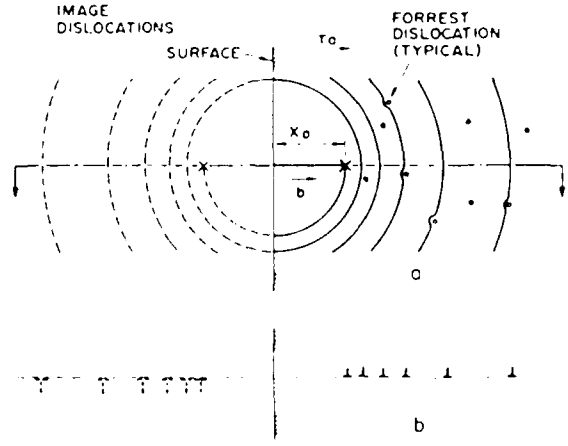

Fig. 5 Schematic diagram of the operation of a dislocation surface source.

the fastest. The trailing dislocation is being repelled by all the leading dislocations and thus will be the slowest moving dislocation. This will eventually lead to an inverse pile-up configuration as shown in Fig. 5. For the surface source case a high dislocation density due to inverse pile-up will develop at the surface. Each dislocation moves forward by thermally activated jumping over a short-range barrier.

For the i^{th} dislocation the activation free energy ΔG_i as a function of effective stress τ_i^* is determined by

$$\Delta G_i = \Delta G_0 \left[1 - \left(\frac{\tau_i^*}{\tau_0^*}\right)^{n_1}\right]^{n_2} \tag{1}$$

where the activation energy ΔG_0 at zero stress and the effective stress τ_0^* are determined experimentally; n_1 and n_2 are determined by fitting the experimentally determined ΔG versus τ^* curves. The effective stress for the i^{th} dislocation at x_i is calculated using a modified version of Head's formula [34] for coplanar parallel edge dislocations under the applied stress τ_a. The line tension term τ_L is included in order to account for the curvature of the loops (because the dislocations near the free surface are not straight) and is estimated to be equal to $Gb/2x_i$:

$$\tau_i^* = \tau_a + \tau_L + A\left[-\frac{1}{2x_i} + \sum_{\substack{j=1 \\ j\neq i}}^{N}\left(\frac{1}{x_i - x_j} - \frac{1}{x_i + x_j} + \frac{2x_j(x_j - x_i)}{(x_i + x_j)^3}\right)\right] \tag{2}$$

where $A = Gb/2\pi(1-\nu)$, N is the total number of dislocations, G is the shear modulus, b is the Burgers vector, x_j is the position of the other dislocations in the array and ν is Poisson's ratio. A new dislocation is generated whenever the effective stress at the source is larger than the source operating stress. As a result, an inverse pile-up is formed under a constant applied stress (Fig. 6(a) and (b)). Further details of the numerical methods have been discussed elsewhere [32].

The velocity of each dislocation was determined by first determining the mean time required to jump a given barrier.

$$\Delta t_{i,q} = t_0 \exp(\Delta G_i/kT) \tag{3}$$

where t_0 is related to the attempt frequency of the dislocation, which in turn equals the ratio of the Debye frequency to the average dislocation span between short-range barriers. Finally the average velocity is defined as follows.

$$\bar{v}_i = \sum_{q=1}^{Q} \Delta L_q \Big/ \sum_{q=1}^{Q} \Delta t_{i,q} \tag{4}$$

where q is a specific barrier, Q is the total number of barriers met and ΔL_q is related to the area moved by the unit length of dislocation in the given thermally activated jump.

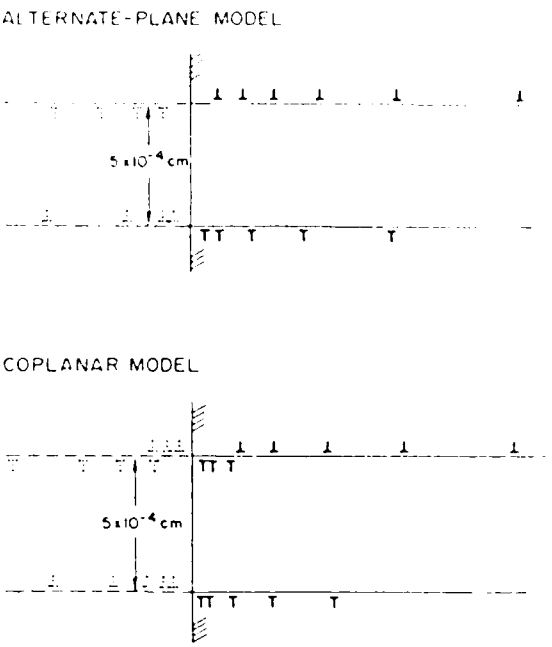

Fig. 6. (a) The alternate-plane model under reverse loading; (b) the upper plane alone is the single-coplanar model, and the two slip planes together are the double-coplanar model.

An approximation was used in order to reduce the computer time involved in the simulations [33]. An empirical equation has been used to approximate the relationship between the dislocation velocity v_i and the effective stress τ_i^* [35].

$$v_i = B(\tau_i^*)^m \tag{5}$$

where B and m are empirical constants.

Equation 5 applies not only to forward-moving dislocations but also to retreating dislocations when the appropriate algebraic sign is used. It is obvious that a single slip plane with coplanar dislocation loops generated during the loading stage cannot represent reverse loading in a reasonable manner because all the existing mobile dislocations will soon be exhausted. Some modifications or extra features must be included in this model.

Basically, as a result of the above experimental observations, two new features were considered in the current model. First, during the reverse loading, new slip planes are activated in addition to the deslipping of the original plane. Second, the same source that generated the original dislocations will create dislocations of the opposite sign under reverse loading. These two arrays of dislocations of opposite sign will move toward each other and become annihilated when they meet. The consideration of these experimental observations leads to several additional models. These additional models are described elsewhere [30].

2.5 Simulation results

The purpose of the computer modelling is to simulate the discrete motion of individual dislocations under a specified condition of multiplication and a governing equation of motion. The present approach is not a numerical solution of an assumed constitutive equation. At any instant, there was a value of applied stress chosen according to whether the test was under a constant applied stress or a constant strain rate. The plastic strain was determined by the summation of all the dislocation displacements. The applied stress divided by the elastic modulus yields the elastic strain. Therefore, at every instant, there was a one-to-one correspondence between the applied stress and the total strain. The total shear strain versus the resolved shear stress curve could thus be constructed.

The basic shapes of the shear stress versus shear strain curves are quite similar for the three models. Therefore, only the single-coplanar case will be presented as an example. As shown in Fig. 7, the elastic portion of the constant-strain-rate loading curve ended at a stress of 0.65 MPa. The loading curve then went through a yield point and gradually work hardened. The loading was stopped when 20 dislocations had been generated from the surface source. The external load was then gradually decreased so as to maintain a constant strain rate in the reverse direction during the unloading stage. The reverse loading portion was basically a continuation of the unloading process until the applied stress became negative, i.e., an applied stress in the reverse direction. The reverse loading curve went through earlier yielding and work hardened without yield point development. The same data plotted as an absolute shear stress versus the accumulative shear strain curve can demonstrate the magnitude of the BE better (Fig. 8).

To determine the effect of surface removal by 'etching', the usual strain curve was simulated to the point of complete unloading. Then the position of the surface was redefined such that a given amount was removed (generally 250 μm). Because the portion removed contained the highest density of dislocations, the number of dislocations on the given slip plane was significantly reduced. After removal, the reverse loading was continued in exactly the same manner as if surface removal had not taken place. Figure 8 shows a reduction in the BE after surface removal. It can be seen that the compression curve after surface removal has an increment of shear stress over the original curve.

All of the models predicted a reduction of the BE strain factor, the minimum being 35% and the maximum 63%.

The agreement between the experimental results and the model predictions are very good.

3 RESIDUAL STRESS

3.1 Experimental results

The composite materials used and the testing procedures are described elsewhere [36]. However, before discussing the experimental results obtained from the BE investigation, we shall briefly define the parameters which were used to measure the magnitude of the BE. Figures 1(a) and (b) are schematic representations of a Bauschinger test. The Bauschinger strain ϵ_B which is used as a measure of the BE when the flow stress in the reverse direction becomes equal to the flow stress at the end of the forward strain (Fig. 1(a)). These curves were obtained

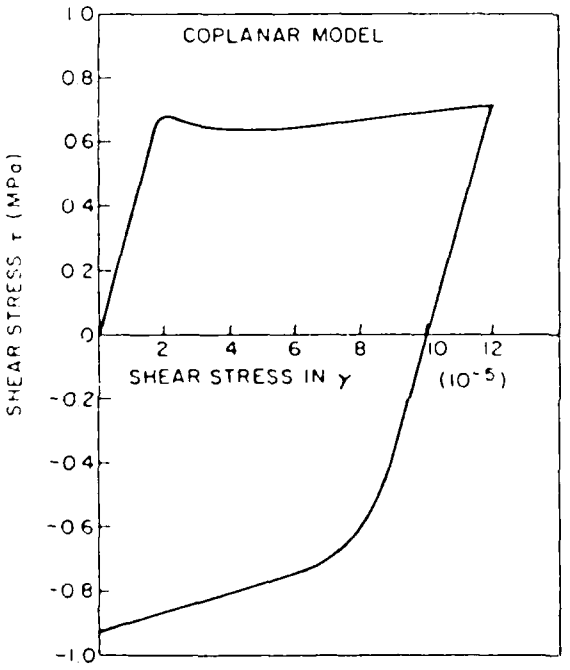

Fig. 7. The shear stress vs. shear strain curve for the single-coplanar model when 20 dislocations have been generated in the loading direction.

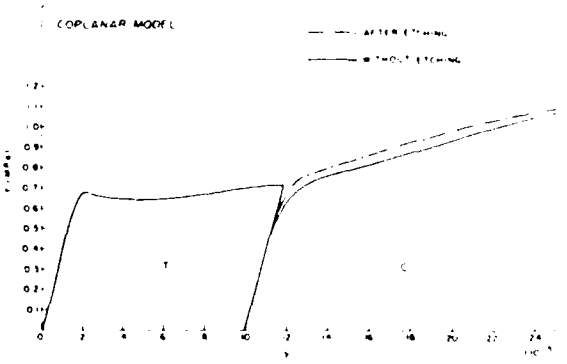

Fig. 8. The absolute shear stress vs. accumulated shear strain curve for the single-coplanar model — — — —, after etching, ————, without etching.

from a test conducted first in tension followed by compression. If there is permanent softening upon reverse loading then the difference between the projected flow stress in the forward direction minus the maximum flow stress in the reverse direction (this difference is defined as the Bauschinger stress) is used to define the magnitude of the BE (Fig. 1(b)). This is a typical result for tension first followed by compression. It is possible that the stress–strain curves may have a complicated shape when a second phase is present [37].

The stress–strain curve upon reverse loading did not have any unusual shape change, their shapes are the same as shown in Fig. 9(a), (b), and (c). Therefore, the model proposed by Asaro [38] based on strong precipitates as the cause of the complicated shape cannot apply to SiC–Al composites, even though SiC particles are equivalent to very strong precipitates. Ideally, it would have been useful to determine the

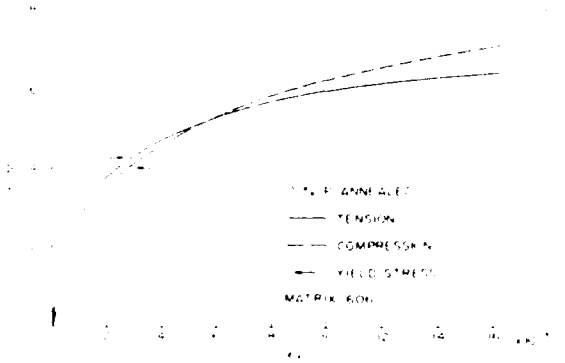

Fig. 9a A plot of the absolute tensile stress vs. the total strain for annealed 0 V% particulate composite samples tested in both tension and compression

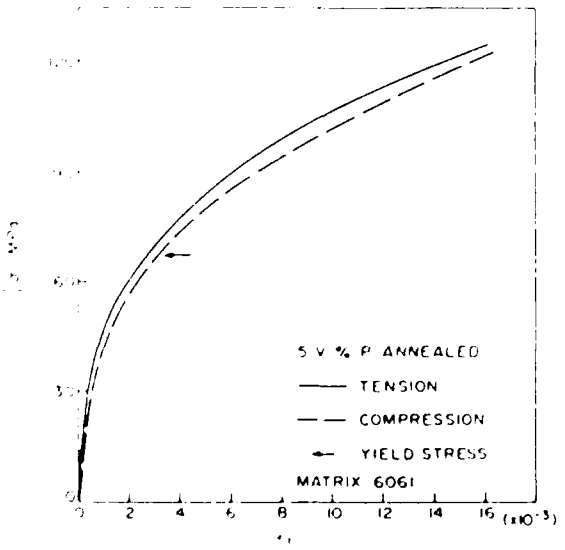

Fig. 9b A plot of the absolute tensile stress vs. the total strain for annealed 5 V% particulate composite samples tested in tension and compression

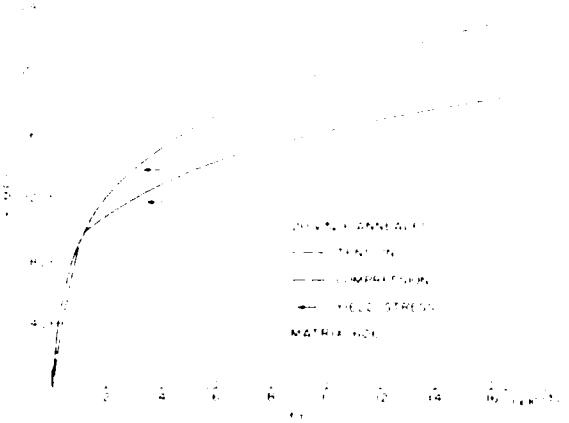

Fig. 9c A plot of the absolute value of the tensile stress vs. the total strain for annealed 20 V% particulate composite samples tested in tension and compression.

effect of strain on the BE. However, this could only be accomplished for the lower volume fractions of SiC. At higher volume fractions of SiC the maximum strain that could be used consistently was a plastic strain of 1.5%. Therefore, this was the strain that was chosen as the forward strain for all tests that are reported here. Some results were obtained as a function of strain, and these were compatible with the previous results, i.e., the BE increased with forward strain.

The BE (Fig. 10) of the 0, 5, and 20 V% whisker composite material is higher than that of the HP and

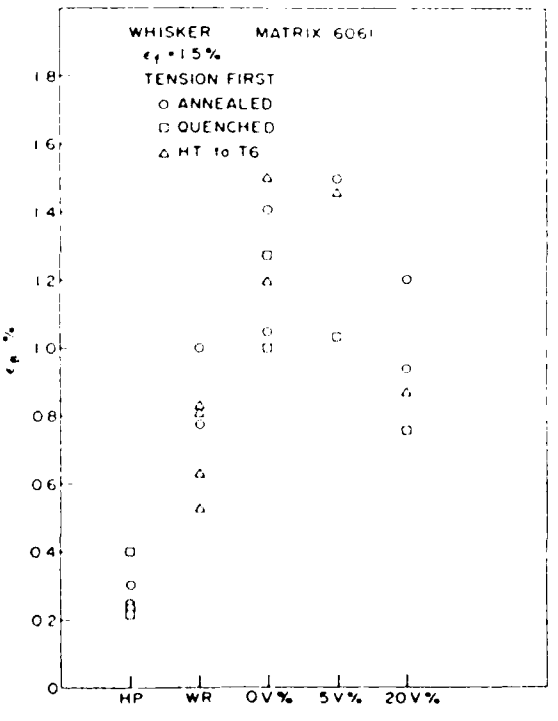

Fig. 10 A plot of the Bauschinger strain vs. volume fraction of whisker composite material. In this case, the tests were initially conducted in tension. Also, plotted is the Bauschinger strain for high purity aluminium and wrought 6061 alloy

WR materials when initially tested in tension. In general, there are two data points plotted for each condition of the material, i.e., 2 for annealed, 2 for quenched and 2 for HT to T6. These two data points cover the range of data obtained. If there is only one data point plotted, this indicates that the range of data was very narrow. From a consideration of the data there is no obvious trend with respect to heat treatment.

If we now consider the case where the initial test was conducted in compression first, then the magnitude of the BE is significantly increased. If the BE strain is plotted (Fig. 11) then the BE strain increase from 1% to 2% to infinity (∞) for the 5 and 20 V% SiC whisker composite. In Fig. 12 are plotted the BE stress value and the BE strain for tests initially conducted in compression. As can be seen, there is somewhat of a general increase in the BE as the volume fraction of SiC increased.

A similar series of experiments were conducted with particulate SiC-Al composites. Figure 13 is a plot of particulate SiC in 6061 Al matrix for the case of initially tested in tension. As the results were obtained for the whisker material, there is no obvious increase in the Bauschinger strain with an increase in volume fraction of the particulate. Secondly, the Bauschinger strain is about the same for the 20 V% material as compared to the wrought 6061 material and, as before, the Bauschinger strain of the HP material is less than that of the 20 V% material. Again, as in the case of the whisker composite material (Fig. 14), the magnitude of the BE increased when the test was initially conducted in compression. And again there is an increase in the BE as the volume increases.

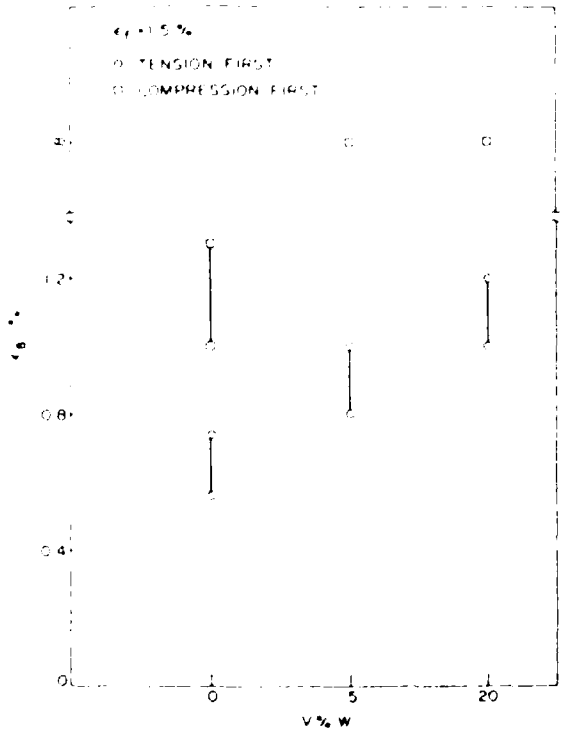

Fig. 11 A plot of the Bauschinger strain vs. volume fraction of whisker composite of a 6061 alloy matrix for both tension-first and compression-first testing.

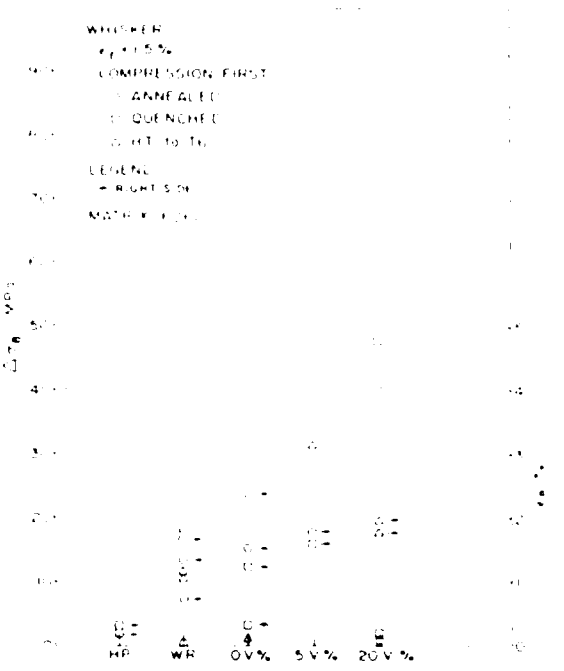

Fig. 12 A plot of the Bauschinger stress factor vs. volume fraction of whisker composite material and the Bauschinger strain vs. volume fraction. Also plotted are the values obtained for high purity aluminium and wrought 6061 alloy.

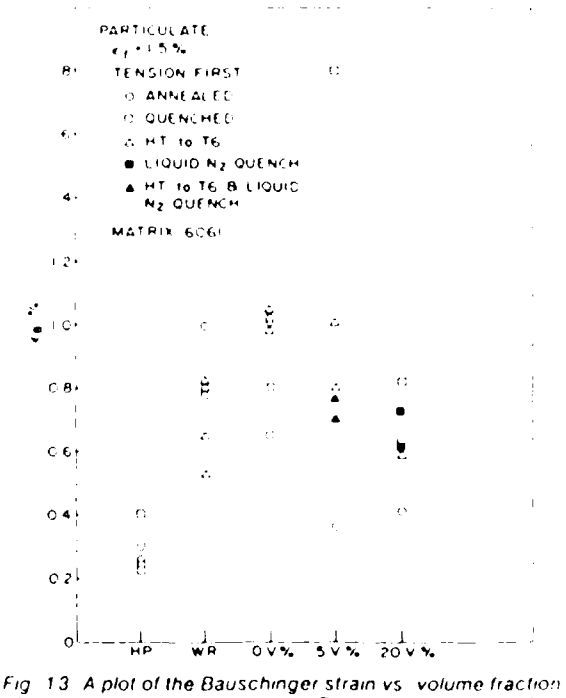

Fig. 13 A plot of the Bauschinger strain vs. volume fraction of particulate composite material. These are for tension-first results. Also plotted are the results obtained from high purity aluminium and wrought 6061 alloy material.

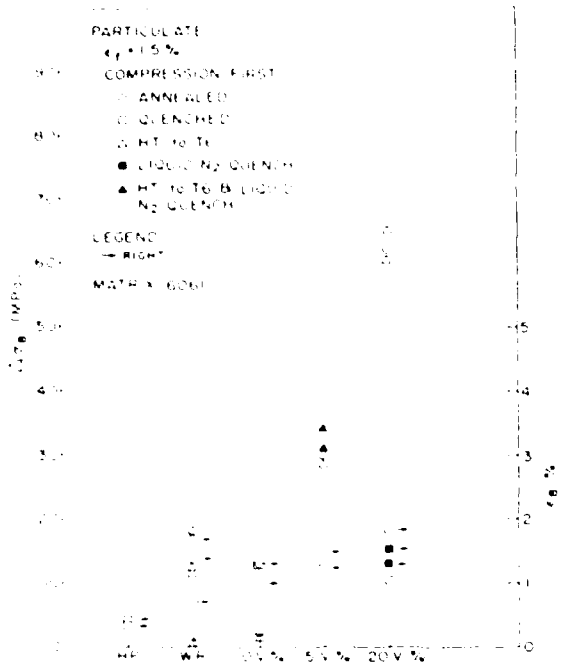

Fig. 14 A plot of the Bauschinger stress factor and Bauschinger strain for compression-first test of particulate composite material and for high purity aluminium and wrought 6061 alloy

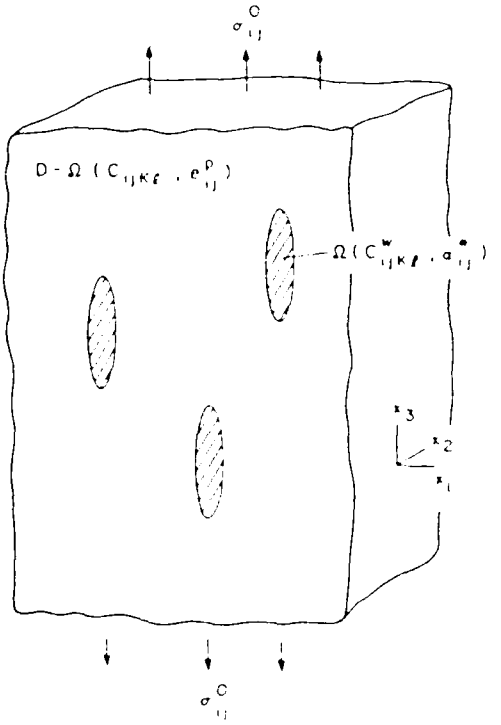

Fig. 15 Theoretical model, actual case

3.2 Model

The theoretical model developed was based on Eshelby's equivalent inclusion model. Mori and his co-workers [39-41] extended Eshelby's method to predict the yield stress (σ_y) and work-hardening rate of aligned short whisker composites. Wakashima et al. [42] extended the above approach to predict σ_y by considering the mismatch of the thermal expansion coefficients of the matrix and whisker. Following the above models, Takao and Taya [43] have recently computed the stress field in and around a short fiber in a short-fiber composite where the whisker is anisotropic both in stiffness and thermal expansion.

Consider an infinite body (D) which contains ellipsoidal whiskers (Ω) aligned along the x_3-axis (Fig. 15). This composite body D is subjected to the applied stress field σ^0_{ij}. The stiffness tensors of the matrix (D−Ω) and fiber (Ω) are denoted by C_{ijkl} and C^f_{ijkl} respectively. Following Eshelby, the transformation strain [44] or eigenstrain [45] is given in the fiber domain Ω as σ^*_{ij}, the strain due to the mismatch of the thermal expansion coefficients and the uniform plastic strain ε^p_{ij} is prescribed in the matrix [39]. As far as the stress field is concerned, the model of Fig. 16 is equivalent to that of Fig. 15. Thus, the present problem is reduced to the 'inhomogeneous inclusions problem' (Fig. 16) [45]. The model of Fig. 15 will be used not only to predict the yield stress and work-hardening rates, but also to compute the thermal residual stresses. For the latter case, we will set $\sigma^0_{ij} = e^p_{ij} =$

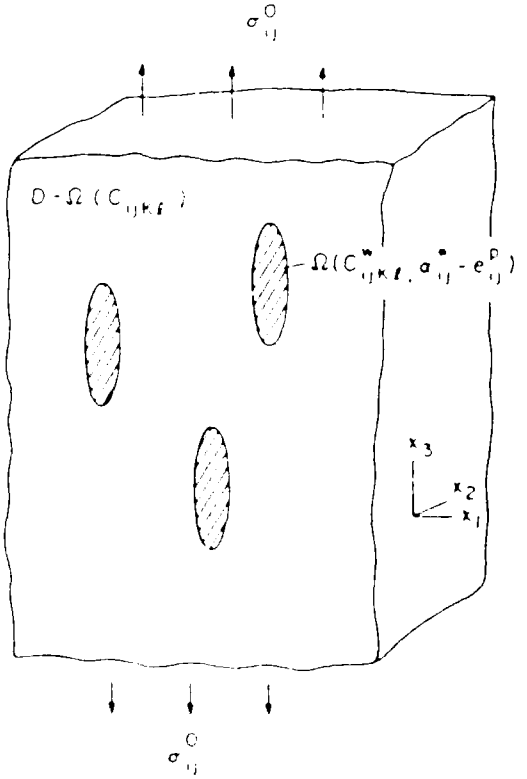

Fig. 16 The equivalent inclusion model converted from Fig. 15

0. Further details of the model will be published elsewhere [31].

The above model as applied to the BE predicts that there would be a difference in the magnitude of BE depending on the direction of initial testing. The model predicts a larger BE if the sample is initially tested in compression. Also the model predicts that the magnitude of the BE should increase with increasing volume fraction of reinforcement. There is an assumption in the application of the Arsenault-Taya model to the BE, that plastic deformation does not significantly reduce the elastic residual stress. The experimental evidence obtained in this investigation suggests that this is a valid assumption.

The predicted difference in the BE due to the direction of the test is simply due to the average elastic residual tensile stress. The flow stress in tension is reduced due to the average tensile residual stress. The difference in BE due to the direction of the test is not related to a difference in dislocation configurations that may occur as a result of initially testing in tension or compression.

4 CONCLUSIONS

Surface removal has an effect on the Bauschinger effect. The experimental results on both the Bauschinger stress factor and the Bauschinger strain factor agree with the computer simulation results very well. The agreement is within 10%, especially for the single- and double-coplanar models. Although the BE was not completely removed by the surface removal, the results show that the surface layer is the dominant factor in determining the BE in the early stages of deformation.

There are differences between the stress–strain curves obtained experimentally and those obtained by simulation: a yield point exists in the simulated curves. It is known that high-purity single crystals with a nearly perfect structure will develop a yield point at the initiation of a constant-strain-rate plastic deformation [46]. This development is due to a sudden increase in the mobile dislocation density. The samples used in the present investigation did not fit the requirement of the existence of such a yield point. However, in the simulation the sample has a low initial dislocation density and thus showed a yield point.

The experimentally observed BE was affected by surface removal provided that the sample was deformed a small amount, i.e. less than 2% plastic strain. When the sample was deformed more than 5%, the magnitude of the BE increased, but the effect of surface removal on the BE decreased. This decrease was due to the number of operating sources in the interior of the sample which contributed to the BE. As the surface is removed, the relative change in the magnitude of the BE is thus smaller. In the computer simulation modelling, no such internal sources were considered.

All the simulation models successfully demonstrated that the BE exists and that a consideration of a periodic internal stress will enlarge the BE. The surface removal of 250 μm reduces the Bauschinger stress factor by 8.7%–30% and the Bauschinger strain factor by 35%–62.8%.

Arsenault and Taya [31] developed an analytical theory which predicts that there will be an average tensile residual stress in a SiC-Al composite sample. The SiC has to be in the form of aligned whiskers or platelets. If the SiC is spherical then there is zero average residual tensile stress. If it is assumed that the average tensile residual stress is not significantly reduced by plastic deformation then the larger Bauschinger effect for the case of an initial test in compression followed by tension is explained simply as a result of the residual tensile stress.

ACKNOWLEDGEMENT

The research was supported by the Office of Naval Research Grant No. N0014-85-K-0007.

REFERENCES

1. J. Bauschinger, *Civiling.*, 1881, **27**, 289
2. A. H. Cottrell, *Dislocations and Plastic Flow in Crystals*, 1953 (Oxford), p. 114
3. G. E. Dieter, *Mechanical Metallurgy*, 1976 (McGraw-Hill, New York), p. 144
4. H. G. VanBueren, *Imperfections in Crystals*, 1960 (North-Holland, Amsterdam), p. 240
5. S. N. Buckley and K. M. Entwistle, *Acta Metall.*, 1956, **4**, 352
6. E. Orowan, *Internal Stress and Fatigue of Metals*, 1960 (Elsevier, Amsterdam), p. 240
7. F. A. McClintock and A. S. Argon, *Mechanical Behavior of Materials* (Addison-Wesley, Reading, MA), p. 185
8. O. B. Pederson, L. M. Brown, and W. M. Stobbs, *Acta Metall.*, 1981, **29**, 1843
9. R. L. Wooley, *Philos. Mag.*, 1953, **44**, 597
10. H. Mori and H. Fujita, *Mater. Sci. Eng.*, 1974, **13**, 41
11. P. Charsley and M. P. E. Desvaux, *Mater. Sci. Eng.*, 1969, **4**, 211
12. N. Ibrahim and J. D. Embury, *Mater. Sci. Eng.*, 1975, **19**, 147
13. G. D. Moran and J. D. Embury, *Acta Metall.*, 1979, **27**, 903
14. M. S. Paterson, *Acta Metall.*, 1955, **3**, 491
15. D. S. Kemsley and M. S. Paterson, *Acta Metall.*, 1960, **8**, 453
16. W. L. Phillips, Jr., *Trans. AIME*, 1962, **224**, 845
17. M. P. E. Desvaux and P. Charsley, *Mater. Sci. Eng.*, 1969, **4**, 221
18. R. C. Daniel and G. T. Horne, *Metall. Trans.*, 1971, **2**, 1161
19. K. Marukawa and T. Sanpei, *Acta Metall.*, 1971, **19**, 1161
20. H. Mori and H. Fujita, *J. Phys. Soc. Jpn.*, 1975, **38**, 1342
21. E. H. Edwards, J. Washburn and E. R. Parker, *Trans. AIME*, 1953, **197**, 1525
22. T. Kishi and I. Gokyu, *Metall. Trans.*, 1973, **4**, 390
23. S. P. Gupta and S. P. Kodali, *Scr. Metall.*, 1976, **10**, 111
24. G. D. Moran and J. D. Embury, *Scr. Metall.*, 1977, **11**, 925
25. T. Kishi and T. Tanabe, *J. Mech. Phys. Solids*, 1973, **21**, 303
26. S. T. Rolphe, R. P. Haak and J. H. Gross, *J. Basic Eng.*, September 1968, 403

27 C. C. Li, J. D. Plassk, J. A. Yasen and W. C. [illegible] *Metall. Trans. A*, 1978, **9**, 85
28 N. H. Polakowski, *Proc., ASTM*, 1963, **63**, 535
29 S. Mador, A. Seeger and C. Lotz, *J. Appl. Phys.*, 1963, **34**, 3368
30 R. Hsu and R. J. Arsenault, *Mat. Sci. Eng.*, 1984, **66**, 35
31 R. J. Arsenault and M. Taya, *Proceedings of ICCM 5*, 1985, ed. by W. Harrigan, San Diego, p. 21, *Acta Metall.*, 1987
32 R. Hsu, Ph.D. Thesis, University of Maryland, 1982
33 R. J. Arsenault and R. Hsu, *Metall. Trans. A*, 1982, **13**, 1199
34 A. K. Head, *Proc. Phys. Soc., London, Sect. B*, 1953, **66**, 793
35 W. G. Johnston and J. J. Gilman, *J. Appl. Phys.*, 1959, **30**, 129
36 R. J. Arsenault and S. B. Wu, to be published
37 T. [illegible] Hatayetoglu, P. N. Pita and V. I. [illegible], *Mat. Sci. and Eng.*, 1985, **73**, 65
38 R. J. Asaro, *Acta Met.*, 1975, **23**, 1255
39 K. Tanaka and T. Mori, *Acta Metall.*, 1970, **18**, 931
40 K. Tanaka, K. Wakashima and T. Mori, *J. Mech. Phys. Solids*, 1973, **21**, 207
41 S. C. Lin, T. Mura, M. Shibata and T. Mori, *Acta Metall.*, 1973, **21**, 505
42 K. Wakashima, S. Kurihara and S. Umekawa, *Japan Soc. Comp. Mater.*, 1976, **2**, 1
43 Y. Tanao and M. Taya, *J. Appl. Mech.*, under review
44 J. D. Eshelby, *Proc. Roy. Soc., London*, 1957, **A241**, 376
45 T. Mura, *Micromechanics of Defects in Solids*, 1982 (Martinus Nijhoff Publishers)
46 K. Kamada and B. T. Tanner, *Philos. Mag.*, 1974, **29**, 369

Materials Science and Engineering, *81* (1986) 175–187

Dislocation Generation Due to Differences between the Coefficients of Thermal Expansion

R. J. ARSENAULT and N. SHI

Engineering Materials Group, and Metallurgical Materials Laboratory, University of Maryland, College Park, MD 20742 (U.S.A.)

(Received January 30, 1986)

ABSTRACT

There have been several investigations of the elastic stresses and strains generated about an inclusion, which has a coefficient of thermal expansion different from that of the matrix, as a result of heating or cooling. Also, there have been a few investigations of the magnitude of the plastic strain and the plastic zone under the above conditions wherein the plastic deformation induced by the difference between the thermal expansion coefficients was treated in a continuum manner. Since individual dislocation motion was not considered, the dislocation arrangement and densities cannot be specified by the above-mentioned investigations. Therefore, an in situ transmission electron microscopy investigation was undertaken of dislocation generation at the inclusions due to the differential thermal contraction. A simple model based on prismatic punching was developed to account for the relative dislocation density due to the differential thermal contraction.

1. INTRODUCTION

Arsenault and Fisher [1] proposed that the increased strength observed in Al-SiC composites could be accounted for by a high dislocation density in the aluminum matrix, as observed in transmission electron microscopy (TEM) samples taken from bulk composite material annealed for as long as 12 h at 810 K (Fig. 1). In this investigation a representation of at least three Burgers vectors was found in any given location. Also, it was observed that for intermediate or small particle spacings a subgrain structure existed with the subgrain diameter about equal to the inter-particle spacing. However, for very large SiC particles (250 μm) the subgrain size is much smaller than the inter-particle spacing (Fig. 2).

The dislocation generation mechanism proposed by Arsenault and Fisher to account for this high dislocation density is based on the large difference (10:1) between the coefficients of thermal expansion of aluminum and SiC [2]. Therefore, when the composite is cooled from the elevated temperatures of annealing or processing, misfit strains which are sufficient to generate dislocations occur because of differential thermal contraction at the Al-SiC interface.

Chawla and Metzger [3], in an elegant investigation of Cu-W composites using etch-pitting techniques, observed a high dislocation density at the Cu-W interface which decreased with increasing distance from the interface. They observed that, if the volume fraction of tungsten was 15%, the minimum dislocation density in the matrix was $7 \times 10^{11}\,m^{-2}$, increasing to $4 \times 10^{12}\,m^{-2}$ at the Cu-W interface and concluded that the dislocations were caused by the difference (4:1) between the thermal expansion coefficients of copper and tungsten. Recalling that the difference between the thermal expansion coefficients of aluminum and silicon carbide is 10:1, *i.e.* more than twice as great as in the Cu-W system, we would expect thermal stresses in Al-SiC to be certainly sufficient to generate dislocations also in this composite.

Other causes may also contribute to the high dislocation density observed in annealed Al-SiC material. Specifically, dislocations are introduced into this material during the

0025-5416/86/$3.50

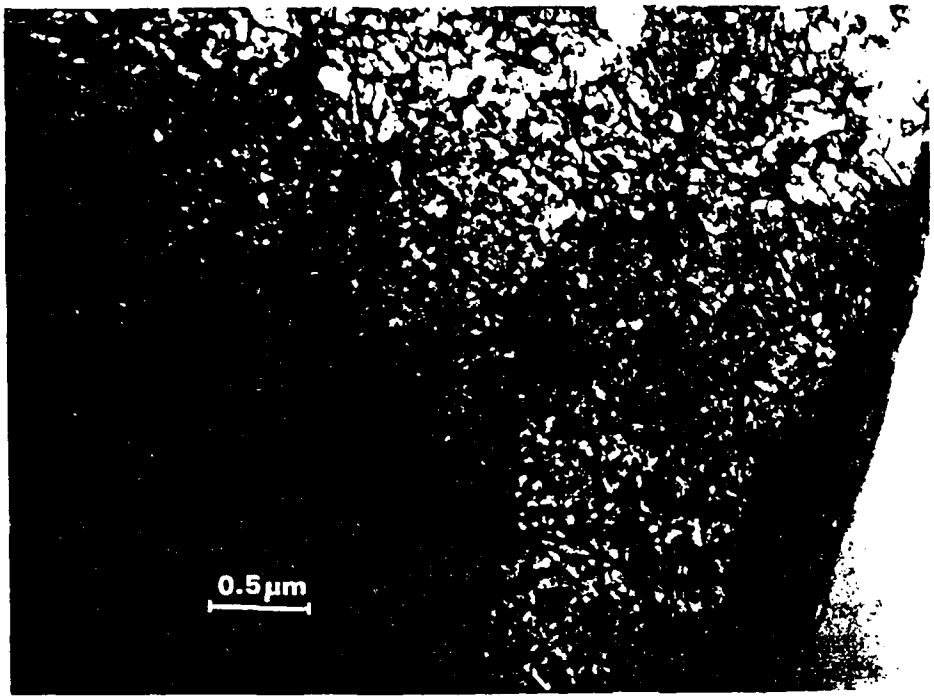

Fig. 1. A micrograph from a TEM foil taken from a bulk sample with 20 vol.% SiC, which was annealed for 12 h at 810 K and furnace cooled. The right-hand side of the micrograph is an SiC particle and to the left is the matrix material containing a high dislocation density.

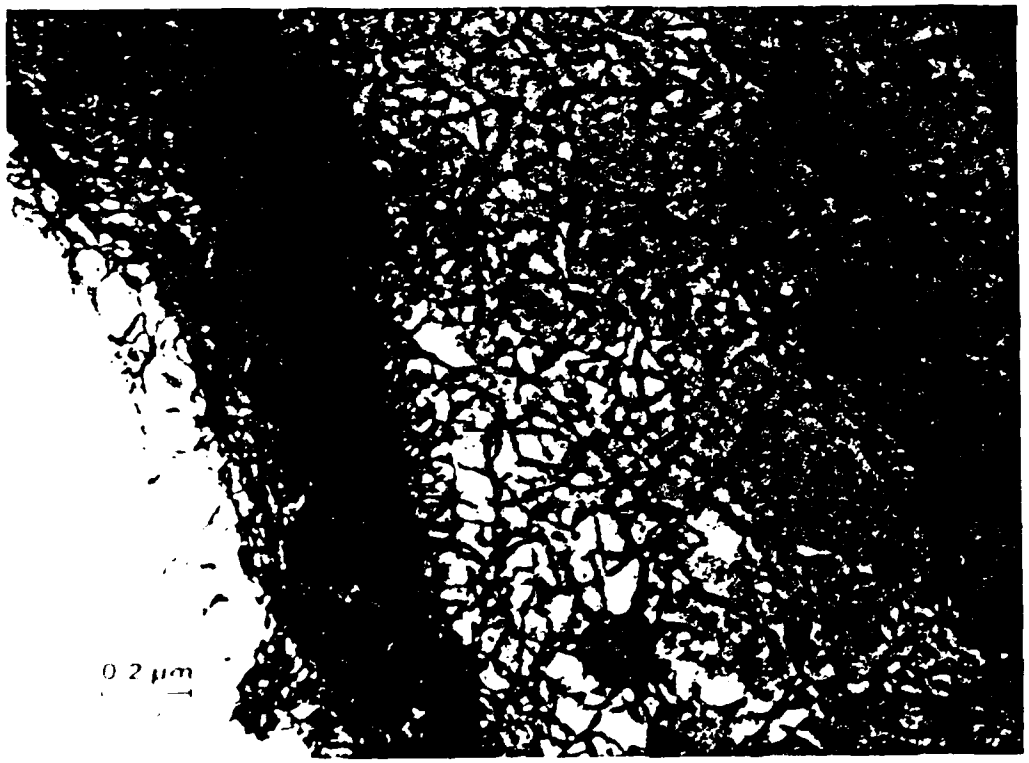

...ary in a composite with 250 μm SiC particles in an aluminum alloy 1100 matrix about ... A second subgrain boundary was found some 2-7 μm from the SiC particle, which is ... material

plastic deformation processes of manufacturing, such as extrusion. During annealing, these dislocations might not be annihilated but could be trapped by the SiC, resulting in a high dislocation density even after annealing.

It is important to determine the origins of the high dislocation density in the composite since the strength of the composite is affected by that high density. If it is not the above alternative process but it is indeed differential thermal contraction that is the cause of the dislocations, as Arsenault and Fisher [1] have suggested, then the generation of dislocations should be observed in composite thin foil samples on cooling from annealing temperatures in an *in situ* high voltage electron microscopy (HVEM) experiment. The present paper is the record of such a test.

In situ dynamic HVEM experiments have certain advantages over other experimental techniques. The major advantage is that direct observation of the alteration of a microstructure by a dynamic process is possible while a deforming force, in this case a thermal stress, is operating. Operating at higher voltages allows penetration of thicker samples so that surface effects are minimized and bulk behavior is more closely approximated. Also, a high voltage microscope can better accommodate special stages required for *in situ* work because of the large pole piece region.

Previously, several theoretical investigations had been undertaken to predict the magnitude of the plastic strain in the plastic zone around a particle, as follows: the relaxation of the misfit caused by the introduction of an oversized spherical particle into a spherical hole in the matrix was analyzed by Lee *et al.* [4]. Using the misfitting sphere model, they calculated strains in the plastic zone that surround a hard sphere and also the plastic zone radius.

Hoffman [5] calculated the overall total strains in a tungsten-fiber-reinforced 80Ni-20Cr matrix, using a thick wall, long cylinder model and assuming that a hydrostatic stress state exists within each constituent.

Garmong [6], assuming uniformity of stresses and strains in the matrix, calculated deformation parameters for a hypothetical eutectic composite and reported values of matrix plastic strains of the order of 0.4%.

Dvorak *et al.* [7] developed a new axisymmetric plasticity theory of fiber composites involving large thermal changes. The long composite cylinder model was adopted as a composite unit cell, and microstress distribution as well as yielding surfaces were obtained for Al-W composites.

Mehan [8] calculated residual strains in an Al-α-Al_2O_3 composite due to cooling from the fabricating temperature. He considered an idealized composite consisting of a long sapphire cylinder surrounded by an aluminum matrix, *i.e.* equivalent to the long cylinder composite model used by Dvorak *et al.*

None of the above models predicts the local dislocation density or the average dislocation density. Correspondingly, as they are not capable of predicting dislocation densities, then predictions of arrangements of dislocations are certainly not possible from these theories.

The purpose of this investigation of temperature cycling samples in the high voltage electron microscope was to fill this gap in our knowledge and to determine whether dislocation generation occurs at the Al-SiC interface on cooling a composite from annealing temperatures. The subsequent theoretical analysis tests whether a simple model of dislocation generation during cooling based on prismatic punching can account for the experimental results.

2. MATERIAL

The Al-SiC composite with 20 vol.% SiC in aluminum alloy 6061 (together with an aluminum alloy 6061 sample with no SiC as a control sample) was purchased from DWA (Chatsworth, CA); the SiC was of platelet morphology. The platelets are 5-7 μm long and have an aspect ratio D/t, where t is the thickness of the platelet and D is the diameter, of 2-3. This composite is a powder metallurgy product supplied in the form of a plate. As a second control material, wrought aluminum alloy 1100 in the form of a rod 12.5 mm in diameter was purchased from ALCOA (Aluminum Company of America) and tested in the as-received condition.

3. SAMPLE PREPARATION AND EXAMINATION PROCEDURE

An ion-milling technique was required for the production of TEM samples on account of the SiC in the aluminum matrix.

The two types of composite, *i.e.* the powder-compacted aluminum alloy 6061 matrix with 20 vol.% SiC and the control with no SiC, were machined into rods (12 mm in diameter and 4 cm long), annealed for 12 h at a solutionizing temperature of 810 K and furnace cooled. After annealing, slices of 0.76 mm thickness were cut by electric discharge machining at 80–100 V.

Deformation damage from electric discharge machining is estimated to extend 0.20 mm beneath the surface [9, 10]. Therefore the slices were fixed to a brass block with double-sided tape and surrounded by brass shims and then mechanically thinned on a rotating water-flooded wheel covered with 400 and then 600 grit paper to remove the electric discharge machining damage and to reduce the thickness of the slices to approximately 0.127 mm. Final thinning was carried out using argon ion plasma bombardment, operating at 6 kV, at an ion current of 50 μA and a sample inclination of 15° to the ion beam. For these operating parameters the projected range or average distance that the argon ion travels into the foil is only 20 nm [11, 12]. As Dupuoy [13], who conducted an *in situ* ion thinning experiment on iron and Al–Ag specimens using a 3 MV microscope, showed, dislocation arrangements and microstructures in Al–Ag and iron are not altered by ion thinning, even though some point defects are introduced into the near-surface region of the sample by ion bombardment. Therefore, it may be concluded that ion milling does not introduce or remove dislocations in the present TEM foils, either.

The aluminum alloy 1100 control samples were prepared from the as-received wrought rod in the same manner as the Al–SiC composite samples, except that electropolishing was employed instead of ion thinning.

The thinned samples were observed in the high voltage electron microscope operating at 800 kV with a beam current of 2.3 μA. A double-tilt side-entry furnace type of heating stage was used to heat the specimens. While being observed in the microscope, the samples were heated to 800 K, held at that temperature for 15 min and then cooled to ambient temperature. Subgrains exhibiting dislocations in contrast were chosen for observation. During heating and cooling, thermal drift of the stage and thermal expansion and contraction of the sample caused the chosen subgrain to move. In order to maintain the same subgrain in the field of view at the same crystallographic orientation, it was therefore necessary to translate slightly and to tilt the specimen almost continuously. Since changing to selected area diffraction conditions during cycling to monitor the orientation would have resulted in loss of the chosen area from the field of view, the orientation was maintained constant by monitoring the contrast of some specific microstructural features such as a subgrain boundary or Al–SiC interface in the bright field mode.

One thermal cycle required about 1 h, and most of the samples were observed throughout several thermal cycles. The thickest regions of the sample penetrated by the beam were chosen for observation, and at an operating voltage of 800 kV the beam is known to penetrate aluminum 0.8 μm thick [14].

The dislocation density ρ was determined by a line intercept method adapted from that of Hale and Henderson-Brown [15]. A grid of lines is placed over the TEM micrograph, and the intersections of dislocation lines with the grid lines are counted. The dislocation density ρ is given by

$$\rho = \frac{2N}{LT}$$

where N is the number of dislocation intersections with the grid lines, L is the length of the grid lines divided by the magnification and T is the thickness of the sample (in our case, 0.8 μm), while the length of the grid lines was 0.58 m. Each reported dislocation density is an average value obtained from three to ten micrographs.

4. EXPERIMENTAL RESULTS

The discussion of the experimental results pertains to the three materials tested:

aluminum alloy 6061 with no SiC, aluminum alloy 6061 with 20 vol.% SiC, and aluminum alloy 1100 rod. In all cases, typical results will be described. A total of 300 micrographs were taken.

4.1. The controls, aluminum alloy 6061 with no SiC, and aluminum alloy 1100

The aluminum alloy 6061 control sample with no SiC had a large subgrain size (approximately 5 μm) and a low dislocation density (8×10^{12} m^{-2}) (Fig. 3(a)). A few of the larger second-phase precipitate particles (Mg_2Si) were surrounded by dislocation tangles bowing out from the precipitate interface (Fig. 3(b)). On heating, the dislocations began to move in the sample, migrating away from the particles. Similarly, dislocations were also generated in other areas of the subgrain and moved through the matrix, occasionally being pinned by precipitate particles. Eventually, at elevated temperatures (670 K), all the dislocations disappeared. Slip traces left behind when the dislocations moved also disappeared at temperatures close to 700 K, possibly because of surface diffusion. After the sample was held at 800 K for about 15 min, it was cooled down again.

The image tended to be out of focus at high temperatures because of thermal drift of the stage. On cooling, dislocations reappeared at the large particle interfaces at about 500 K. Sometimes these moved faster than could be seen individually. The dislocations formed tangles in the vicinity of the precipitate while most of the matrix did not accumulate any dislocations (Fig. 3(c)). Only a few dislocations were generated about the precipitates (Fig. 3(d)).

The aluminum alloy 1100 sample had a dislocation density initially of 4×10^{12} m^{-2}, and a large subgrain size of 5 μm (Fig. 4). Relatively thick regions containing few precipitates were chosen for observation. On heating, most of the dislocations had disappeared by 673 K. At this temperature, the heating stage mechanism failed; therefore, the sample never reached 800 K, but heating had been sufficient to remove the dislocations from the area under observation. The dislocations in this area did not return on cooling, except for a few which were connected to precipitate particles (Fig. 5).

Fig. 4. Wrought aluminum alloy 1100 control sample in the as-received condition. Before in situ thermal cycling, this control sample with no SiC had a high dislocation density. Like the aluminum alloy 6061 control, this sample has a large subgrain size, and the dislocations present are often associated with precipitates.

4.2. 20 vol.% SiC composites

In the 20 vol.% SiC platelet samples (Fig. 6(a)), most of the dislocations disappeared on reaching 650 K (Fig. 6(b)) and the dislocations reappeared on cooling (Figs. 6(c) and 6(d)). In the cases where the Burgers vectors of the dislocations were determined, it was found that in general three different Burgers vectors could be found in a given location, on either side of the platelet. However, certain aspects of the microstructural alterations on cooling were surprising in these platelet samples; in the first cycle, the dislocations disappeared and then reappeared on cooling, whereby at least one (unusual) subgrain was observed to be filled with slip traces. The area of that subgrain was chosen as the area of focus from then on and it was seen that the parallel lines disappeared on heating. Then,

Fig. 5. The same areas in Fig. 4 after *in situ* thermal cycling. In the absence of SiC, few dislocations reappear in a thermally cycled sample; the few dislocations present are associated with second-phase precipitate particles.

on subsequent cooling, packets of slip traces appeared to emanate from the SiC platelet. The slip traces formed in three directions at angles of about 82° and 45° to each other and were associated with newly generated dislocations. At deep slip traces the dislocations causing them had moved too quickly to be seen individually. From those deep slip line traces the important conclusion can be drawn that some kind of dominant dislocation generator must have been responsible for the dislocation generation in specific locations. This effect is explained below through a simple theoretical model. After the third thermal cycle, many (rather than only isolated) subgrains were filled with slip traces originating at the SiC platelet interface.

4.3. Dislocation densities

The dislocation densities of all samples before and after *in situ* annealing are shown in Table 1. When subgrains with slip lines (out of which heavy dislocation losses occurred) are disregarded, the densities are higher in the 20 vol.% SiC composite samples than in the control samples, both before and after *in situ* thermal cycling. However, the dislocation densities listed are lower limit densities since there was difficulty in taking selected area diffraction patterns of a given subgrain and then tilting to a specific reflection, *e.g.* [420], and assuring that the same orientation was maintained throughout. Therefore the reported densities could be as low as one-half to one-third of the actual densities [16].

As expected, the distribution of the dislocations within the samples was not uniform, in that there was a higher density near the SiC particles. Also, greater dislocation generation was observed at larger SiC platelets than at the smaller ones, and more dislocations were generated at the ends of the SiC platlets, where plastic strain during cooling is greatest, than at the middle of the platelet. Also, as already implied by the above observations, in these composite samples there was a significant number of dislocations which escaped from the surface, leaving only slip lines.

As a consequence of all the dislocation generation at the platelet surfaces, there is a theoretical possibility of void formation at the Al–SiC interface. However, no voids were observed in any of the samples.

5. THEORETICAL MODEL

A simple model based on prismatic punching was adopted with the following assumptions.

(1) Both SiC and aluminum were assumed to be elastically isotropic (which they are not) but the effect of anisotropy is small.

(2) The resolved shear stress required to move a dislocation is very small. (This is reasonable, for the dislocation motion occurs at relatively high temperatures and thus low frictional stresses.)

(3) The SiC reinforcement is assumed to be parallelepiped particles.

(4) Prismatic punching is assumed to occur equally on all faces of the particles.

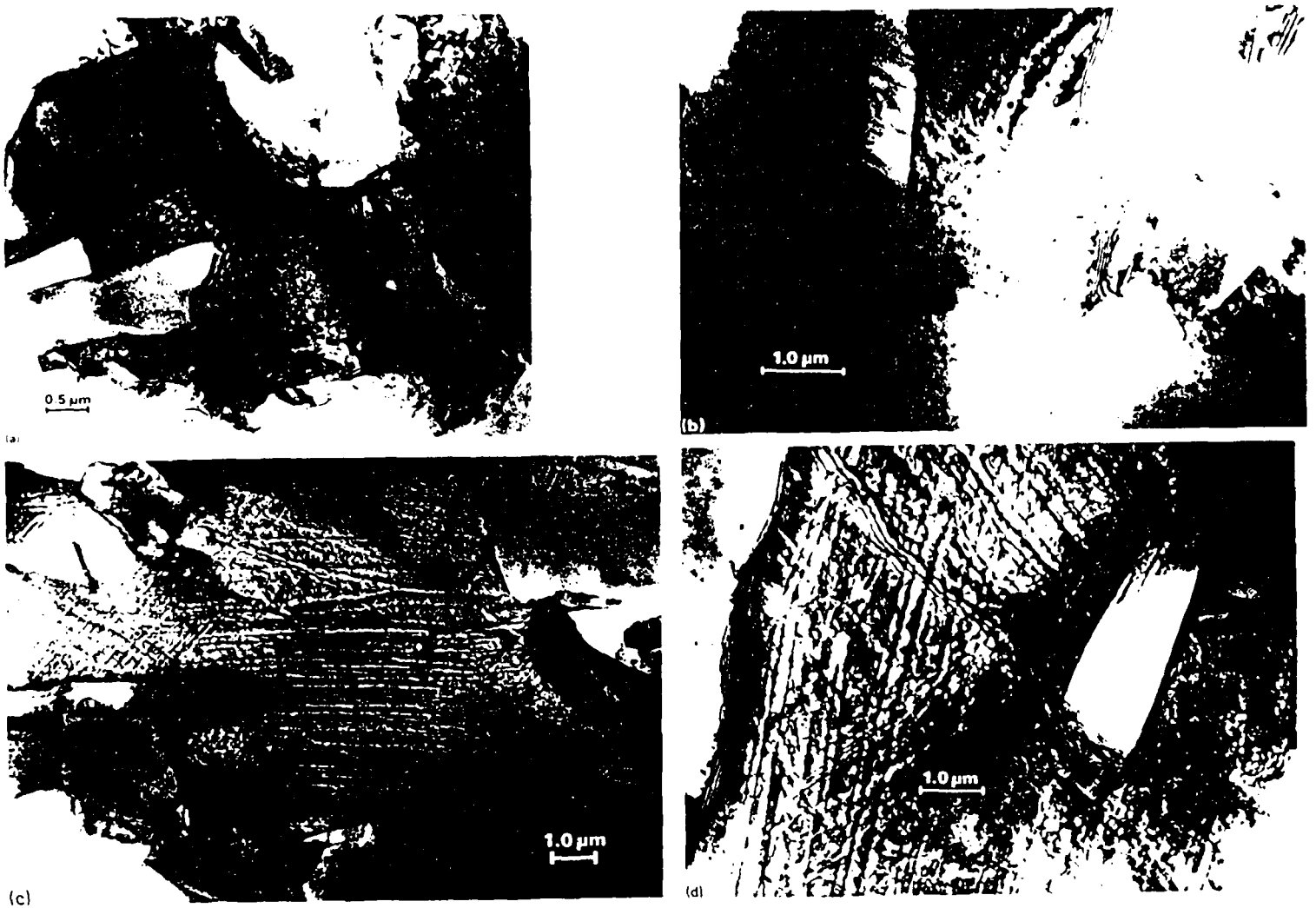

Fig. 6. (a) The diffraction contrast of the high dislocation density in the central subgrain darkens the subgrain in this 20 vol.% SiC platelet composite. The subgrain is surrounded by at least three irregularly shaped SiC platelets which are approximately the same size as the subgrain. (b) During heating to 650 K, most of the dislocations disappeared from the sample. The pebble-like second-phase precipitates can be clearly distinguished here. The same area is shown in (d) filled with slip traces. (c) On cooling to 340 K, dislocations reappeared, resulting in the formation of dense slip traces showing the paths of the dislocations as they moved across or out of the sample. (d) This is the same area as shown in (b) after cooling to 340 K. The area was free of almost all dislocations at high temperatures. The subgrain is now filled with slip traces and dislocations. The slip traces are clearly associated with the SiC platelets, indicating that the origin of the dislocations seen in the sample at low temperatures is at the Al-SiC interface.

TABLE 1

Dislocation density before and after thermal cycling of samples

Sample	*Dislocation density* (m^{-2})	
	Before thermal cycle	*After thermal cycle*
Al alloy 6061 - 20 vol.% SiC platelet[a]	2.0×10^{13}	1.0×10^{13} [b]
Al alloy 6061 control[a]	8.0×10^{12}	6.4×10^{12}
Al alloy 1100[c]	4.0×10^{12}	5.3×10^{11}

[a] Bulk annealed for 12 h at 800 K.
[b] Subgrains without slip lines.
[c] As-received wrought alloy.

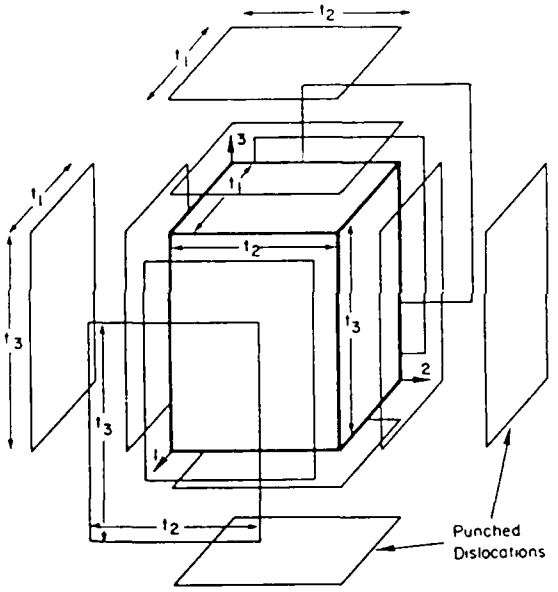

Fig. 7. A schematic diagram of the particle and several prismatic punched dislocations.

Let us consider a composite material strengthened by parallelepiped particles of height t_1, width t_2 and thickness t_3 (Fig. 7) [17]. The misfit strain due to the difference ΔCTE between the thermal coefficients of expansion of aluminum and SiC is

$$\epsilon = \frac{\Delta t_i}{t_i} = \Delta\mathrm{CTE} \times \Delta T \tag{1}$$

where ΔT is the difference between the previous annealing and test temperatures. If we consider the dislocation generation by prismatic punching, then the total number of dislocation loops may be expressed as

$$N_i = t_{ii} \frac{\epsilon}{b} \tag{2}$$

where N_i is the number of prismatic loops punched in the ith direction, ϵ is the misfit strain, b is the length of the Burgers vector and t_{ii} is the contribution of particle height in the ith dimension in punching a dislocation along the same direction. It is believed that, by taking account of dislocation back stress and dislocation interaction, t_{ii} can be written in a general form

$$t_{ii} = f\left(t_i, \frac{k^*}{k}, \nu, \nu^*\right) \tag{2'}$$

where k^* and k are the bulk modulus of the particle and the matrix respectively, ν^* and ν are Poisson's ratio for the particle and the matrix respectively, and t_i is the actual dimension in the ith dimension of the particle.

Then the total length of the dislocation loops punched out in the ith direction is given by

$$l_1 = \frac{2\epsilon}{b} t_{11}(t_{12} + t_{13})$$

$$l_2 = \frac{2\epsilon}{b} t_{22}(t_{21} + t_{23}) \tag{3}$$

$$l_3 = \frac{2\epsilon}{b} t_{33}(t_{31} + t_{32})$$

i.e. in general symbols

$$l_i = \frac{2\epsilon}{b} t_{ij}\delta_{ij}t_{ik}(1 - \delta_{ik}) \tag{3'}$$

where δ_{ij} and δ_{ik} are the Kronecker deltas, t_{ij} is the contribution of the particle height in the jth dimension in punching a dislocation loop in the ith direction and the Einstein suffix notation is used here.

In this work, further assumptions, simplifications, facts and parameters which are reasonable in terms of experimental results are introduced as follows.

(1) The back stress between dislocations which are punched out was neglected. At any rate it is partly balanced by the image force.

(2) It is assumed that the misfit strain is completely relaxed by the prismatic dislocations, *i.e.* no elastic residual stress remains. (In fact it has been shown that there is a small elastic residual stress.)

(3) Interaction stresses among different particles and those between punched dislocations from one particle with the dislocations punched out by another platelet are neglected.

The proceeding formulations can be further simplified. On the assumption of rigid expansion, all the misfit is relaxed, *i.e.* there are no dislocation–dislocation and dislocation–particle interactions

$$t_{ii} = t_i \tag{4}$$

Then

$$N_i = t_i \frac{\epsilon}{b} = \frac{\Delta t_i}{b} \quad (i = 1, 2, 3) \tag{4'}$$

and it is also reasonable to assume that

$$t_{ij} = t_{kl} = t_j \tag{5}$$

Therefore, eqn. (3) can be expanded in the simple form

$$l_1 = \frac{2\epsilon}{b} t_1(t_2 + t_3)$$

$$l_2 = \frac{2\epsilon}{b} t_2(t_1 + t_3) \tag{5'}$$

$$l_3 = \frac{2\epsilon}{b} t_3(t_1 + t_2)$$

which may also be directly extracted from Fig. 7. Thus the total length of dislocations generated by one particle is

$$L = \Sigma l_i$$
$$= l_1 + l_2 + l_3 \tag{6}$$

Without considering the dislocation back stresses and dislocation–particle interaction (as outlined before) the arrangement of the particles will not affect the dislocation density ρ due to the difference between the thermal expansion coefficients of aluminum and SiC. The number of particles in unit volume is

$$n = \frac{A}{t_1 t_2 t_3} \tag{7}$$

where n is the number of particles in unit volume and A is the volume fraction of particles. Therefore from eqns. (6) and (7) the length of the dislocations generated by all particles will be

$$L_L = (l_1 + l_2 + l_3) \frac{A}{t_1 t_2 t_3} \tag{8}$$

and the dislocation density in the matrix is found to be

$$\rho = \frac{L_L}{1 - A}$$
$$= \frac{4A\epsilon}{b(1 - A)} \left(\frac{1}{t_1} + \frac{1}{t_2} + \frac{1}{t_3} \right) \tag{9}$$

It should be noted here that the dislocation density is proportional to the sum of the inverse of t_i. This means that for the same volume fraction, in general, the smaller the particle size the higher a dislocation density will be produced (Fig. 8).

Let us consider the cases of composites *with (i) rods ("whiskers") and (ii) with* platelets of aspect ratio R equal to 2 and of the same volume fraction. The dislocation densities for both cases are

$$\rho_w = \frac{10A\epsilon}{b(1 - A)} \frac{1}{t} \tag{10}$$

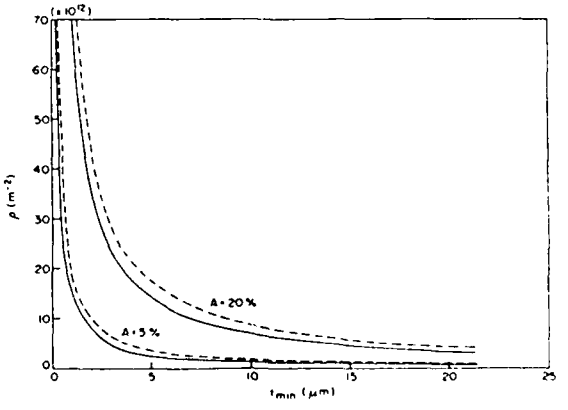

Fig. 8. Calculated dislocation density ρ due to prismatic punching as a function of minimum particle thickness t, for both rods ("whiskers") (- - -) and platelets (——) of the same volume fraction A, according to eqn. (9) (R = 2).

$$\rho_p = \frac{8A\epsilon}{b(1-A)}\frac{1}{t} \tag{11}$$

with t designating the smallest dimension, while ρ_w and ρ_p stand for the dislocation densities in the whisker and platelet composite respectively. It is readily seen that the theoretical dislocation density due to prismatic punching is higher in a whisker composite than in a platelet composite of the same volume fraction. Figure 8 shows the calculated values according to eqn. (9) for whisker and platelets with an aspect ratio of 2, the latter as for the samples studied.

In general, the dislocation density ρ due to punching can be written as

$$\rho = \frac{BA\epsilon}{b(1-A)}\frac{1}{t} \tag{12}$$

where B is a geometric constant which is theoretically between 4 (for one dimension very small compared with the other two) and 12 (for equiaxed particles) and t is the smallest dimension of the particle as before. It should be noted also that empirically there exists an upper limit to the dislocation density of about 10^{16} m^{-2}. This would correspond to a minimum dimension of the particles of 0.01 μm.

The dislocations produced as a result of punching in accordance with Fig. 7 have one set of Burgers vector of a single type along each side (*i.e.* at a given location) whereas experimentally three different groups of slip traces, each of which represents one type of Burgers vector, are generally observed. Thus, ideally punched dislocations seem unlikely to lead to the formation of subgrain boundaries. As such, they represent a high energy configuration. Therefore, additional dislocations may be generated to assist the production of the low energy dislocation configuration of subgrain boundaries. These are in fact observed in bulk samples (Fig. 2) but not in *in situ* thermally cycled TEM foils. In the course of the dislocation rearrangements leading to subboundaries, additional dislocations may be formed, but more probably there is a net decrease in dislocation density ρ due to mutual dislocation annihilation. Yet the density of dislocations produced as a result of this punching model is a factor of 2 or 3 lower than that observed experimentally for the small-size particles. It is suspected that for larger-size particles, the model correspondingly underestimates the density.

Although the actual dislocation density and arrangements were not obtained, it is possible to calculate a lower bound value for the strength increase due to the dislocations formed through thermal strains.

For the strengthening due to the presence of dislocations generated by the differential thermal contraction, the following equation may be used:

$$\Delta\sigma = \alpha\mu b\rho^{1/2} \tag{13}$$

where $\Delta\sigma$ is the increase in tensile strength, μ is the shear modulus of the matrix and α is a geometric constant. Hansen [18] obtained an α value of 1.25 for aluminum, which we shall use.

Now, when eqn. (12) is substituted into eqn. (13), the following is obtained:

$$\Delta\sigma = \alpha\mu b\left(\frac{A}{1-A}\frac{B\epsilon}{b}\right)^{\frac{1}{2}}\left(\frac{1}{t}\right)^{\frac{1}{2}} \tag{14}$$

Equation (14) yields the $\Delta\sigma$ values plotted *versus* the platelet diameter in Fig. 9. Admittedly, these data are associated with some uncertainty. In particular, experimentally it is much easier to measure the platelet diameter, and it is for this reason

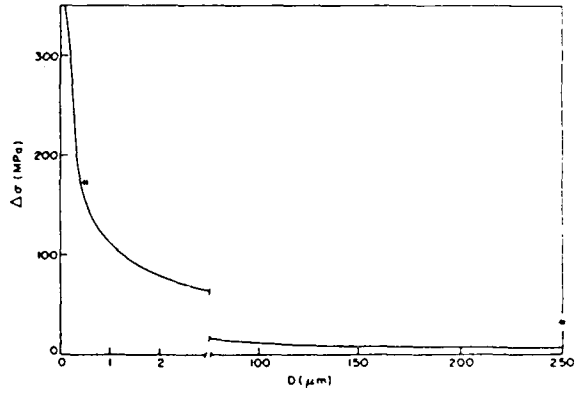

Fig. 9. The calculated increase in tensile strength of the composite over that of the matrix material on account of the dislocations due to the differential thermal contraction of aluminum and SiC and given by $\Delta\sigma = \sigma_{yc} - \sigma_{ym}$ where σ_{yc} is the yield stress of the composite and σ_{ym} is the yield stress of the matrix on the basis of eqn. (14) using $B = 8$, $A \doteq 0.2$, $\mu = 26 \times 10^3$ MPa, $b = 2.86 \times 10^{-10}$ m, $R = D/t = 2$, and $R = 2$; $*$, experimental point.

that it was chosen in the evaluation and not the minimum dimension.

Yet, the aspect ratio must be known in order to find B which is similarly not well known.

As can be seen in Fig. 9, there is a significant decrease in the predicted strengthening with increasing platelet size. This is to be expected, however, also on account of particle strengthening independent of the differential thermal contraction effect. Included in Fig. 9 are two experimental data points for the SiC particles 0.5 μm in diameter and 250 μm in diameter in an aluminum alloy 1100 matrix [19]. It seems, then, that a significant portion of but not all the strengthening due to the SiC particles may be ascribed to the differential thermal contraction effect. The effect of a reduced subgrain size due to SiC particles probably also contributes to the strengthening.

6. DISCUSSION

The presence of SiC particles of platelet morphology in an aluminum metal matrix composite resulted in the generation of dislocations at the Al-SiC interface when the composite was cooled from the annealing temperature. In general, the high density of dislocations originally present in the composite samples disappeared at 500-650 K and then reappeared on cooling at densities close to the high densities originally observed in the annealed specimens. In contrast, dislocations were not generated to the same extent in either of the control samples during cooling.

However, there are specific differences between the *in situ* cooled TEM foils and the TEM foils taken from a bulk sample. The dislocations within the bulk foil are generally in very tangled arrangements (Fig. 1), whereas in the *in situ* cooled foil the dislocations are much more uniformly arranged. The reason is that, in *in situ* cooled foils, dislocations are lost out of the free surfaces and that, secondly, buckling of the foil occurs which accommodates some of the strain field due to the differential thermal contraction. In the *in situ* foils, generation of subgrain boundaries was not observed.

The intensity of dislocation generation at the Al-SiC interface is related to size and shape of the SiC particles. The intensity of generation is lowest for small, nearly spherical particles. As the particle size increases, *i.e.* from 1 to 5 μm, the intensity of generation increases significantly. Also the intensity is much greater at the corners of a particle. This accounts for the observed strong slip traces. The increased number of dislocations generated per particle as the size increases is predicted by the theoretical model (eqn. (4′)); also at a constant volume fraction the average dislocation density decreases as the particle size increases (eqn. (9)).

The control samples were invaluable in determining the fact that the dislocations generated on cooling were not artifacts due to the effects of electron irradiation. In the aluminum alloy 6061 control sample with no SiC, only a few dislocations were generated at a few large precipitates. Similarly, the aluminum alloy 1100 control samples were also exposed to the high energy electron beam, and yet substantial formation of dislocations did not occur (Fig. 3). Also, experimentally and in agreement with theory, the intensity of dislocation generation can be correlated with the size, volume fraction and shape of the SiC or second-phase precipitate particles present, proving that the particles and not the electrons in the beam caused the dislocations to be generated. It should also be pointed out that slip line generation about an SiC cylinder in an aluminum disk due to thermal cycling has been demonstrated by Flom and Arsenault [20].

Because of the difficulty associated with tilting a very-fine-subgrain material to the various diffracting conditions required to image all the dislocations in the subgrain, the reported densities could be one-third to one-half of the actual number. Moreover, many dislocations escape from the foil surfaces. Although more rigorous tilting would give more precise values, a good idea of the relative densities in the samples can be obtained by imaging dislocations in many subgrains for each material and assuming that the value will be systematically low for all the samples.

The net result of considering all the experimental factors which may influence the experimentally determined dislocation densities after a thermal cycle is (1) that the

dislocation generation observed during cooling can be readily attributed to the differential thermal contraction of the aluminum and SiC and (2) that the observed densities are lower than the densities which would be observed if bulk samples could be examined and if diffracting conditions were controlled to image all dislocations.

The observed changes in dislocation density on cooling are in general agreement with the simple prismatic punching model. The model of thin platelet predicts a dislocation density of 2.4×10^{13} m^{-2} for an average size platelet of 5 μm.

7. CONCLUSIONS

From a consideration of the experimental results and the prismatic punching model, the following conclusions can be drawn.

(1) The densities of dislocations observed in *in situ* TEM foils (10^{13} m^{-2}) could well equal the high densities previously observed in bulk annealed composites if it were not for dislocation loss through the surfaces.

(2) The high dislocation density (10^{14} m^{-2}) previously observed in bulk annealed composites is due to differential thermal contraction of aluminum and SiC on cooling from the elevated temperatures of annealing. It was observed that, on heating to the annealing temperature, all the dislocations disappeared in the *in situ* samples.

(3) The density of dislocations observed in this experiment as a result of thermal cycling is lower than the actual density generated during thermal cycling because dislocations are lost through the surfaces of the thin foil samples during cooling.

(4) A simple model based on the prismatic punching of dislocations predicts dislocation densities which are comparable with those measured for small particles.

(5) Thermal cycling causes the disappearance of dislocations at high temperatures and the generation of dislocations at Al–SiC interfaces and precipitates on cooling.

ACKNOWLEDGMENTS

This research is supported by the Office of Naval Research under Grant N00014-85-K-0007.

The authors wish to acknowledge M. Vogelsang of the University of Maryland for assistance with the experiments. Effective liaison with Dr. Steve Fishman of the Office of Naval Research in Arlington, VA, has been very helpful to the project. The authors wish to express special acknowledgment to Professor D. Kuhlmann-Wilsdorf for her encouragement in the model analysis.

REFERENCES

1 R. J. Arsenault and R. M. Fisher, *Scr. Metall., 17* (1983) 67.
2 A. Taylor and R. M. Jones, in J. R. O'Connor and J. Smiltens (eds.), *Silicon Carbide*, Pergamon, Oxford, 1960, pp. 147–154.
3 K. K. Chawla and M. Metzger, *J. Mater. Sci., 7* (1972) 34.
4 J. K. Lee, Y. Y. Earmme, H. I. Aaronson and K. C. Russell, *Metall. Trans. A, 11* (1980) 1837.
5 C. A. Hoffman, *J. Eng. Mater. Technol., 95* (1973) 55.
6 G. Garmong, *Metall. Trans., 5* (1974) 2183.
7 G. J. Dvorak, M. S. M. Rao and J. Q. Tarn, *J. Compos. Mater., 7* (1973) 194.
8 R. L. Mehan, *Metal Matrix Composites, ASTM Spec. Tech. Publ. 438*, 1968, p. 29.
9 A. Szirmae and R. M. Fisher, *Techniques of Electron Microscopy, Diffraction, and Microprobe Analysis, ASTM Spec. Tech. Publ. 372*, 1963, p. 3.
10 L. E. Samuels, *Metallographic Polishing Methods*, Pitman, Melbourne, 1971, p. 79.
11 D. G. Howitt, in R. H. Geis (ed.), *Analytical Electron Microscopy*, San Francisco Press, San Francisco, CA, 1981, p. 252.
12 P. D. Townsend, J. C. Kelly and N. E. W. Hartley, *Ion Implantation, Sputtering, and Their Applications*, Academic Press, London, 1976, p. 311.
13 G. Dupuoy, in P. R. Swann, C. J. Humphreys and M. J. Goringe (eds.), *Proc. 3rd Int. Conf. on High Voltage Electron Microscopy*, Academic Press, London, 1974, p. 447.
14 H. Fujita, T. Tabata, N. Sumida and K. Yoshida, in P. R. Swann, C. J. Humphreys and M. J. Goringe (eds.), *Proc. 3rd Int. Conf. on High Voltage Electron Microscopy*, Academic Press, London, 1974, p. 427.
15 K. F. Hale and M. Henderson-Brown, *Micron, 4* (1973) 69.
16 P. B. Hirsch, R. B. Nicholson, A. Howie, D. W. Pashley and M. J. Whelan, *Electron Microscopy of Thin Crystals*, Butterworth, London, 1965, p. 423.
17 D. Kuhlmann-Wilsdorf, University of Virginia, personal communication, 1985.
18 N. Hansen, *Acta Metall., 25* (1977) 863.
19 Metallurgical Materials Laboratory, University of Maryland, unpublished research, 1985.
20 Y. Flom and R. J. Arsenault, *Mater. Sci. Eng., 77* (1986) 191.

Deformation of SiC/Al Composites

Y. Flom and R.J. Arsenault

Author's Note: This work was supported by the Office of Naval Research under Contract No. N00014-85-C-0007

This article reviews some aspects of plastic deformation of Al/SiC composites with an emphasis on strengthening mechanisms, the role of coefficient of thermal expansion (CTE), the role of particle-matrix interfaces (PMI), and the fracture process. There is a tremendous potential for structural applications of SiC/Al composites. However, a complete understanding of the mechanisms of strengthening and fracture have not yet been obtained. Therefore, continued detailed fundamental investigations are required.

INTRODUCTION

Discontinuously reinforced metal matrix composites represent a group of materials that combine the strength and hardness of the reinforcing phase with the ductility and toughness of the matrix. Powder metallurgy (p/m) aluminum alloys reinforced with SiC in particulate, platelet, or whisker form are receiving a great deal of attention from researchers and engineers. The interest in Al/SiC composites is related to: their high elastic modulus, high strength, and light weight[1-4] (see Table I); the ability to economically produce SiC whiskers, platelets, and particulates;[5,6] the ability to use standard shaping methods such as forging, rolling, extrusion, etc.; and much less dependence of the engineering properties on directions than with continuous composites.[3,4]

Despite all these advantages, Al/SiC composites, to our knowledge, have not been used in critical areas such as the manufacture of aircraft frames. The main obstacles to using Al/SiC composites in aerospace technology are low ductility and fracture toughness.

STRENGTHENING PHENOMENA

The experimental results of a number of investigations provide quite high values for the yield strength σ_y and ultimate strength σ_{uts} of Al/SiC discontinuous composites (Table I). Predicted or calculated values of σ_{uts}, based on a classical continuum mechanics model of a composite material, is by a factor of four lower than that determined from the experiment.[2] This discrepancy becomes even more significant in light of the fact that assumptions that are made in the continuum mechanics approach (i.e., perfect alignment of the whiskers or platelets and a void-free matrix[7]) do not represent the situation in the real Al/SiC composite. Experimental observations show, however, that there are a significant number of voids present in the matrix and the alignment of the whiskers and/or platelets is far from perfect.[2,3] A modified continuum mechanics approach has been proposed for theoretical prediction of σ_{uts} and σ_y.[8] This approach takes into account the tensile load transfer from the matrix to the whisker and/or particulate ends. An assumption is made that the presence of SiC does not affect matrix behavior and one can use properties of the matrix and the concept of the load transfer to predict the strength of the composite. Whisker and particulate 6061 Al/SiC composites had calculated yield strength values of about 500 MPa and 450 MPa, respectively and observed yield strength values of about 450 MPa and 420 MPa, respectively.[8] However, there are several assumptions in this formulation which are not valid.[9]

Table I. Mechanical Properties of SiC/Al Composites

Composite and Heat Treatment	Volume Fraction of SiC, %	Yield Strength, MPa	Ultimate Tensile Strength, MPa	Elastic Modulus, GPa	Ductility $\epsilon_f = \frac{A_o}{A_f}$, %	% Elong. ϵ_p	Fracture Toughness, K_{IC} MPa $\sqrt{m}$	Source
SiCp/6061 T6	20	400-356	434-428	108	4.9	1.5		(2), (3) (27)
SiCp/6061 T6	25	345	410	99		4.4	15.8	(4), (28)
SiC$_w$/6061 T6	20	470-321	607-423	106-103	5.4	3-2.2	22.4	(2), (3) (4), (27)
SiCp/2024 T6	30	405	456	118	.8			(3), (27)
SiC$_w$/2024 T4	20		524-455	117-97		1-2		(1)
SiCp/7075 T6	30	392	439	119	.9			(3), (27)
SiC$_w$/7075 T6	20	407	549	101	3.5			(3), (27)

where B is a geometric constant which varies theoretically between 4 for whiskers and 12 for equiaxed particles, A is the volume fraction of particles, b is the length of Burger's vector, t is the smallest dimension of particle, and ε is the misfit strain due to difference in CTE, i.e.,

$$\varepsilon = (\Delta CTE) \times \Delta T \quad (3)$$

Expression 2 implies that for the same volume fraction, smaller particles will produce higher dislocation densities (Figure 2).

Several investigations were conducted to evaluate the residual thermal stresses in the Al/SiC composite. An x-ray diffraction technique was used for experimental evaluation of the residual stresses. It was found that the residual stress state in the composite was tensile, ranging from 34.5 MPa to 407 MPa (Table II).[16] Theoretical analysis of thermal stresses was based on Eshelby's equivalent inclusion model. Ellipsoidal aligned whiskers in the infinite body were considered and mechanical properties of annealed 6061 Al matrix and SiC whisker with the aspect ratio L/d = 1.8 (length-to-diameter ratio) were used for the calculations. Resultant stress distribution is shown in Figure 3. In addition, the difference in the yield strength $\Delta\sigma_y$ between tension and compression resulting from the thermal residual stresses was determined experimentally and calculated theoretically using the previously cited model. Very good agreement was obtained between the experimental and theoretical results[16] (Figure 4).

It should be mentioned that there are some negative aspects to the difference in CTE between SiC and Al. Degradation of the yield and ultimate strength was reported as a result of thermal cycling of 2124 Al/SiC composite.[17] Prolonged exposures of SiC/Al to elevated temperatures, however, showed no apparent effect on the composite's mechanical properties at room temperature.[18]

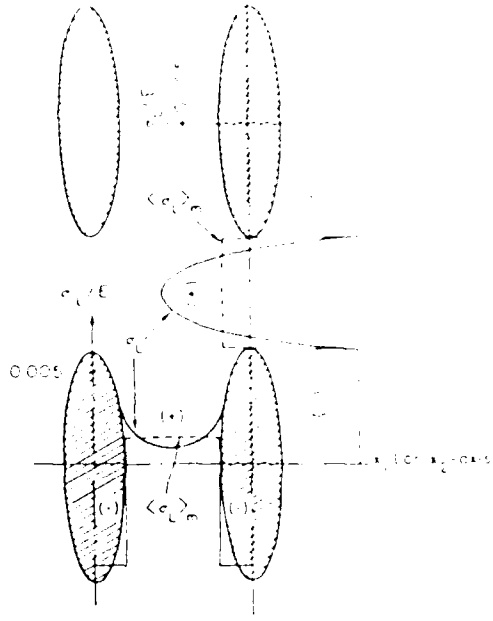

Figure 3. Schematic distribution of the stress in the matrix and the reinforcement due to the difference in thermal coefficient of expansion between the SiC and Al.

SiC/Al INTERFACES

It is probably not an exaggeration to say that the interfaces play the most important role in the behavior of a composite. The interface is a necessary link between the matrix and the reinforcement to accomplish the load transfer as well as a site of dislocation generation during thermal changes and/or plastic deformation.

Previously, the importance of a strong particle-matrix bond was emphasized by a number of investigators. It was shown that strengthening of the two-phase alloys was possible only in the case of the strong PMI.[19] Also, strong PMI prevents or delays the onset, in an internal necking mechanism, of the ductile fracture process.[20] In general, the bond between SiC and Al is quite strong in SiC/Al composites.[1,3,21] Direct experimental measurements of the bond strength have not been reported in the literature. Indirect measurements of SiC/Al interfacial strength, based on Neuber's theory of notches, provided values on the order of 1600 MPa.[22] The fact that the obtained value is quite high supports qualitative observations made by various investigators.

A recent study of SiC/2124 Al composite using high resolution electron microscopy showed that the Al-SiC interface regions consist of numerous small precipitates of MgO, $CuMgAl_2$, $CuAl_2$ and some Al_2O_3 phases ranging in size from 10 nm to 100 nm.[23] No voids were observed at the whisker-matrix interfaces, indicating the presence of a "perfect" bonding. The structure of the interfaces, however, was found to be rather complicated and not a planar Al-SiC interface.[23] This observation does not speak in favor of the classical load transfer-type strengthening theories developed for composites.[7]

Another interesting phenomenon associated with SiC-Al interfaces was recently reported in the course of fracture surface analysis performed with a scanning Auger electron microscope.[24] Both SiC_w/6061 Al and SiC_w/2124 Al materials were fractured in-situ and composition analyses were performed on individual whiskers exposed on the surface (Figure 5). In most cases, Si or C could not be detected on the whiskers. Detection of Si and C was possible only after considerable ion sputtering. This means that "pulled out" whiskers are coated with an Al layer which is the indication of a good SiC/Al bond. Also, an anomalous diffusion of Al into SiC was observed (Figure 6).

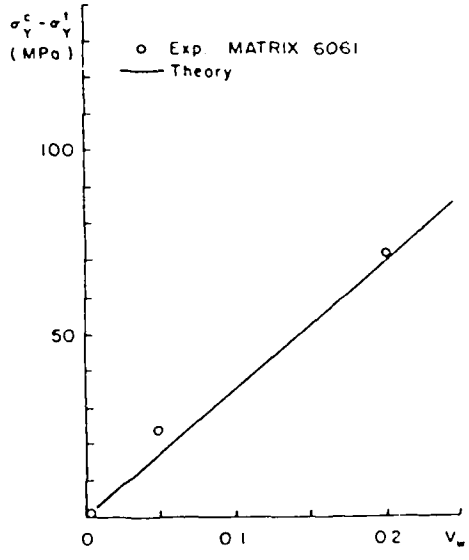

Figure 4. The difference in yield stress between compression and tension as a function of volume percent silicon carbide whisker.

FRACTURE

Ductility and fracture toughness of SiC/Al composites are quite low (Table I) and require an intensive study to reach a compromise between two extremes: a very strong and brittle composite versus a weak and ductile composite. As of now, this compromise has not been reached

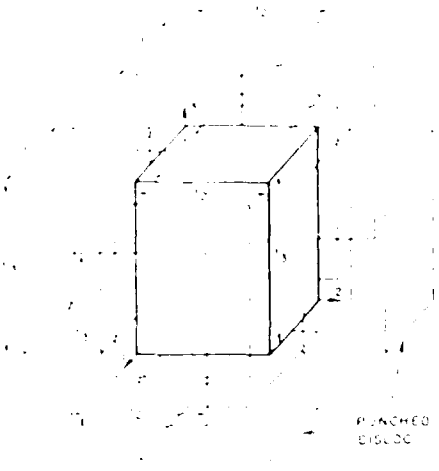

Figure 1. A schematic representation of prismatic punching of a parallelepiped shaped SiC particle.[14]

Another possible explanation of the mechanism of Al/SiC strengthening is based on the Orowan theory which enables one to estimate the stress required for dislocation to bypass the particle.[10] Particle separation is a major parameter controlling this stress. Taking the average particle spacing of 2 μm yields about a 5 MPa increase in composite strength, which is obviously too small compared with a 60 to 110 MPa increase observed experimentally.

Yet another approach is based on the increase of the dislocation density in the Al alloy matrix. It was shown that the strength of the thermomechanically treated 6061 Al alloy can be as high as 400 MPa.[11] If this value is used for calculation of the theoretical strength of the composite, then calculated σ_{uts} agrees well with experimental results. The increase of the dislocation density in Al matrix in the Al/SiC composite was attributed to the relaxation of the misfit strain between SiC particles and the matrix. This misfit strain arises from the difference between CTE of SiC and that of Al (of about a factor of 10) on cooling down from the annealing or processing temperature.[2]

Transmission electron microscopy (TEM) investigations of these composite materials do indeed reveal a high dislocation density (10^{10} cm^{-2}) and small subgrain size (1.0-2.5 μm).[12] The following expression was proposed for the ultimate strength:[2]

$$\sigma_{uts} = \sigma_{dis} + \sigma_{sg} + \sigma_{wh} + \sigma_{comp} + \sigma_{ah} \qquad (1)$$

where σ_{dis} is the term due to dislocation density increase; σ_{sg} is the increase in strength due to subgrain boundaries; σ_{wh} is the increase due to work hardening; σ_{comp} is the increase due to continuum mechanics strengthening, and finally σ_{ah} is the increase in the strength due to the heat treatment. The evaluation of these terms results in a value of about 630 MPa for σ_{uts}, whereas the experimental value is about 640 MPa.

Table II. The Thermal Residual Stresses (Tensile) as Measured by X-ray Defraction Techniques

Material	Transverse MPa	Longitudinal MPa
0 V% Whisker SiC 6061 Matrix	0.0	0.0
5 V% Whisker SiC 6061 Matrix	407	34.5
20 V% Whisker SiC 6061 Matrix	228	55.2
Wrought	0.0	0.0

ROLE OF CTE

In the course of studying plastic deformation of two-phase alloys, it was observed that second phase particles can act as a dislocation source when a material is cooled from an elevated temperature or is deformed.[13] Recent observations of the local plastic deformation around SiC particles in Al/SiC composites subjected to the thermal cycle showed that the size of the plastically deformed zone around the particle is ~1.5 particle radius. Interestingly, plastic deformation, i.e., formations of the slip bands near the SiC particle, was also observed on heating from room temperature. Subsequent in-situ high voltage TEM investigations of Al/SiC composites showed dislocation generation on heating,[12] which corresponds to observation of the slip bands. A simple model, based on prismatic punching (Figure 1), was developed to account for the relative [illegible] due to the difference in CTE.[15]

Dislocation density in the matrix was found to be

$$\rho = \left\{ \begin{matrix} B A \epsilon \\ b(1-A) \end{matrix} \right\} \frac{1}{t}$$

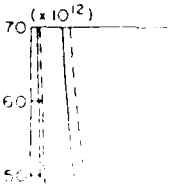

Figure 2. [illegible] to prismatic [illegible] mum pa[illegible] and pa[illegible] a cer[illegible]

AD-A189 258 COMPOSITES STRENGTHENING(U) MARYLAND UNIV COLLEGE PARK 2/2
METALLURGICAL MATERIALS LAB R J ARSENAULT NOV 87
MML-1987-1 N00014-85-K-0007

UNCLASSIFIED F/G 11/4 NL

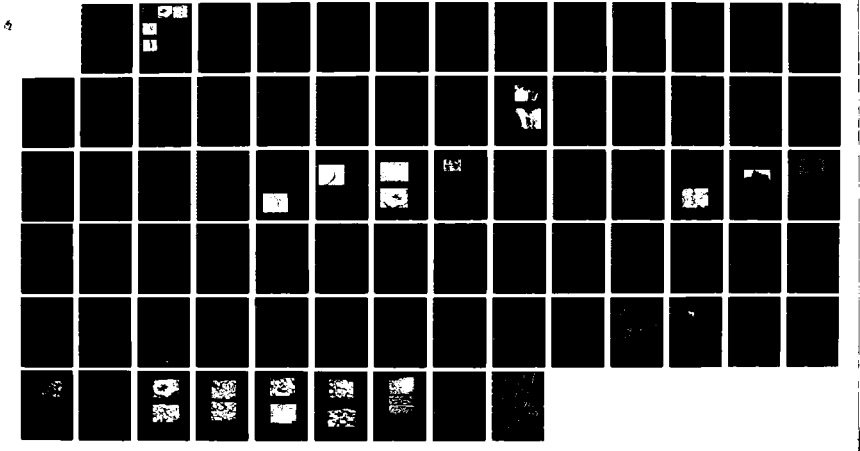

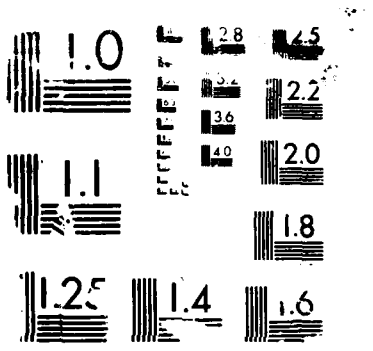
1.0
1.1
1.25
1.4
1.6
1.8
2.0
2.2
2.8
3.2
3.6
4.0
4.5

(a) × 1000

(b) × 8000

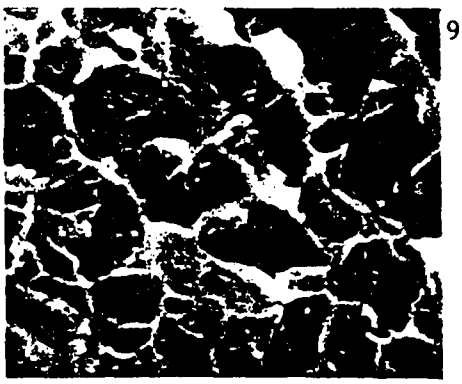

(c) × 5000

Figure 7. Large intermetallic inclusion ("fish eyes") (a), cluster of whiskers (b), and individual SiC particles (c) as an acting fracture initiating sites.

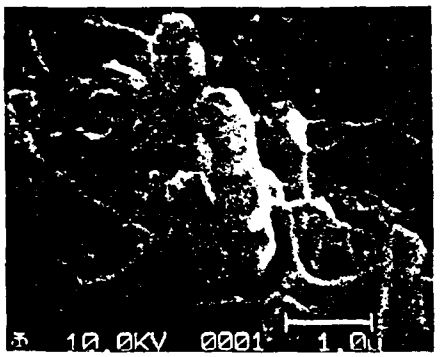

Figure 5. A SEM micrograph taken in the Auger microprobe of the fracture surface of a whisker SiC/Al composite.

Al trace Si trace

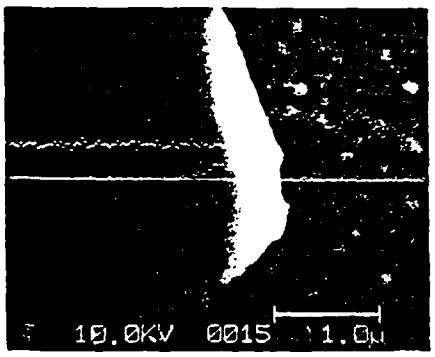

Figure 6. A SEM micrograph taken in the Auger microprobe, on which the Al and Si Auger probe traces have been superimposed.

ACKNOWLEDGEMENTS

The authors wish to acknowledge Dr. S. Fishman for his continuing support as well as that of previous and present graduate students.

ABOUT THE AUTHORS

Y. Flom and **R.J. Arsenault** are currently with the Engineering Materials Group at the University of Maryland in College Park, Maryland

Generally, observations of the fracture surface of SiC/Al composites do not reveal the presence of SiC particulates and/or whiskers in the quantities corresponding to their volume fraction.[1,21,23] Of specific interest are the following features:[25]

- There appear to be fracture initiation sites.
- Fracture has a macroscopically brittle characteristic, but on the microscale, it is ductile, i.e., has a dimple morphology.
- There is no indication of fracture of SiC (if SiC is less than 10 μm in size).
- Some secondary cracking takes place (cracks are formed perpendicular to the fracture surfaces).

The fracture process is very localized and occurs without warning, i.e., no apparent necking is observed.

It seems that the following fracture initiation sites can be identified: the large intermetallic (Fe, Cr)$_3$ SiAl$_2$ inclusions termed "fish eyes;" clusters of SiC whiskers or particulates; and voids initiated at the SiC whiskers or particulates (Figure 7).

It is generally accepted that a ductile fracture in the presence of second-phase particles occurs by nucleation of voids at the particles; growth of these voids; and their linkage which manifests the actual physical separation. The extent of the void growth determines the ductility of the material. If this stage is very limited, then material behaves in a brittle manner. In SiC/Al composites, the void growth stage is very limited. This can be seen from the dimple sizes (3-5 μm) observed on the fracture surfaces. Void growth almost stops when the volume fraction of the SiC particulates or whiskers approaches 20%.[25]

At present, an effort is under way to give a quantitative description of the fracture process in a SiC/Al composite using 1100 Al alloy matrix.[26] Commercially pure Al alloy has been chosen to minimize the influence of various inclusions present in conventional matrix material.

References

1. A.P. Divecha, S.G. Fishman and S.D. Karmarkar, *Journal of Metals*, 9 (1981) 12.
2. R.J. Arsenault, *Mat. Sci. & Eng.*, 64 (1984) 171.
3. D.L. McDanels, *Met. Trans.*, 16A (1985) 1105.
4. C.R. Crowe, R.A. Gray and D.F. Hasson, *Proceedings of ICCM V*, ed. by W. Harrigan, San Diego, 1985.
5. I.B. Cutler, *Am. Ceram. Soc. Bull.*, 52 (1973) 425.
6. W. Harrigan, DWA Composite Specialists, Chatsworth, CA, personal communications, 1982.
7. M.R. Piggott, *Load-Bearing Fibre Composites*, Pergamon, Oxford, 1980, pp. 141-144.
8. V.C. Nardone and K.W. Prewo, *Scripta Met.*, 20 (1986) 43.
9. R.J. Arsenault and M. Taya, to be submitted to *Scripta Met.*
10. R.J. Lederich and S.M.L. Sastry, *Mat. Sci. Eng.*, 55 (1982) 143.
11. H.J. Rack and R.W. Krenzer, *Met. Trans.*, 8A (1977) 335.
12. M. Vogelsang, R.J. Arsenault and R.M. Fisher, *Met. Trans.*, 17A (1986) 379.
13. I.L. Mogford, *Metall. Rev.*, 12 (1967) 114, 49-68.
14. Y. Flom and R.J. Arsenault, *Mat. Sci. & Eng.*, 75 (1985) 151.
15. R.J. Arsenault and N. Shi, to be published in *Mat. Sci. and Eng.*
16. R.J. Arsenault and M. Taya, *Proceedings of ICCM V*, p. 21, ed. by W. Harrigan, San Diego, 1985.
17. W.G. Patterson and M. Taya, *Proceedings of ICCM V*, p. 53, ed. by W. Harrigan, San Diego, 1985.
18. A. Skinner, M. Koczak and A. Lawley, *Ceramic Eng. & Sci. Proceedings*, American Ceramic Society, Vol. 2 #7-8, 1981, p. 827.
19. B.I. Edelson and W.M. Baldwin, Jr., *Trans. of ASM*, 55 (1962) 230.
20. P.F. Thomason, *Met. Sci.*, 5 (1971) 64.
21. T.G. Nieh, R.A. Rainen and D.J. Chellman, *Proceedings of ICCM V*, p. 825, ed. by W. Harrigan, San Diego, 1985.
22. Y. Flom and R.J. Arsenault, *Mat. Sci. & Eng.*, 77 (1986) 191.
23. S.R. Nutt and R.W. Carpenter, *Mat. Sci. & Eng.*, 75 (1985) 169.
24. R.J. Arsenault and C.S. Pande, *Scripta Met.*, 18 (1984) 1131.
25. R.J. Arsenault and Y. Flom, to be published in the Proceedings of AIME Annual Conference in Toronto, 1985.
26. Y. Flom and R.J. Arsenault, unpublished results, University of Maryland, 1986.
27. D.L. McDanels and C.A. Hoffman, NASA Technical Paper 2302, July 1984.
28. T.J. Hsieh, Masters Thesis, University of Maryland, 1985.

Scripta METALLURGICA Vol. 21, pp. 349-354, 1987 Pergamon Journals, Ltd.
Printed in the U.S.A.

A COMPARISON BETWEEN A SHEAR LAG TYPE MODEL AND AN ESHELBY TYPE MODEL IN PREDICTING THE MECHANICAL PROPERTIES OF A SHORT FIBER COMPOSITE

M. Taya*
Department of Engineering Science
University of Oxford
Parks Road, Oxford OX1 3PJ
United Kingdom

R. J. Arsenault
Engineering Materials Group
University of Maryland
College Park, MD 20742 USA

(Received November 3, 1986)
(Revised December 1, 1986)

Introduction

As the usage of Metal Matrix Composites (MMCs) is becoming more popular, a body of literature is being developed on the mechanical properties of these composites. Among various composites, short fiber composites are attractive, owing to their ease and modest cost of fabrication, and experimental data on their mechanical properties are now reasonably well documentated. Among the mechanical properties, the properties related to the stress-strain curve of a short whisker composite, i.e., stiffness, yield stress, work-hardening rate and strength (fracture stress) are considered to be the most basic data. Two types of analytical models seem to have been used extensively, the shear lag type and the Eshelby type models. The former model which was originally developed by Cox (1) is simple and has been used for prediction of stiffness (2), yield stress (3), strength and creep strain-rate (4). In the case of continuous whisker composite, a shear lag type model was also applied to prediction of load concentration factor successfully (5). However, it is known that the properties predicted by the shear lag type model will become a crude approximation when the aspect ratio of the short fiber (ℓ/d) is small or the short fibers are misoriented. Nardone and Prewo (3) have recently proposed a variation of the shear lag type model to obtain a larger estimated tensile yield stress of a short whisker MMC with smaller values of ℓ/d.

On the other hand, in the Eshelby type model, the short whisker is assumed to be a prolate ellipsoidal inhomogeneity. The analytical model to predict the thermal and mechanical properties of a composite was first developed by Eshelby who considered a single ellipsoidal inclusion or inhomogeneity embedded in an infinite elastic body (6), thus it is valid only for a small volume fraction of fiber V_f. Mori and Tanaka (7) modified the original Eshelby model for a finite volume fraction of inclusions or inhomogeneities. The thermal and mechanical properties that can be predicted by the modified Eshelby type models are stiffness (8), yield stress and work-hardening rate (9-11), thermal expansion (12,13), and thermal conductivity (14). The Eshelby type model has also been used to predict the thermal residual stress in a composite (10,13,15). The detailed summary of the Eshelby type models is given in a book by Mura (16).

In this short paper, we attempt to compare the above two models with the aim of investigating their advantages and limitations. To this end, we focus on the stiffness (E_c) and yield stress (σ_{yc}) of a short whisker MMC. First we review briefly the important assumptions used in the models and also the final formula to predict the above properties of an aligned short fiber MMC in Section II. Then a comparison between the values predicted by the models and the existing experimental data is made in Section III. Finally concluding remarks on the models are given in Section IV.

Models

1. Shear Lag Type Model

The original shear lag model, developed by Cox (1), with its detailed derivation of the

* Permanent address: Mechanical Engineering Department, University of Washington, Seattle, WA.

0036-9748/87 $3.00 + .00

stiffness (2) and yield stress (2) has already been discussed elsewhere. Thus it is omitted here. The standard shear lag model that has often been used for an aligned short fiber composite system is shown in Fig. 1(a) where short fibers of the same size are assumed to be distributed in the matrix in a hexagonal array. The repeated cell (unit cell) is identified as in Fig. 1(b) which is used for the detailed derivation. The most important assumption in the shear lag type model is that load transfer occurs between a short whisker and matrix by means of shear stresses at the matrix-whisker interface. In the original shear lag model (1,2) the load transfer by the normal stress at the whisker ends and side surfaces was ignored. Nardone and Prewo (3) recently suggested that the load transfer at the fiber ends should be accounted for in predicting the yield stress, but still ignored the normal load at the side surface of fiber for the case of ℓ/d values. Below, we list the final formulae based on the shear lag type model to predict the stiffness (1,2) and the end result of a derivation of the tensile yield stress, including normal stresses on the end of the fiber of a short fiber composite. For the stiffness,

$$E_c/E_m = (1 - V_w) + V_w(E_w/E_m)(1 - \frac{\tanh x}{x}) \tag{1}$$

$$x = (\ell/d)\{(1 + \nu_m)(E_w/E_m)\ell n[V_w]^{-1/2}\}^{-1/2}$$

For the yield stress,

$$\sigma_{yc}/\sigma_{ym} = 0.5\, V_w(2 + \ell/d) + (1 - V_w) \tag{2}$$

where E_m, E_w and E_c are Young's moduli of the matrix, whisker and composite, respectively, V_w is the volume fraction of whiskers, σ_{ym} and σ_{yc} are the yield stresses of the matrix and composite, respectively, and ℓ/d is the whisker aspect ratio.

In the shear lag model of Fig. 1, there exists an uncertainty regarding the relation between ℓ/d and L/D which is usually found from observations of SEM photos. In deriving Eq. (1), we have used the same assumption as Kelly and Street (4), i.e., $L = \ell$. This assumption would certainly induce errors in the analysis for the case of smaller whisker aspect ratios.

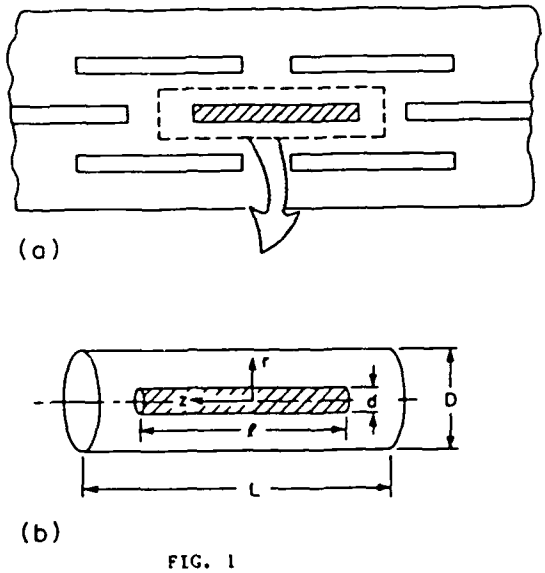

FIG. 1
Shear lag model for an aligned short fiber composite (a), and its unit cell (b).

2. Eshelby Type Model

The original Eshelby model (6) is based on the assumption that an ellipsoidal inclusion with uniform non-elastic strain (eigenstrain) $\underset{\sim}{e}^*$ is embedded in an infinite elastic body. Eshelby (6) derived the formula to compute the stress field induced in and around an inclusion and also the associated strain energy of this system. Mori and Tanaka (7) modified the original Eshelby model to account for the interaction between inclusions. If we apply the modified Eshelby model to prediction of the stiffness of an aligned short fiber composite (Fig. 2), we must first solve for unknown eigenstrain $\underset{\sim}{e}^*$ in a representative fiber domain (Ω) by using the following equations (8,11,13,16):

$$\underset{\sim}{\sigma}_0 + \underset{\sim}{\sigma} = \underset{\sim}{C}_w \cdot (\underset{\sim}{e}_0 + \bar{\underset{\sim}{e}} + \underset{\sim}{e})$$

$$= \underset{\sim}{C}_m \cdot (\underset{\sim}{e}_0 + \bar{\underset{\sim}{e}} + \underset{\sim}{e} - \underset{\sim}{e}^*) \tag{3}$$

$$\underset{\sim}{e} = \underset{\sim}{S} \cdot \underset{\sim}{e}^* \tag{4}$$

$$\underset{\sim}{\sigma}_0 = \underset{\sim}{C}_m \cdot \underset{\sim}{e}_0 \tag{5}$$

where $\underset{\sim}{\sigma}_0$ and $\underset{\sim}{e}_0$ are the uniform stress and strain field, respectively, $\underset{\sim}{\sigma}$ and $\underset{\sim}{e}$ are the stress and strain distributed by the existence of a short fiber, $\bar{\underset{\sim}{e}}$ is the average disturbance of strain

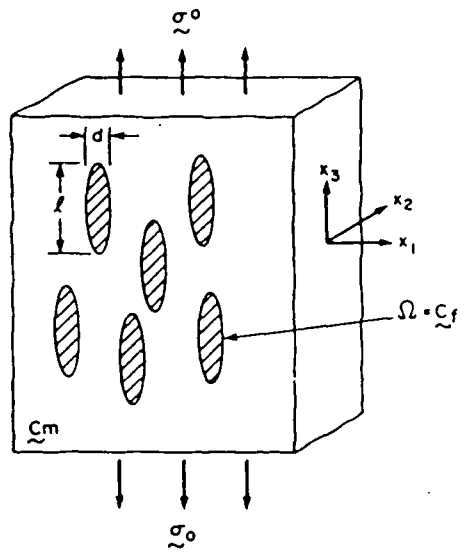

FIG. 2
Eshelby type model for aligned short fiber composites.

in the matrix, $\tilde{e}^*$ is the unknown eigenstrain with a non-zero value of Ω ($\tilde{e}^*$ is zero otherwise), $\tilde{C}_m$ and $\tilde{C}_w$ are the stiffness tensors of the matrix and fiber, respectively, and $\tilde{S}$ is Eshelby's tensor, which is a function of the matrix Poisson's ratio and the whisker aspect ratio. Then, the following equation for equivalency in strain energy is used to obtain the stiffness of the composite (16):

$$\frac{1}{2}\tilde{\sigma}_0 \cdot \tilde{C}_c^{-1} \cdot \tilde{\sigma}_0 = \frac{1}{2}\tilde{\sigma}_0 \cdot \tilde{e}_0 + \frac{1}{2} V_w \tilde{\sigma}_0 \cdot \tilde{e}^* \qquad (6)$$

where $\tilde{C}_c$ is the stiffness tensor of the composite. By applying various far field stresses $\tilde{\sigma}_0$, we can compute the various stiffnesses of the composite (up to five in the case of Fig. 2). For example, in the case of $\tilde{\sigma}_0 = (0, 0, \sigma_0, 0, 0, 0)$, the Young's modulus along the fiber axis (x_3 - axis in Fig. 2) E_c can be obtained as,

$$E_c/E_m = 1/(1 + V_w(E_m/\sigma_0)e^*_{33}) \qquad (7)$$

where e^*_{33} is to be computed from Eqs. (3)-(5) and the results are expressed in term of $c_o(\sigma_0/E_m)$ and c_o is some numerical value.

The above formulation (Eqs. (3)-(5)) can also be applied to the computation of the yield stress if one replaces $\tilde{e}$ by $\tilde{e} - \tilde{e}_p$ in Eq. (3), where $\tilde{e}_p$ is the uniform plastic strain in the matrix (9-11). When the thermal residual stress is accounted for in the model to predict the yield stress (10,11), one must replace $\tilde{e}$ by $\tilde{e} - \tilde{e}_p - \tilde{\alpha}^*$ in Eq. (3) where $\tilde{\alpha}^*$ is the mismatch strain caused by the difference in coefficients of thermal expansion (CTEs) between the fiber and the matrix. The yield stress of the composite can then be obtained by using the follcwing energy balance equation:

$$\delta U = -\delta Q \qquad (8)$$

where δU is the change in the total potential energy arising from the change in the plastic strain in the matrix, and δQ is the plastic work done in the matrix. The eigenstrain $\tilde{e}^*$ that is determined as described above is used to evaluate δU and δQ. The formula to predict the yield stress is finally reduced to (17):

$$\sigma_{yc} = c_1\sigma_{ym} + c_2 e_p \qquad (9)$$

where c_1 is a non-dimensional parameter (the yield stress raiser), c_2 is the work-hardening rate and e_p is the plastic strain in the matrix along the fiber axis.

Numerical Results and Discussion

In order to compare these models, we have computed the stiffness (E_c) and the yield stress (σ_{yc}) of an aligned short whisker MMC by using Eqs. (1) and (2) (shear lag type model) and Eqs. (7) and (9) (Eshelby type model). The target short whisker MMCs are spherical SiC (SiC_s) and SiC whiskers (SiC_w)/1100 Al matrix composites (18). The numerical results of E_c/E_m based on the shear lag type and Eshelby type models are plotted as dashed and solid curves, respectively, as a function of whisker aspect ratio ℓ/d in Fig. 3. The experimental results (18) are also plotted as a circles in Fig. 3. The material constants used in this calculation are given in Table I. It can be seen in Fig. 3 that the stiffnesses predicted by the shear lag type model are always less than those predicted by the Eshelby type model and that the shear lag model is a rather crude approximation for smaller ℓ/d. A comparison with the experimental results reveals

that the Eshelby type model gives a better prediction.

TABLE I.
Material data used to predict E_c and σ_{yc}

Material Constants	Unit	Al 1100 (Al 6061-T6)	SiC Whisker
E	GPa	74.	483.
ν	1.	0.33	0.17
α	10^{-6}/C	23.6	4.3
σ_y	MPa	35.2 (357)	--
V_f	1.	--	0.2

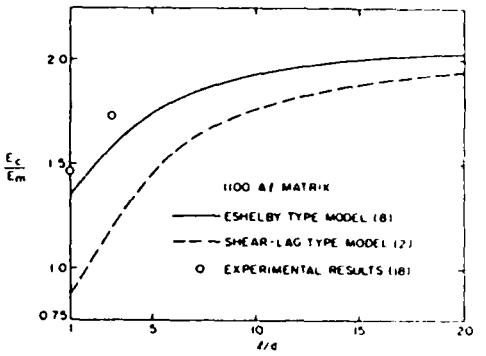

FIG. 3
The ratio of modulus of the composite to modulus of the matrix versus length to diameter ratio of fiber.

It was assumed in the above models that short whiskers of the same size are aligned in a certain direction. However, in actual short whisker composites, some (sometimes most) of the short whiskers are misoriented and also the length of short whiskers varies because of the processing. The effect of the misorientation and variable whisker aspect ratio of short whiskers on the stiffness of the composite has recently been studied by Takao and his co-workers (19,20), who concluded that the use of the mean value of ℓ/d can give rise to reasonably good prediction of the stiffness unless the distribution of variable whisker aspect ratio is too widely scattered (20) and that the width (β) of the distribution of fiber misorientation angle (θ) about the x_3-axis (Fig. 2) has a strong effect on E_c for $\beta > 10$ degree (19). Thus, more accurate data on the distribution of ℓ/d and θ is needed to better predict the stiffness and other properties. The modified Eshelby model that we have developed to predict the thermal and mechanical properties of composites (19,20) can accommodate such detailed information. This is another advantage of the Eshelby type model in comparison to the shear lag type model.

Next we have computed the values of σ_{yc}/σ_{ym} based on Eqs. (2) and (9), the results of which are plotted as dashed and solid curves, respectively in Fig. 4, where the closed circles denote the experimental results for a specific SiC_w/Al 6061-T6 composite (3) and the predicted values based on the modified Eshelby model, with residual stress accounted for, are plotted as a dash-dot curve. All predictions are plotted as a function of ℓ/d. In the range of small ℓ/d the Eshelby type model gives an accurate prediction, particularly at $\ell/d = 1$, while the shear lag model gives an underestimate. However, at larger ℓ/d's, both models predict basically the same order of composite tensile yield stress. In the same figure, our recent results for various SiC_w/Al composite systems are also plotted as open symbols. Though the Eshelby type model gives reasonable predictions for the case of the T6-treated composite (●), the stress prediction of both models is low compared to the experimental results for most of the data (○, ◇, □ and △). The poorest prediction occurs for the case of an annealed 1100 aluminum composite (○).

The experimental σ_{yc} and σ_{ym} correspond to the stress at 0.2% offset, and σ_{ym} is for a 0 V% material produced in the same manner as the composite. The reason that both of these models are not capable of predicting the observed strengthening, is that these models assume that the matrix has the same strength as it has in the non-reinforced condition. In other words, these models assume that the addition of SiC does not change the strength of the matrix. It has been clearly shown that the dislocation density in the SiC/Al composites is much higher than in the non-reinforced Al (21,24).

If the absolute magnitude of the increase σ_{yc} compared to σ_{ym} is considered, then the apparent differences caused by the various matrix alloys is much less. The data shown in Table II indicates that $\Delta\sigma$ ($\Delta\sigma = \sigma_{yc20V\%} - \sigma_{ym0V\%}$) is relatively independent of the composite matrix except for the T6-heat treated case.. The lack of a difference in $\Delta\sigma$ occurs because the thermal stress developed upon cooling is very large compared to the yield stress of the matrix in the annealed condition. The dislocations are generated in the initial cool down whether the sample

is furnace cooled or quenched prior to aging. Therefore, the increased density of dislocations generated is for all practical purposes independent of the matrix.

Since the observed increase in the experimental σ_{yc} is much greater than is predicted by the shear lag type model or the Eshelby type model, the increase in σ_{yc} must be caused by the increased dislocation density in the composite matrix. This increase in dislocation density is the result of relaxation of a portion of the stresses developed upon cooling of the composite. The stresses arise from the differences in coefficients of thermal expansion between the SiC and Al. The effect of this thermal expansion mismatch strain ($\Delta\alpha\Delta T$) has been considered in the Eshelby model, with residual stress accounted for (dot-dot curve in Fig. 4) (11,17). However, in the model $\Delta\alpha\Delta T$ is simulated by the equivalent surface dislocations (15) that are present at the matrix-whisker interfaces. In reality, the surface dislocations are more like to relax by punching (27), resulting in the localization of dislocations around a whisker.

TABLE II.
The Absolute Difference in Yield Strength (Ref. 23)

Matrix	Reinforcement	Heat Treatment	$\Delta\sigma$ (MPa)
1100	20 V% whisker	Annealed	104 to 145
6061	20 V% whisker	Annealed	101
6061	20 V% whisker	HT to T6	207
7091	20 V% whisker	Annealed	131

If we now consider the proportional limit of the composite, an interesting correlation can be obtained. The proportional limits of the composites (22,25) are approximately equal to σ_{ym}. This correlation gives rise to two important points. First, the modulus (E_c) that is predicted by the Eshelby type model, which is in agreement with the experimental data, is for the initial portion of the stress-strain curve, i.e., for stresses up to the proportional limit. Therefore, the Eshelby type model does operate up to the proportional limit, and the model predicts a very small increase in the proportional limit upon the addition of the reinforcement, again in agreement with the experimental data. Second, the increase in stress with strain in the stress region from the proportional limit to σ_{yc} is caused by an exhaustion phenomena. In this stress-strain region, dislocation motion occurs in the lower dislocation density regions within the matrix. The increase in stress between the proportional limit and the σ_{yc} is not caused by work hardening, for there is no general increase in dislocation density (26). After tensile fracture of the composite sample there is an increase in dislocation density in the region of the fracture, i.e., within 100 μm of the fracture surface. The dislocation density in the remainder of the sample is identical to that of the undeformed sample. However, only limited deformation can occur, because of the small volume of matrix. In order to have macrodeformation, i.e., to reach 0.2% offset strain, additional dislocation motion must occur in the higher stress regions of the matrix which are often quite localized in the specimen. Therefore, the macroyielding of the composite is controlled by the inhomogeneous matrix which is a mixture of the high-low dislocation regions.

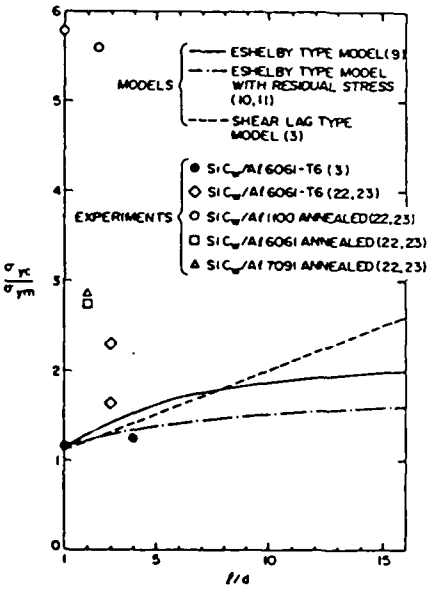

FIG. 4
The ratio of the yield stress composite to matrix versus length to diameter ratio of fiber. For 20 V% SiC.

Concluding Remarks

A comparison between the shear lag type and Eshelby type models was made in terms of their capabilities of predicting the stiffness and yield stress of a short fiber MMC. This has led to the following concluding remarks:

1. The shear lag type model underestimates the modulus, especially for small ℓ/d values, whereas the Eshelby type model is in good agreement with experimental data.
2. For a specific To-treated SiC/Al composite, the Eshelby type model gives good predictions of the yield stress and the agreement with the experimental results is excellent at ℓ/d = 1, whereas the shear lag type model underestimates the yield stress.
3. Both models, in general, predict a yield stress which is much less than that experimentally determined. This is caused by strengthening of the matrix by dislocation generation as a result of differences in thermal coefficients of expansion.
4. The Eshelby type model can account for the stress-strain curve of the composite for stresses up to the proportional limit.
5. The increase in stress between the proportional limit and the macroscopic yield stress is caused by an exhaustion process and not a work hardening mechanism.
6. The Eshelby type model is also applicable to non-mechanical properties of a composite, such as thermal conductivity, while the shear lag type model has been applied only to the mechanical behavior.

Acknowledgements

One of the present authors (M.T.) is greatly thankful to the Royal Society for its financial support, and to Drs. J. Harding and B. Derby of Oxford for their valuable comments, and the other (R.J.A.) to the Office of Naval Research for its financial support under Contract No. N00014-85-K-0007. The authors gratefully acknowledge the discussion with Dr. V. Nardone.

References

1. H. L. Cox, Br. J. Appl. Phys. 3, 72 (1952).
2. A. Kelly, Strong Solids, p. 123, Clarendon Press, Oxford (1966).
3. V. C. Nardone and K. M. Prewo, Scripta Metall. 20, 43 (1986).
4. A. Kelly and K. N. Street, Poc. Roy. Soc. Lond. A328, 283 (1972).
5. J. M. Hedgepeth and P. Van Dyke, J. Comp. Mater. 1, 294 (1967).
6. J. D. Eshelby, Proc. Roy. Soc. Lond. A241, 376 (1957).
7. T. Mori and K. Tanaka, Acta Metall. 21, 571 (1973).
8. M. Taya and T. Mura, J. Appl. Mech. 48, 361 (1981).
9. T. Tanaka, K. Wakashima, and T. Mori, J. Mech. Phys. Solids 21, 207 (1973).
10. K. Wakashima, S. Suzuki, and S. Umekawa, J. Comp. Mater. 13, 288 (1979).
11. R. J. Arsenault and M. Taya, p. 21, Proc. ICCM-V, eds. by W. C. Harrigan Jr., J. Strife, and A. Dhingra, TMS-AIME, Warrendale, PA (1985).
12. K. Wakashima, M. Otsuka, and S. Umekawa, J. Comp. Mater. 8, 391 (1974).
13. Y. Takao and M. Taya, J. Appl. Mech. 107, 806 (1985).
14. H. Hatta and M. Taya, J. Appl. Phys. 58, 2478 (1985).
15. T. Mura and M. Taya, p. 209, Recent Advances in Composites in the United States and Japan, ASTM STP 864, eds. J. R. Vinson and M. Taya, Philadelphia, PA (1985).
16. T. Mura, Micromechanics of Defects of Solids, Martinus Nijhoff Publication, The Hague (1982).
17. R. J. Arsenault and M. Taya, to appear in Acta Metall.
18. A. Wolfenden and R. J. Arsenault, unpublished results.
19. Y. Takao, T. W. Chou and M. Taya, J. Appl. Mech. 49, 536 (1982).
20. Y. Takao, and M. Taya, J. Comp. Mater., in press (1986).
21. M. Vogelsang, R. J. Arsenault, and R. M. Fisher, Met Trans. 17A, 379 (1986).
22. R. J. Arsenault and B. Wu, submitted for publication.
23. R. J. Arsenault, Proc. of Third Japan Conference, Composites '86. Recent Advances in Japan and United States, Ed. by K. Kauata et al., in press.
24. R. J. Arsenault and R. M. Fisher, Scripta Metall. 17, 67 (1983).
25. R. J. Arsenault, Mat. Sci. & Eng. 64, 171 (1984).
26. R. J. Arsenault and C. R. Feng, to be submitted for publication.
27. M. Taya and T. Mori, Acta Metall., in press.

The Strength Differential and Bauschinger Effects in SiC–Al Composites*

R. J. ARSENAULT and S. B. WU

Engineering Materials Group, University of Maryland, College Park, MD 20742 (U.S.A.)

(Received February 3, 1987; in revised form May 22, 1987)

ABSTRACT

An investigation was undertaken to determine the effect of an average elastic residual stress on the strength differential and the Bauschinger effects in SiC-Al alloy composites. It was found that the compressive yield stress of the composites was greater than the tensile yield stress from whisker- and platelet-reinforced composites but, for composites containing spherical SiC reinforcement, the compressive yield stress was slightly less than the tensile yield stress. The experimentally observed differences are in agreement with the differences predicted by an analytical theory. This analytical theory also predicts that the magnitude of the Bauschinger effect will be greater for a test initially begun in compression than for a test initially begun in tension, and the experimental results are in agreement with this prediction.

1. INTRODUCTION

Several years ago, there was a great deal of interest in the strength differential effect (SDE). The SDE is the difference in the yield or flow stress σ_c in compression with the yield or flow stress σ_t in tension. Some of the first theories proposed to explain the SDE include the internal Bauschinger effect (BE), residual stresses, microcracking, retained austenite, and volume expansion due to plastic deformation. A critical review of these various theories as well as a proposed theory of solute-dislocation interactions have been included in the paper by Hirth and Cohen [1].

Subsequently, Pampillo *et al.* [2] concluded that the theory of Hirth and Cohen [1] could not be used to explain the data and proposed a theory based on the "effective modulus". Later, Spitzig and Richmond [3] conducted several investigations and concluded that the SDE is primarily a manifestation of the pressure dependence of the flow stress. The maximum value of SDE predicted is small, for metals, without being subjected to an external hydrostatic pressure.

Recently, Arsenault and Taya [4] have developed an analytical model which would predict a SDE in metal matrix composites, more specifically SiC in aluminum alloys. The SDE would result from residual elastic stress (in the matrix the average residual stress is in tension) due to the difference in the thermal expansion coefficients of the SiC and aluminum. Watt and Jain [5] also concluded that residual stresses are the cause of the SDE. Watt and Jain's conclusion was obtained from a consideration of data from a martensite-ferrite steel.

The model developed by Arsenault and Taya [4] is an analytical solution based on Eshelby's method [6]. The reinforcement is treated as an ellipsoidal inclusion. The ellipsoidal inclusion is a good approximation of the whisker reinforcement. A sphere is a special case of an ellipsoid; therefore, there is no approximation concerning spherical reinforcement. For particulate reinforcement, only qualitative predictions can be made when using the Arsenault and Taya model. The model would predict that the SDE would be large (relative) for the whisker-reinforced composites, smaller for the particulate-reinforced composites and zero for spherically reinforced composites.

From the analytical and numerical results obtained by Arsenault and Taya [4], it is possible to obtain the following expression:

$$\Delta\sigma = \sigma_{yc} - \sigma_{yt} = K V_f^{2/3} \ln\left(\frac{l}{d}\right)\left(\frac{E_w}{E_m}\right)^{1/2} \Delta\alpha\, \Delta T \qquad (1)$$

0025-5416/87/$3.50

where σ_{yc} is the yield stress in compression, σ_{yt} is the yield stress in tension, K is the material constant (for discontinuous SiC in an aluminum matrix, $K = 42.7 \times 10^3$ MPa), V_f is the volume fraction of reinforcement, l is the length of the whisker, d is the diameter of the whisker, E_w is the modulus of whisker, E_m is the modulus of matrix, $\Delta\alpha = \alpha_w - \alpha_m$ (α_w and α_m are the coefficients of thermal expansion of the whisker and matrix respectively) and ΔT is the change in temperature upon cooling. This expression is for the specific case of a ΔT such that yielding, *i.e.* no plastic deformation, does not occur within the matrix on cooling. Therefore the yield strength σ_{ym} of the matrix does not affect the magnitude of $\Delta\sigma$. If two different matrix materials were considered and a given ΔT was chosen such that no plastic deformation occurred in the matrix in one and, in the other, plastic deformation occurred for the same ΔT. Then, it is obvious that the $\Delta\sigma$ would be smaller for the composite in which plastic deformation had occurred. The magnitude cannot be directly calculated from the Arsenault and Taya model but, to a first approximation, $\Delta\sigma$ would scale linearly with a decrease in σ_{ym}. In other words, if ΔT was chosen such that the residual stress is slightly less than necessary to cause yielding in the matrix of the first composite, and the matrix of the second composite had a yield stress half that of the first, then $\Delta\sigma$ of the second composite would be half that of the first composite.

As mentioned above, the BE was a possible explanation of the SDE. More than a century ago, Bauschinger reported that a small permanent strain reduced the elastic limit for reversed stressing. From then on, the BE has been defined in several different ways. Most investigators have chosen to define the BE in terms of a reduction in initial flow stress or yield stress for reverse deformation, while others preferred a more general definition, such as "a certain dependence of the flow stress and rate of work hardening on the strain history", or they simply referred to the existence of different stress-strain curves by loading in the reverse direction. Figure 1 shows schematic representations of a test to measure the BE for two different types of BE.

The number of models or theories that have been developed to explain the BE is

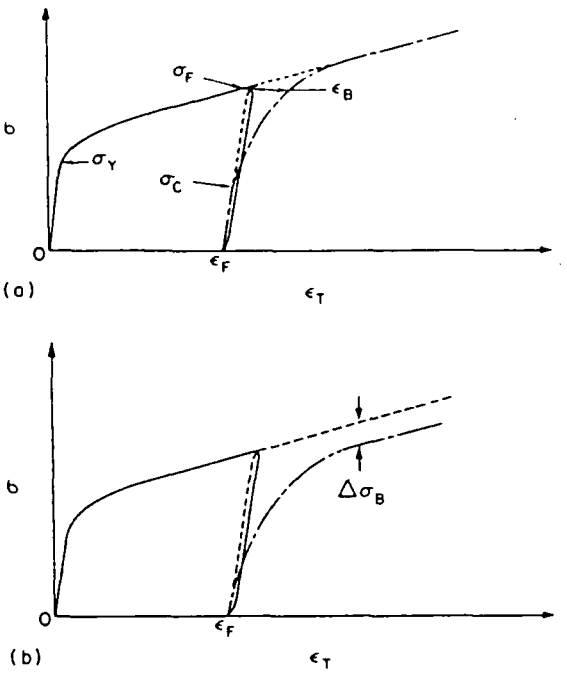

Fig. 1. A schematic plot of absolute stress *vs.* total strain for a Bauschinger test (a) when there is no permanent softening (Bauschinger stress factor, $(\sigma_f - \sigma_c)/\sigma_y$) and (b) when permanent softening has occurred (Bauschinger stress factor, $\Delta\sigma_B$): - - -, reloading, *i.e.* sample tested initially and then retested in the same direction; — · —, reverse loading, *i.e.* direction of loading reversed; ϵ_B, Bauschinger strain case.

almost equal to the number of investigators of the BE. However, all these models can be related to two dislocation mechanisms. The first mechanism is implied in Seeger's work-hardening theory. The long-range internal stress, often called the back stress, which is created by dislocation pile-up at barriers aids dislocation movement and causes a decrease in initial flow stress during reverse loading. The other mechanism is related to Orowan's idea of a directional resistance of dislocation motion due to prestraining. The forward motion of dislocations becomes more difficult because there are an increasing number of stronger barriers ahead of the dislocations as the material work hardens. The barriers behind the dislocations are believed to be weaker and more sparsely spaced than those immediately in front. Thus the stress needed to push the dislocations backward is lower.

Pedersen *et al.* [7] have proposed a "composite model" for the BE and obtained the

following expression for Bauschinger strain ϵ_B:

$$\epsilon_B = 2\frac{\sigma_f - \sigma_y}{\mu V_f \gamma} \quad (2)$$

where σ_f is the flow stress at the end of the forward strain ϵ_F, σ_y is the initial yield stress, μ is the shear modulus, V_f is the volume fraction of the reinforcement and γ is Eshelby's accommodation factor which depends on the aspect ratio of the reinforcement.

The model of Arsenault and Taya [4] can be extended to a consideration of the BE. This model predicts that there would be a difference in the magnitude of the BE depending on the direction of initial loading. If initially the sample was tested in tension and then followed by compression, a smaller BE would result than if the sample was initially tested in compression and then followed by tension. The difference in the BE depending on the initial mode of testing would depend on the shape of the reinforcement. The difference in the predicted BE would be largest for whisker reinforcement and zero for spherical reinforcement. In the other theories and models that have been put forward to predict the magnitude of the BE, the direction of initial loading is irrelevant.

The present investigation was undertaken to determine the magnitude of the SDE and the BE in discontinuous SiC-Al composites and to relate these results to the current theories.

2. MATERIALS

The materials used in this investigation consisted of high purity aluminum (designated HP), a wrought aluminum alloy (6061) (designated WR) and several different SiC-Al alloy composites. The specifics of these materials are given in Table 1. The SiC-whisker-reinforced composite was purchased from ARCO Silag, together with the spherically reinforced composite (diameter of SiC spheres, 0.5 μm). This material was supplied in the form of extruded rods 12.5 mm in diameter. For the whisker-reinforced composite, approximately 95% of whiskers were aligned with the rod axis. Also, a 12.5 mm extruded rod was purchased from ARCO Silag which contained 0 vol.% SiC. This rod was made in the same manner as the rods containing the spherical SiC and the whisker SiC. This material is designated as 0 vol.% SiC_w (where SiC_w denotes SiC whiskers). SiC-particulate-reinforced composites were purchased from DWA Composite Specialties and supplied in the form of as-pressed plate. The particulate SiC has the general shape of platelets, and the platelets are preferentially aligned with the plate parallel to the axis of the sample. Again the 0 vol.% SiC_p (where SiC_p denotes SiC particulates) was produced in the same manner as the composites containing 20 vol.% SiC_p.

The commercially extruded 12.5 mm rod of aluminum alloy 6061, which was defined as WR, was purchased from ALCOA. ALCOA

TABLE 1

Materials

Designation	*Material*	*Volume fraction of SiC* (vol.%)	*Form of SiC*
HP (high purity)	99.99% Al		
WR (wrought)	Al alloy 6061		
Whisker composite	Al alloy 6061	0.0	
Whisker composite	Al alloy 6061	5.0	Whisker, $l/d \approx 2$
Whisker composite	Al alloy 6061	20	Whisker, $l/d \approx 2$
Whisker composite	Al alloy 1100	20	Whisker, $l/d \approx 3$
Spherical composite	Al alloy 1100	20	Spherical, diameter of 0.5 μm
Particulate	Al alloy 6061	0	
Particulate	Al alloy 6061	5	Platelets, $D/t \approx 4$
Particulate	Al alloy 6061	20	Platelets, $D/t \approx 4$

l, length of whisker; d ($\approx$ 0.5 μm), diameter of whisker; D, diameter of particulate platelet; t ($\approx$ 1 μm), thickness of particulate platelet.

also presented a gift of a 12.5 mm extruded rod of 99.99% Al.

Test samples were machined from the extruded rod or the pressed plate into the configuration shown in Fig. 2. After the samples had been machined, they were annealed, quenched or heat treated in the following manner: annealed, 12 h at 810 K and then furnace cooled over a 12 h period; quenched, 3 h at 810 K and then quenched into water at 273 K; heat treated to T6 condition, 3 h at 810 K and then quenched into water at 273 K, followed immediately by 8 h at 450 K; liquid nitrogen quenched, following a water quench or heat treatment to T6 quench, quenched into liquid nitrogen.

3. TESTING PROCEDURE

Initially, cylindrically shaped compression samples with an aspect ratio of 2 and 3 were tested, using a technique, which has been developed previously [8]. The tensile testing was undertaken with a sample configuration described elsewhere [9]. However, this method, *i.e.* two different sample configurations, could not be easily used for the BE tests. These sample configurations were discarded in favor of the single configuration for both tensile and compression testing. The compressive strengths obtained from the cylindrical compression samples were almost identical with those obtained from the single-sample-configuration tests, *i.e.* the configuration shown in Fig. 2. All the data reported in this paper is from the sample configuration shown in Fig. 2.

Most of the testing was performed with an Instron testing machine (some tests were performed with an M/B servohydraulic machine) with the gripping apparatus shown in Fig. 3. The purpose of this grip arrangement was to ensure that very good alignment was obtained; the maximum misalignment was 1.4×10^{-2}°. This maximum misalignment would result in a surface tensile or compressive stress because of a bending of 0.2% of the applied compressive stress.

Since the lower end of the sample was immersed in the Woods metal, there could be a slight temperature rise (of about 50 K) in the gauge portion of the sample. This was prevented by placing a moistened paper towel around the gauge section of the sample during the insertion of the sample into the molten Woods metal and while solidification was taking place.

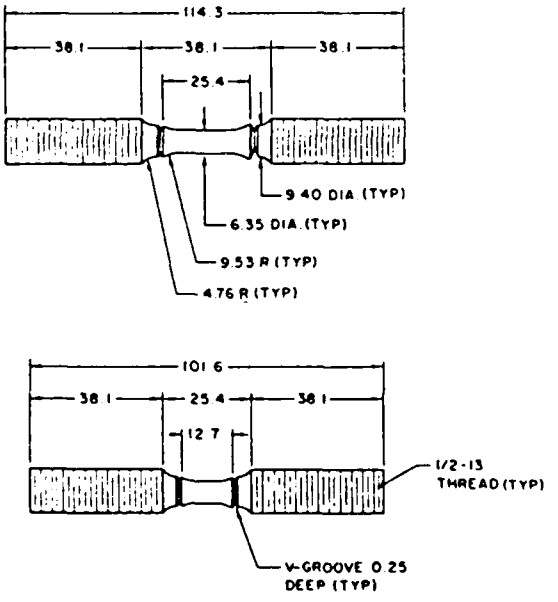

Fig. 2. A diagram of the single sample configuration which was used for both tension and compression testing (for strength differential effect tests) and reverse loading testing (for Bauschinger effect tests) (all dimensions are in millimeters): DIA, diameter; R, radius; TYP, typical.

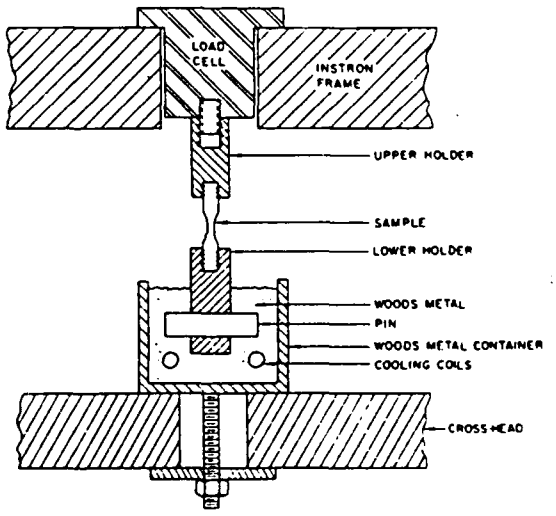

Fig. 3. A schematic representation of the testing apparatus which was used to ensure very good alignment of the sample in both tension and compression.

The effective gauge length of the samples was determined by gluing strain gauges on the center portion of the sample and comparing the results obtained from a clip-on extensometer which was mounted into the V-grooves. If the extensometer is mounted directly onto the uniform gauge section, there is a high probability that the sample will fracture where the knife edge of the extensometer makes contact with the sample. Several tests in the low stress range were conducted using both the extensometer and the strain gauge; from these tests the effective gauge length was determined. Subsequent tests were conducted using only the extensometer.

In Fig. 2, there are two gauge lengths shown. It was determined that this difference in gauge length had a very small effect (less than 10%) on the results obtained. The yield stress was defined as the stress at a 0.2% offset strain. The choice of 0.2% offset strain to define the yield stress was chosen to conform with data previously generated, and 0.2% offset strain is a widely accepted choice for defining the strains at the yield stress.

Initially, several different strain rates were used in the testing, from 5×10^{-5} to 5×10^{-3} s^{-1} and, as expected, only small differences were observed. All data reported in this paper were obtained at the strain rate of $5 \times 10^{-4} s^{-1}$.

4. EXPERIMENTAL RESULTS

The experimental results are divided into two parts: the SDE, *i.e.* the difference in compressive and tensile yield stresses, and the BE. Approximately 200 samples were tested in the generation of the experimental results. In the plots, only data points are shown; error bars were not placed on the plots, because the plots would become too confusing. In the case where there is only one data point for a given condition, then the scatter in the data was very small from at least three tests of that condition. If there are two data points for a given condition, then these two points cover the range of the scatter, and in all cases the average was at the midpoint between the two data points.

4.1. Strength differential effect

The shapes of the stress-strain curves obtained from the same material, whether tested in compression or tension, were very similar; however, in most cases the compression test resulted in overall higher values of stress at a given strain. The examples given in Fig. 4 are typical of the results obtained. These curves were obtained from annealed matrix aluminum alloy 6061 with 0 vol.% SiC_p, 5 vol.%

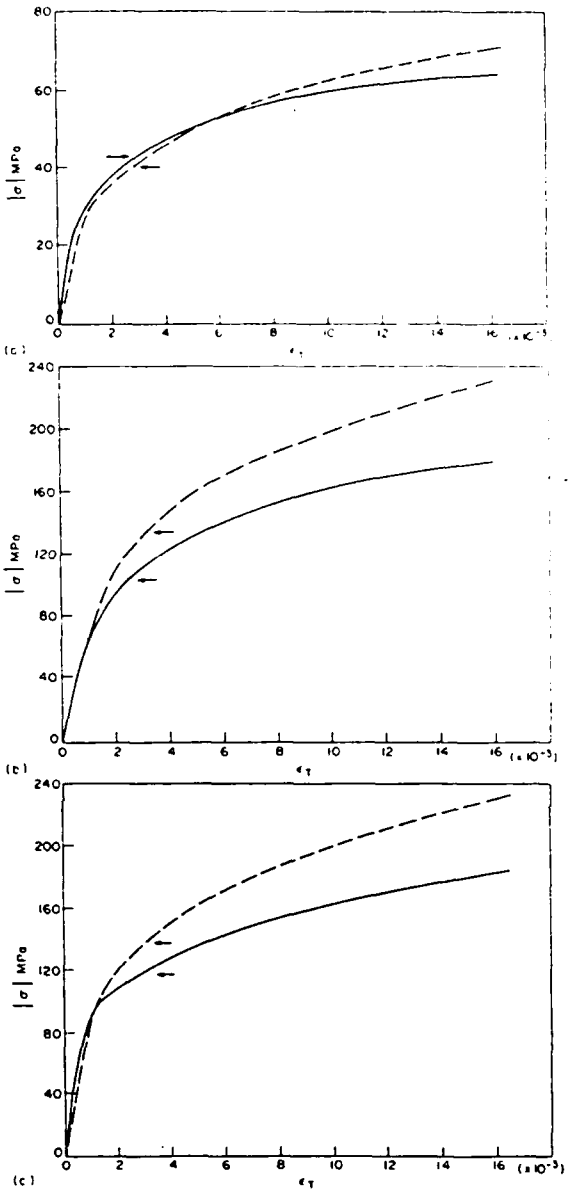

Fig. 4. Typical plots of the absolute stress *vs.* the total strain (a) for the annealed 0 vol.% SiC_p composite, (b) for the annealed 5 vol.% SiC_w composite and (c) for the annealed 20 vol.% SiC_p composite: (matrix, aluminum alloy 6061): ——, sample tested in tension; - - -, another sample tested in compression; •——, yield stress.

SiC_w and 20 vol.% SiC_p. However, when the stress-strain curves of SiC whisker composites were examined in detail at small strains, there were differences between the tensile and compressive test results. The extent of the linear region, *i.e.* the proportional limit, is higher for a compressive test than for a tensile test, as shown in Fig. 5. This difference was readily detectable in both the aluminum alloy 6061 and the aluminum alloy 1100 matrix composites containing whisker SiC reinforcement. The difference was greater for the 20 vol.% SiC_w composite than for the 5 vol.% SiC_w composite. For the particulate-reinforced composite, the difference in the proportional limit between tension and compression was not consistent, *i.e.* the proportional limit in most cases was approximately the same for tension as for compression. If only the proportional limit in tension is considered for all SiC composites, then there is a good correlation between the proportional limit of the composite and yield strength of the comparable matrix material [9]. In other words, the yield stress of age-hardened (T6) aluminum alloy 6061 is within 10% of the proportional limit of 20vol.%SiC_w-aluminum alloy 6061 composite in the age-hardened (T6) condition. Similarly the proportional limit of the 20vol.%SiC_s-aluminum alloy 1100 composite (where SiC_s denotes SiC spheres) in the annealed condition is approximately equal to the yield stress of annealed aluminum alloy 1100. Another point should be made; the yield stress of the powder metallurgical product which has been designated as 0 vol.% SiC_w and 0 vol.% SiC_p is within ±10% of the yield stress of the wrought alloys when tested in the same condition (*e.g.* comparing annealed powder metallurgical alloy with annealed wrought alloy).

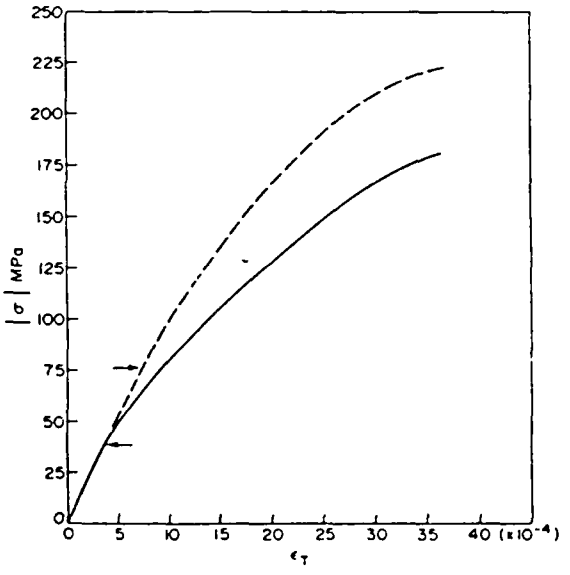

Fig. 5. A plot of the absolute stress *vs.* total strain showing an expanded region for small strains for both tension (——) and compression (- - -) testing of annealed 20 vol.% SiC_w composite samples (matrix, aluminum alloy 1100): ——, proportional limit.

There are several different methods of quantitatively describing the SDE. The absolute magnitude of the SDE was defined as $\Delta\sigma$, which is $\sigma_{yc} - \sigma_{yt}$. The magnitude of the SDE can also be expressed in terms of a percentage

$$\text{SDE} = \frac{2(\sigma_{yc} - \sigma_{yt})}{\sigma_{yc} + \sigma_{yt}} \times 100 \qquad (3)$$

The remainder of the discussion of the experimental results of the SDE will be divided into three parts: (1) aluminum alloy 6061 matrix with SiC whisker reinforcement, (2) aluminum alloy 6061 matrix with SiC particulate reinforcement and (3) aluminum alloy 1100 with spherical and whisker SiC reinforcement.

4.1.1. Aluminum alloy 6061 matrix with SiC whisker reinforcement

The data obtained for matrices of various aluminum alloy 6061 materials as a function of the volume fraction of SiC whiskers as well as wrought commercial aluminum alloy 6061 (WR) and 99.99% Al (HP) are plotted in Fig. 6. For HP there was no difference between the compressive and tensile yield stress, as expected. It was assumed that there would be no difference between wrought aluminum alloy 6061 and the 0 vol.% SiC_w-aluminum alloy 6061, since there is no difference in the yield stresses. However, for the heat-treated wrought aluminum alloy 6061, there was a difference between the compressive and tensile yield stress whereas, in the 0vol.%SiC_w-aluminum alloy 6061, there was no difference between the compressive and tensile yield stress. Also, there were no differences between the compressive and tensile yield stresses for the 0vol.%SiC_w-aluminum alloy

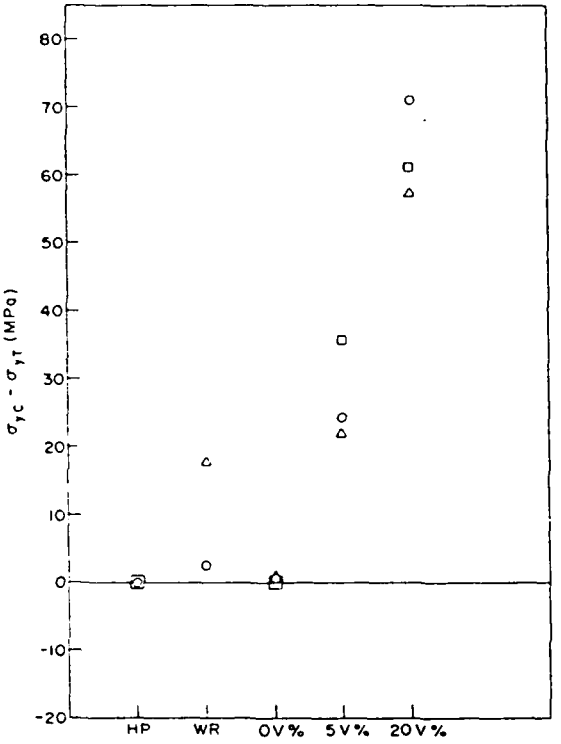

Fig. 6. A plot of the difference between the compressive yield stress and the tensile yield stress for various volume fractions of whisker composite materials (matrix, aluminum alloy 6061): ○, annealed; □, quenched; △, heat treated to T6 condition. Also plotted is the difference in yield stress for high purity aluminum and wrought aluminum alloy 6061.

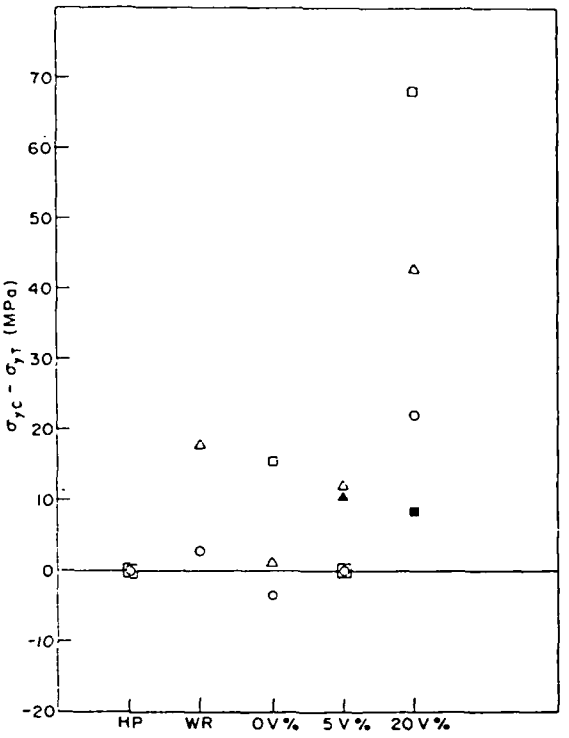

Fig. 7. A plot of the difference in yield stress for various volume fractions of particulate composite materials: (matrix, aluminum alloy 6061): ○, annealed; □, quenched; △, heat treated to T6 condition; ■, liquid nitrogen quenched; ▲, heat treated to T6 condition and liquid nitrogen quenched. Also, the difference in yield stress for high purity aluminum and wrought aluminum alloy 6061.

6061, the quenched samples and the annealed samples.

The effect of increasing the volume fraction of SiC whiskers was to increase the magnitude of the difference between σ_{y_c} and σ_{y_t}. For all three conditions, *i.e.* annealed, quenched and heat treated to T6, as the volume fraction of SiC whiskers increases, the magnitude of $\Delta\sigma$ increases. However, the relative increase is not consistent. In other words, for the 5 vol.% SiC_w composite, the quenched condition results in a larger $\Delta\sigma$, but for the 20 vol.% SiC_w composite the annealed condition results in the largest $\Delta\sigma$. If the SDE is considered as a percentage, then for the 20 vol.% SiC_w composite in the annealed condition the SDE is equal to about 12%, which results in about the same value of SDE as 14% martensite in ferritic steel [5].

For samples that were quenched or heat treated, there was also an increase in the magnitude of $\Delta\sigma$ with increasing volume fraction of SiC whiskers. The data obtained from samples which were annealed, quenched and heat treated did not exhibit any consistent trait, *e.g.* the quenched samples did not consistently produce a larger value of $\Delta\sigma$. The data indicated that the condition, *i.e.* annealed *vs.* quenched or heated *vs.* quenched, had very *little effect on the magnitude of* $\Delta\sigma$.

4.1.2. Aluminum alloy 6061 matrix with SiC particulate reinforcement

Particulate SiC in an aluminum alloy 6061 matrix had the same general trends as those of the whisker composite samples. That is, as the volume fraction of particulate increases, so does $\Delta\sigma$, but there are differences as plotted in Fig. 7. The data for HP and WR are the same as those plotted in Fig. 6 and are plotted here for the purpose of comparison. The data

from the particulate composites do not follow any uniform trend. There is not a uniform increase in $\Delta\sigma$ with increasing volume fraction of SiC particulates, *e.g.* there is very little difference between the 0 and 5 vol.% SiC_p composites. For the quenched 20 vol.% SiC_p composite, $\Delta\sigma$ is much larger than $\Delta\sigma$ for the annealed 20 vol.% SiC_p composite, whereas $\Delta\sigma$ for the annealed 20 vol.% SiC_w composite was slightly larger than $\Delta\sigma$ for the quenched 20 vol.% SiC_w composite. When the 20 vol.% SiC_p composite was subjected to a liquid nitrogen quench after a water quench, a much smaller difference between σ_{yc} and σ_{yt} resulted. The water quench only resulted in a $\sigma_{yc} - \sigma_{yt}$ value of 70 MPa, whereas the liquid nitrogen quench after a water quench resulted in a $\sigma_{yc} - \sigma_{yt}$ value of 8 MPa. If the difference between σ_{yc} and σ_{yt} is initially small, *e.g.* for a heat-treated 5 vol.% SiC_p composite, then the effect of the subsequent liquid nitrogen quench was minimal, as expected.

4.1.3. Aluminum-alloy 1100 matrix with spherical and whisker reinforcement

For the aluminum alloy matrix, the volume fraction was held constant at 20 vol.% and the morphology of the SiC was changed from whisker to spherical SiC 0.5 μm in diameter. From a comparison of the data in Table 2 with that in Fig. 6, it is obvious that the difference between σ_{yc} and σ_{yt} is larger for the aluminum alloy 6061 matrix, by a factor of about 2 for the 20 vol.% SiC_w composite. In Table 2, it is possible to compare the effect of different reinforcement morphologies. The theoretical prediction is that $\Delta\sigma$ should be zero for the spherical SiC case and a large positive value for the whisker case. The experimental data (Table 2) indicate that $\Delta\sigma$ is negative for the spherical SiC morphology, *i.e.* $\sigma_{yt} > \sigma_{yc}$.

TABLE 2

Difference $\Delta\sigma$ ($= \sigma_{yc} - \sigma_{yt}$) in the yield stresses

Matrix	*Condition*	*Volume fraction* (vol.%)	$\Delta\sigma$ (MPa)
Al alloy 1100	Annealed	0	3.80
Al alloy 1100	Annealed	20 SiC_w	42.92
Al alloy 1100	Annealed	20 SiC_s	−15.46

4.2. Bauschinger effect

Before discussing the experimental results obtained from the BE investigation, we shall briefly define the parameters that were used to measure the magnitude of the BE. Figure 1 shows schematic representations of Bauschinger tests. The Bauschinger strain ϵ_B, which is used as a measure of the BE when the flow stress in the reverse direction, becomes equal to the flow stress at the end of the forward strain (Fig. 1(a)). The curves obtained from tests conducted first in tension followed by compression are very similar to the curve in Fig. 1(a). If there is permanent softening on reverse loading, then the difference between the projected flow stress in the forward direction minus the maximum flow stress in the reverse direction (this difference is defined as the Bauschinger stress) is used to define the magnitude of the BE (Fig. 1(b)). This is a typical result for tension first, followed by compression. It is possible that the stress-strain curves may have a complicated shape when a second phase is present [10].

The stress-strain curves on reverse loading did not have any unusual shape change; their shapes are as shown in Fig. 4. Therefore the model proposed by Asaro [11], based on strong precipitates as the cause of complicated shape, cannot apply to SiC-Al composites, even though SiC is equivalent to very strong precipitates. Ideally, it would have been useful to determine the effect of strain on the BE. However, this could only be accomplished for the lower volume fractions of SiC. At higher volume fractions of SiC, the maximum strain that could be used consistently was a plastic strain of 1.5%. Therefore, this was the strain that was chosen as the forward strain for all tests that are reported here. Some results were obtained as a function of strain, and these were compatible with the previous results, *i.e.* the BE increased with forward strain.

The BE (Fig. 8) for the 0, 5 and 20 vol.% SiC_w composite material is higher than that of the HP and WR materials when initially tested in tension. From a consideration of the data, there is no obvious trend with respect to heat treatment.

If we now consider the case where the initial test was conducted in compression first, then the magnitude of the BE is significantly increased. If the BE strain is plotted

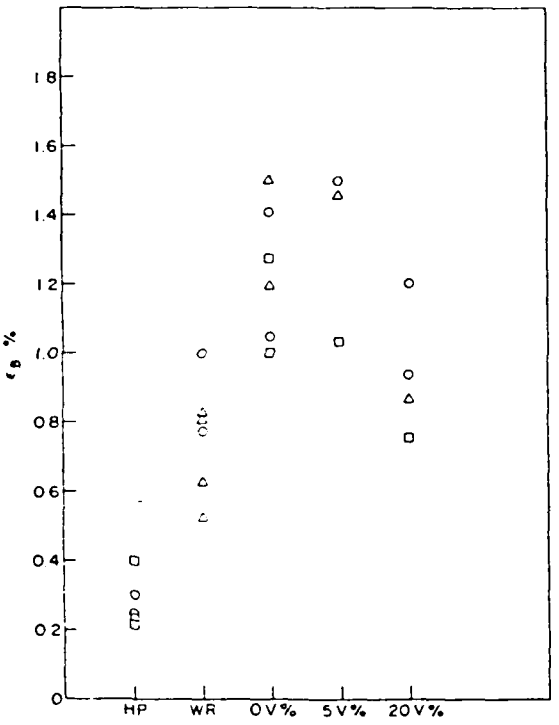

Fig. 8. A plot of the Bauschinger strain *vs.* the volume fraction of whiskers in a composite material (matrix, aluminum alloy 6061; $\epsilon = 1.5\%$): ○, annealed; □, quenched; △, heat treated to T6 condition. In this case, the tests were initially conducted in tension. Also plotted is the Bauschinger strain for high purity aluminum and wrought aluminum alloy 6061.

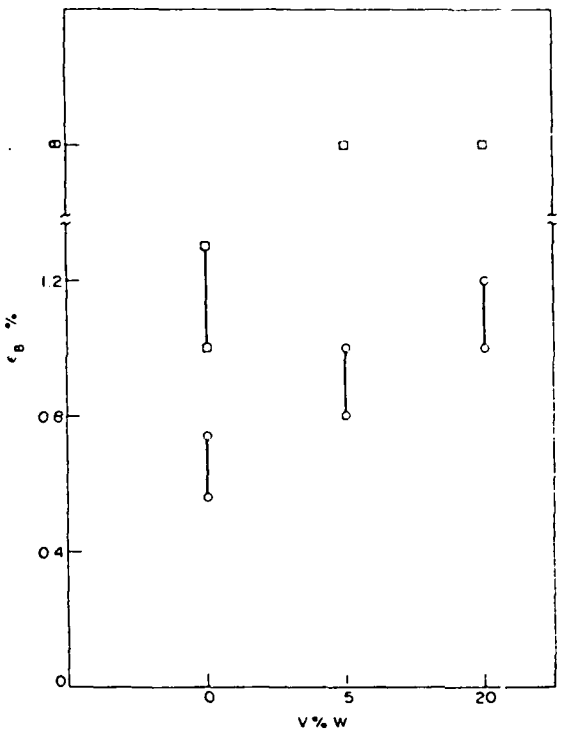

Fig. 9. A plot of the Bauschinger strain *vs.* the volume fraction of whiskers in a composite with an aluminum alloy 6061 matrix for both tension-first (○) and compression-first (□) testing ($\epsilon_F = 1.5\%$).

(Fig. 9), then the BE strain increases from 1% to 2% to infinity for the 5 and 20 vol.% SiC_w composites. In Fig. 10 are plotted the BE stress value and the BE strain for tests initially conducted in compression. As can be seen, there is somewhat of a general increase in the BE as the volume fraction of SiC increased.

A similar series of experiments was conducted with particulate SiC-Al composites. Figure 11 is a plot of data obtained from particulate SiC in an aluminum alloy 6061 matrix for tests initially conducted in tension. Similar to the results obtained for the whisker material, there is no obvious increase in the Bauschinger strain with an increase in volume fraction of the particulate. Secondly, the Bauschinger strain is about the same for the 20 vol.% SiC_p material as for the wrought aluminum alloy 6061 and, as before, the Bauschinger strain of the HP material is less than that of the 20 vol.% SiC_p material. Again, as for the whisker-reinforced composite material (Fig. 12), the magnitude of the BE increased when the test was initially conducted in compression. There is a general increase in the BE as the volume fraction increases.

5. DISCUSSION

The discussion is divided into two parts: in the first part the SDE is dealt with and in the second part the BE is considered.

5.1. Strength differential effect

As mentioned in Section 1, most of the theories developed to account for the SDE (excluding the theories based on residual stresses [4, 5]) are not capable of accounting for the magnitude of the SDE in discontinuous SiC-Al composites. The model of Arsenault and Taya [4] can be used to predict the magnitude of the difference between the compressive yield stress and the tensile yield stress. Figure 13 is a plot of $\Delta\sigma$ *vs.* volume fraction of whisker SiC in an aluminum alloy

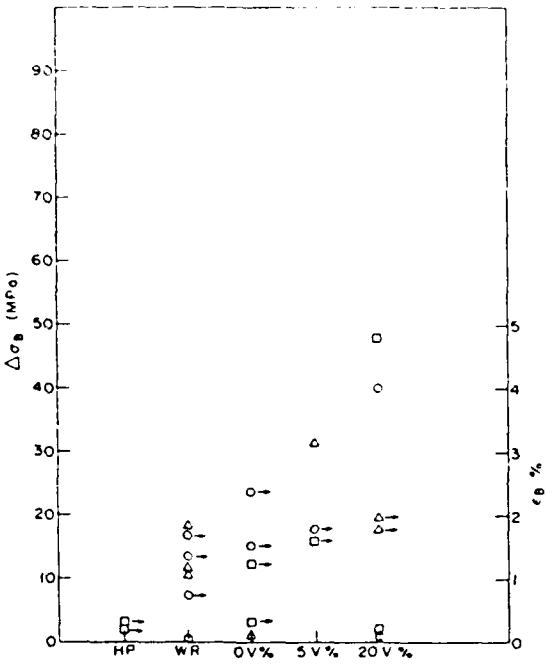

Fig. 10. A plot of the Bauschinger stress factor *vs.* the volume fraction of whiskers in a composite material and the Bauschinger strain *vs.* volume fraction for compression-first testing (matrix, aluminum alloy 6061; $\epsilon_F = 1.5\%$): ○, annealed; □, quenched; △, heat treated to T6 condition; ○, □, △, *left-hand ordinate axis*; ○→, □→, △→, right-hand ordinate axis. Also plotted are the values obtained for high purity aluminum and wrought aluminum alloy 6061.

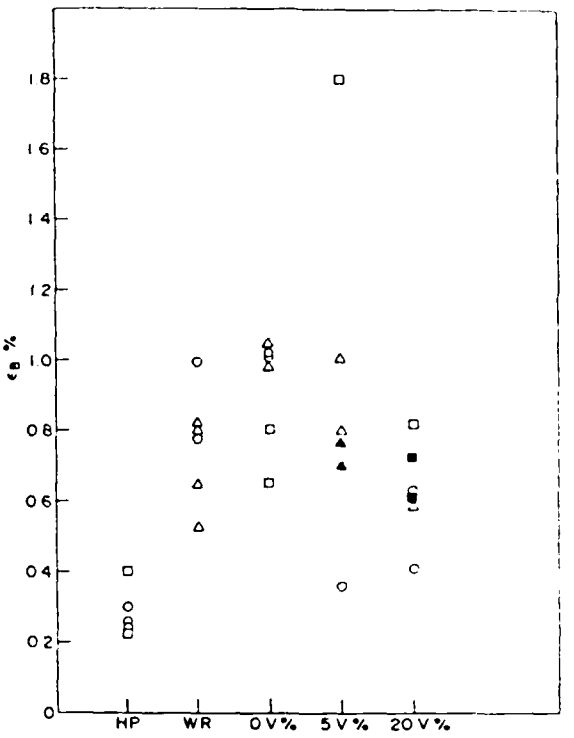

Fig. 11. A plot of the Bauschinger strain *vs.* the volume fraction of particulates in a composite material for tension-first results (matrix, aluminum alloy 6061; $\epsilon_F = 1.5\%$): ○, annealed; □, quenched; △, heat treated to T_6 condition; ■, liquid nitrogen quenched; ▲, heat treated to T_6 condition and liquid nitrogen quenched. Also plotted are the results obtained for high purity aluminum and wrought aluminum alloy 6061 material.

6061 matrix. The agreement between the experimental results and the theoretical predictions is very good. If 20 vol.% SiC_w in an aluminum alloy 1100 matrix is considered, there are two competing efforts. The magnitude of $\Delta\sigma$ should increase with an increase in l/d (eqn. (1)), for the average l/d in the aluminum alloy 1100 matrix is 2.76 *vs.* 1.8 in the aluminum alloy 6061 matrix. However, the yield stress of the aluminum alloy 6061 matrix is greater than the yield stress of the aluminum alloy 1100 matrix, and the magnitude of the yield stress of the matrix plays an important role in determining the magnitude of the residual stress. In fact, σ_y for the aluminum alloy 1100 matrix is so low that the model [4] cannot properly handle the problem because significant localized plastic deformation would occur, but it can be inferred that $\Delta\sigma$ would be less for the aluminum alloy 1100 matrix composite than for the aluminum alloy 6061 matrix composite.

For the 20 vol.% SiC_s composite, the model of Arsenault and Taya [4] predicts zero $\Delta\sigma$ but, surprisingly, $\Delta\sigma$ is slightly negative, *i.e.* σ_{y_t} is greater than σ_{y_c}.

The effect of quenching into water or heat treatment does not consistently result in a larger $\Delta\sigma$. This indicates that the tensile residual stress in the quenched or heat-treated samples are not significantly different from that of the annealed samples. It has been argued that the rate of dislocation generation, *i.e.* plastic relaxation, is very rapid and the magnitude of remaining elastic residual stress is not dependent on the quench rate [12]. Quenching into liquid nitrogen followed by testing at room temperature results in a reduction in $\Delta\sigma$. If the sample is heated, *i.e.* from room temperature to some higher temperature, there is a reduction in the magnitude of the elastic residual stress. Therefore, heating

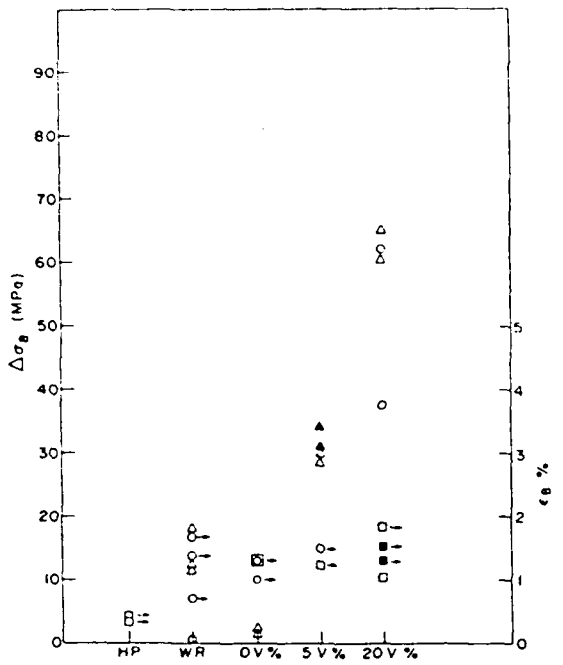

Fig. 12. A plot of the Bauschinger stress factor and Bauschinger strain for compression-first tests of a particulate composite material (matrix, aluminum alloy 6061; $\epsilon_F = 1.5\%$): ○, annealed; □, quenched; △, *heat treated to T_6 condition*; ■, *liquid nitrogen* quenched; ▲, heat treated to T_6 condition and liquid nitrogen quenched; ○, □, △, ▲, left-hand ordinate axis; ○→, □→, ■→, right-hand ordinate axis. Also plotted are the results obtained for high purity aluminum and wrought aluminum alloy 6061.

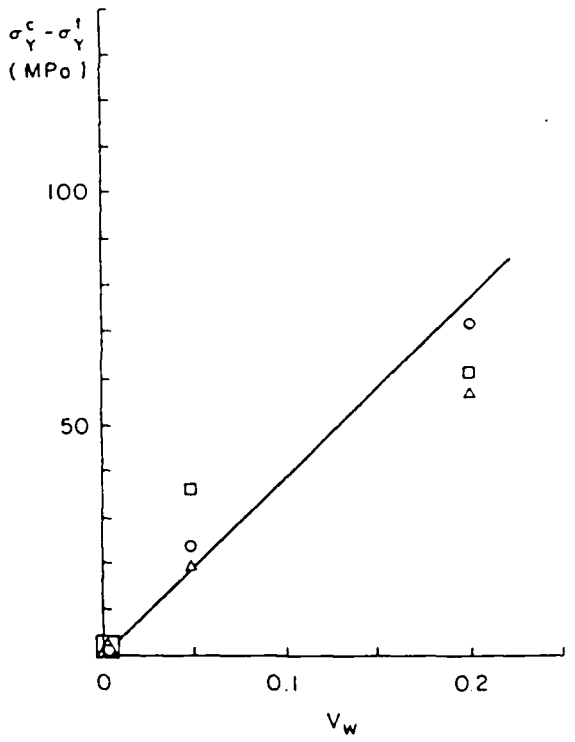

Fig. 13. A plot of the difference in yield strength *vs.* the volume fraction of whiskers in a composite material with an aluminum alloy 6061 matrix: ——, theoretically predicted increase; ○, experimental results, annealed; □, experimental results, quenched; △, experimental results, heat treated to T_6 condition.

from liquid nitrogen to room temperature results in a reduction in the residual stress.

5.2. *Bauschinger effect*

SiC-Al composites should be an ideal material for an investigation to test the validity of the "composite" theory of the BE [7]. This theory predicts that, for a given aspect ratio of the reinforcement, an increase in the volume fraction from 5 to 20 vol.% should result in a decrease of a factor of 4 [4] in the Bauschinger strain (eqn. (2)). Experimentally the opposite is observed, *i.e.* the Bauschinger strain increases with an increase in the volume fraction of reinforcement, for tests initially begun in compression followed by tension. If the tests were initially begun in tension followed by compression, the BE is independent of the volume fraction of the reinforcement.

The "composite" theory also predicts that the magnitude of the BE is not a function of the initial direction of the test. In other words, the BE should be the same if the test is initially conducted in tension or compression. The model of Arsenault and Taya [4], when considering whisker-reinforced composites, as applied to the BE predicts that there would be a difference in the magnitude of BE depending on the direction of initial testing, *i.e.* a larger BE if the sample is initially tested in compression. Also, the model predicts that the magnitude of the BE should increase with increasing volume fraction of reinforcement. There is an assumption in the application of the Arsenault-Taya [4] model to the BE, and that is that plastic deformation does not significantly reduce the elastic residual stress. The experimental evidence obtained in this investigation suggests that this is a valid assumption.

The predicted difference in the BE due to the direction of the test is simply due to the average elastic residual tensile stress. The flow stress in tension is reduced because of the

average tensile residual stress. The difference in BE due to the direction of the test is not related to a difference in dislocation configurations that may occur as a result of initially testing in tension or compression.

6. CONCLUSIONS

The following experimental observations are in good agreement with the Arsenault-Taya theory, as discussed above.

(1) The compressive yield stress of whisker and platelet SiC in aluminum composites is larger than the tensile yield stress.

(2) The compressive yield stress of spherical SiC in aluminum composites is slightly less than the tensile yield stress.

(3) The magnitude of the SDE increases with increase in the volume fraction of SiC.

(4) The magnitude of the BE increases with increase in the volume fraction of SiC.

(5) The magnitude of the BE is greater if the test is initially conducted in compression, and the difference increases, *i.e.* whether tested in tension first or compression first, with increasing volume fraction of SiC.

ACKNOWLEDGMENTS

This research was supported in part by the Office of Naval Research under Contract N00014-85-K-0007.

REFERENCES

1 J. P. Hirth and M. Cohen, *Metall. Trans., 1* (1970) 3.
2 C. A. Pampillo, L. A. Davis and J. C. M. Li, *Scr. Metall., 6* (1972) 765.
3 W. A. Spitzig and O. Richmond, *Acta Metall., 32* (1984) 457.
4 R. J. Arsenault and M. Taya, in W. Harrigan (ed.), *Proc. 5th Int. Conf. on Composite Materials, San Diego, CA, 1985*, 1985, p. 21; *Acta Metall.*, to be published.
5 D. F. Watt and M. Jain, *Scr. Metall., 18* (1984) 1379.
6 T. Mura, *Micromechanics of Defects in Solids*, Martinus Nijhoff, The Hague, 1982.
7 O. B. Pederson, L. M. Brown and W. M. Stobbs, *Acta Metall., 29* (1981) 1843.
8 C. R. Crowe and R. J. Arsenault, *Acta Metall., 24* (1976) 925.
9 R. J. Arsenault, *Mater. Sci. Eng., 64* (1984) 171.
10 T. K. Hidayetoglu, P. N. Pica and W. L. Haworth, *Mater. Sci. Eng., 73* (1985) 65.
11 R. J. Asaro, *Acta Metall., 23* (1975) 1255.
12 W. R. Tyson, *Metall. Trans. A, 6* (1975) 1674.

The Strengthening of SiC/Al Composites due to Differences in the Matrix and SiC Morphology*

R. J. Arsenault

Engineering Materials Group, University of Maryland, College Park, MD 20742, U.S.A.

ABSTRACT

It has been proposed that the strengthening due to the addition of spherical SiC to an Al matrix would be approximately the same as the strengthening observed due to the addition of whisker SiC to an Al matrix. The experimental results are in agreement with this proposal. A second proposal was made, which was related to the intrinsic strength of the matrix. If the intrinsic strength was greater than the incremental increase in strength due to the addition of SiC would be greater. In this case the experimental data indicates that absolute magnitude of the incremental increase is not a function of the intrinsic strength of the matrix.

INTRODUCTION

Arsenault and Fisher (1) proposed that the increased strength observed in Al/SiC composites could be accounted for by a high dislocation density in the aluminum matrix, as observed in transmission electron microscopy (TEM) samples taken from bulk composite material annealed for as long as 12 hours at 810 K (Fig. 1). In this investigation a representation of at least three Burgers vectors was found in any given location. Also, it was observed that for intermediate or small particle spacings a subgrain structure existed with the subgrain diameter about equal to the inter-particle spacing. However, for very large SiC particles (250 μm) the subgrain size is much smaller than the inter-particle spacing (Fig. 2).

The dislocation generation mechanism proposed by Arsenault and Fisher to account for this high dislocation density is based on the large difference (10:1) in the coefficients of thermal expansion of aluminum and SiC (2). Therefore, when the composite is cooled from the elevated temperatures of annealing or processing, misfit strains which are sufficient to generate dislocations occur because of the differential thermal contraction at the Al/SiC interface. In an investigation of *in situ* HVEM, Vogelsang and et al.

* This research was supported by the Office of Naval Research under Contract No. N00014-85-K-0007.

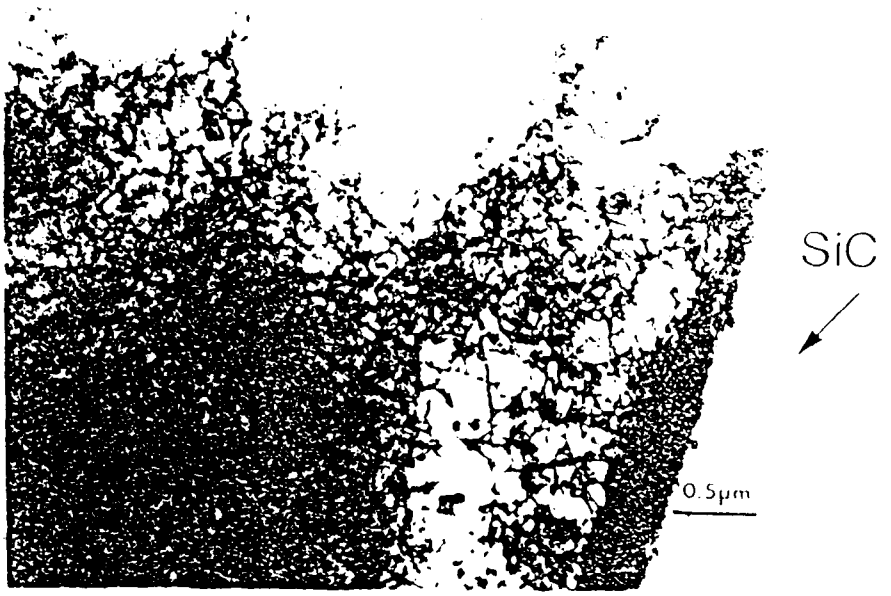

FIG. 1

A micrograph from a TEM foil taken from a bulk sample with 20 vol.% SiC, which was annealed for 12 hours at 810 K and furnace cooled. The right-hand side of the micrograph is an SiC particle and to the left is the matrix material containing a high dislocation density.

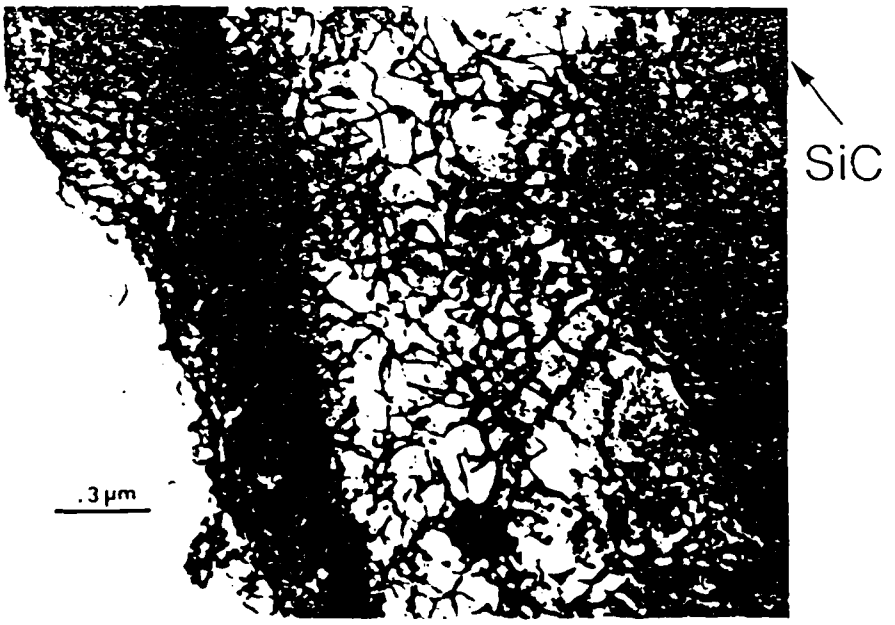

FIG. 2

A subgrain boundary in a composite with 250 μm SiC particles in an aluminum alloy 1100 matrix about 2 μm from an SiC particle. A second subgrain boundary was found some 2-7 μm from the SiC particle, which is the typical subgrain size in this material.

(3) it was demonstrated the dislocation generation of about SiC particles upon cooling.

None of the above models predicts the local dislocation density or the average dislocation density. Correspondingly, as they are not capable of predicting dislocation densities, the predictions of arrangements of dislocations are certainly not possible from these theories.

A simple model was developed by Arsenault and Shi (4) based on prismatic punching with the following assumptions.

1. Both SiC and aluminum were assumed to be elastically isotropic (which they are not) but the effect of anisotropy is small.
2. The resolved shear stress required to move a dislocation is very small. (This is reasonable, for the dislocation motion occurs at relatively high temperatures and thus low frictional stresses.)
3. The SiC platelets are assumed to be parallelepiped particles.
4. Prismatic punching is assumed to occur equally on all faces of the particles.

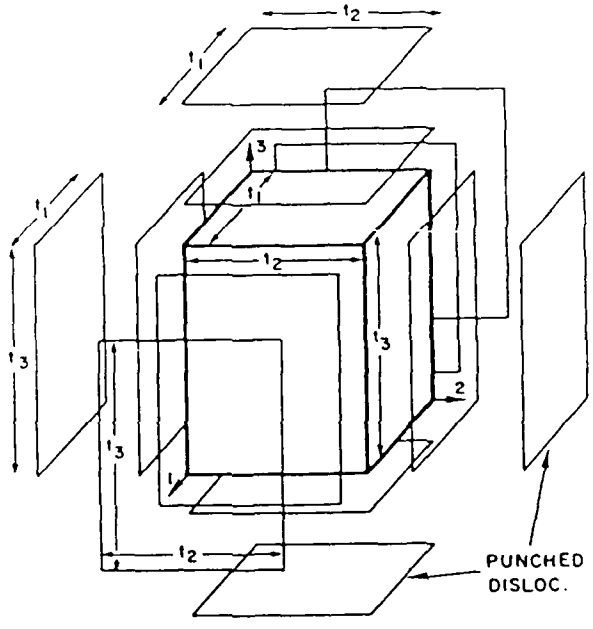

FIG. 3

A schematic diagram of the particle and several prismatic punched dislocations.

Figure 3 is a representation of the SiC particle, by varying the dimension of t_1, t_2 and t_3 it is possible to obtain a shape resembling a whisker, a sphere or a platelet. The following equation was derived for the dislocation density for equiaxed particles (spheres)

$$\rho_s = \frac{12A\,\varepsilon}{b(1-A)}\,\frac{1}{t} \qquad (1)$$

where A is the volume function of SiC, ε is the misfit strain due to difference in coefficients of thermal expansion, b is the Burgers vector and t is the diameter of the sphere. The following equation was derived for the dislocation density for whisker SiC

$$\rho_w = \frac{BA\,\epsilon}{b(1-A)}\,\frac{1}{t} \qquad (2)$$

where B is a constant depending upon the aspect ratio, and t is the diameter of whisker. When comparing dislocation densities for different morphologies, it is necessary that the volume of particle has to remain constant along with a constant volume fraction of particles. Now if the aspect ratio of the whisker ranges from 2 to 10 B is $\tilde{=}$ 12.60 and 18.10 respectively. The experimentally determined aspect ratio varies from 1.8 to 3. The dislocation density as a function of the volume of the particle with different aspect ratios is shown in Fig. 4.

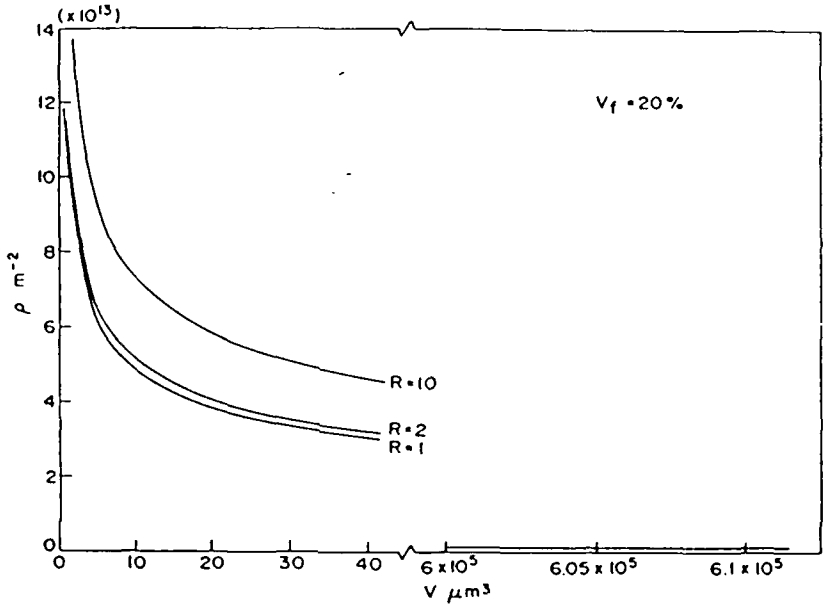

FIG. 4

Calculated dislocation density (ρ) due to prismatic punching as a function volume of particle for whiskers of aspect ratios of 10, 2 and 1. The aspect ratio of 1 corresponds to a cube or a sphere.

The dislocations produced as a result of punching in accordance with Fig. 3 have one set of Burgers vector of a single type along each side (i.e., at a given location) whereas experimentally three different groups of slip traces, each of which represents one type of Burgers vector, are generally observed. Thus, ideally punched dislocations seem unlikely to lead to the formation of subgrain boundaries. As such, they represent a high energy configuration. Therefore, additional dislocations may be generated to assist the production of the low energy dislocation configuration of subgrain boundaries. These are in fact observed in bulk samples (Fig. 2) but not in in situ thermally cycled TEM foils (3). In the course of the dislocation rearrangements leading to subboundaries, additional dislocations may be formed, but more probably there is a net decrease in dislocation density ρ due to mutual dislocation annihilation. Yet the density of dislocations produced as a result of this punching model is a factor of 2 or 3 lower than that observed experimentally for the small-size particles. It is suspected that for larger-size particles, the

model correspondingly underestimates the density.

Although the actual dislocation density and arrangements were not obtained, it is possible to calculate a lower bound value for the strength increase due to the dislocations formed through thermal strains.

For the strengthening due to the presence of dislocations generated by the differential thermal contraction, the following equation may be used:

$$\Delta\sigma = \alpha\mu b\rho^{1/2} \tag{3}$$

where $\Delta\sigma$ is the increase in tensile strength, μ is the shear modules of the matrix and α is a geometric constant. Hansen (5) obtained an α value of 1.25 for aluminum which we shall use.

Now, when Eq. (2) is substituted into Eq. (3), the following is obtained:

$$\Delta\sigma = \alpha\mu b\left[\left(\frac{A}{1-A}\frac{B\epsilon}{b}\right)\left(\frac{1}{t}\right)\right]^{1/2} \tag{4}$$

where B is equal to 12 for spheres and 12.60 for whiskers. Therefore, whiskers should be slightly more effective in producing an increase in strength.

However, it is necessary to consider the residual elastic stress. The model of Arsenault and Taya (6) predicts that there should be a tensile residual stress in the case of a whisker composite and average residual stress for the spherical composite case should be zero. Therefore, the spherical composite should have a higher tensile yield stress as compared to the whisker composite.

The net result of these two considerations is a canceling effect, and the yield stress of the whisker and the spherical composites should be approximately equal.

It has been proposed that a stronger matrix will result in a larger increase in strength upon the addition of the reinforcement. The basic reason for this difference in strengthening is due to the change in magnitude of the dislocation density and of the tensile residual stress. For example, proposed is the case of the 1100 Al matrix, there is a maximum dislocation generation due to the difference in coefficients of thermal expansion and a minimum tensile residual stress, because the yield stress of the 1100 matrix is much less than the yield stress of the 7091 Al alloy matrix.

The purpose of this investigation was to determine whether a difference in the morphology of SiC reinforcement had an effect on the yield strength of the composite and to determine whether differences in matrix strength had any major effect on the strengthening of the composite.

MATERIALS AND EXPERIMENTAL PROCEDURE

All of the composites used in this investigation were purchased from ARCO Silag in the form of 12.5 mm extruded rods. For the investigation of SiC morphology 1100 Al was chosen as the matrix, and for the investigation of matrix strength, 6061 and 7091 were used. In the morphology studies the SiC were in the form of 0.5 μm spheres in one case and whiskers (average $\ell/d \tilde{=} 3$) with a diameter ranging from 0.1 to 0.5 μm. In the matrix studies, whisker SiC was used as the reinforcement.

The extruded rods were machined into tensile samples, the configuration of the samples is defined elsewhere (7) and samples were then annealed for 12 hours at 803 K and furnace cooled over a 12 hour period of time.

The tensile testing procedure was the same as that used previously (7).

EXPERIMENTAL RESULTS

In a comparison of the strengthening of SiC reinforcement in an Al alloy matrix, it is necessary to make the comparison with 0 V% composite alloy produced in the same manner as the SiC reinforced composite. In Table I are listed the yield strengths of 0 V%, 20 V% spherical SiC and 20 V% whisker SiC composites. Also listed is the extent of uniform plastic elongation.

The spherical SiC results in larger strengthening than the whisker SiC, but the ductibility are about the same.

Table I

Effect of Morphology of Strengthening

SiC V%	SiC Shape	Yield Strength MPa	Ultimate Tensile Strength MPa	Uniform Elongation ϵ_p, %
0		34.38	10.80	19.0
20	spherical	204.1	271.52	4.2
20	whisker	183.23	312.0	5.2

A change in the matrix has very little effect on the absolute increase in the yield stress as shown in Table II. However, in terms of a percentage increase, in the case of 1100 Al matrix there is a much larger increase, as compared to 6061 and 7091.

Table II

Differences in Yield Stress for Different Matrices

Matrix Material Annealed	$\Delta\sigma_y$* MPa	$\%\Delta\sigma_y$
1100	144.9	420
6061	100.5	181
7091	131.1	190

* $\Delta\sigma_y = \sigma_{y20\ v\%\ w} - \sigma_{y0\ v\%\ w}$

DISCUSSION AND CONCLUSIONS

In the introduction it was mentioned that in considering the strengthening of Al by SiC of different morphologies, that there were compensating factors when comparing spherical vs. whisker SiC. From the experimental data it appears that the effect of a tensile residual elastic stress overcame the slight advantage whiskers have in generating a higher dislocation density.

The data obtained from spherical SiC strengthened 1100 Al is in complete disagreement with predicted strengthening of Nardone and Prewo (8). They predict a 20% increase in strength for spherical SiC. The experimental results indicate a 420% increase, a factor of 21 larger increase than what they had predicted.

In regards to intrinsic strength of the matrix on the increase in strength due to the addition of the reinforcement, there appears to be very little effect when considered on an absolute basis. Therefore, the original proposal is not valid.

ACKNOWLEDGEMENTS

The author wishes to acknowledge the assistance of Mr. Ben Wu in performing the experimental testing, and the support of Dr. S. Fishman of the Office of Naval Research.

REFERENCES

(1) Arsenault, R. J. and Fisher, R. M., Scr. Metall., 17, 1983, 67.
(2) Taylor, A. and Jones, R. M. in O'Connor, J. R. and J. Smiltens (eds.), Silicon Carbide, Pergamon, Oxford, 1960, 147-154.
(3) Vogelsang, M., Arsenault, R. J. and Fisher, R. M., Met. Trans., 17A, 1986, 379.
(4) Arsenault, R. J. and Shi, N., Mat. Sci. and Eng., 81, 1986, 175.
(5) Hansen N., Acta Metall., 25, 1977, 863.
(6) Arsenault, R. J. and Taya, M., Proceedings of ICCM-V, ed. by W. Harrigan, San Diego, 1985, 21.
(7) Arsenault, R. J., Mat. Sci. and Eng., 64, 1984, 171.
(8) Nardone, V. C. and Prewo, K. W., Scripta Met., 20, 1986, 43.

DEFORMATION OF SIC/AL COMPOSITES*

Y. Flom and R. J. Arsenault
Engineering Materials Group
University of Maryland
College Park, MD 20742

ABSTRACT

The strengthening of discontinuous SiC/Al composites has shown to be the result of the high dislocation density in the Al matrix. This high dislocation density is the result of the difference in thermal coefficients of expansion between Al and SiC and the very strong bond between Al and SiC. The fracture process in these composites is controlled by the degree of plastic constraint of the matrix by SiC particulates. Low volume percent composites exhibit ductile fracture controlled by void nucleation. In composites with a high content of SiC (> 20%), void nucleation does not seem to be a controlling factor.

KEYWORDS

Composites; discontinuous; coefficients of thermal expansion; bond strength; void nucleation.

INTRODUCTION

Discontinuously reinforced metal matrix composites represent a group of materials that combine strength and hardness of the reinforcing phase with ductility and toughness of the matrix. Powder metallurgy (p/m) aluminum alloys reinforced with SiC in particulate, platelet or whisker form are receiving a great deal of attention from researchers and engineers. The interest in Al/SiC composites can be related to: (1) its high elastic modulus, high strength and light weight (Arsenault, 1984), (2) economic production of SiC whiskers, platelets and/or particulates, (3) ability to use standard shaping methods such as forging, rolling, extrusion, etc. and (4) much less dependence of the engineering properties on directions compare with continuous composites.

* This work was supported by the Office of Naval Research under Contract No. N00014-85-C-0007.

Our paper will review some aspects of plastic deformation of Al/SiC composites with emphasis on strengthening mechanisms, role of coefficient of thermal expansion (CTE) and particle-matrix interfaces (PMI), fracture process.

STRENGTHENING PHENOMENA

The experimental results of a number of investigations provide quite high values for the yield strength σ_y and ultimate strength σ_{uts} of Al/SiC discontinuous composites (Table I). Predicted or calculated values of σ_{uts} based on a classical continuum mechanics model of a composite material, is by a factor of 4 lower than that determined from the experiment (Arsenault, 1984). What makes this discrepancy even worse is the fact that several assumptions that are made in continuum mechanics approach do not represent the situation in the real Al/SiC composite. These assumptions are: (1) perfect alignment of the whiskers or platelets and (2) void-free matrix (Piggott, 1980). Experimental observations show, however, that there is a significant number of voids present in the matrix and also the alignment of the whiskers and/or platelets is far from being perfect (Arsenault, 1984). A modified continuum mechanics approach has been proposed for theoretical prediction of σ_{uts} and σ_y [3]. It takes into account the tensile load transfer from the matrix to the whisker and/or particulates ends. An assumption is made that the presence of SiC does not affect matrix behavior and one can use properties of the matrix and the concept of the load transfer to predict the strength of the composite. Calculated values for yield strength for the whisker and particulate 6061 Al/SiC composites were about 500 MPa and 450 MPa and observed yield strength values were about 450 MPa for whisker and 420 MPa for particulate composites (Nardone, 1986). However, there are several assumptions in this formulation which are not valid (Taya, to be published).

TABLE I Mechanical Properties of SiC/Al Composites

Composite and Heat Treatment	Volume Fraction of SiC, %	Yield Strength, MPa	Ultimate Tensile Strength, MPa	Elastic Modulus, GPa	Ductility $\epsilon_f = \frac{A_o}{A_f}$, %	% Elong. ϵ_p	Fracture Toughness, K_{IC} MPa $\sqrt{m}$
SiCp/6061 T6	20	400-356	434-428	108	4.9	1.5	
SiCp/6061 T6	25	345	410	99		4.4	15.8
SiCw/6061 T6	20	470-321	607-423	106-103	5.4	3-2.2	22.4
SiCp/2024 T6	30	405	456	118	.8		
SiCw/2024 T4	20		524-455	117-97		1-2	
SiCp/7075 T6	30	392	439	119	.9		
SiCw/7075 T6	20	407	549	101	3.5		

Another possible explanation of the mechanism of Al/SiC strengthening is based on the Orowan theory which enables one to estimate the stress required for dislocation to bypass the particle. Particle separation is a major parameter controlling this stress. Taking the average particle spacing of 2 μm yields about a 5 MPa increase in composite strength which is obviously too small compared with a 60 to 110 MPa increase observed experimentally. Yet another approach is based on the increase of the dis-

location density in the Al alloy matrix. It was shown that the strength of the thermomechanically treated 6061 Al alloy can be as high as 400 MPa (Rack, 1977). If this value is used for calculation of the theoretical strength of the composite than calculated σ_{uts} agrees well with experimental results. The increase of the dislocation density in Al matrix in Al/SiC composite was attributed to the relaxation of the misfit strain between SiC particles and the matrix. This misfit strain arises from the difference between CTE of SiC and that of Al (of about a factor of 10) on cooling down from the annealing or processing temperature (Arsenault, 1984). Transmission electron microscopy (TEM) investigations of these composite materials do indeed reveal a high dislocation density (10^{10} cm^{-2}) and small subgrain size (1.0 - 2.5 μm)(Vogelsang, 1986). The following expression was proposed for the increase of the yield strength above that of 0 V% matrix (1100 Al),

$$\Delta\sigma_{yc} = \Delta\sigma_{Disl} + \Delta\sigma_{Sg} + \sigma_{Comp} \qquad (1)$$

where $\Delta\sigma_{Disl}$ is the term due to dislocation density increase, σ_{Sg} is the increase in strength due to the small subgrain size, and σ_{Comp} is the increase due to continuum mechanics strengthening. The evaluation of these terms results in a value of about 130 MPa for σ_{uts} whereas experimental values is about 138 MPa.

ROLE OF CTE

In the course of studying plastic deformation of two-phase alloys it was observed that second phase particles can act as a dislocation source when a material is cooled from an elevated temperature or is deformed. Recent observations of the local plastic deformation around SiC particles in Al/SiC composites subjected to the thermal cycle showed that the size of the plastically deformed zone around the particle is ~ 1.5 particle radii (Flom, 1985). It is interesting to mention that plastic deformation, i.e., formations of the slip bands about the SiC particle was observed also on heating from room temperature. Subsequent in-situ high voltage TEM investigations of Al/SiC thin foils showed dislocation generation on heating (Vogelsang, 1986) which corresponds to the observation of the slip bands. A simple model, based on prismatic punching, (Figure 1) was developed to account for the relative dislocation density due to the difference in CTE (Arsenault, 1986). Dislocation density in the matrix was found to be:

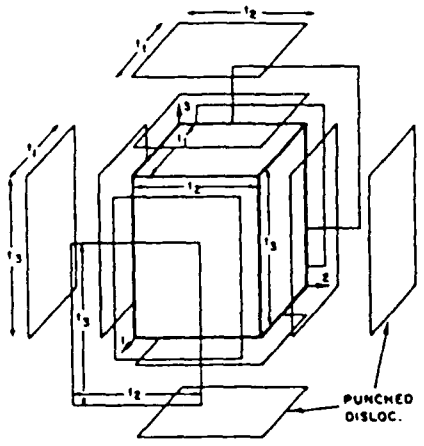

Fig. 1. A schematic representation of prismatic punching about a parallelepiped shaped SiC particle.

$$\rho = \left\{\frac{B\ A\ \epsilon}{b(1 - A)}\right\} \frac{1}{t}, \qquad (2)$$

where B is a geometric constant which varies theoretically between 4 for whiskers and 12 for equiaxed particles, A is the volume fraction of particles, b is the length of Burger's vector, t is the smallest dimension of particle, and finally ϵ is the misfit strain due to difference

in CTE, i.e.,

$$\epsilon = (\Delta CTE) \times \Delta T \ . \qquad (3)$$

The expression (2) implies that for the same volume fraction smaller particles will produce higher dislocation densities (Figure 2).

Several investigations were conducted in order to evaluate the residual thermal stresses in Al/SiC composite. An x-ray diffraction technique was used for experimental evaluation of the residual stresses. It was found that residual stress state in the composite was tensile ranging from 55 MPa to 407 MPa (Table II) (Arsenault, 1985). Theoretical analysis of thermal stresses was based on Eshelby's equivalent inclusion model. Ellipsoidal aligned whiskers in the infinite body were considered and

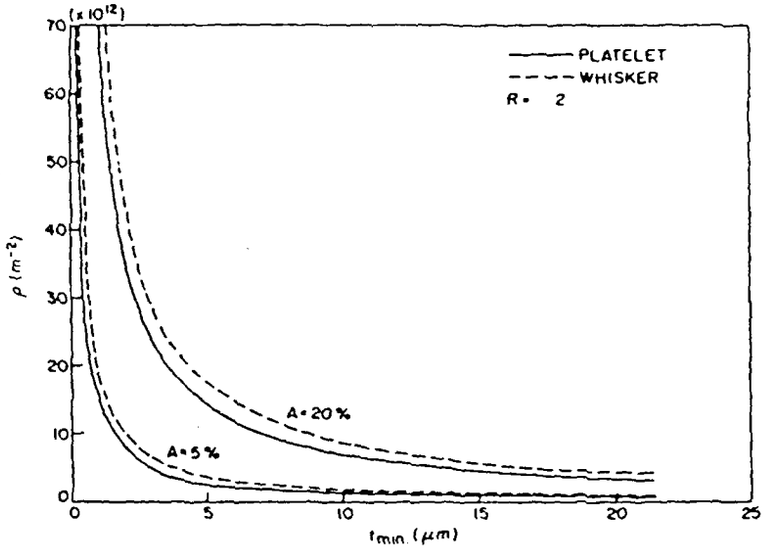

Fig. 2. Calculated dislocation density (ρ) due to prismatic punching as a function of minimum particle thickness (t), for both whiskers and platelet of the same volume fraction A according to Eq. 2.

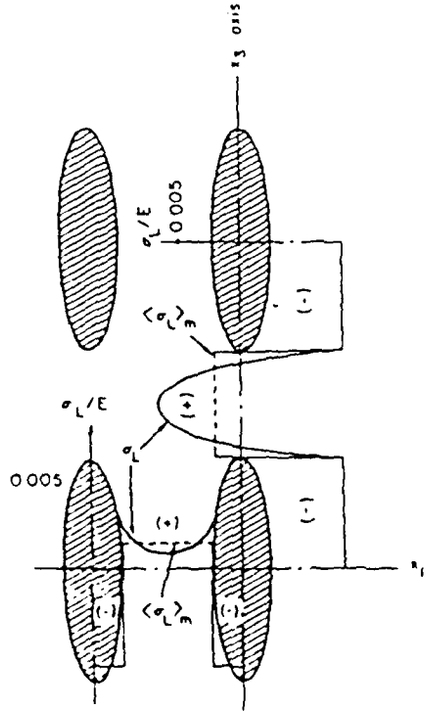

TABLE II The Thermal Residual Stresses (Tensile) as Measured by X-ray Defraction Techniques.

Material	Longitudinal MPa	Transverse MPa
0 V% Whisker SiC 6061 Matrix	0.0	0.0
5 V% Whisker SiC 6061 Matrix	34.5	407
20 V% Whisker SiC 6061 Matrix	55.2	228
Wrought	0.0	0.0

Fig. 3. Schematic Distribution of the stress in the matrix and the reinforcement due to the difference in thermal coefficient of expansion between the SiC and Al.

mechanical properties of annealed 6061 Al matrix and SiC whisker with aspect ratio L/d = 1.8 (length-to-diameter ratio) were used for the calculations. Resultant stress distribution is shown in Figure 3. In addition, the difference in the yield strength $\Delta\sigma_y$ between tension and compression resulting from the thermal residual stresses, was determined experimentally and calculated theoretically using the model cited above. Very good agreement was obtained between the experimental and theoretical results (Arsenault, 1985) (Figure 4).

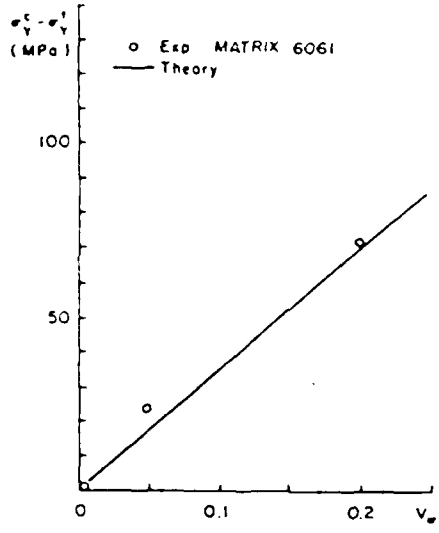

Fig. 4. The difference in yield stress between compression and tension as a function of volume percent silicon carbide whisker.

SiC/Al INTERFACES

It is probably not an exaggeration to say that the interfaces play the most important role in the behavior of a composite.

An interesting phenomena associated with SiC-Al interfaces was reported recently in the course of fracture surface analysis performed in scanning Auger electron microscope (Arsenault, 1984). Both SiC_w/6061 Al and SiC_w/2124 Al materials were fractured in-situ and composition analysis were performed on individual whiskers exposed on the surface (Figure 5). In most cases Si or C could not be detected on the whiskers. Detection of Si and C was possible only after considerable ion sputtering. This means that "pulled out" whiskers are coated with an Al layer which is the indication of a good SiC/Al bond. Also an anomoalous diffusion of Al into SiC was observed (Figure 6).

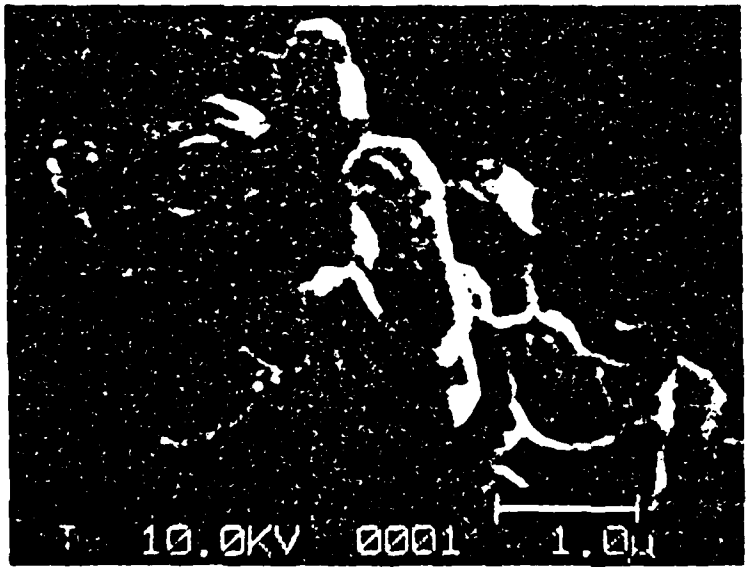

Fig. 5. A SEM micrograph taken in the Auger microprobe of the fracture surface of a whisker SiC/Al composite.

FRACTURE

Ductility and fracture toughness of SiC/Al composites are quite low and require an intensive study in order to reach a compromise between two extremes: very strong and brittle composite on one hand, and weak, ductile one on the other. As of now this compromise has not been reached.

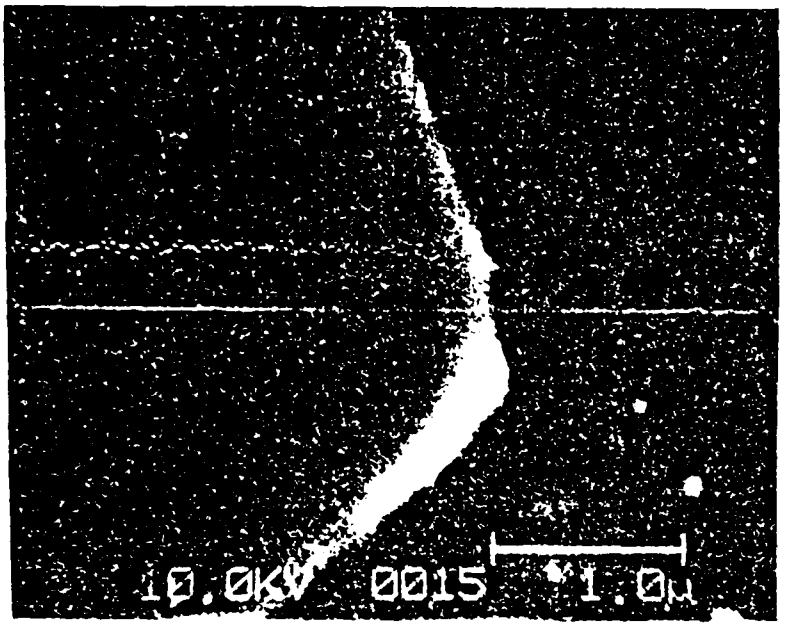

Fig. 6. A SEM micrograph taken in the Auger microprobe, on which the Al and Si Auger probe traces have been superimposed.

Generally, the observation of the fracture surface of SiC/Al composites does not reveal the presence of SiC particulates and/or whiskers in the quantities corresponding to their volume fraction. The following features should be mentioned specifically (Arsenault, to be published):

1. There appears to be fracture initiation sites.
2. Fracture has a macroscopically brittle characteristic, but on the microscale it is ductile, i.e., has a dimple morphology.
3. There is no indication of fracture of SiC (if SiC is less than 10 μm is size).
4. Some secondary cracking takes place (cracks are formed perpendicular to the fracture surfaces).

The fracture process is very localized and occurs without warning, i.e., no apparent necking is observed.

It seems that the following fracture initiation sites can be identified; one is the large intermetallic $(Fe, Cr)_3 SiAl_2$ inclusions termed "fish eyes" (Fig. 7a), second is clusters of SiC whiskers or particulates (Fig. 7b), third is the voids initiated at the SiC whiskers or particulates and fourth large "chuncks" of SiC > 10 μm (Fig. 7c).

It is generally accepted that a ductile fracture in the presence of a second-phase particles occurs by i) nucleation of voids at the particles, ii) growth of these voids and iii) their linkage which manifestates the actual physical separation. In SiC/Al composites, the fracture process depends on the content of SiC particles and/or whiskers. Void nucleation is a significant factor when the volume percent of SiC is low. The extent

Fig. 7. Large intermetallic inclusion ("fish eyes") (a), cluster of whiskers (b), and individual SiC particles (c) as an acting fracture initiating sites.

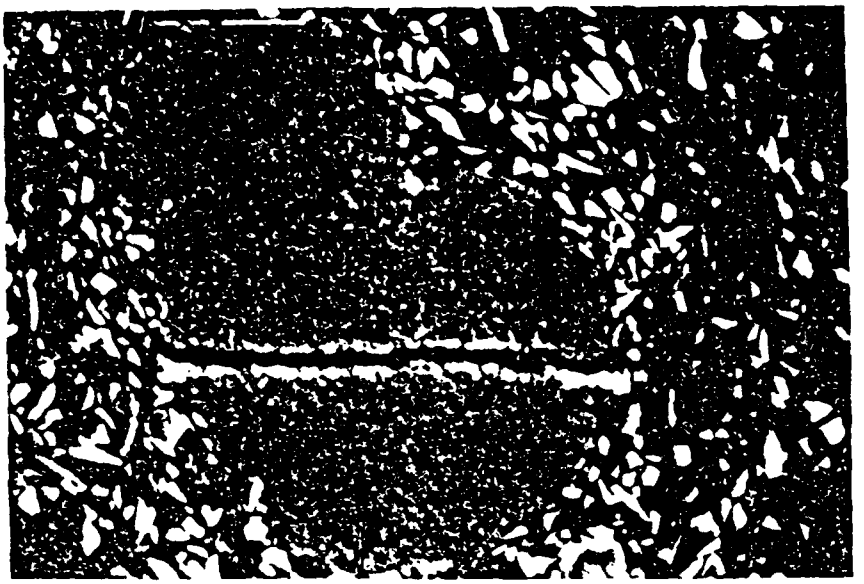

(a) × 1000

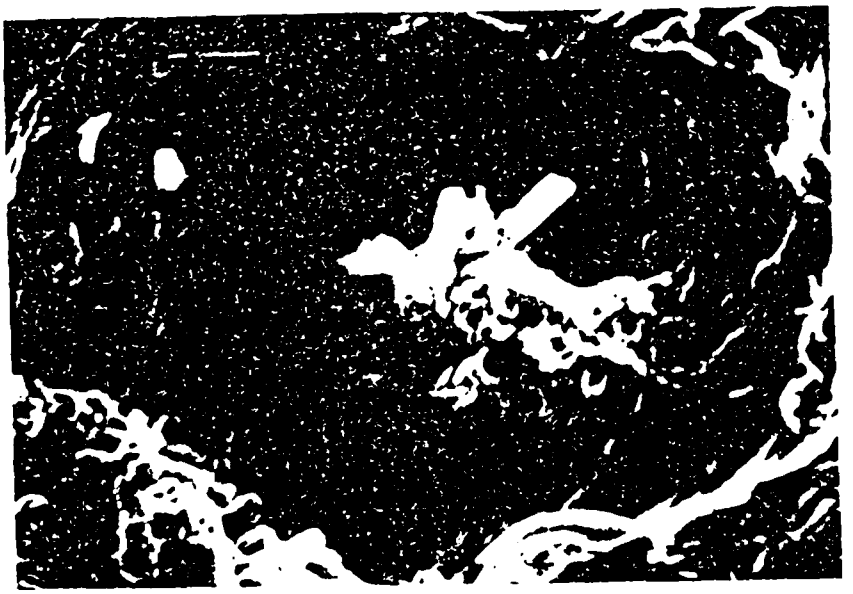

7(b) × 8000

of the void growth determines the ductility of the material. In the high SiC content (> 20%), composites matrix is in the state of significant plastic constraint. Thus, dislocation motion, i.e., plastic flow in the bulk of the composite is impeded. It appears, therefore, that void nucleation is not a controlling parameter. Crack initiates at the pre-existing voids and propagates through the composite in a catastrophic

manner. Void growth almost stops in SiC/Al composites with a SiC content of 20% and higher. This can be seen from the dimple sizes (3 - 5 μm) observed on the fracture surfaces.

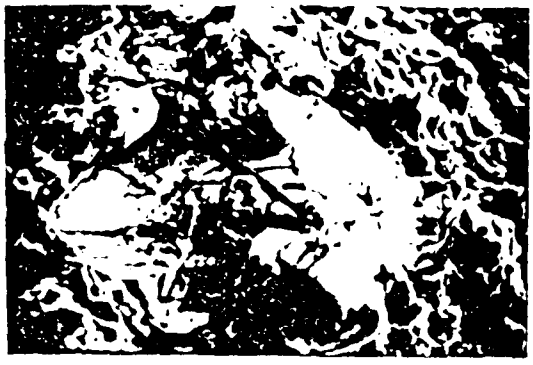

7(c) × 2000

CONCLUSIONS

1. High strength of the SiC/Al interface and a big difference in CTE between SiC and Al results in the generation of a large number of dislocations.
2. The high dislocation density provides the main contribution to the strengthening of the discontinuous SiC/Al composite.
3. The improvement of ductility and fracture toughness properties of SiC/Al composites can be achieved in two steps. First is to eliminate the presence of large inclusions and clusters of SiC particulates and/or whiskers. Further improvement, it is believed, can be obtained by tailoring SiC/Al interfaces.

REFERENCES

1. Arsenault, R. J. (1984). Mat. Sci. & Eng., 64, 171.
2. Piggott, M. R. (1980). Load-Bearing Fibre Composites, Pergamon, Oxford, 141-144.
3. Nardone, V. C., and K. W. Prewo (1986). Scripta Met., 20, 43.
4. Taya M., and R. J. Arsenault. Scripta Met. To be published.
5. Rack, H. J., and R. W. Krenzer (1977). Met. Trans. A, 8, 335.
6. Vogelsang, M., R. J. Arsenault, and R. M. Fisher (1986). Met. Trans. 174, 379.
7. Flom, Y., and R. J. Arsenault (1985). Mat. Sci. & Eng., 75, 151.
8. Arsenault, R. J., and N. Shi (1986). Mat. Sci. & Eng., 81, 175.
9. Arsenault, R. J., and M. Taya (1985). Proceedings of ICCM-5, 21, San Diego, CA.
10. Flom, Y., and R. J. Arsenault (1986). Mat. Sci. & Eng., 77, 191.
11. Arsenault, R. J., and C. S. Pande (1984). Scripta Met., 8, 1131.
12. Arsenault, R. J., and Y. Flom (1985). Proceedings of AIME Annual Conference, Toronto, Canada, to be published.

FRACTURE OF SIC/AL COMPOSITES

Y. Flom and R. J. Arsenault
Engineering Materials Group
University of Maryland
College Park, MD 20742

ABSTRACT

Discontinuous SiC/Al composites were fabricated with different size SiC particles in order to study the role of particle size on the fracture process. Tensile test data shows that the Young's modulus is independent of SiC particle size, whereas yield stress and ultimate strength decreases, and strain to fracture and ductility increases as SiC particle size increases. The fracture behavior of SiC/Al is unique in the sense that it has features of brittle and ductile mechanisms. The fracture process is matrix controlled up to SiC particle sizes of 20 μm and above where fracture of SiC begins to dominate. The matrix is influenced by residual hydrostatic tension and high density of dislocations generated at SiC/Al interfaces due to the difference in coefficient of thermal expansion (CTE) between SiC and Al matrix. Crack initiation fracture toughness does not depend on SiC particle size. Crack growth fracture toughness increases as the size of the SiC particles increase.

INTRODUCTION

Low ductility and fracture toughness of discontinuous SiC/Al composites remains a major obstacle to the practical application of these materials. Despite the significant improvement in the processing of SiC/Al composites in the recent years, fracture toughness is still in the range of 12 to 20 MPa $\cdot \sqrt{m}$ [1,2,3]. It is not clear how the interfacial SiC/Al bond strength, difference in CTE between SiC and Al, size of the SiC reinforcement affect the toughness. It has already been established that the increase in the volume fraction of SiC particles and/or whiskers and the increase of the matrix strength influence adversely the toughness of SiC/Al composites [3,4]. This paper will examine the dependence of the toughness and tensile properties of the SiC/Al composites containing various sizes of SiC particles.

MATERIALS AND TEST METHODS

SiC particles of 2.4, 3.2, 8 and 20 μm average size were mixed separately with 1100 Al powder and hot pressed, extruded and hot rolled to produce tensile test samples and compact tension specimens (CTS). Also a SiC/Al composite containing 250 μm size SiC particles was purchased from DWA. The volume fraction of the SiC reinforcement was constant in all composites and equal to 20 volume percent. An 1100 Al alloy was selected in order to minimize the influence of the alloying elements which would otherwise introduce additional complicating factors. Tensile samples were machined in the rolling direction and tested at a standard crosshead speed of 0.05 cm/min. The CTS were machined and tested using single specimen J-integral testing technique in accordance with ASTM E813 standard [5]. All samples were tested in the annealed condition. Also, the energy separation technique, developed at the University of Maryland [6] was utilized as a supplemental method of analyzing load-unload records to increase the confidence in the data obtained. The later technique implies that the area under the load versus displacement curve, which corresponds to the work done by external load, can be separated into the stored elastic strain (potential) energy, U_s, the elastic energy, U_e, released during crack extension, and the plastic energy, U_p, dissipated during crack extension as shown on Fig. 1.

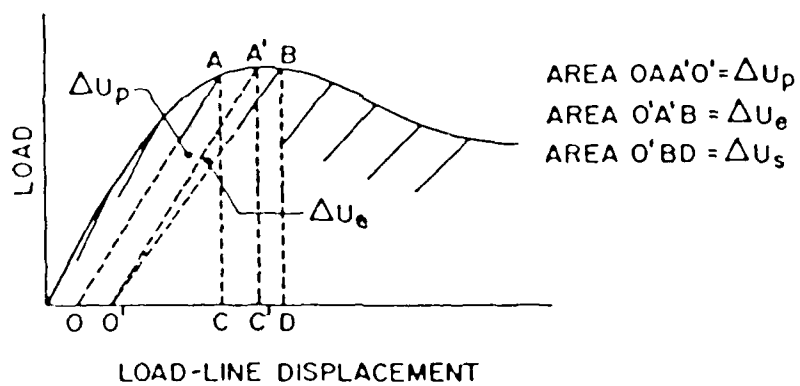

Fig. 1. Schematic of the energy separation principle between two successive unloadings.

The rate of the plastic energy dissipation $I = 1/B_N\ dU_p/da$ and the elastic energy release rate $G = 1/B_N\ dU_e/da$ represent the plastic and elastic parts of the J-integral, i.e., $J = I + G$, where B_N is the thickness of the CTS between the side grooves and a is the crack length. Crack initiation fracture toughness can be determined as $K_{IC} = (GE_c/1 - \nu^2)^{1/2}$ [7], where E_c is the composite Young's modulus and ν is the Poissons ratio ($\nu = 0.31$). Also, a direct evaluation of K_{IQ} is possible by taking maximum load P_m from the load-unload record and substituting into the expression $K_{IQ} = P_m/B_N(W)^{1/2} f(a/w)$ [7], where w is the width of the CTS and values of $f(a/w)$ are readily available. Crack growth fracture toughness is evaluated by dimensionless tearing modulus T which is equal to [7,8]: $T = E_c/\sigma_y^2\ dJ/da$, where σ_y is the composite yield stress and dJ/da is the slope of the stable crack extension portion of the J versus a plot constructed in accordance with ASTM E813. Crack extension was determined using unloading compliance technique [5,7]. In order to verify the

calculated crack extension values, the tested CTS were exposed to elevated temperature and then fractured. Physical crack lengths are within 5 to 10% from the values calculated by compliance technique.

The interaction between the fracture path and SiC particles is analyzed by counting the number of SiC particles along a random path (RP), and the fracture path (FP) and comparing SiC particle densities and size distributions. Particle size is represented by the longest dimension of the SiC particle. Random path particle count (RPPC) is performed by counting the particles along the perpendicular lines forming a square mesh which is placed on the micrographs of the metallographically polished cross sections of SiC/Al composites. Fracture path particle count (FPPC) is done by incorporating the SiC particles touching both matching sides of the crack on the cross sections of the tested but not separated CTS. In addition, the number of SiC particles fractured by the crack path can be reasonably estimated since both matching halves of the same crack are present on the micrograph. The latter can be used to determine the percent of SiC particles fractured by the crack path using the ratio of,

$$\frac{\#\text{ of particles fractured by crack path}}{\text{FPPC}} .$$

RESULTS AND DISCUSSION

Tensile Tests

The Young's modulus of the tested SiC/Al composites does not change as a function of SiC particle size and remains constant ~ 89.7 GPa. This agrees quite well with the classical treatment of the composites where Young's modulus E_c is the function of the volume fraction of the reinforcement [4,9]. Constancy of the modulus indicates good reproducibility during the manufacturing process of SiC/Al composites with various SiC particle sizes in terms of the bonding between SiC/Al. The yield stress and ultimate tensile strength decrease as the size of SiC particles increases. This is consistent with the experimental data collected by various investigators [10]. A recent model of the composite strengthening based on dislocation generation due to the difference in coefficient of thermal expansion (CTE) between SiC and Al [11] is in accord with the data obtained in the current investigation. Uniform strains to the point of instability remain within 6 to 7% range independent of the SiC particle size. This fact suggests that: i) there is no large scale "bulk" yielding in the composites and deformation takes place within a narrow band surrounding the fracture path (thus the observation of possible difference in strain to ultimate load between SiC/Al tensile samples is rather difficult), which correlates quite well with the previous observations in SiC/6061 Al composites [3,12], ii) the difference in the total amount of plastic deformation to fracture between the composite samples containing various sizes of the SiC particles comes mainly at the expense of the deformation taking place during the necking, i.e., plastically unstable portion of the tensile test.

SiC Particle Analysis

The experimental data show that the ratio of SiC particle densities measured along RP and FP does not depend on the SiC particle size, i.e., RPPC/FPPC = constant = 0.75 for 2.4, 3.2, 8 and 20 μm average SiC size

composites. This means that one finds more SiC particles along FP then along any other direction. Thus crack path is attracted towards the SiC particles. The significance of the specific value of 0.75 is not understood. Attraction of the crack front by the second phase particles is discussed elsewhere [13]. The attraction or deflection is determined by the sign of the residual stresses. In case of a tensile residual stress the crack front is attracted towards the particles [13]. The residual hydrostatic tension was reported to exist in SiC/Al composites due to the difference in CTE [14]. The influence of the residual stresses on the fracture path morphology in two phase system was treated theoretically using computer modeling [15]. Considering various levels of hydrostatic tension superimposed on the random arrangement of voids it was shown that the higher residual tension resulted in the lower strain to fracture. Also fracture propagated along the path which had the smallest fracture strain. The percent of SiC particles fractured by the crack path remains around 8% for 2.4, 3.2 and 8 μm average SiC particle size composites and increases to ~ 25% for 20 μm SiC/Al composite. This result can be treated on the basis of the critical flaw size used in the Griffith fracture mechanics. The probability of finding a critical flaw size in small SiC particle is less than in the coarse one [16].

Fractrography

The results of the fracture surface observation can be divided into three groups: 1) fracture surfaces have a dimple morphology, 2) there are two dimple populations: the first, which is associated with SiC particles, and increases its size as the size of the SiC particles increases, and second type consisting of very small dimples located in the space between the SiC related dimples, 3) no indication of fracture of SiC in the case of small SiC sizes (< 10 μm) (see Fig. 2).

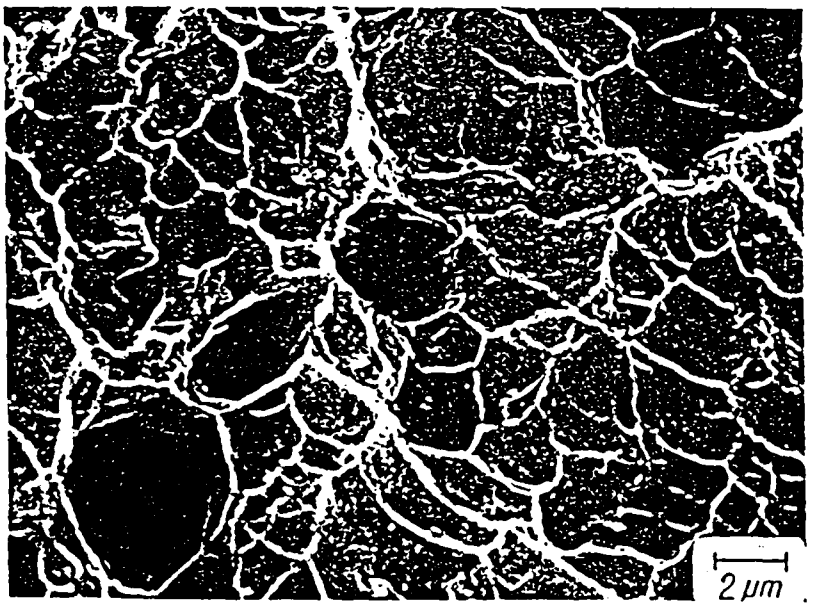

Fig. 2. Fracture surface of 3.2 μm average size SiC/Al composite.

When the SiC size increases the fracture of the particles becomes more apparent. The shape of the dimples is rather equiaxial and there is no

difference in the appearance between fracture surfaces of the tensile and CT specimens. Despite the correlation between the coarse dimples and SiC particles on the fracture surfaces of SiC/Al composites, not all the SiC particles are completely exposed. This corresponds to the earlier observations of the fracture surfaces of SiC/Al composites [2,12], and indicates good bonding between SiC and Al matrix.

Metallography

Observation of the polished cross sections of the tested tensile and CTS does not reveal the presence of the voids below the fracture path (see Fig. 3).

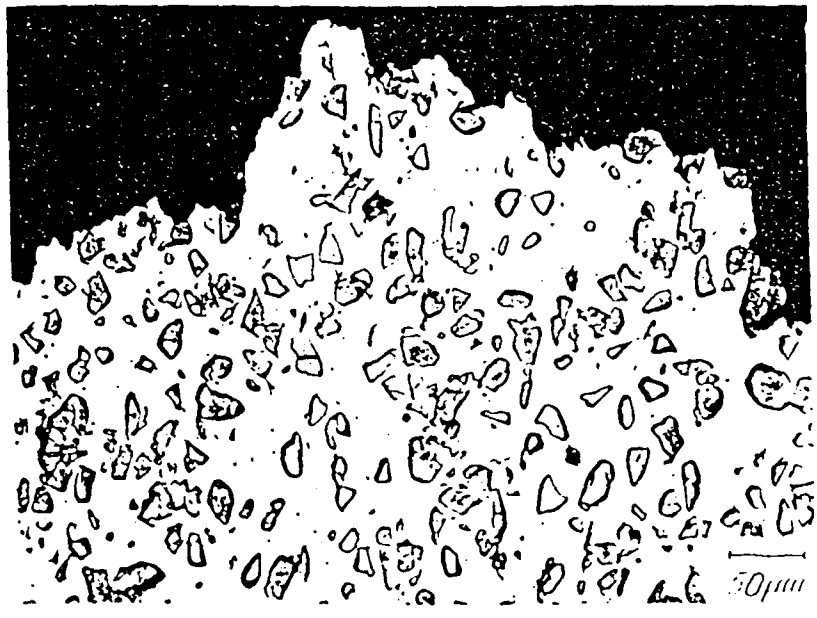

Fig. 3. Polished cross section of 20 μm average size SiC/Al composite tested tensile sample.

This means that fracture process is confined to an extremely narrow band and there is no apparent damage zone adjacent to the fracture surface which generally exists in the classical void nucleation and growth type ductile fracture. Also, very little pull out of the SiC particles from the Al matrix can be found which is indicative of a good SiC/Al interfacial bonding. No voids can be seen in the vicinity and ahead of the crack tip. Instead, a series of short cracks can be seen in the matrix in front of the continuous crack as shown on Fig. 4. Apparently this cracking takes place in the matrix ahead of the crack tip and forms some sort of the damage zone. This primary cracking can be observed as far as ≈ 50 μm away from the crack tip for the fine SiC particle (2.4 and 3.2 μm average size) SiC/Al composite and about 110 to 150 μm for the coarse SiC particle size (8 and 20 μm) composites. It is believed that crack propagation occurs by connecting these discontinuous microcracks. It seems that the short microcracks are associated with the clusters of SiC particles (see Fig. 4). Even though the distribution of the SiC particles is predominately homogeneous, on the microscale there are islands of high and low density of SiC particles. The clusters of the inclusions are considered to be a sites

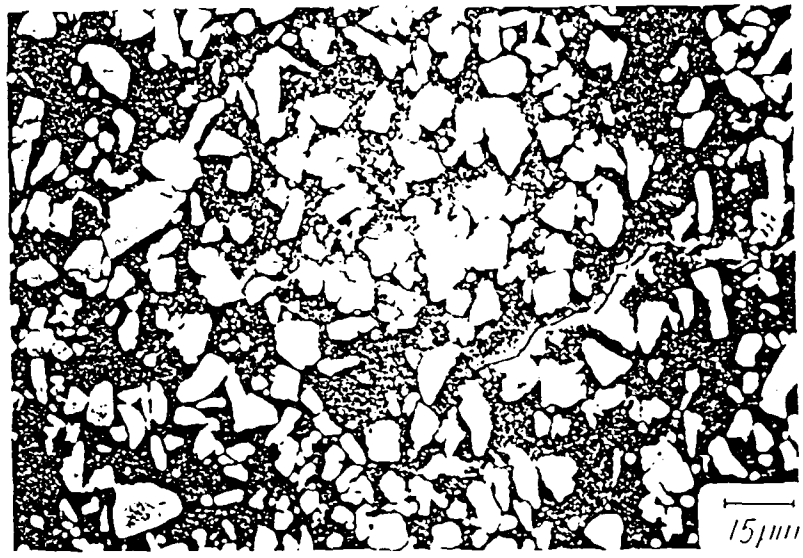

Fig. 4. Cross section through the tested 8 μm average size SiC/Al composite CTS showing the area around the crack tip.

where the damage level reaches extreme values causing the fracture of the entire system [17]. The degree of plastic constraint within the clusters could be much higher than in the rest of the matrix as a result of: i) residual hydrostatic tension and high dislocation density due to the difference in CTE [11,14], and ii) increase of hydrostatic tension during the deformation due to the plastic constraint in the matrix between the particles. These factors make SiC clusters quite favorable for crack initiation. A necessary condition for crack initiation is that the strain energy U stored at the inclusion is sufficient to provide the surface energy S of the newly formed crack surfaces, or U > S. The critical stress for crack nucleation can be obtained from the expression [18]:

$$\sigma = \frac{1}{q}\left(\frac{E_c \gamma}{d}\right)^{1/2} ,$$

where σ is the applied uniaxial stress, q is the average stress concentration factor at the inclusion, γ is the specific surface energy of the crack, E_c is the composite Young's modulus and d is the particle size. The location of the crack formation depends on the relative values of γ and q within the inclusion, at the interface or within the matrix [18]. It seems that stress concentration factor q would be quite high between closely spaced particles which is not inconsistent with our observation of the crack formation within the SiC particle clusters.

The very sharp appearence of the crack tip (see Fig. 4) shows that crack blunting between subsequent crack extensions is quite limited. The estimate of the width of the blunted crack δ based on void nucleation and growth model [19] predicts the blunting of about ~ 10 μm for 2.4 μm average size SiC/Al composite. This is much higher than the separation (1 to 2 μm) observed between the matching sides of the crack in CTS machined from SiC/Al composite containing 2.4 μm average size SiC particles. Thus the classical void nucleation and growth mechanism of ductile fracture does not give satisfactory description of the crack propagation in SiC/Al composites.

Fracture Initiation Toughness

Crack initiation fracture toughness measured as K_{IC} and K_{IQ} is plotted as a function of the average SiC particle size and is shown on Fig. 5.

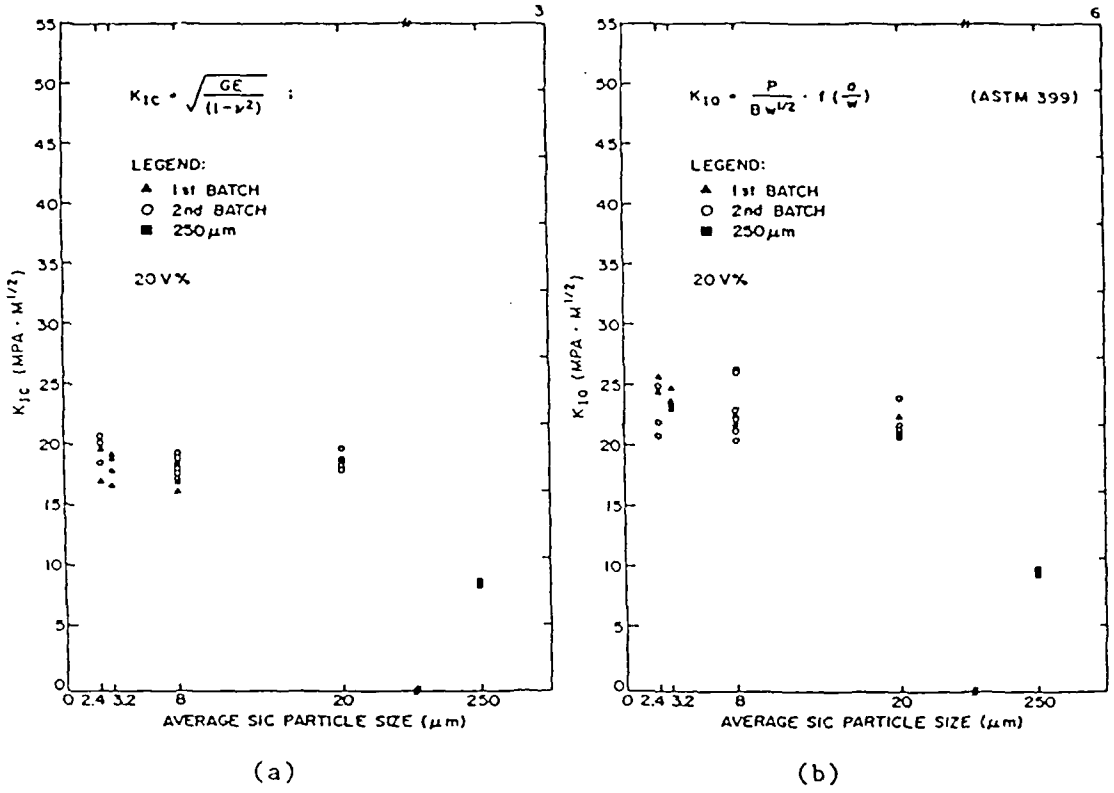

Fig. 5. Crack initiation fracture toughness of SiC/Al composites measured as K_{IC} (a) and K_{IQ} (b).

The fact that both of these values show the same trend, i.e., no dependence on the size of the SiC particles increases the confidence in the results obtained and supports the energy separation method as a new and powerful tool. The numerical difference ($K_{IC} \approx 18$ MPa · $\sqrt{m}$ and $K_{IQ} \approx 23$ MPa · $\sqrt{m}$) between the values of K_{IC} and K_{IQ} can be explained as follows. A finite notch with a root radius of ~ 150 μm was machined in CTS in order to start the crack (as opposed to ASTM E399 requirement of a pre-fatigued crack starter resulting in a geometrically sharp crack). Thus it is reasonable to expect higher values of K_{IQ} which are obtained in accordance with ASTM E399. Using the result of the study of the influence of notch acuity on the fracture initiation toughness [3] in SiC/Al composites we may write

$$K_{IQ} = K_{IC(r)} = K_{IC} \frac{(1 + r/2c)^{3/2}}{(1 + r/c)} ;$$

where $K_{IC(r)}$ is the initiation toughness of the notch with radius r, K_{IC} is the toughness of geometrically sharp crack and c is the adjustable constant related to the microstructure. Substituting values for $K_{IC(r)} = 23$ MPa · $\sqrt{m}$, $K_{IC} = 18$ MPa · $\sqrt{m}$ and $r \approx 150$ μm we obtain value for $c = 20$ μm. It is rather comparable with the size of the fracture process zone observed in 2.4 μm average SiC particle size composite. Initiation fracture toughness for 250 μm SiC/Al composite is almost by the factor of 2 less than for the

rest of the tested composites. This is apparently due to the premature cracking of 250 μm size SiC particles.

Crack Growth Toughness

Crack growth toughness measured as tearing modulus, T, and plastic part, I, of J-integral is plotted versus the average size of SiC particles in Fig. 6.

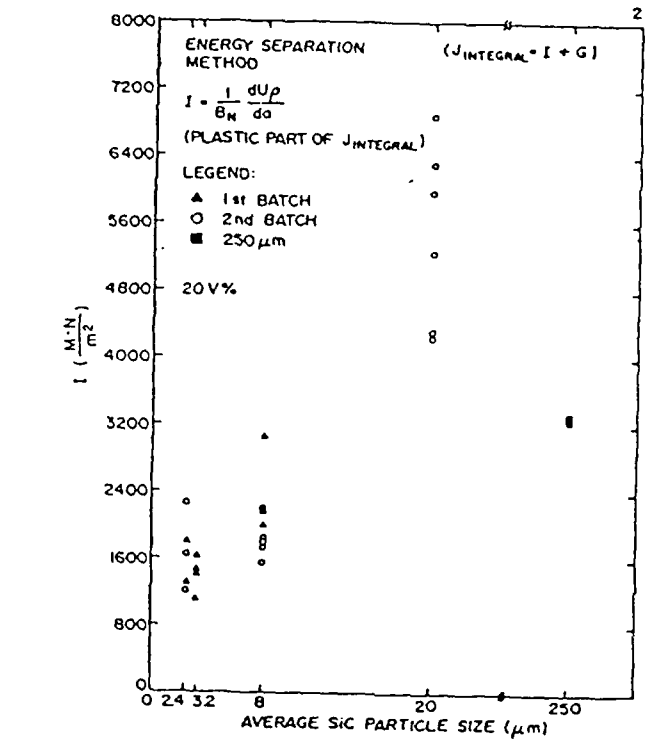

Fig. 6. Crack growth fracture toughness of SiC/Al composites measured as I (a) and T (b).

The increase of the crack growth toughness with an increase of the SiC particle size means that more energy is dissipated during crack extension in the composite with a larger size of SiC particles. As tensile test data shows the yield stress of the SiC/Al composites drops with the increase of the SiC particle size. The same behavior was reported in literature for various alloys containing second phase particles [10]. The size of the plastic zone is inversely proportional to the square of the yield stress [20]. Thus as the size of SiC particles increase, the size of the plastic zone also increases resulting in the increase of dissipated plastic energy which in turn increases the crack growth fracture toughness.

Conclusions

From the data obtained, the following conclusions can be made:

1. Fracture behavior of SiC/Al composites is quite unique and features of both brittle (limited crack blunting, microcracking in front of the crack tip, confinement of the fracture process to a very narrow band) and ductile (dimple morphology of the fracture surface) mechansims.
2. Fracture process is matrix controlled up to very large particle sizes (> 20 μm) and strongly influenced by: i) residual hydrostatic tension and hydrostatic tension due to inhomogeneous plastic deformation, ii) high dislocation density in the regions adjacent to the SiC particles, and iii) local fluctuations in distribution of SiC particles.
3. Crack initiation fracture toughness K_{IC} is independent of the SiC particle size up to very coarse grit sizes when SiC particle fracture takes over.
4. Low values of the crack initiation toughness can be related to a high dislocation density and residual hydrostatic tension due to the difference in CTE between SiC and Al.
5. Young's modulus is not a function of the SiC particle size at a given volume fraction.
6. Yield stress and ultimate strength of the SiC/Al composite decreases as SiC grit size increases.
7. SiC/Al interfacial bond strength is quite high.
8. Crack growth fracture toughness measured by T (tearing modulus) and I dissipation rate of the plastic energy) increases with the increase of SiC particle size.
9. Increase in the initiation fracture toughness can be expected only when the plastic constraint of the matrix is decreased. This can be achieved by tailoring SiC/Al interfaces to control the interfacial bond strength. By lowering the bond strength the dislocation density could be reduced. This however will result in the decrease of yield stress.

ACKNOWLEDGEMENT

This research was supported by the Office of Naval Research under Contract No. N00014-85-K-0007. The authors wish to acknowledge the continued support and encouragement of Dr. S. Fishman of the Office of Naval Research.

REFERENCES

1. Divecha, A. P., Fishman, S. G., and Karmarkar, S. D., J. of Metals, 1981, 9, 12.

2. Logsdon, W. A. and Liaw, P. K., Tensile, Fracture Toughness and Fatigue Crack Growth Rate Properties of SiC Whisker and Particulate Reinforced Al Metal Matrix Composites, Westinghouse Scientific Paper 83-1D3-NODEM-P1, December 1983.

3. Crowe, C. R., Gray, R. A., and Hasson, D. F., Proceedings of ICCM-5, ed. by W. Harrigan, San Diego, 1985, p.

4. McDanels, D. L., Met. Trans. A, 1985, 16, 1105.

5. ASTM Standards, Section 3, Vol. 03.01, E813 (1986).

6. Mecklenburg, M. F., Joyce, J. A., Albrecht, P., "Separation of Energies in Elastic-Plastic Fracture", presented at the Third Internation Symposium on Nonlinear Fracture Mechanics, ASTM, October 1986, Knoxville, Tenn.

7. Latzo, D. G. H., Turner, C. E., Landes, J. D., McCabe, D. E., and Hellen, T. K., Post Yield Fracture Mechanics, 2nd Ed., Elsevier Pub., NY, 1984.

8. Richie, R. O. and Thompson, A. W., Met. Trans. A, 1985, 16, 233.

9. Mogford, I. L., Metallurgical Reviews, 1967, 114, 12, 49-65.

10. Schoutens, J. E., Introduction to Metal Matrix Composite Materials, MMCIAC, 3rd ed., 1982.

11. Arsenault, R. J. and Shi, N., Mat. Sci. & Eng., 1986, 81, 175-87.

12. Nieh, T. G., Rainen, R. A., and Chellman, D. J., Proceedings of ICCM-5, ed. by W. Harrigan, San Diego, 1985, p. 825.

13. Faber, K. T. and Evans, A. G., Acta Met., 1983, 31, 565.

14. Arsenault, R. J. and Taya, M., The Effects of Differences in Thermal Coefficients of Expansion in SiC Whisker 6061 Aluminum Composites, in the Proceedings of a ICCM-5, ed. by W. Harrigan, San Diego, 1985, p. 21.. Also accepted for publication in Acta Met.

15. Melander, A., Mat. Sci. and Eng., 1979, 39, 57-63.

16. Davidge, R. W., Mechanical Behavior of Ceramics, Cambridge University Press, 1980.

17. Embury, J. D. and Burger, G., The Role of Microstructure in the Fracture of Structural Steels, in the Proceedings of a Conference on "Inclusions and Residuals in Steels: Effects on Fabrication and Service Behavior", Ottawa, March, 1985.

18. Gurland, J. and Plateau, J., Trans. ASM, 1963, 56, 442.

19. McMeeking, R. M., J. Mech. Physics Solids, 1977, 29, 337.

20. Thomason, P. F., Int. Journ. of Fracture Mech., 1971, 7, 409-419.

5

Strengthening Mechanisms in Discontinuous SiC/Al Composites

R. J. ARSENAULT

Engineering Materials Group, University of Maryland, College Park, Maryland 20742-2105, USA

ABSTRACT

The various potential factors which could affect the yield strength of discontinuous SiC/Al composites, such as load transfer mechanisms, residual elastic stresses, differences in texture, etc., were considered. It was found that the high dislocation density and small subgrain size generated as a result of the difference in thermal coefficient of expansion between the SiC and Al was the major contribution to the strengthening. The classical load transfer mechanism and the texture difference had no effect on the strength. The thermal elastic residual stress was on average in tension (for whisker composite) and it reduced the tensile yield stress of the whisker composite.

INTRODUCTION

The framework of a mechanism is slowly evolving to account for the strengthening due to the addition of SiC to an Al alloy matrix. However, it should be kept in mind that the number of detailed investigations of these composites is rather limited.

The basic strengthening mechanism is the high dislocation density, which is produced as a result of the differences in the thermal coefficients of expansion between SiC and Al, and the small subgrain size that results.

There could be other contributing causes to the strengthening, such as:

1. Residual elastic stresses.
2. Differences in texture.
3. Classical composite strengthening (load transfer).

The classical models based on continuum mechanics models will have to be considered in detail.

Two types of continuum models seem to have been used extensively, the shear lag type and the Eshelby type models. The former model, which was originally developed by Cox,[1] is simple and has been used for prediction of stiffness,[2] yield stress,[3] strength and creep strain rate.[4] In the case of continuous whisker composite, a shear lag type model was also applied to prediction of load concentration factor successfully.[5] However, it is known that the properties predicted by the shear lag type model will become a crude approximation when the aspect ratio of the short fiber (l/d) is small or the short fibers are misoriented. Nardone and Prewo[3] have recently proposed a variation of the shear lag type model to obtain a larger estimated tensile yield stress of a short whisker MMC with smaller values of l/d.

On the other hand, in the Eshelby type model, the short whisker is assumed to be a prolate ellipsoidal inhomogeneity. The analytical model to predict the thermal and mechanical properties of a composite was first developed by Eshelby, who considered a single ellipsoidal inclusion or inhomogeneity embedded in an infinite elastic body,[6] thus it is valid only for a small volume fraction of fiber V_f. Mori and Tanaka[7] modified the original Eshelby model for a finite volume fraction. The modified Eshelby type models are stiffness,[8] yield stress and work-hardening rate,[9-11] thermal expansion[12,13] and thermal conductivity.[14] The Eshelby type model has also been used to predict the thermal residual stress in a composite.[10,13,15] The detailed summary of the Eshelby type models is given in a book by Mura.[16]

The purpose of this investigation was to reconsider the load transfer mechanism of composite strengthening, and to consider elastic residual stress and texture differences which could exist on the strengthening of discontinuous composites.

MODELS

1. Shear Lag Type Model

The original shear lag model, developed by Cox,[1] with its detailed derivation of the stiffness[2] and yield stress[3] has already been discussed elsewhere. Thus it is omitted here. The standard shear lag model has often been used for an aligned short fiber composite system where short fibers of the same size are assumed to be distributed in the matrix in a hexagonal

array. The repeated cell (unit cell) is used for the detailed derivation.[17,18] The most important assumption in the shear lag type model is that load transfer occurs between a short whisker and matrix by means of shear stresses at the matrix–whisker interface. In the original shear lag model[1,2] the load transfer by the normal stress at the whisker ends and side surfaces was ignored. Nardone and Prewo[3] recently suggested that the load transfer at the fiber ends should be accounted for in predicting the yield stress, but still ignored the normal load at the side surface of fiber for the case of l/d values. Below is the final formulae based on the shear lag type model to predict the stiffness[1,2] and the end result of a derivation of the tensile yield stress, including normal stresses on the end of the fiber of a short fiber composite. For the stiffness,

$$E_c/E_m = (1 - V_w) + (V_w E_w/E_m)[1 - (\tanh x)/x] \tag{1}$$
$$x = (l/d)\{(1 + \nu_m)(E_w/E_m)\ln[V_w]^{-1/2}\}^{-1/2}$$

For the yield stress,

$$\sigma_{yc}/\sigma_{ym} = 0{\cdot}5V_w(2 + l/d) + (1 - V_w) \tag{2}$$

where E_m, E_w and E_c are Young's moduli of the matrix, whisker and composite, respectively; V_w is the volume fraction of whiskers; σ_{ym} and σ_{yc} are the yield stresses of the matrix and composite, respectively; and l/d is the whisker aspect ratio.

In the shear lag model, there exists an uncertainty regarding the relation between l/d and L/D, which is usually found from observations of SEM photos. In deriving eqn. (1), we have used the same assumption as Kelly and Street,[4] i.e. $L = l$. This assumption would certainly induce errors in the analysis for the case of smaller whisker aspect ratios. This model is described in greater detail elsewhere.[17,18]

2. Eshelby Type Model

The original Eshelby model[6] is based on the assumption that an ellipsoidal inclusion with uniform nonelastic strain (eigenstrain) $\mathbf{e}^*$ is embedded in an infinite elastic body. Eshelby[6] derived the formula to compute the stress field induced in and around an inclusion and also the associated strain energy of this system. Mori and Tanaka[7] modified the original Eshelby model to account for the interaction between inclusions, i.e. an aligned short fiber composite.

The Young's modulus along the fiber axis E_c can be obtained as

$$E_c/E_m = 1/(1 + V_w(E_m/\sigma_0)e^*_{33}) \tag{3}$$

where e^*_{33} is to be computed from formulation defined elsewhere,[17,18] and the results are expressed in terms of $c_0(\sigma_0/E_m)$ and c_0 is some numerical value.

The formula to predict the yield stress is finally reduced to[17,18]

$$\sigma_{yc} = c_1\sigma_{ym} + c_2 e_p \tag{4}$$

where c_1 is a nondimensional parameter (the yield stress raiser), c_2 is the work-hardening rate and e_p is the plastic strain in the matrix along the fiber axis.

NUMERICAL RESULTS

In order to compare these models, the stiffness (E_c) and the yield stress (σ_{yc}) of an aligned short whisker MMC are computed by using eqns (1) and (2) (shear lag type model) and eqns (3) and (4) (Eshelby type model). The target short whisker MMCs are spherical SiC (SiC_s) and SiC whiskers (SiC_w)/1100 Al matrix composites.[18] The numerical results of E_c/E_m based on the shear lag type and Eshelby type models are plotted as dashed and solid curves, respectively, as a function of whisker aspect ratio l/d in Fig. 1. The experimental results[19] are also plotted as a circle in Fig. 1. The material constants used in this calculation are given in Ref. 18. It can be seen in Fig. 1

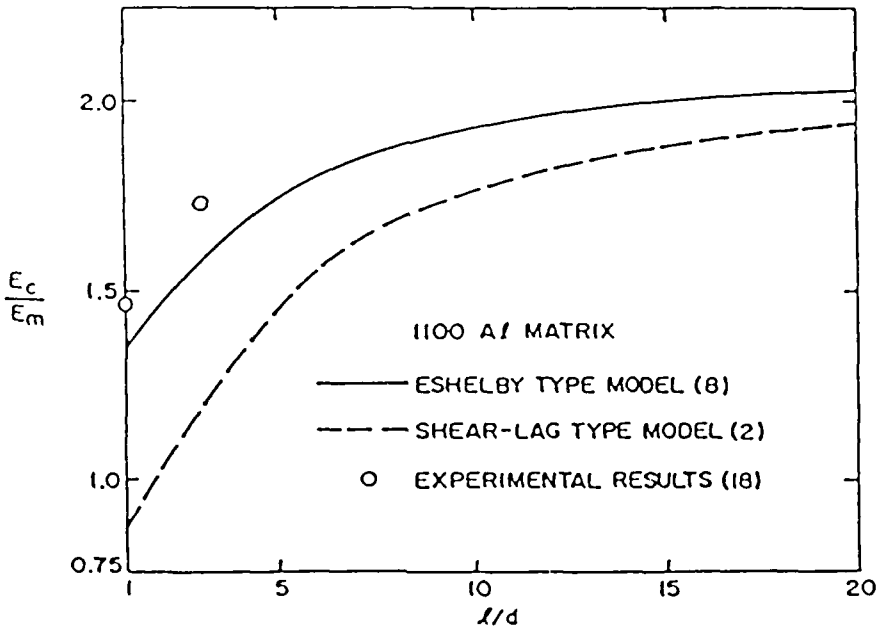

FIG. 1. The ratio of modulus of the composite to modulus of the matrix versus length to diameter ratio of fiber.

that the stiffnesses predicted by the shear lag type model are always less than those predicted by the Eshelby type model and that the shear lag model is a rather crude approximation for smaller l/d. A comparison with the experimental results reveals that the Eshelby type model gives a better prediction.

Next we have computed the values of σ_{yc}/σ_{ym} based on eqns (2) and (4), the results of which are plotted as dashed and solid curves, respectively, in Fig. 2, where the closed circles denote the experimental results for a specific SiC_w/Al 6061-T6 composite[3] and the predicted values based on the modified Eshelby model, with residual stress accounted for, are plotted as a dash-dot curve. All predictions are plotted as a function of l/d. In the range of small l/d the Eshelby type model gives an accurate prediction,

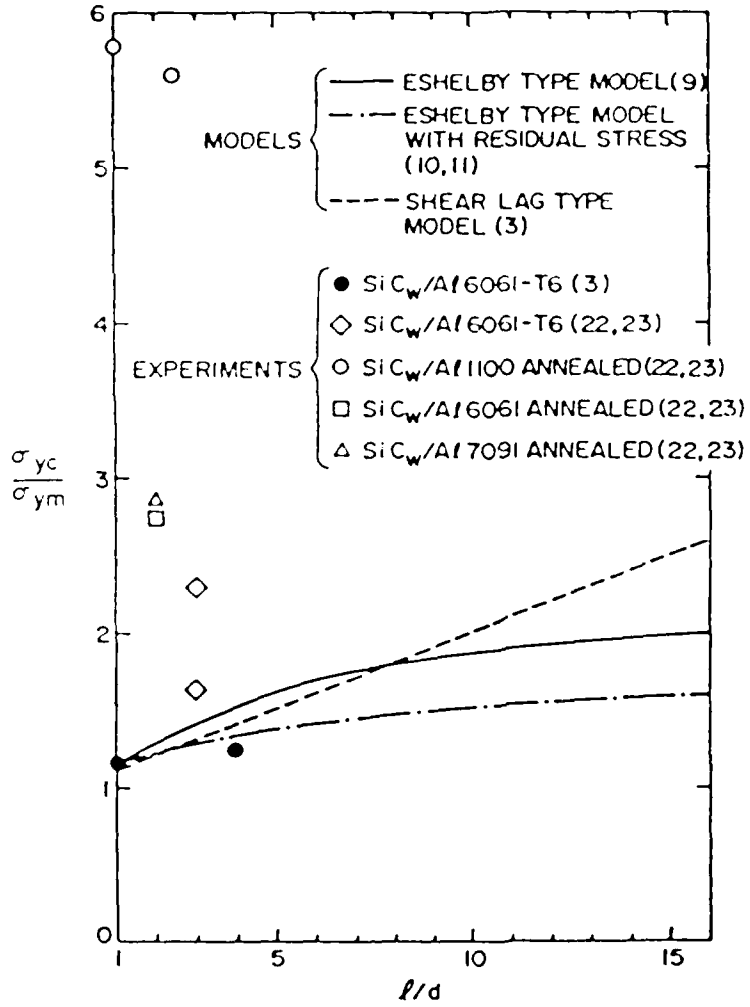

FIG. 2. The ratio of the yield stress composite to matrix versus length to diameter ratio of fiber. For 20V% SiC.

particularly at $l/d = 1$, while the shear lag model gives an underestimation. However, at larger l/ds both models predict basically the same order of composite tensile yield stress. In the same figure, our recent results for various SiC_w/Al composite systems are also plotted as open symbols. Though the Eshelby type model gives reasonable predictions for the case of the T6-treated composite (●), the stress prediction of both models is low compared to the experimental results for most of the data (○, ◇, □ and △). The poorest prediction occurs for the case of an annealed 1100 aluminum composite (○).

The experimental σ_{yc} and σ_{ym} correspond to the stress at 0·2% offset, and σ_{ym} is from a 0 V% material produced in the same manner as the composite. The reason that both of these models are not capable of predicting the observed strengthening is that these models assume that the matrix has the same strength as it has in the nonreinforced condition. In other words, these models assume that the addition of SiC does not change the strength of the matrix. It has been clearly shown that the dislocation density in the SiC/Al composites is much higher than in the nonreinforced Al.[20,21]

If the absolute magnitude of the increase in σ_{yc} compared to σ_{ym} is considered, then the apparent differences caused by the various matrix alloys is much less. The data[18] indicate that $\Delta\sigma$ ($\Delta\sigma = \sigma_{yc20V\%} - \sigma_{ym0V\%}$) is relatively independent of the composite matrix except for the T6 heat-treated case. The lack of a difference in $\Delta\sigma$ occurs because the thermal stress developed upon cooling is very large compared to the yield stress of the matrix in the annealed condition. The dislocations are generated in the initial cool down whether the sample is furnace cooled or quenched prior to aging. Therefore, the increased density of dislocations generated for all practical purposes is independent of the matrix.

Since the observed increase in the experimental σ_{yc} is much greater than that predicted by the shear lag type model or the Eshelby type model, the increase in σ_{yc} must be caused by the increased dislocation density in the composite matrix. This increase in dislocation density is the result of relaxation of a portion of the stresses developed upon cooling of the composite. The stresses arise from the localization of differences in coefficients of thermal expansion between the SiC and Al. The effect of this thermal expansion mismatch strain ($\Delta\alpha\Delta T$) has been considered in the Eshelby model, with residual stress accounted for (dot-dot curve in Fig. 2).[11,17] However, in the model $\Delta\alpha\Delta T$ is simulated by the equivalent surface dislocations[15] that are present at the matrix–whisker interfaces. In reality, the surface dislocations are more likely to relax by punching,[24] resulting in the localization of dislocations around a whisker.

If we now consider the proportional limit of the composite, an interesting correlation can be obtained. The proportional limits of the composites[22,25] are approximately equal to σ_{ym}. This correlation gives rise to two important points. First, the modulus (E_c) that is predicted by the Eshelby type model, which is in agreement with the experimental data, is for the initial portion of the stress–strain curve, i.e. for stresses up to the proportional limit. Therefore, the Eshelby type model does operate up to the proportional limit, and the model predicts a very small increase in the proportional limit upon the addition of the reinforcement, again in agreement with the experimental data. Second, the increase in stress with strain in the stress region from the proportional limit to σ_{yc} is caused by an exhaustion phenomena. In the stress–strain region, dislocation motion occurs in the lower dislocation density regions within the matrix. The increase in stress between the proportional limit and the σ_{yc} is not caused by work-hardening, for there is no general increase in dislocation density.[26] There is an increase in dislocation immediately below the fracture surface, i.e. within 100 μm of the fracture surface. The dislocation density in the remainder of the sample is identical to that of the undeformed sample. However, only limited deformation can occur, because of the small volume of matrix. In order to have macro-deformation, i.e. to reach 0·2% offset strain, additional dislocation motion must occur in the higher stress regions of the matrix which are often quite localized in the specimen. Therefore, the macro-yielding of the composite is controlled by the inhomogeneous matrix which is a mixture of the high–low dislocation regions.

RESIDUAL ELASTIC STRESS

An analytical model by Arsenault and Taya[11] based on an ellipsoidal-shaped SiC particle in Al matrix was developed, which predicts that a tensile thermal residual should exist in the matrix for a whisker of l/d of 1·8 and the longitudinal residual stress should be higher than the transverse residual stress. The actual experimental data obtained from an X-ray analysis are shown in Table 1. The X-ray results do indicate that the matrix is in tension and that the longitudinal residual stress is higher than the transverse residual stress. However, the X-ray data indicate a higher value of residual stress than predicted.

The model of Arsenault and Taya[11] predicts that the yield stress in compression should equal the yield stress in tension if the SiC is in the form of spheres. The surprising result is that in the case of spherical SiC

TABLE 1
Thermal residual stress (tensile) X-ray measurements

Material	Longitudinal (MPa)	Transverse (MPa)
0 Vol. % whisker SiC 6061 matrix	0·0	0·0
5 Vol. % whisker SiC 6061 matrix	408	35
20 Vol. % whisker SiC 6061 matrix	231	58
Wrought 1100 Al	0·0	0·0

composite, the tensile stress is higher than that of the compressive yield stress, whereas the difference predicted by the model is zero. However, the point to be made is that for the whisker case $\sigma_y^C > \sigma_y^T$. The model of Arsenault and Taya successfully predicts the differences in the tensile and compressive yield stress due to the thermal residual stresses. However, the model is completely incapable of predicting the absolute magnitude of the

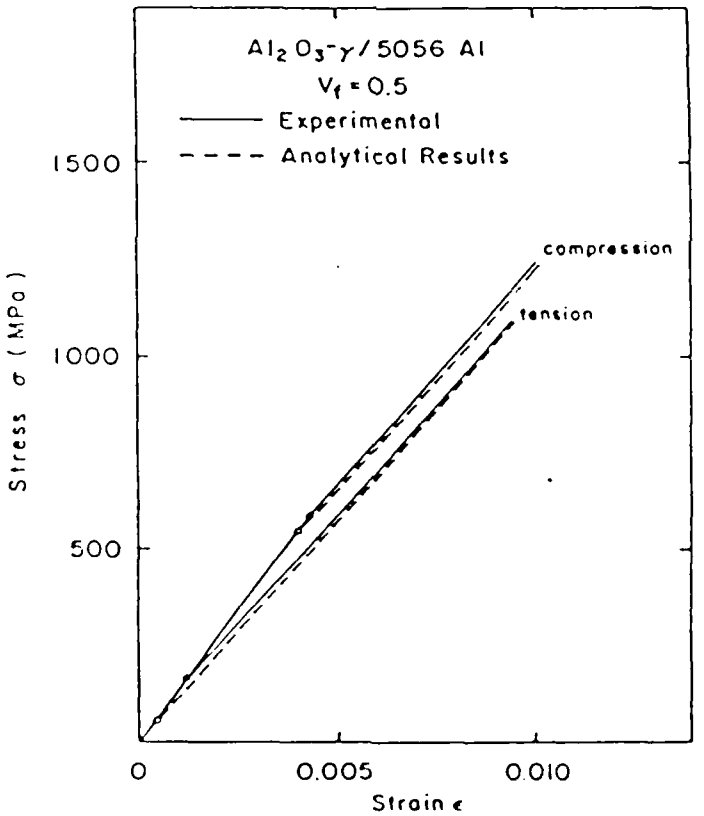

FIG. 3. Tension and compression stress–strain curves of continuous Al_2O_3 fiber/5056 Al composite with $V_f = 0{\cdot}5^{\prime}$. The experimental and theoretical results are denoted by solid and dashed curves, respectively. The solid and open circles denote the yield stress of the experimental and theoretical results, respectively.

increase in yield stress, for it does not have the capability of predicting the increase in the matrix strengthening.

In a case where the matrix strengthening is not such a predominant factor, i.e. continuous filament deposits, the model is excellent in predicting the differences between tension and compression, and the absolute values as shown in Fig. 3.

TEXTURE

A texture investigation was undertaken and from a comparison of the data it is apparent that there is little difference in the texture of 99·99% Al, 0 V%, 6061 Al alloy and 20 V% 6061 Al alloy matrix composite, as shown in Fig. 4.

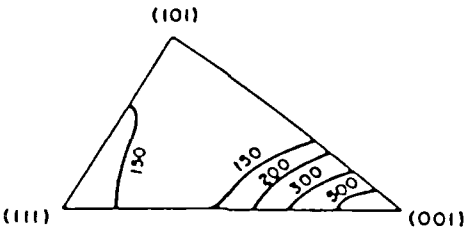

TEXTURE FOR EXTRUDED & ANNEALED
99.99% Al

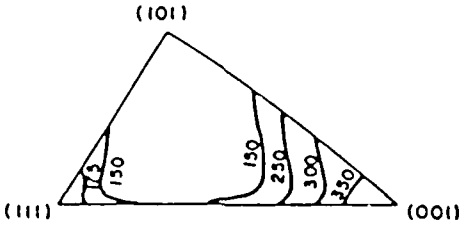

TEXTURE FOR EXTRUDED & ANNEALED
0V% SiC 1100 MATRIX

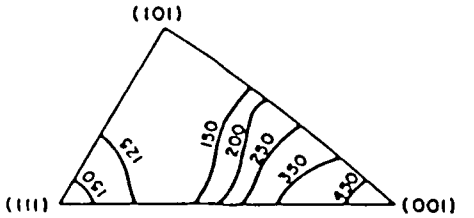

TEXTURE FOR EXTRUDED & ANNEALED
20V% SiC 1100 MATRIX

FIG. 4. The texture of two control Al samples and a 20 V% SiC whisker composite in the annealed condition as determined by an X-ray technique.

DISCUSSION

Some time ago, a listing of the components of the strengthening mechanisms was proposed:

$$\Delta\sigma_{yc} = \Delta\sigma_{dist} + \Delta\sigma_{sg} \pm \Delta\sigma_{res} + \Delta\sigma_{tex} + \Delta\sigma_{comp}$$

where $\Delta\sigma_{dist}$ is the increase in strengthening due to the increase in dislocation density resulting from the differences in thermal coefficients of expansion between the SiC and Al, $\Delta\sigma_{sg}$ is the increase in strengthening due to the reduced subgrain size, $\Delta\sigma_{res}$ is the difference in strengthening due to the thermal residual elastic stresses, $\Delta\sigma_{tex}$ is the strengthening due to differences in texture between the 0 volume % and the higher volume % composites, and $\Delta\sigma_{comp}$ is the strengthening due to classical composite strengthening, e.g. load transfer.

If the strengthening components are considered in detail, it is now necessary to consider the morphology of SiC. Table 2 is a listing of the

TABLE 2
A listing of the strengthening components for the spherical SiC in 1100 Al matrix

$\Delta\sigma_{ys} = \Delta\sigma_{dist} + \Delta\sigma_{sg} \pm \Delta\sigma_{res} + \Delta\sigma_{tex} + \Delta\sigma_{comp}$	
$\Delta\sigma_{dist} = 124{\cdot}2$ MPa	
$\Delta\sigma_{sg} = 55{\cdot}2$ MPa	
$\Delta\sigma_{res} = 0$	
$\Delta\sigma_{tex} = 0$	
$\Delta\sigma_{comp} = 0$	
$\Delta\sigma_{ys} = 179{\cdot}4$ MPa	$\Delta\sigma_{ysexp} = 172{\cdot}5$ MPa

TABLE 3
A listing of the strengthening components for the whisker SiC 1100 Al matrix

$\Delta\sigma_{yw} = \Delta\sigma_{dist} + \Delta\sigma_{sg} \pm \Delta\sigma_{res} + \Delta\sigma_{tex} + \Delta\sigma_{comp}$	
$\Delta\sigma_{dist} = 124{\cdot}2$ MPa	
$\Delta\sigma_{sg} = 55{\cdot}2$ MPa	
$\Delta\sigma_{res} = -34{\cdot}5$ MPa	
$\Delta\sigma_{tex} = 0$	
$\Delta\sigma_{comp} = 0$	
$\Delta\sigma_{yw} = 144{\cdot}9$ MPa	$\Delta\sigma_{ywexp} = 144{\cdot}9$ MPa

strengthening components for the spherical SiC case. The strengthening due to $\Delta\sigma_{tex}$ and $\Delta\sigma_{comp}$ is equal to zero. The summation of the predicted strengthening and the observed strengthening are in very good agreement. Table 3 is a listing of the strengthening components for the whisker SiC case, The strengthening due to $\Delta\sigma_{disl}$ may be a little higher than the value given, however, again the agreement between the predicted and experimental results is very good.

CONCLUSIONS

From the data presented in this paper, several conclusions can be drawn:

1. The data generated further support the concept that the strengthening mechanism is due to the difference in the thermal coefficient of expansion between SiC and Al, which results in a higher dislocation density and a small subgrain size.
2. The thermal residual stress, as measured by the X-ray technique, indicates that the matrix is in tension.
3. There is a difference between 6061 and 2124 in terms of the fracture of SiC whiskers and/or the bonding to SiC whiskers.
4. A model based on load transfer is completely incapable of explaining the increase in strength due to the addition of SiC to the Al alloy matrix.

ACKNOWLEDGEMENT

This research was supported by the Office of Naval Research under grant No. N00014-85-K-007.

REFERENCES

1. Cox, H. L. Jr, *J. appl. Phys.*, 3 (1952), 72.
2. Kelly, A., *Strong Solids*, Oxford, Clarendon Press, 1966.
3. Nardone, V. C. and Prewo, K. M., *Scripta Metall.*, 20 (1986), 43.
4. Kelly, A. and Street, K. M., *Proc. Roy. Soc. Lond.*, A328 (1972), 283.
5. Hedgepeth, J. M. and Van Dyke, P., *J. Comp. Mater.*, 1 (1967), 294.
6. Eshelby, J. D., *Proc. Roy. Soc. Lond.*, A241 (1957), 376.
7. Mori, T. and Tanaka, K., *Acta Metall.*, 21 (1973), 571.

8. TAYA, M. and MURA, T., *J. appl. Mech.*, 48 (1981), 361.
9. TANAKA, T., WAKASHIMA, K. and MORI, T., *J. Mech. Phys. Solids*, 21 (1973), 207.
10. WAKASHIMA, K., SUZUKI, S. and UMEKAWA, S., *J. Comp. Mater.*, 13 (1979), 391.
11. ARSENAULT, R. J. and TAYA, M., *Proc. ICCM-V* (Harrigan, W. C. Jr, Strife, J. and Dhingra, A. eds), TMS-AIME, Warrendale, PA, 1985, p. 21.
12. WAKASHIMA, K., OTSUKA, M. and UMEKAWA, S., *J. Comp. Mater.*, 8 (1974), 391.
13. TAKAO, Y. and TAYA, M., *J. appl. Mech.*, 107 (1985), 806.
14. HATTA, H. and TAYA, M., *J. appl. Phys.*, 58 (1985), 2478.
15. MURA, T. and TAYA, M., *Recent Advances in Composites in the United States and Japan*, ASTM STP 864 (Vinson, J. R. and Taya, M. eds), Philadelphia, PA, 1985, p. 209.
16. MURA, T., *Micromechanics of Defects of Solids*, The Hague, Martinus Nijhoff Publ., 1982.
17. ARSENAULT, R. J. and TAYA, M., to appear in *Acta Metall.*
18. TAYA, M. and ARSENAULT, R. J., to be published in *Scripta Metall.* (March 1987).
19. WOLFENDEN, A. and ARSENAULT, R. J., unpublished results.
20. VOGELSANG, M., ARSENAULT, R. J. and FISHER, R. M., *Met. Trans.*, 17A (1986), 379.
21. ARSENAULT, R. J. and FISHER, R. M., *Scripta Metall.*, 17 (1983), 67.
22. ARSENAULT, R. J. and WU, B., submitted for publication.
23. ARSENAULT, R. J., *Proc.-of Third Japan Conference, Composites '86. Recent Advances in Japan and United States* (Kauata *et al.* eds), in press.
24. ARSENAULT, R. J. and SHI, N., *Mater. Sci. Engng*, 81 (1986), 175.
25. ARSENAULT, R. J., *Mater. Sci. Engng*, 64 (1984), 171.
26. ARSENAULT, R. J. and FENG, C. R., to be submitted for publication.

ROLE OF INTERFACES IN SiC/Al COMPOSITES

by

R.J. ARSENAULT and Y. FLOM

Reprinted from:

Structure and Deformation of Boundaries

Proceedings of a symposium "Phase Boundary Effects on Deformation" sponsored by the Physical Metallurgy, Structural Materials and Mechanical Metallurgy Committees of The Metallurgical Society of AIME and the Flow and Fracture Activity of American Society for Metals held at the 1985 TMS-AIME Fall meeting, Toronto, Canada, October 13-17, 1985.

Edited by

K. N. Subramanian
Michigan State University
East Lansing, Michigan

M. A. Imam
Naval Research Laboratory
Washington, D.C.

CONFERENCE PROCEEDINGS

The Metallurgical Society of AIME

Role of Interfaces in SiC/Al Composites*

R. J. Arsenault and Y. Flom

Metallurgical Materials Laboratory
Chemical Engineering Building
University of Maryland
College Park, MD 20742

Abstract

In discontinuous metal matrix composites, specifically SiC whiskers or platelets in an Al alloy matrix, the interface is a dominate factor. The strengthening produced by the addition of SiC to Al is due to the high dislocation density in the matrix. It has been shown by in situ HVEM that dislocation generation does occur in thermal cycling, also, if a good bond does not exist at the interface then dislocation generation does not occur. The degree of bonding also affects fracture mechanism, i.e., the degree of void nucleation and growth. In the fracture studies, the fracture surfaces have a dimpled appearance. The size of the dimples range from tens of microns down to a fraction of a micron. SiC particulates can be observed at the bottom of some dimples.

* This research was supported by the Office of Naval Research under Grant No. N00014-85-K-0007.

Introduction

The quality of interfacial bond between Al and SiC is important in composite strengthening, independent of the strengthening mechanism that is assumed to be operative. One of the key elements in the continuum mechanics treatment of the composite strengthening is that the interface transfers the load from the matrix into the reinforcement[1-3]. The rule of mixtures that emerges from the continuum mechanics relates a given property of the composite to the properties of its constituent materials. The credibility of this approach depends on, agmong other things, the bond integrity and the efficiency of the load transfer from the matrix to the reinforcement.

Recently it has been shown[4-6] that in Al/SiC systems the interfaces are a major source of the dislocation generation (on cooling from fabricating temperature due to the difference in the coefficient of thermal expansion). The resultant dislocation densities at the Al/SiC interfaces can be very high (10^9 to 10^{10} cm^{-2}), which significantly contributes to the overall composite strength.

Several investigators have reported that the bond between Al/SiC is generally good[7,8], but a systematic evaluation of the bond strength has not been, to our knowledge, reported in the literature. Direct measurements of the interfacial shear strength in metal matrix systems have been made using flat plate and fiber pullout tests[9]. The fiber pullout test, which is of more interest for this investigation, was used to determine interfacial shear strength in Cu/W and Cu/Mo systems[10]. Several attempts were made to carry out a direct measurement of the interfacial bond shear strength in Al/SiC using the pullout test due to its apparent simplicity. However, all these attempts resulted in brittle failure of SiC (single crystal, very large grain, and sintered SiC were used) at very moderate loads.

In addition, an effort was made to perform a punch test using Al disks with pieces of the SiC embedded in the center. This effort also resulted in premature failure in SiC.

Another way to evaluate the interfacial bond strength is based on the general understanding of the mechanism of the ductile fracture [11-14] which was applied for the determination of the interfacial bond strength in spheroidized 1045 steel, Cu-0.6 pct. Cr alloy, and maraging steel containing Fe_3C and TiC particles, respectively[15,16]. Providing that the ductile fracture starts by void nucleation at the inclusions and second phase particles, the theoretical bounding analysis[14] allows the evaluation of the interfacial strength in the systems with the small volume fraction of the second phase.

A ductile fracture, especially in the presence of second-phase particles or inclusions, is assumed to be the end result of a sequence of three processes: i) nucleation of the voids at the second-phase particles, ii) growth, iii) linkage of voids[17-20].

It is generally thought that the nucleation of voids requires the attainment of a critical normal stress at the particles matrix interface[14], which is a local condition. This depends upon the size, shape and location of the particles and sometimes their interaction[12]. In the case of SiC/Al composites that have been produced to date, it is possible that this event, i.e., the nucleation may be reduced at some of the Al/SiC interfaces because of the pre-existing voids.

The growth rate of the voids is determined by the rate of specimen extension and the stress rate[12,20]. Experimental observations of void growth have been made in many studies, primarily under simple tensile loading, and the analysis is based on this mode.

The strain for void initiation, i.e., nucleation and that for growth before linkage can be defined for multiloading state. A weakness in all of the theories of ductile fracture is the arbitrary nature of the condition of void linkage and failure. It is usually assumed that voids connect when the void length reaches some multiple of the distance between the neighboring void[17,18]. Some criteria ignore the geometric or material instabilities that can lead to flow localizations: yet they appear to give adequate descriptions of the experimental results. A small word of caution should be made, and that is, these results apply to the ductile fracture, only when the matrix is quite soft, i.e., if the matrix is strengthened by some mechanism, such as age hardening or solid solution strengthening the agreement between the experimental results and theory is definitely not as good. This mechanism predicts that fracture strain, which may be related to fracture toughness, is independent of platelet size at a given volume fraction.

As stated above, dislocation generation due to differences in coefficient of thermal expansion between SiC and Al is a major contributing factor to strengthening. However, the role of interfacial bond on the dislocation has not been demonstrated and knowledge of plastic zone dimensions, i.e., the extent of the region about SiC of a high dislocation density should contribute to the understanding of the mechanism of composite strengthening.

The experimental determinations of plastic strains and plastic zone radii about a particle in the matrix due to differences in coefficient of thermal expansion (CTE), to our knowledge, have not been reported in the literature.

Several theoretical investigations have been undertaken to predict the magnitude of the plastic strain in the plastic zone around a particle. The relaxation of the misfit caused by the introduction of the oversized spherical particle into a spherical hole in the matrix was analytically described by Lee et al.[21]. Using the misfitting sphere model, they calculated strains in plastic zone that surrounds a hard sphere and also the plastic zone radius. Hoffman[22] calculated the overall total strains in the tungsten-fiber-reinforced 80Ni + 20Cr matrix, using a thick wall, long cylinder approach and assuming that a hydrostatic stress-state exists within each constituent.

Garmong[23], assuming uniformity of stresses and strains in the matrix, calculated deformation parameters for a hypotetical eutectic composite, and reported values of matrix plastic strains were of the order of 0.4%.

Dvorak and Rao[24] developed a new axisymmetric plasticity theory of fiberous composites involving large thermal changes. The long composite cylinder model was adopted as a composite unit cell and microstress distribution as well as yielding surfaces were obtained for Al-W composites.

Mehan[25] calculated residual strains in an Al/α - Al_2O_3 composite due to cooling from fabricating temperature. He considered an idealized composite consisting of a long sapphire cylinder surrounded by an Al matrix. This is equivalent to the long cylinder composite model used by Dvorak and Rao.

The above-mentioned composite models, however, do not give an accurate description of the plastic strain state in the short composite cylinder model. A short cylinder model nearly duplicates the stress-strain

distribution about whisker and platelet in SiC-Al composites.

The purpose of these investigations was to experimentally determine the bond strength between SiC and Al in a commerical composite material using the analysis of separation of the inclusion from the matrix under the negative pressure, and relate the bond strengths to the observed fracture surfaces. The second and third purposes of this investigation were to determine experimentally the magnitude of the local plastic strain produced in the Al matrix around a short SiC cylinder during a thermocycle, to estimate the extent of the plastic zone around the cylinder, and also to determine if a relationship could be found between the fracture process and bond strength at the Al/SiC interface.

Experimental Procedure

One volume (1 V%) SiC particulate in a 6061 Al alloy matrix composite purchased from DWA was used for the bond strength investigation. The low volume percent of the particulate was necessary in order to provide favorable conditions for a ductile fracture and thus activate the mechanism of void nucleation and growth type failure. At higher volume concentrations, the Al/SiC composites exhibits very little ductility. The theoretical analysis of the inclusion separation from the matrix that was used in this investigation was based on the assumption that there is no interaction between the particles, which is a reasonable statement for a small-volume concentration.

The composite material was machined to a standard tensile test specimen. In order to introduce a local triaxial stress state, a circumferential groove was electrical discharge machined (EDM) in the center of the specimen (Fig. 1).

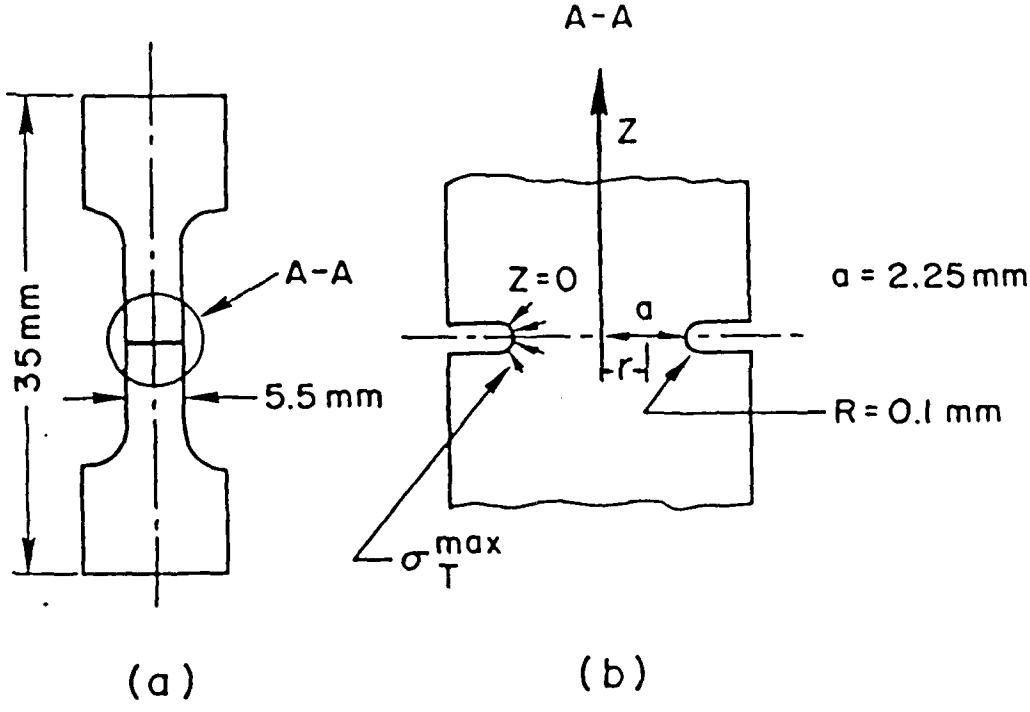

Figure 1 - A schematic view of the specimen (a) and enlarged portion of the groove (b) showing groove geometry and location of the maximum triaxial stresses.

Subsequently, the specimen was annealed and quenched, in order to keep the Mg_2Si phase in the solution and thus limit the presence of particles other than SiC. The specimens were tested in tension to fracture using an Instron testing machine. The fracture halves were cut longitudinally (parallel to the tensile axis) using EDM and mechanically polished.

Polished surfaces were examined for voids between SiC particles and the matrix. The fracture surfaces were examined in the scanning electron microscope (SEM).

The experimental determination of the local plastic strain at the SiC/Al interface in a commercially available Al/SiC composite is practically an impossible task due to very small particle interspacing (several μm). Thus, a composite model consisting of a SiC cylinder embedded into an Al matrix was fabricated to attempt direct strain measurements.

Aluminum of 99.99% purity (to minimize the influence of the alloying elements) and commercial carborundum were used to produce the composite model.

Platelets of SiC were separated from carborundum conglomerates that are used in the production of abrasives. These platelets were spark planed on an EDM to approxiamtely 1 mm thick plates. These flat plates were cut into rectangular ~ 1 mm x 1 mm rods. After this, each rod was spark machined to a cylindrical shape with ~ 1 mm cross sectional diameter.

Pure Al rods, 12.5 mm in diameter in the as-received condition, were cut into 37 mm long studs. Two Al studs and one SiC rod were assembled together and put in a specially built compaction die, where they were hot pressed to produce one compact. Compaction was done on an Instron Testing Machine. During the entire compaction cycle, a vacuum of ~ 10^{-3} torr was maintained using a mechanical vacuum pump.

The central portion of the compacted sample was sliced in the transverse direction into 1 mm thick disks using EDM, set at a low power, and each disk contained a SiC cylinder very close to perfect center (Fig. 2). All Al/SiC disks were metallographically and then electrolitically polished to remove the thin cold worked surface layer of Al.

The method adopted for evaluation of plastic deformation was based on the direct observation of slip bands on the polished surface of the sample around the SiC particles. The amount of slip is a characteristic of the amount of plastic deformation (when deformation occurs by slip) in a crystalline solid. Plastic strain can be evaluated if the number of slip bands and displacement on each band are known. The concept of combined platic shear strain γ_{cpss} has been introduced, where γ_{cpss} is equivalent to a product of slip band density (N) and the amount of slip (S), i.e.,

$$\gamma_{cpss} = K \cdot N \cdot S ,$$

where K = coefficient, taking into consideration different crystallographic situations (K ≈ 3). A detailed treatment of γ_{cpss} and K is given elsewhere[26]. Thus, the method reduces the data collection to the measurements of slip band densities and their heights in the area of interest.

The electropolished Al-SiC disks were separated into three groups: A, B, and C. Each group was heated to about 823 K and then cooled as indicated:

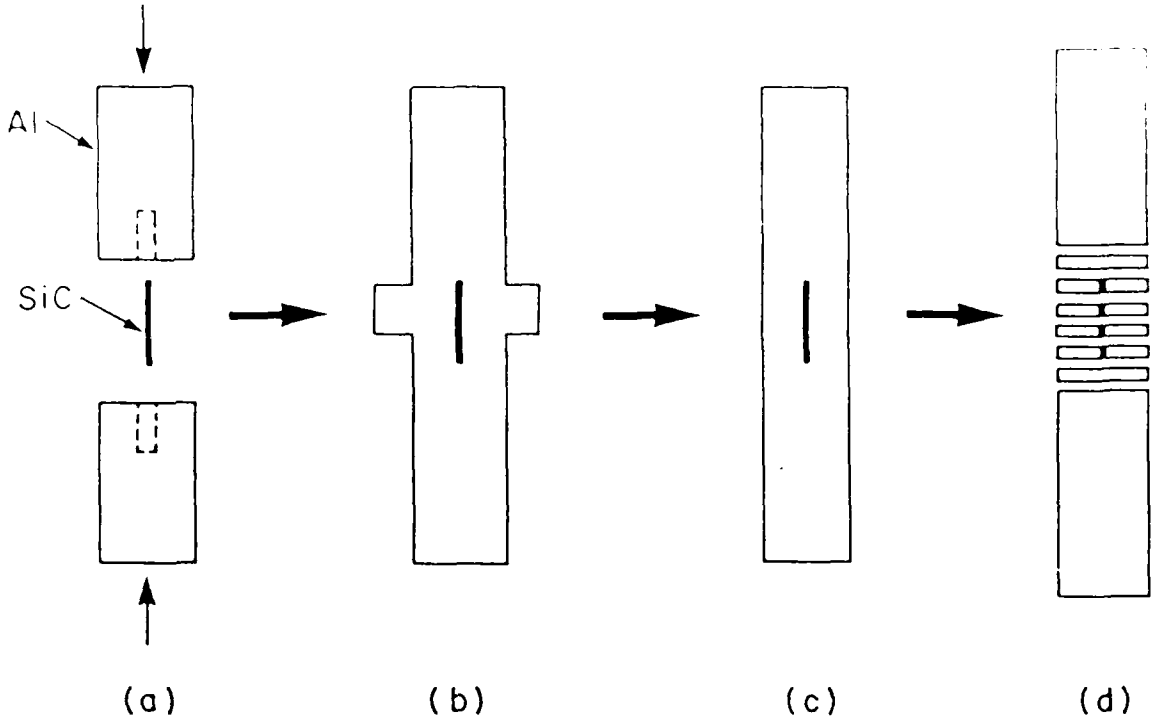

Figure 2 - A schematic of the fabrication sequence of the Al/SiC composite model.

Group A - furnace cooled,
Group B - air cooled,
Group C - quenched in alcohol.

Since the surface of each disk had a high quality polish, slip bands could be observed around SiC in an optical microscope. The slip band density and height measurements were obtained from a Zeiss Interference Microscope. Areas containing slip bands were photographed in white light and in green monochromatic light. Pictures taken in white light gave the actual image of the slip bands. Pictures of the same areas taken in monochromatic light gave interference fringe patterns (Fig. 3). Thus the correlation between slip bands and interference fringes was established which enabled a determination of the height of a given slip band.

Experimental Results and Discussion

Bond Strength

The experimental technique adopted in this work for the Al/SiC interface bond strength estimation was based on the determination of local stresses during plastic deformation under a triaxial stress state[15]. The bond analysis[15] showed that the interfacial stress σ_{rr} can be expressed as

$$\sigma_{rr} = \sigma_T + Y(\bar{e}_p) \quad , \qquad (1)$$

where σ_T is the local negative pressure (triaxial tensile stress), $Y(\bar{e}_p)$ is true flow stress in tension corresponding to the local average plastic strain, had the second phase particle been absent. This analysis was based on the assumption that: (1) particles have an equiaxed shape, and (2) volume fraction of the second phase is small.

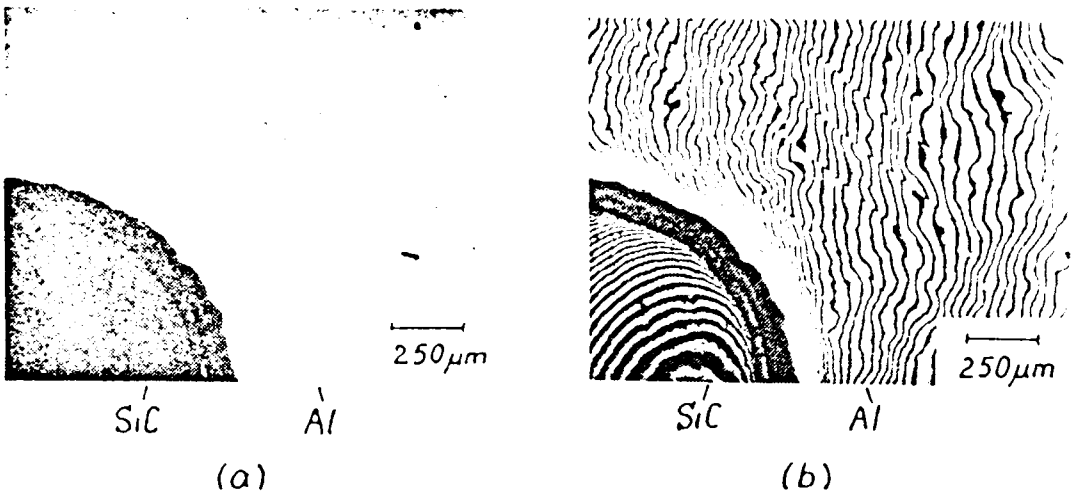

Figure 3 - Slip bands (a) and interference fringe patterns (b) of different areas around SiC.

The distribution of the triaxial tensile stress along the radial line in the plane of the groove was obtained from the theory of stress concentrations on circumferentially grooved elastic bars originally given by Neuber and expressed[15] as

$$\frac{\sigma_T}{\sigma_o} = \frac{c}{\left[1 - \left(\frac{r}{a}\right)^2\right]^{1/2}} \qquad \text{at } z = 0, \qquad (2)$$

where σ_T/σ_o represents the triaxiality. σ_T is the negative pressure, σ_o is the flow stress or average ligament stress, "z" is equal to the vertical distance along the z axis and "r" is the half width of the groove (Fig. 1).

Parameters c and $\bar{a}$ are defined as follows:

$$c = \frac{1 + \frac{a}{R} + \left(1 + \frac{a}{R}\right)^{1/2}}{2\left[2 + \frac{a}{R} + \left(1 + \frac{a}{R}\right)^{1/2}\right]}, \text{ and} \qquad (3)$$

$$\bar{a} = \frac{\left(1 + \frac{a}{R}\right)^{1/2}}{\left(\frac{a}{R}\right)^{1/2}}, \qquad (4)$$

where "a" is the radius of the specimen in the plane of the groove and "R" is the groove radius.

The longitudinal sections of the tested specimen are shown on Fig. 4. In general, the number of voids associated with debonding of SiC particulates was much smaller than the total number of voids related to the fracture. Several examples of the areas where debonded SiC particulates can be observed are shown in Fig. 5. Debonding shown in Fig. 5 is a rather rare event and is not typical of Al/SiCp fractured samples.

According to the Neuber analysic, the largest negative pressure occurs at the outer surface of the groove (see Fig. 1). Since, in general, no separation between the SiC particulates and Al matrix was observed, it is reasonable to assume that for Al/SiC bond:

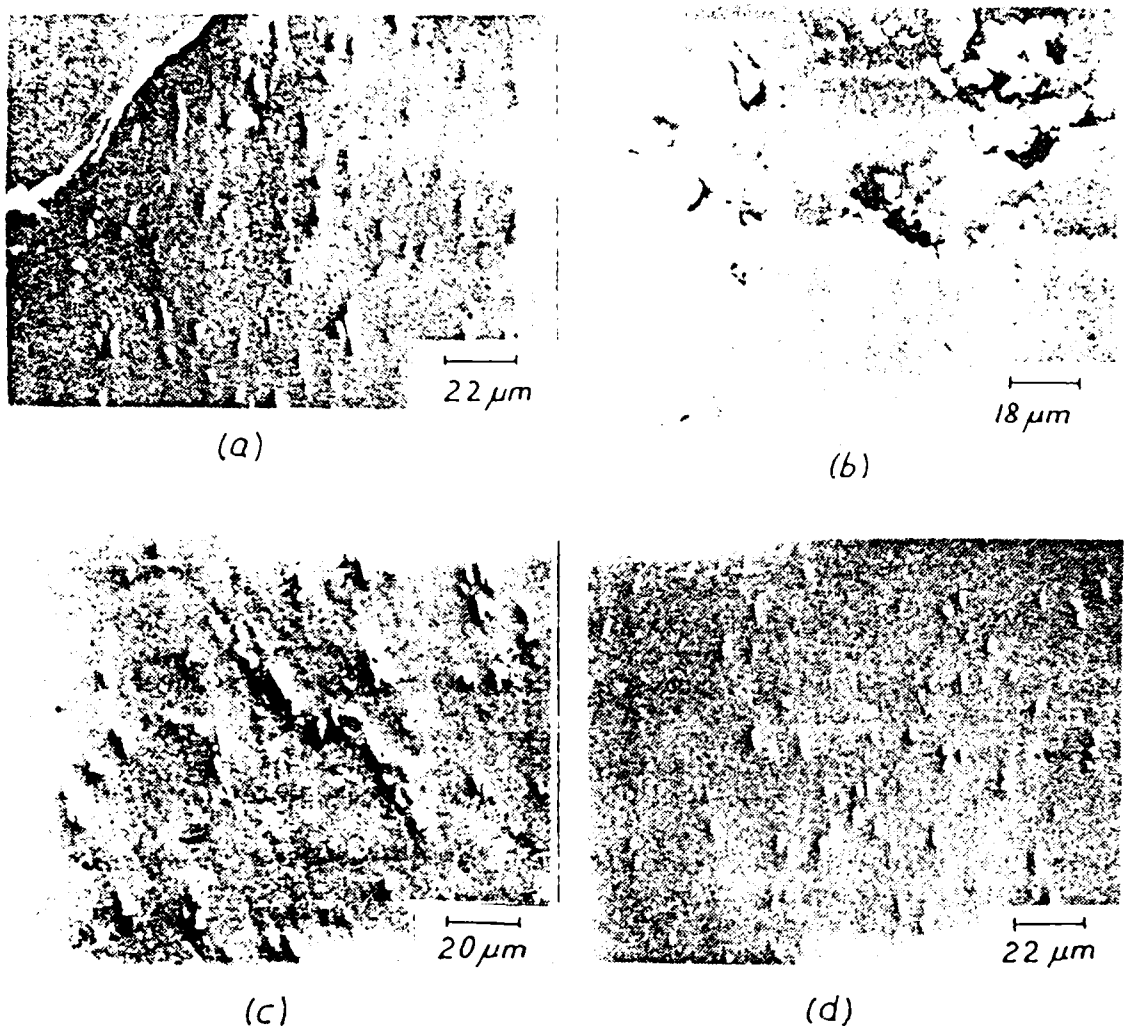

Figure 4 - Electron micrographs of the different areas of the longitudinal cross sections of the fractured 1 V% Al/SiCp specimens. (a) - taken in the vicinity of the bottom of the groove. No apparent debonding is present at the position of maximum triaxial stress. (b) - taken below the fracture surface away from the groove. (c,d) - taken far away from the fracture and represent the bulk of the specimen.

$$\sigma_{rr} > \sigma_T^{max} + Y(\bar{e}_p) \ .$$

Value of $Y(\bar{e}_p)$ was obtained from stress-strain curve as

$$Y(\bar{e}_p) = \frac{P_f}{A_f} = \sigma_o = \text{flow stress} \ , \qquad (5)$$

where P_f will equal the load at failure which will equal 750 kg and A_f will equal the area across the grooved region. The values of "c" and "$\bar{a}$" we get from expressions (3) and (4), respectively. At the bottom of the circumferential groove ($z = 0$) these values are $c = 0.48$ and $\bar{a} = 0.09$.

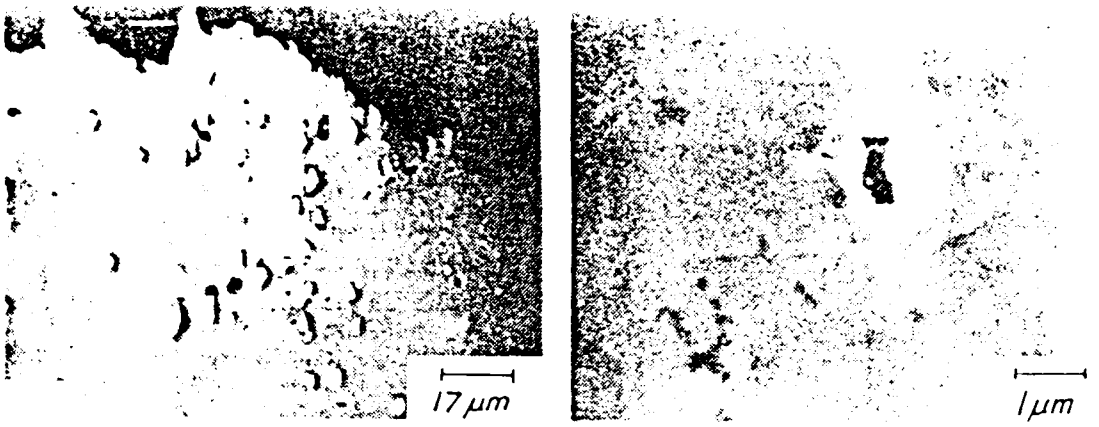

Figure 5 - Electron micrographs of the areas below fracture surface at the bottom of the groove (a) and away from it (b) where debonding was observed.

Substituting Eqs. (5) and (2) into Eq. (1) we obtain:

$$\sigma_{rr} = \sigma_o \frac{c}{\left[1 - \left(\frac{r}{a}\right)^2\right]^{1/2}} + \sigma_o \tilde{=} 1690 \text{ MPa} . \qquad (6)$$

Thus, the lower bound value for Al/SiC bond strength is 1690 MPa. This value is a minimum of 40 times larger than the yield strength of the Al matrix. Therefore, it can be safely stated that the bond is fairly good.

Plastic Zone Size

The experimentally determined values of combined plastic shear strain γ_{cpss} are plotted vs. distance in the form of histogram on Fig. 6. On the same figure we have a plot of effective strain $\bar{\epsilon}$, which was determined theoretically[26]. The histogram represents the actual discrete character of the measurement of γ_{cpss}. Each horizontal portion of the histogram corresponds to the average value of γ_{cpss} obtained from the increment of the area of the specimen.

The largest combined plastic shear strain γ_{cpss} = 1.3% was observed at the SiC-Al interface in Group A samples. Group C showed the lowest amount of strain = 0.99%. In addition, the extent of plastic zone (i.e., the largest distance from the interface at which slip bands can still be measured) was smaller in samples from group C than in samples from groups A and B. This result corresponds to the effect of strain rate (which is proportional to the cooling rate) on the relative amount of plastic and elastic strains during deformation. Generally, higher heating and cooling rates will cause elastic stresses to be larger and lower heating and cooling rates will allow greater plastic relaxation[23].

The height of the slip bands was measured to ± 0.1 band interval. This gives an error of ± 0.1 × 0.27 μm = ± 0.027 μm in the height values. As was mentioned before, the slip band density measurement introduce much less error.

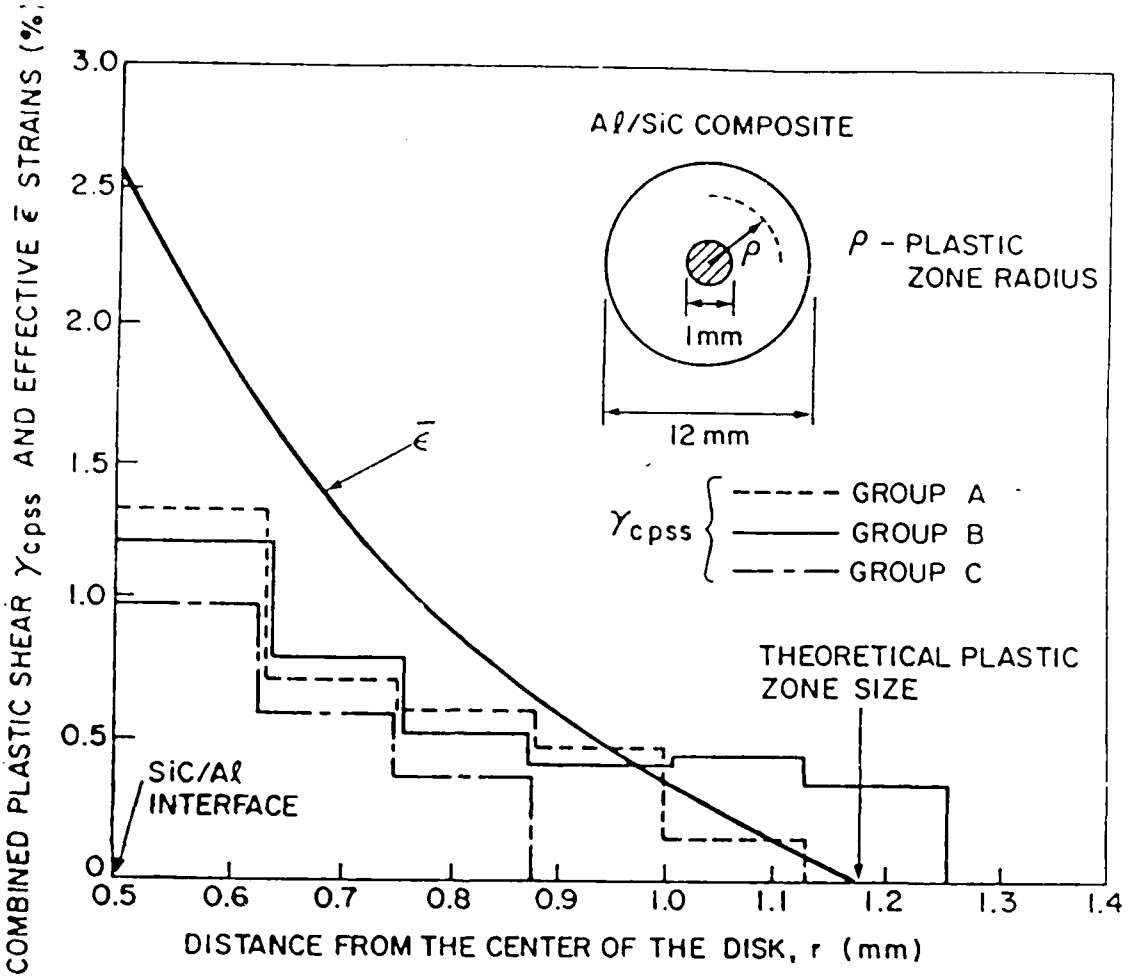

Figure 6 - Theoretical $\bar{\epsilon}$ vs. r and experimental γ_{cpss} vs. r profiles around SiC in Al-SiC composite disks thermocycled between 298 K and 823 K.

Therefore, the error range for γ_{cpss} determination can be evaluated as $\frac{0.027}{0.135} \times 100 \simeq 20\%$ where 0.135 μm is taken as an average slip band height. This is obviously a big range for an error.

The resultant profile of the effective plastic strain $\bar{\epsilon}$ around the SiC particle and the extent of the plastic zone are shown in Fig. 6. As one can see $\rho \simeq 1.15$ mm, and $\bar{\epsilon} = 2.5\%$ at the interface. The theoretical plastic strain is higher than the observed plastic strain, and the theoretical plastic zone radius is smaller than the observed one. The theoretical plastic zone size is estimated on the assumption that deformation is homogeneous, i.e., uniform around the SiC particle. In the real case we have "bursts" of plastic flow in accordance with a particular crystallographic situation. Thus, the extent of the "burst" of plastic deformation can be larger than that of homogeneous deformation since the same amount of plastic flow must be accomodated. The explanation of the difference between observed and calculated strains can be given as follows. On heating, due to differential expansion between Al and SiC, the matrix tends to pull away from SiC. If the bonding between Al and SiC is sufficient to resist the

pulling action, the matrix undergoes deformation proportional to ΔT of the cycle. If, on the other hand, bonding is weak, the matrix breaks away from SiC at a certain temperature T_B and subsequent temperature increase has no effect on matrix deformation since it is now free to expand.

Hot stage observations showed that slip band formation started under 373 K. Accurate evaluation of the temperature at which slip became visible was not possible because thermocouple in the hot stage was not sensitive enough in the temperature range between 298 K and 373 K. It was noticed that more slip bands were formed on the heating half of the thermocycle than on the cooling half. The slip band arrangement on the cooling half repeated the one developed during the heating half. When the temperature approached ~ 773 K, slip bands began to disappear.

Another possible explanation of the stoppage of slip band development is that the Al matrix breaks away from SiC and continues to expand freely without any restraint from SiC. It is also possible that very fine slip bands still continued to form (high temperature creep, for example), but we did not see this due to the limitation in resolution of our optical system. It should be mentioned, however, that disappearance of the slip bands corresponds to similar observations made by Vogelsang, Arsenault and Fisher[4] in their in situ TEM investigation of Al-SiC composites. They observed "slip lines" in thermal-cycled TEM foils, and these slip lines disappeared at high temperatures.

The fact that slip band patterns formed on cooling repeat themselves shows that the same slip systems are engaged in the "reversed" deformation, proving at least partially that there is a certain reversibility of the plastic deformation that occurs when the load is reversed.

Fractography

The observations from the fracture surface can be divided into four groups (almost independent of test method, SiC morphology and volume fraction of SiC): 1) There appears to be initiation sites, 2) macroscopically very brittle but microscopically ductile, i.e., dimple formation, 3) no indication of fracture of SiC; if the SiC particles are < 10 μm in diameter 4) some secondary cracking.

The observations of fracture initiation sites come from three modes; one is fracture of large intermetallic inclusions "fish eyes"; second, clumps of SiC whiskers or particulate and third, void initiation at the SiC whiskers or particulate.

Low magnification observations of the fracture surface shows a single stage appearance. The deep pits of approximately 40 to 100 μm in diameter can be seen throughout the fracture surface (Fig. 7). Each large pit contains an inclusion that has a flat surface (this indicates a brittle character of these inclusions). X-ray analysis revealed a high concentration of Fe and Cr in these inclusions. Subsequently, these inclusions had been termed as "fish eyes" (Fig. 8) due to their shape, and it is believed that they are insoluable intermetallics $(Fe, Cr)_3 SiAl_2$. This compound is encountered in 6061 Al cast and wrought structures. Metallographic examinations of the longitudinal cross-sections of the fractured halves of the tensile samples reveal a large number of the "fish eyes" cracked in the direction perpendicular ot the tensile axis, as shown on Fig. 8. It is possible that these cracks can act as the originators of the fracture.

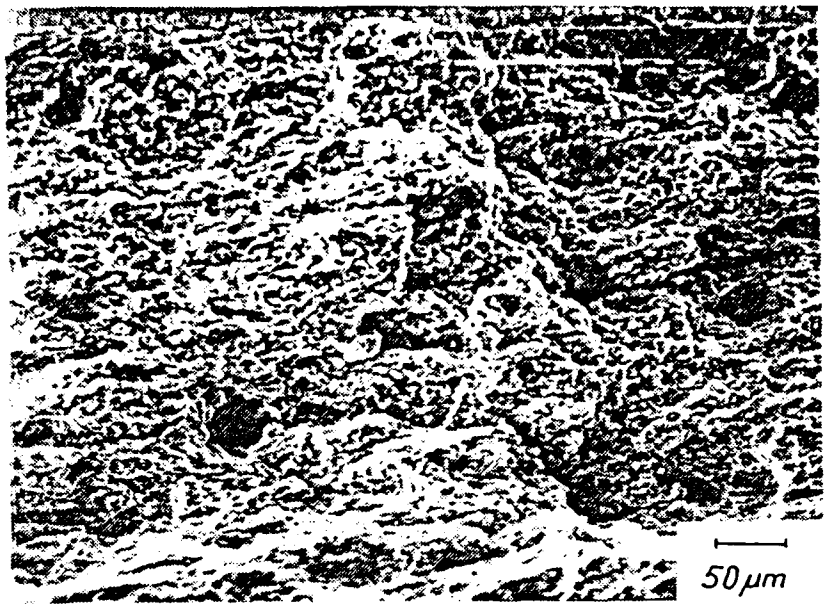

Figure 7 - Fracture surface of DWA 6061 Al/20 V% SiCp in T6 condition.

In a whisker reinforced composite material, a cluster of whiskers can be observed (Fig. 9). These clusters have the appearance of large voids (~ 20 μm) containing clusters of fibers that have not been wetted by matrix during the manufacturing process.

The macro appearance is that of a very brittle fracture, i.e., there is very little reduction in area on fracture. However, at high magnification one can see that the fracture surface consists of very fine dimples, where dimple size is comparable to the size of the SiC particulates (3 to 5 μm). SiC particulates can be seen inside some of the dimples as shown on Fig. 10.

In general, SiC whiskers or particulates are not readily seen on the fracture surface which indicates the presence of the strong bonding between SiC and Al matrix and also shows that fracture of SiC does not take place during the fracture of Al/SiC composite.

At this point an apparent discrepancy between the difficulty of observing SiC particulates on the fracture surface on one hand and a requirement that each dimple must have a nucleation site (partiles, inclusions, imperfections, etc.) on the other hand will be addressed. At the bottom of the dimples in low volume fraction composite, one can notice very fine (fraction of the micron) openings as shown on Fig. 11. Observation of the dimples at high magnification shows that these openings can be traced to the SiC particulates which can be seen on Fig. 12. Etching of the fracture surface and more delicate ion sputtering of the specimens in the chamber of the Auger microscope indeed reinforces this observation (see Fig. 13).

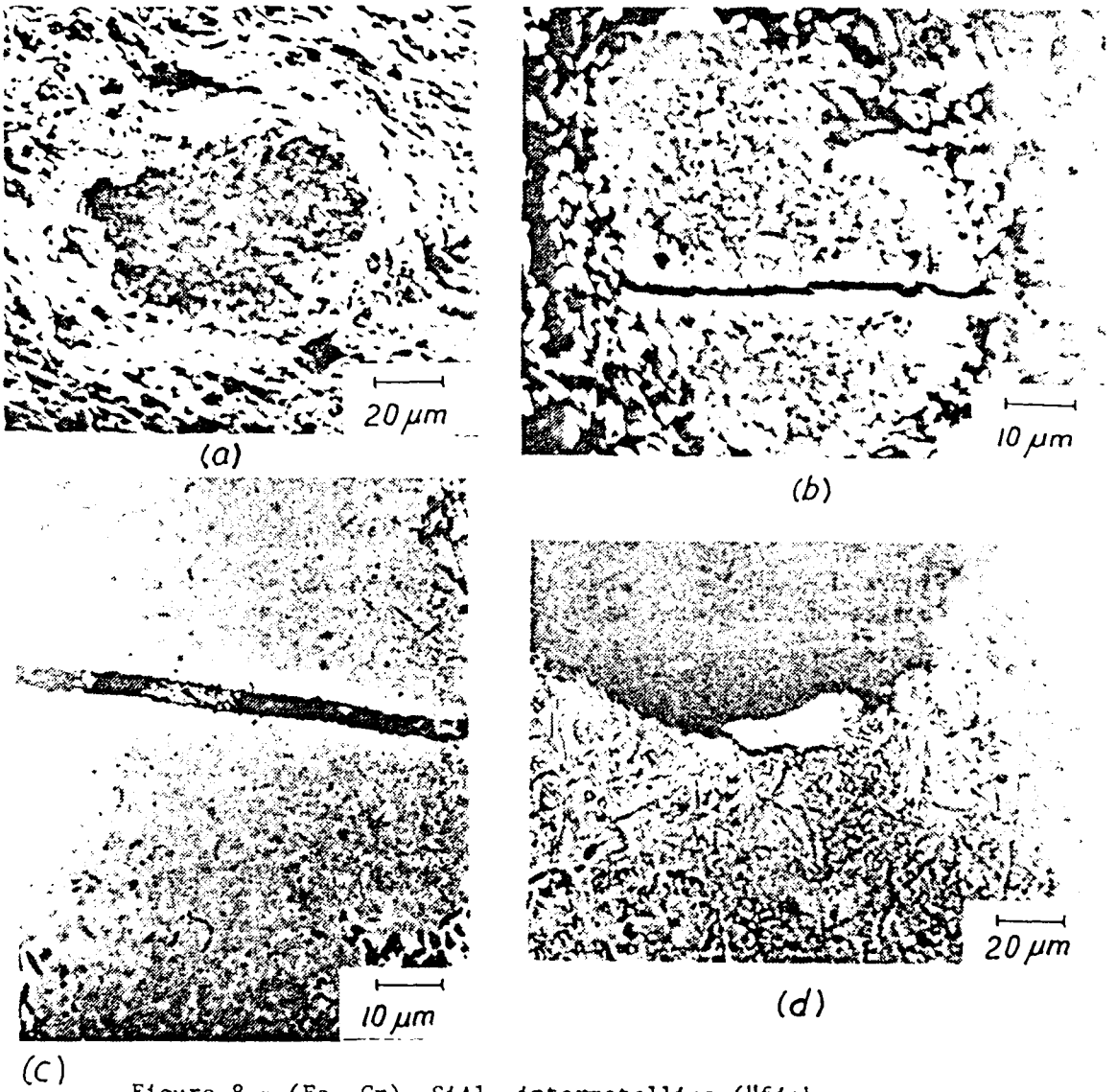

Figure 8 - $(Fe, Cr)_3 SiAl_2$ intermetallics ("fish eyes") on fracture surface (a) and on metallographically polished cross section of the tensile samples (b,c,d). Fracture "fish eye" (d) exposed on the fracture can be seen on micrograph (d). Material is DWA 6061 Al/SiCp - 5 V% and 20 V% SiC.

Voids nucleated in the very small region of the Al/SiC interface grow into the matrix surrounding the particulate as far as interparticle spacing allows them to do so. Thus, in low volume fraction composite these voids grow to the size somewhere in the order of one half of the interparticle spacing as shown on Fig. 14.

On the other hand, in high volume percent composite material, packing of the particles is very tight and, therefore, voids do not have room to grow limiting themselves to the size of the particles on which they initiated (see Fig. 15).

Figure 9 - Cluster of whiskers observed on the fracture surface of Silag 6061 Al/SiCw - 5 V% tested in annealed condition.

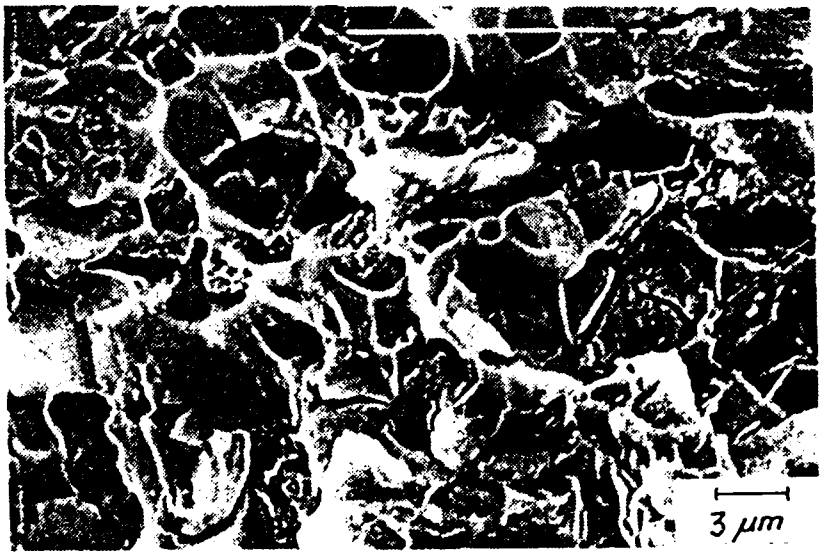

Figure 10 - Typical appearance of the fracture surface of DWA 6061 Al/SiCp composite material viewed under SEM at high magnification.

In addition, it should be pointed out that during the manufacturing process not all SiC whiskers or particulates form a satisfactory Al/SiC bond and, therefore, there is a number of pre-existing voids that do not have to be nucleated to participate in fracture process.

It seems that aforementined observations can be related to the fracture toughness of the composite material. The more room for the void to grow, the higher the resistance of the material to fracture.

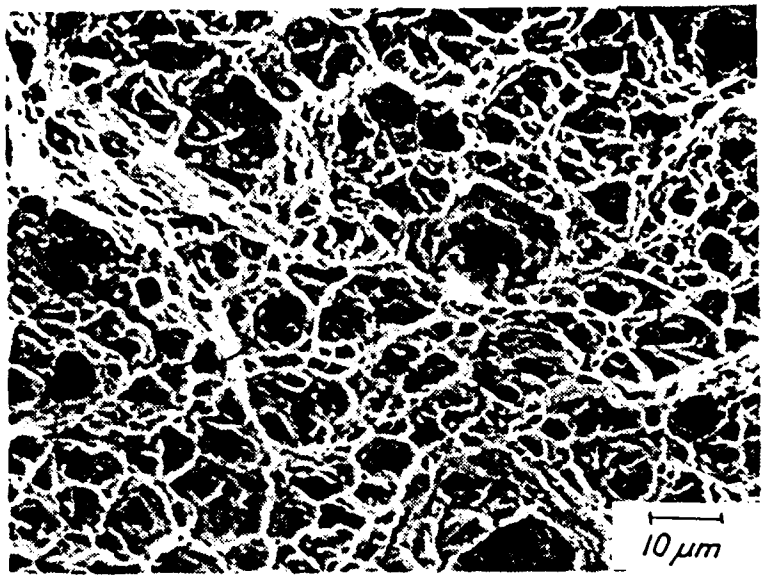

(a)

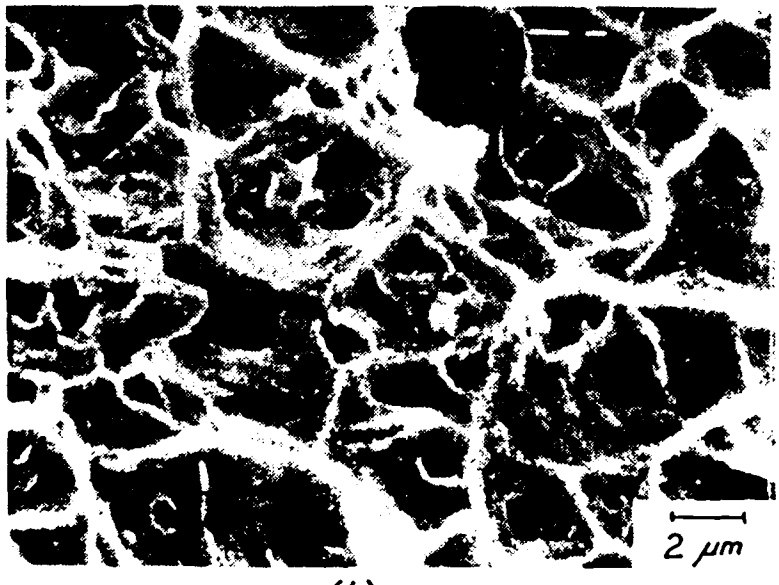

(b)

Figure 11 - Dimpled appearance of the fracture surface with fine openings in the bottom of the dimples at low (a) and high (b) magnfication (1 V% 6061 Al/SiCp).

To further determine if fracture of the SiC whiskers or platelets was occurring, several samples were fractured in the scanning Auger microprobe. The SiC whiskers which could be found as "pulled out" whiskers or at the bottom of dimples were examined, and in most cases Si or C could not be detected on the whisker. Detection of Si and C was possible only after considerable sputtering.

Some fine cracks can be observed on the fracture surfaces of many tensile and/or compact tension specimens. These cracks are oriented perpendicular to the fracture surface and subsequently received the name "secondary" cracks. Several of them are shown on Fig. 16.

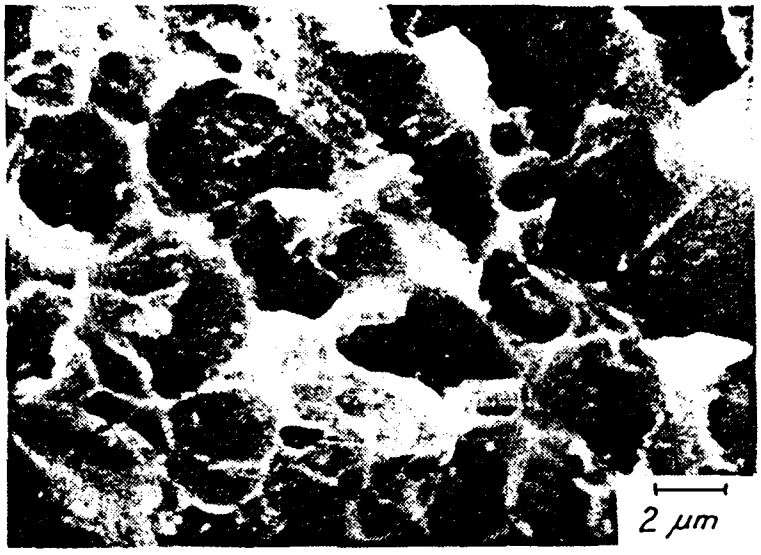

Figure 12 - High magnification of dimpled fracture surface reveals SiC particles.

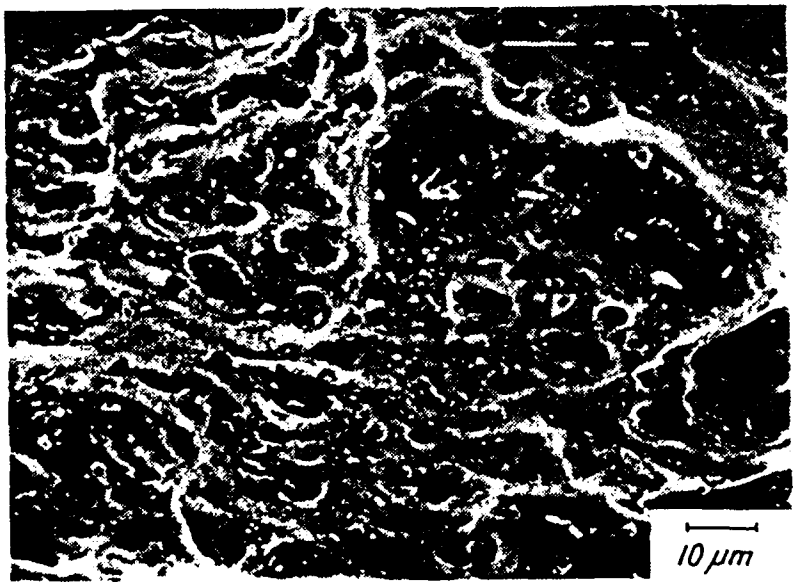

Figure 13 - Chemically etched fracture surfaces of 1 V% 6061 Al/SiCp composite.

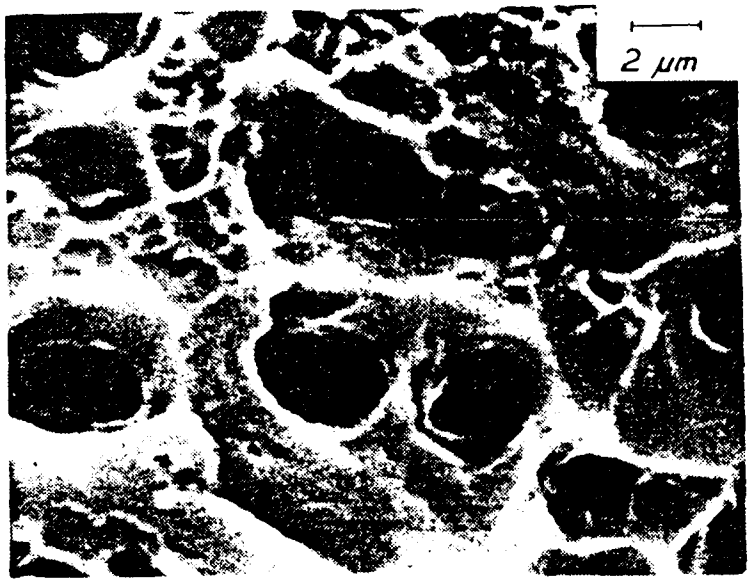

Figure 14 - High magnification of the fracture surface of 1 V% 6061 Al/SiCp showing the extent of dimple growth in the course of fracture.

Figure 15 - Very limited dimple growth taking place during the fracture of 20 V% 6061 Al/SiCp.

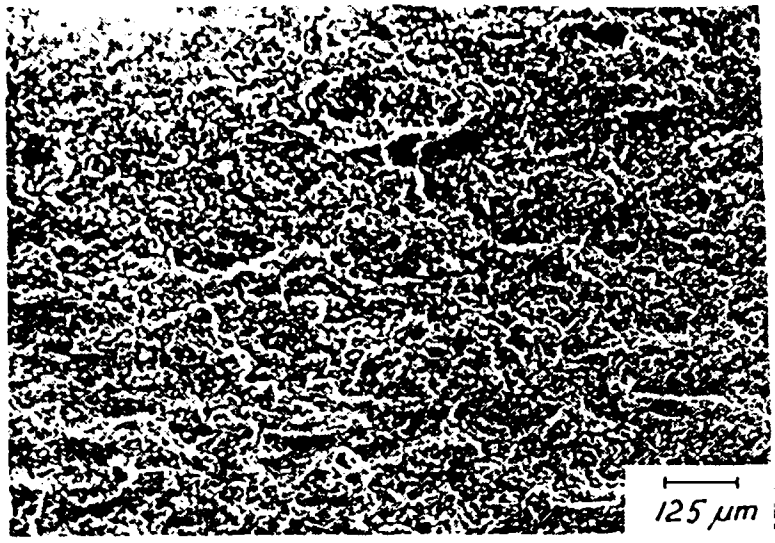

(a)

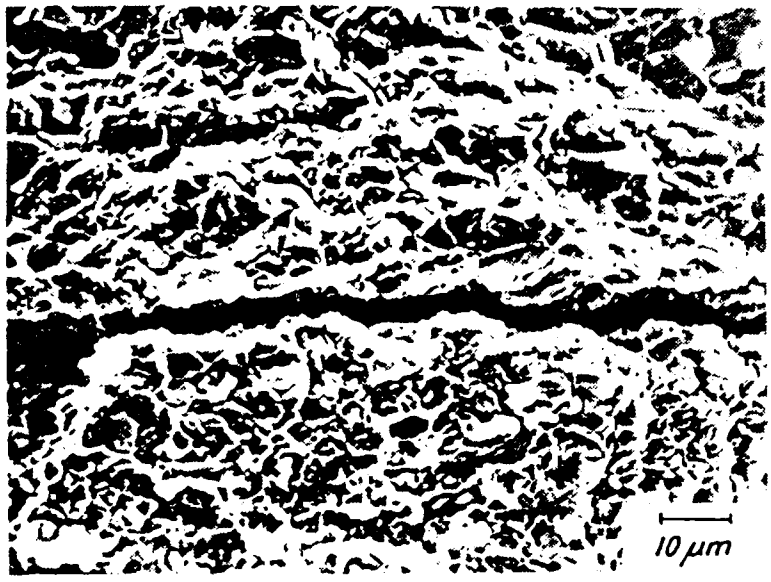

(b)

Figure 16 - Secondary cracks on the fracture surface of compact tension test sample of DWA 6061 Al/SiCp - 25 V% composite material in T6 condition. Both low (a) and high (b) magnifications are shown.

Conclusions

Providing that the above-mentioned assumptions concerning the Neuber analysis are reasonable (and there is no reason to question the assumptions) it can be concluded that the 6061 Al/SiCp bond strength is at least 1690 MPa. (This is 40 times higher than the yield stress of the annealed 6061 Al alloy.) It is thought that debonding can be attributed to the defects during fabrication of the composite material. Ductile fracture of low-volume percent 6061/SiCp occurs by void nucleation at SiC particulates and also at the matrix imperfections (preexisting voids, inclusions, $MgSi_2$, etc.).

From the experimental data obtained concerning the plastic zone size and the theoretical model of plastic zone, it is possible to conclude the following: First, the theoretical treatment of the short composite cylinder

gave the distribution and extent of the plastic strains, which are in fair agreement with experimental results. There is, however, a disagreement between experimental and theoretical values of plastic strains immediately at the Al/SiC interface. Secondly, an Al/SiC bond is a very important factor influencing the plastic deformation around SiC particles.

The fractographic data when examined on a microscopic level gives an impression of void nucleation and growth on the fracture mechanisms, but the observations of voids about SiC is a rare event due to high Al/SiC interfacial bond strength.

Void nucleation and growth is identified as the mechanism governing the fracture process and nucleation part is significantly supplemented by pre-existing voids due to manufacturing defects. Growth of the voids is dependent on the concentration of the SiC particulates or whiskers diminishing almost completely when concentration reaches high (20 V% and higher) values.

References

1. A. Kelly, Strong Solids, 2nd Ed., Clarendon Press, Oxford, 1972.
2. M. R. Piggott, Load-Bearing Fibre Composites, Pergamon Press, 1980.
3. B. D. Agarwal and L. J. Broutman, Analysis and Performance of Fiber Composites, John Wiley & Sons, 1980.
4. R. J. Arsenault and R. M. Fisher, Scripta Met., 17 (1983) 67.
5. M. Vogelsang, R. J. Arsenault and R. M. Fisher, Met. Trans. 17A (1986) 379.
6. R. J. Arsenault, Mat. Sci. & Eng., 64 (1984) 171.
7. A. P. Divecha, S. G. Fishman and S. D. Karmarkar, Journal of Metals, September 1981, p. 12.
8. D. L. McDanels, NASA Technical Memorandum 83610, 1984.
9. L. J. Broutman and R. H. Krock, Interfaces in Metal Matrix Composites, Composite Materials, Vol. 1, Ed. by A. G. Metcalfe, Academic Press, 1974.
10. A. Kelly and W. R. Tyson, J. Mech. Phys. Solids, 13 (1965) 328.
11. L. M. Brown and J. D Embury, Proc. of 3rd Int. Conf. on Strength of Metals and Alloys, Cambridge, U.K., 1973, p. 164.
12. G. LeRoy, J. D. Embury, G. Edward, and M. F. Ashby, Acta Met., 29 (1981) 1509.
13. J. D. Embury, Ductile Fracture in Strength of Metals and Alloys, Vol. 3, Ed. by R. G. Gifkins, Pergamon Press, 1983.
14. A. S. Argon, J. Im, and R. Safoglu, Met. Trans. A, 6A (1975) 825.
15. A. S. Argon, J. Im, and A. Needleman, Met. Trans. A, 6A (1975) 815.
16. A. S. Argon and J. Im, Met. Trans. A, 6A (1975) 839.
17. F. A. McClintock, Ductility, ASM, 1968, p. 235.
18. P. F. Thomason, J. Inst. of Metals, 98 (1968) 360.
19. A. S. Argon, J. Engng. Mater. Tech., 98 (1976) 60.
20. J. D. Embury, Strength of Metals and Alloys ICSMA, 6th ed. by R. C. Gifkins, 1982.
21. J. K. Lee, Y. Y. Earmme, H. I. Aaronson, and K. C. Russell, Met. Trans. A, 11A (1980) 1837.
22. C. A. Hoffman, Journal of Engineering Materials & Technology Transactions of the ASME, (1973) 55.
23. G. Garmong, Met. Trans., 5 (1974) 2183.
24. G. J. Dvorak, M. S. M. Rao, and J. Q. Tarn, J. Composite Materials, 7 (1973) 194.
25. R. L. Mehan, Metal Matrix Composites, ASTM STP 438, American Society of Testing and Materials, 1968, 29.
26. Y. Flom and R. J. Arsenault, Mat. Sci. & Eng., 75 (1985) 151.

END
DATE
FILMED
3-1988
DTIC